GOETHE
UNIVERSITÄT
FRANKFURT AM MAIN

MACROSCOPIC AND MICROSCOPIC POST-MERGER DYNAMICS IN BINARY NEUTRON STARS

Dissertation
zur Erlangung des Doktorgrades
der Naturwissenschaften

vorgelegt beim Fachbereich Physik
der Johann Wolfgang Goethe -Universität
in Frankfurt am Main

von **Luke Bovard**
aus West Vancouver, Kanada

Frankfurt am Main, January 2018
(D 30)

Erstbetreuer: Prof. Dr. Luciano Rezzolla
Zweitbetreuer: Prof. Dr. Almudena Arcones

vom Fachbereich Physik der
Johann Wolfgang Goethe-Universität als Dissertation angenommen.

Dekan: Prof. Dr. Owe Philipsen

Gutachter: Prof. Dr. Luciano Rezzolla
Prof. Dr. Almudena Arcones

Datum der Disputation:

Contents

1 Introduction **1**
1.1 Overview 1
1.2 Notation 5

2 Background **6**
2.1 The Einstein field equations 6
2.2 3+1 formalism 8
2.3 Einstein equation formulations 11
2.4 General relativistic hydrodynamics 15
2.5 Equation of State 19
2.6 Neutrinos 20

3 Tracer particles in numerical simulations **22**
3.1 Introduction 22
3.2 Mathematical and numerical setup 26
3.2.1 Relativistic hydrodynamics and neutrino transport 26
3.2.2 Initial data and grid setup 27
3.2.3 Tracer evolution 28
3.2.4 Tracer mass flux 29
3.3 Tracing unbound material 31
3.3.1 Initial placement 33
3.3.2 Three-dimensional dynamics of unbound tracers 37
3.3.3 Distribution dynamics of unbound tracers 42
3.3.4 Tracer and fluid information 45
3.4 Tracing bound material 50
3.4.1 Initial placement 51
3.4.2 Dynamics of the HMNS 51
3.5 Conclusions 56

4 Rotational properties of HMNS 58
4.1 Introduction 58
4.2 General Framework 61
  4.2.1 Mathematical and numerical setup 61
  4.2.2 Microphysical matter treatment 62
4.3 High-mass binaries 65
  4.3.1 Density evolution and gravitational-wave emission 66
  4.3.2 Angular-velocity evolution: 2D slices 70
  4.3.3 Angular-velocity evolution: azimuthal averages 73
  4.3.4 Temperature evolution 74
4.4 Low-mass binaries 77
4.5 Tracer particles evolution 79
4.6 "Quasi-universal" behaviour 84
  4.6.1 Averaged profiles 84
  4.6.2 Mass in the disk 91
  4.6.3 Influence of the thermal component 94
4.7 On the Bernoulli constant 95
4.8 Time-averaging, symmetries, and resolutions 98
4.9 Conclusions 104

5 Post-merger dissipation 107
5.1 Introduction 107
5.2 Thermal equilibration 108
5.3 Shear dissipation 110
5.4 Bulk viscosity 111
5.5 Conclusions 117

6 Nucleosynthesis in BNS mergers 120
6.1 Introduction 120
6.2 Physical setup and initial data 122
6.3 Methods 124
  6.3.1 Tracer particles and outflow detectors 124
  6.3.2 Selection of unbound material 125
  6.3.3 Nuclear network overview 126
6.4 Overview of simulations 127
6.5 Matter-outflow properties 131
  6.5.1 Ejected-mass 131
  6.5.2 Electron-fraction distributions 135
  6.5.3 Specific-entropy distributions 137
  6.5.4 Ejection-velocity distributions 139
6.6 Comparison of criteria for unbound material 140

6.7 r-process nucleosynthesis 143
  6.7.1 Tracer-input comparison 143
  6.7.2 Heavy-element nucleosynthesis 147
  6.7.3 Angular distributions of ejected matter 149
  6.7.4 Kilonova 153
6.8 Constraints on BNS merger rates 155
6.9 Conclusions 158

7 Conclusions **160**

Acknowledgements **163**

Zusammenfassung **164**

CV **169**

Publications **171**

Chapter 1

Introduction

1.1 Overview

The era of gravitational wave multimessenger astronomy is here. The simultaneous detection of both gravitational and electromagnetic waves by the LIGO Scientific Collaboration and collaborators in August 2017 [263, 264, 148] from the merger of neutron stars heralds the beginning of a new era of astronomy. The simultaneous detection confirms long held conjectures of neutron stars mergers being the origin of short gamma-ray bursts (SGRBs) [184, 78, 210, 27, 36] and the origin of the heavy elements in the universe [139, 138, 78].

It is also an equally exciting time for the field of numerical relativity. Due to the complicated nonlinear nature of the Einstein equations, binary neutron stars can only be modelled numerically and numerical relativity has a critical role to play in the explanation of what has been observed: from the computation of the gravitational wave signal, to the modelling of the merger remnant, to the formation of an electromagnetic counterpart. In the coming years, numerical relativity will play a fundamental role in the emerging field of gravitational wave astronomy.

In anticipation of the detection of gravitational waves from GW170817, the modelling of neutron stars has become increasingly sophisticated in the previous years and significant progress has been made over the last decade to accurately simulate their inspiral, merger and post-merger dynamics [23, 192]. Advances in treatments of more sophisticated microphysics, such as neutrino transport and magnetic fields, have lead to increasingly more realistic simulations and are uncovering a wealth of new physics in both the gravitational and electromagnetic spectrum.

As observed in GW170817, the electromagnetic spectrum of merging neutron stars is rich. In particular, one electromagnetic counterpart that has recently received significant attention is that of a kilonova [146, 222, 196, 107, 194, 272, 123, 228, 201, 124, 229, 174, 258, 26, 219, 275, 168]. A kilonova is an infrared/optical signal powered by the decay of a variety of heavy elements, with a dominant contributions from the elements near the second r-process peak (i.e., $^{133}\mathrm{I}$, $^{132}\mathrm{Te}$ and $^{133}\mathrm{Xe}$), and subdominant ones from the third r-process peak and unstable transuranian elements. These elements can be formed after a BNS merger due to the onset of rapid neutron-capture process. A kilonova has been observed with GW170817 [263], however prior other strong kilonova candidates have potentially already been observed in GRB 130603B [37, 260], GRB 060614 [277, 122] and GRB 050709 [121], but the very large uncertainties in these measurement have so far prevented an unambiguous identification.

The power source of kilonovae is the decay of elements produced during the r-process and throughout the history of our universe this process has given rise to about half of the elements heavier than iron. While its fundamental concept has been known for decades [52], its astrophysical origin has not been unambiguously identified yet. For matter to undergo r-process nucleosynthesis, in fact, a very neutron-rich and explosive environment is required and this puts constraints on the potential astrophysical sites where the process should take place. The two commonly suggested astrophysical sites are core-collapse supernovae and BNS mergers. Recent simulations of core-collapse supernovae (CCSN) have shown that the environment in the outer layers of the explosion is not neutron-rich enough and have been unable to reproduce the observed solar system abundances of heavy elements [117, 116, 83, 273], although rare forms of CCSN driven by magnetic fields are also a possibility [274, 179, 185]. In contrast, neutron star mergers are considered an increasingly likely source of heavy elements. Recent observations of ultrafaint dwarf galaxies [120] have strongly pointed towards BNS mergers being the main site of production of r-process elements.

Furthermore, increasingly sophisticated numerical-relativity simulations with neutrino transport have shown that not only significant amounts of material are ejected (due to a variety of physical processes) in BNS mergers, but the environment in the ejecta provides the necessary conditions to trigger and sustain robust r-process nucleosynthesis. Numerous simulations ranging from Newtonian to full relativistic, with a variety of microphysical treatments, have shown four broad ejection mechanisms. These are: dynamical ejecta [221, 209, 214, 137, 216, 31, 87, 114, 272, 228, 229, 201, 142, 68], neutrino-driven winds [67, 194, 123, 164, 163, 124, 181, 93], magnetically driven winds [237, 131, 245, 211, 59], and viscous evolution of the accretion disk [35, 172, 103, 82]. Their typical time scales are approximately $\sim 10\ \mathrm{ms}$ for dynamical ejecta, $\sim 100\ \mathrm{ms}$ for magnetically driven or neutrino-driven winds, and $\sim 1\ \mathrm{s}$ for viscous evolution. Due to the high computational cost of performing long-term fully relativistic simulations, mostly dynamical ejecta have been studied in full relativity, while other mechanisms have been the subject of mostly Newtonian simulations.

In this thesis I develop a new technique of the use of tracers to study problems in the micro- and macroscopic aspects of post-merger dynamics in binary neutron star mergers, with particular attention to the dynamical ejecta and resulting r-process nucleosynthesis. The use of tracers is a novel concept [45] but has been relatively unexplored in the context of neutron star mergers. Tracers, while appearing to be relatively simple theoretically, do have subtle technical issues that need to be resolved before their use in numerical simulations. Tracers have a long history in the field of fluid dynamics, both in theory and experiment, as they can be used to "trace" the evolution of a fluid that is otherwise inaccessible to the experimentalist. For example, in the evolution of a fluid in a tank, tracers can take the form of a coloured dye which can be used to follow the evolution of vortices in a stratified fluid [46]. In grid based code, the evolution of a fluid is non-trivial to disentangle because the grid is fixed and a fluid element cannot be followed. In contrast, a smoothed-particle hydrodynamics code has this information directly because the evolved quantities are particles which represent the fluid and thus the fluid evolution is trivially obtained.

Although the evolution of tracers is simple - they are passively advected - there are many subtle issues that must be resolved before we can use them in simulations. For example, tracers, by definition are passively advected and thus cannot have any mass as having a mass would violate the passivity condition since they would then have to be taken into account in the energy-momentum tensor. Thus tracers must remain massless. However, despite being massless, it is useful to associate a mass, for example with the calculation of kilonova light curves. In this thesis, we develop a method to do this and apply it to the calculation of r-process nucleosynthesis and kilonova light curves. As we want to compute these physical quantities from the fluid and tracers only represent a sampling of the fluid, in order to ensure that we are correctly sampling the underlying fluid we must ensure that the way the tracers are placed initially is sufficient to properly capture the evolving fluid. I found that the most effective way to place the tracers is uniformly across the distribution of density. At first, this approach seems counter-intuitive as one would expect that when studying material that eventually becomes unbound, one must place a lot of tracers at low-densities near the surface as this material is most likely to be ejected tidally. However in practice this is not the case and doing so oversamples low-density ejecta while undersampling ejecta that comes from deeper in the gravitational potential well.

Using this newly developed tracer method, I apply it to two different areas of the post-merger of binary neutron stars: bound material [110, 8] and unbound material [44]. After the merger of two neutron stars, if there is not prompt collapse to a black hole, a metastable object called a hypermassive neutron star is formed. This object is prevented from promptly collapsing to a black hole through differential rotation [110]. Physically, this represents different regions of the neutron star rotating at different rates and provide additional support to the prevention of collapse. The nature of differential rotation of the hypermassive neutron star is still not a settled question, but recent simulations have shown that the simple model of a constant rotation profile are not found in numerical simulations and that a modification of this law is required. Another interesting feature of the remanent is that there is a phase difference between $m = 2,\ l = 2$ bar mode and the rotation i.e., regions of higher density have lower rotation and regions of lower density have higher rotation. In [110] we found an explanation for this behaviour using tracers restricted to the inner region of the remanent where material remains bounded. Because the tracers allow the fluid lines to be followed, we were able to show that a Bernoulli-like conservation law holds and that as a result of this conservation this reciprocal relationship is a natural consequence of a conserved quantity. Tracers explicitly illustrate this relationship as they allow, for the first time to our knowledge, the evolution of quantities along fluid lines in grid-base numerical relativity simulations.

As further application of tracers to bound material, in [8], tracers were used to analyse the influence of dissipative effects on the post-merger remnant. To model neutron stars, the assumption of a perfect fluid is used, that is a fluid that does not have heat transfer or dissipative effects and the pressure is isotropic. Although this assumption is well met when considering simplified treatments of neutron stars, the inclusion of neutrinos causes the timescales associated with these effects to decrease significantly and potentially become the same order of magnitude as the lifetime of the hypermassive neutron star.

Finally, the tracer method is applied to the creation of the heavy elements in the dynamical ejecta. In order to calculate the nucleosynthesis in a nuclear network, the thermodynamical history of the fluid element is required. This history is needed as it starts the initial reactions in the network. A previously used method [201] required adiabatically extrapolating from a sphere. Although this method is easier to implement it has draw backs as the expansion of the fluid is very close, but not quite adiabatic [45]. Using the tracers, we are able to follow the history of the fluid element that is otherwise inaccessible in a grid-based code. Because tracers are massless, a method must be derived that associates a “mass” with tracers so the final integrated abundances can be properly weighed. Using a variety of equations of state and masses, a systematic investigation of dynamical ejecta with neutrino transport was done using these tracer methods as the central technique to study the resulting r-process. We found that the amount of dynamical ejecta is very sensitive to the various input parameters and faces large systematic errors with the resolution. However, despite these, the average amount of dynamical ejecta is roughly $\sim 10^3 M_\odot$ which is consistent with that observed in GW170817 [265].

This thesis is organised as follows: Chapter 2 deals with all the mathematical, physical, and numerical background needed to study neutron star mergers on supercomputers; Chapter 3 introduces the method of tracers into grid based codes of merging neutron stars and finds the optimum placement to compare with the underlying fluid; Chapter 4 applies this tracer method to bound material and is used to explain the observed phase-difference present in the post-merger remanent of a neutron star merger and its connection to differential rotation; Chapter 5 further applies tracers in bound material to studying the effects of dissipation in the modelling of neutron star mergers; Chapter 6 applies the tracers to the study of unbound material, in particular a comprehensive study of dynamical ejecta from neutron star mergers were simulated and r-process abundances and kilonova light curves were produced; finally Chapter 7 ends with some conclusions and future research directions.

1.2 Notation

Throughout this entire thesis, unless otherwise specified, we use a system of units such that $c = G = M_\odot = 1$, where c is the speed of light in vacuum, G is the gravitational constant, and $M_\odot$ is the mass of the Sun. We use Einstein's convention of summation over repeated indices. Latin indices run over $1, 2, 3$, while Greek indices run over $0, 1, 2, 3$. The spacetime metric signature we adopt is $(-, +, +, +)$.

Chapter 2

Background

This background chapter is meant to provide a bird's eye view of the physics and numerics involved in solving problems in numerical relativity. As much of the material that is presented is standard textbook material, only the most salient features will be discussed. These details given are sufficient to understand the basics of the results presented in this thesis. For detailed discussions of general relativity, numerical relativity, and related topics, we refer the reader to the following numerous excellent textbooks [230, 271, 227, 70, 54, 197, 29, 213, 233].

2.1 The Einstein field equations

We begin with a very high level overview of the Einstein equations. To start we assume that spacetime is represented by a four dimensional manifold $\mathcal{M}$ equipped with a symmetric metric tensor g. For simplicity, we assume that this manifold is sufficiently well behaved to avoid any technical mathematical issues. As the manifold is equipped with a metric, we can represent the infinitesimal distance between two points on the manifold by ds^2, which takes the form

$$ds^2 = g_{\mu\nu} dx^\mu dx^\nu \,, \tag{2.1}$$

where $g_{\mu\nu}$ is the metric tensor and are determined by solving the Einstein equations. This line element defines an invariant distance between two points on our manifold. We choose the signature of this manifold to be $(-,+,+,+)$. This means that there are three different possibilities for the sign of ds^2. We denote $ds^2 > 0$ as *spacelike*, $ds^2 = 0$ as *null* or *lightlike*, and $ds^2 < 0$ as *timelike*. These definitions extend to any scalar, for example the norm of the 4-velocity which we will define later.

From the metric tensor we can now define two important quantities. First are the Christoffel symbols,

$$\Gamma^{\gamma}{}_{\beta\delta} = \frac{1}{2} g^{\gamma\lambda}(g_{\lambda\beta,\delta} + g_{\lambda\delta,\beta} - g_{\beta\delta,\lambda}). \tag{2.2}$$

The Christoffel symbols allow us to define the covariant derivative, which extends the notion of the derivative to curved spaces. For example, for vectors, the covariant derivative is defined

$$\nabla_\mu v^\nu = \partial_\mu v^\nu + v^\alpha \Gamma^{\nu}{}_{\mu\sigma} \,, \tag{2.3}$$

and higher order versions follow similarly. Using the Christoffel symbol, we can define the Riemann curvature tensor

$$R^{\rho}{}_{\sigma\mu\nu} := \partial_\mu \Gamma^{\rho}{}_{\nu\sigma} - \partial_\nu \Gamma^{\rho}{}_{\mu\sigma} + \Gamma^{\rho}{}_{\mu\lambda}\Gamma^{\lambda}{}_{\nu\sigma} - \Gamma^{\rho}{}_{\nu\lambda}\Gamma^{\lambda}{}_{\mu\sigma}. \tag{2.4}$$

The Riemann curvature tensor is defined through the parallel transporting of a vector around in a loop and provides a method of measuring the curvature of a manifold. Although it is a rank-4 tensor, the Riemann curvature tensor possesses numerous symmetries with the most important being the Bianchi identities,

$$\nabla_\lambda R_{\alpha\beta\delta\gamma} + \nabla_\delta R_{\alpha\beta\gamma\lambda} + \nabla_\gamma R_{\alpha\beta\lambda\delta} = 0. \tag{2.5}$$

In total, it can be shown that in 4 dimensions there are only 20 independent components of the Riemann curvature tensor. Continuing with the Riemann curvature tensor, we can define a further tensor from the contraction of two indices. This yields the Ricci tensor and is defined as

$$R_{\mu\nu} := R^{\lambda}{}_{\mu\lambda\nu}, \tag{2.6}$$

which in turn allows us to define the Ricci scalar

$$R := R^{\mu}{}_{\mu}. \tag{2.7}$$

From these ingredients the Einstein equations are defined as

$$G_{\mu\nu} := R_{\mu\nu} - \frac{1}{2} R g_{\mu\nu} = 8\pi T_{\mu\nu} \,, \tag{2.8}$$

where $T_{\mu\nu}$ is the stress-energy tensor that describes the energy-momentum distribution of matter. From the Bianchi identities it can be shown that

$$\nabla_\mu G^{\mu\nu} = 0. \tag{2.9}$$

Given these equations the overall goal is simple, we want to solve the Einstein equations for the metric $g_{\mu\nu}$ for a given fluid configuration $T_{\mu\nu}$. However, due to the complicated non-linear nature of the Einstein equations, there is no possibility of an analytical solution to a neutron star merger. Indeed the idealised two body problem in general relativity cannot be solved exactly so instead a numerical solution must be sought. In the next sections, the machinery required to find such a solution will be developed.

2.2 3+1 formalism

Although general relativity is coordinate independent, in order to solve problems numerically, the computer needs some coordinate system to evolve the equations in. Furthermore, given that the Einstein equations are a set of coupled PDEs, initial data is required. Likewise, because the computer is a finite system, it cannot extend the coordinates to infinity so some boundary conditions must also be specified. Mathematically, the goal is rewrite the Einstein equations as an initial value boundary problem.

We follow the standard approach and derive here the essential features of the 3+1 decomposition of Einstein's equations. The justification for this name is clear, we want to split the equations into a 3D spatial part and a 1D time component. Ideally, this will set-up the Einstein equations as a set of PDEs that evolve in time and can be attacked with numerical methods.

The method to achieve this requirement is to foliate the spacetime into non-intersecting 3D hypersurfaces. It can be shown that if we assume that the spacetime is globally hyperbolic, this condition is always satisfied [213]. With this mathematical technicality satisfied, the idea is simple: spacetime is foliated into non-intersecting spatial hypersurfaces defined by a constant time coordinate t and then these hypersurfaces are evovled according to some evolution equation.

Figure 2.2 illustrates this decomposition. The hypersurfaces Σ are defined by the condition $t =$ constant. Given this constraint, we can define a normal vector **n** to these hypersurfaces. Such a vector can be defined as

$$n_\mu := A\nabla_\mu t = \{A, 0, 0, 0\}\,, \tag{2.10}$$

where the constant A is to be determined. In order to fix this constant, we require that it corresponds to an observer, hence is timelike, and is future-directed. Timelike vectors are normalised such that

$$n^\mu n_\mu = g^{tt}A^2 = -1\,, \tag{2.11}$$

from which we can define

$$\alpha^2 := -\frac{1}{g^{tt}}\,, \tag{2.12}$$

and thus our normalisation vector is chosen to be

$$n_\mu = -\alpha\nabla_\mu t\,. \tag{2.13}$$

with the negative sign chosen to satisfy the future-directed condition. This function α is referred to as the *lapse function* as it measures the rate of changing of

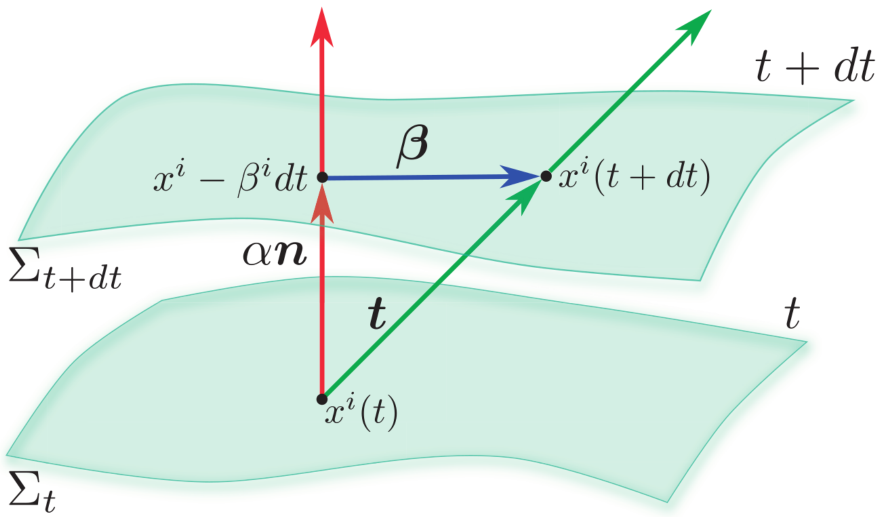

Figure 2.1: figure

Figure 2.2: Illustration of the 3+1 decomposition of spacetime with hypersurfaces of constant time coordinate Σ_t and Σ_{t+dt}. Figure courtesy of [213].

coordinate time along the vector n^μ. Given that we have defined a normal vector, we can also define a projection operators that will project the spatial hypersurfaces. This projection operator is defined as

$$\gamma_{\mu\nu} := g_{\mu\nu} + n_\mu n_\nu \,, \tag{2.14}$$

where $\gamma_{ij} = g_{ij}$ and

$$\gamma^{\mu\nu} := g^{\mu\nu} + n^\mu n^\nu \,, \tag{2.15}$$

where $\gamma^{0\mu} = 0$ but $\gamma^{ij} \neq g^{ij}$. We also denote γ_{ij} as the spatial 3-metric. Another important property of this metric is that $\gamma^{ij}\gamma_{jk} = \delta^i{}_k$ so the spatial 3-metric can raise and lower spatial indices. With this definition, we denote the *spatial projection operator* as

$$\gamma^\mu{}_\nu := \delta^\mu{}_\nu + n^\mu n_\nu \,, \tag{2.16}$$

which will project a given tensor into its spatial, i.e., $i = 1, 2, 3$, components. Similarly we can define *time projection operator* as

$$N^\mu{}_\nu := -n^\mu n_\nu \,. \tag{2.17}$$

In terms of time evolution of the hypersurface, i.e., $\nabla_\mu t$, this is not the direction in which the coordinate t changes. This is clear as

$$n^\mu \nabla_\mu t = \frac{1}{\alpha} \neq 1\,, \tag{2.18}$$

and hence these vectors are not parallel, as the inner product is not 1. To find this vector along which time-evolution is given, we define

$$t^\mu := \alpha n^\mu + \beta^\mu\,, \tag{2.19}$$

where $\beta^\mu = (0, \beta^i)$ is the *shift function*. This vector is constructed[1] from the timelike component αn^μ and spatial component β^μ. This decomposition is illustrated in Figure 2.2 with the green arrow representing $\mathbf{t}$ and the blue and red lines representing the spatial and timelike components respectively. It immediately follows from the definition that

$$t^\mu \nabla_\mu t = 1\,, \tag{2.20}$$

and hence t^μ is parallel to the direction of evolution of the time coordinate.

With the above definitions, it can be shown [106, 213] that the line element in the 3+1 decomposition becomes

$$ds^2 = -\alpha^2 dt^2 + \gamma_{ij}(dx^i + \beta^i dt)(dx^j + \beta^j dt)\,. \tag{2.21}$$

Written in this way, the line element emphasises the origin of the naming of α. If we set $dx^i = 0$ we have that

$$ds^2 = -\alpha^2 dt^2\,, \tag{2.22}$$

which is just a measurement of the proper time between two hypersurfaces, i.e., how much proper time elapses between the two surfaces. Likewise, β^i measures the change in coordinates of a point

$$x^i \to x^i + \beta^i dt\,, \tag{2.23}$$

i.e., how much the point "shifts". Finally the metric written in this form the normal vector becomes

$$n_\mu = \{-\alpha, 0, 0, 0\} \qquad n^\mu = \frac{1}{\alpha}\{1, -\beta^i\}\,, \tag{2.24}$$

and another relation can be derived relating the determinants

$$\sqrt{-g} = \alpha\sqrt{\gamma}\,. \tag{2.25}$$

---

[1] It is easy to verify indeed that $N^\mu{}_\nu t^\nu = \alpha n^\mu$ and $\gamma^\mu{}_\nu t^\nu = \beta^\mu$ as expected.

2.3 Einstein equation formulations

In the previous section, the machinery of the metric was developed that lead naturally to a split into a temporal and spatial part. However, all that has been accomplished is simply re-writing the metric in a different way. To proceed, equations of motion for $\alpha, \beta^i, \gamma_{ij}$ are required. However it is important to note that due to the gauge freedom of general relativity, there is some arbitrariness allowed in the evolution equations. This is due to the Bianchi identities which reduces the number of independent components of the metric from 10 to 6. The remaining four undetermined quantities express the freedom in changing coordinates. It is for this reason that α, β^i are referred to as gauge quantities and can be chosen freely.

To proceed, let us first consider a very general overview of Einstein's equations, with the goal of evolution equations in mind. From Section 1 we have that the Christoffel symbols have a generic structure of

$$\Gamma \sim f(g, \partial g)\,, \tag{2.26}$$

in other words they are some function of the metric and its derivatives. The Riemann tensor, is defined in terms of derivatives of the Christoffel symbols, so the generic structure is

$$R_{ijkl} \sim h(\Gamma, \partial\Gamma) = h(g, \partial g, \partial^2 g)\,, \tag{2.27}$$

in other words the Riemann tensor is some function of the metric and its first and second derivatives. The Ricci tensor is just a contraction of the Riemann tensor so it does not introduce any higher order derivatives. This means that at most, the left-hand side of the Einstein equations is a function of second order derivatives of the metric. A similar situation arises in classical mechanics where Newton's law relates the second order derivative of position $a = \ddot{x}$ to the forces. The common technique in solving Newton's laws is to introduce another variable, the velocity, so the equations change from

$$F = m\frac{d^2x}{dt^2} \to \frac{dx}{dt} = v, \frac{dv}{dt} = F\,. \tag{2.28}$$

In doing this transformation, we have converted a second order differential equation to two coupled first order differential equations. The reason for doing this is that equations of the form

$$\frac{df}{dt} = F(f, t)\,, \tag{2.29}$$

are in practice easier to deal with numerically. Thus our goal is to do a similar thing for the Einstein equations.

To proceed with this decomposition, we first define the following useful operator

$$D_\mu := \gamma^\mu{}_\nu \nabla_\mu \,, \tag{2.30}$$

which is the *three-dimensional covariant derivative* and naturally extends the definition of the covariant derivative to hypersurfaces. It is easy to verify it satisfies the same properties as the regular covariant derivative.

Another useful quantity to define is that of the *extrinsic curvature*, which can be interpreted as how curved a surface is in embedded in a higher dimensional space. Although many equivalent definitions are possible [213], the simplest one is defining it in terms of a Lie derivative of the 3-metric.

$$K_{ij} = -\frac{1}{2}\mathcal{L}_{\mathbf{n}}\gamma_{ij} \,, \tag{2.31}$$

where $\mathbf{n}$ is the normal vector Eq. 2.24. Expanding out the terms results in the expression

$$\partial_t \gamma_{ij} = -2\alpha K_{ij} + D_i\beta_j + D_j\beta_i \,. \tag{2.32}$$

It is important to note that this expression is purely geometrical and the equations of general relativity have not been introduced. This is because the extrinsic curvature plays the analogous role of $v = dx/dt$ is the simple Newtonian example. In order to find an evolution equation for K_{ij} we must use information from the Einstein equations directly.

To achieve this set of evolution equations, we consider projecting the Einstein equations into spatial and temporal quantities.

$$S_{\mu\nu} := \gamma^\alpha{}_\mu \gamma^\beta{}_\nu T_{\alpha\beta} \,, \tag{2.33}$$
$$S_\mu := -\gamma^\alpha{}_\nu n^\beta T_{\alpha\beta} \,, \tag{2.34}$$
$$S := S^\mu{}_\mu \,, \tag{2.35}$$
$$E := n^\alpha n^\beta T_{\alpha\beta} \,. \tag{2.36}$$

With these definitions in place, we first consider the temporal projection

$$n^\alpha n^\beta (G_{\alpha\beta} - 8\pi T_{\alpha\beta}) = 0 \,, \tag{2.37}$$

which yields after some algebra and applications of the Gauss-Codazzi equations [213]

$${}^{(3)}R + K^2 - K_{ij}K^{ij} = 16\pi E \,, \tag{2.38}$$

where ${}^{(3)}R$ denotes the three dimensional spatial Ricci scalar. Likewise K is the tracer of the extrinsic curvature. Continuing with the spatial-temporal projection

$$\gamma^{\alpha\mu} n^{\beta}(G_{\alpha\beta} - 8\pi T_{\alpha\beta}) = 0\,, \tag{2.39}$$

yields

$$D_j(K^{ij} - \gamma^{ij}K) = 8\pi S^i\,. \tag{2.40}$$

Finally the spatial projection

$$\gamma^{\alpha\mu}\gamma^{\beta\nu}(G_{\alpha\beta} - 8\pi T_{\alpha\beta}) = 0\,, \tag{2.41}$$

yields

$$\begin{aligned}\partial_t K_{ij} = &- D_i D_j \alpha + \beta^k \partial_k K_{ij} + K_{ik}\partial_j \beta^k + \alpha({}^{(3)}R_{ij} \\ &+ K K_{ij} - 2K_{ik}K^{k}{}_{j}) + 4\pi\alpha[\gamma_{ij}(S - E) - 2S_{ij}]\,.\end{aligned} \tag{2.42}$$

Thus we have derived the evolution equations for γ_{ij} through Eq. (2.32) and K_{ij} through Eq. (2.42). Additionally, we have two sets of constraints Eqs. (2.40), known as the *Hamiltonian constraint*, and (2.41), known as the *momentum constraints*, which do not involve time derivatives and hence are not evolution equations. Naively, it seems that we have derived an overdetermined system as we have an evolution equation for both K_{ij}, γ_{ij} and a set of four constraints. This is not the case however as Maxwell's equations exhibit similar behaviour with two sets of evolution and equations two sets of constraint equations. Thus in order of a solution to be valid, it must be evolved and satisfy the constraint equations. In typical numerical simulations, this enforcement of the constraints is typically not enforced at each step as doing so involves solving expensive elliptic equations and thus constraints are simply monitored to ensure that violations are not large. Also note that the constraints do not depend on the lapse or shift as the constraints are valid along fixed hypersurfaces and not on their evolution. Thus the lapse and shift must be specified by some other method.

Although we have derived evolution equations, they are still not sufficient for numerical evolution due to their weak hyperbolicity properties. In order to transform them into a more numerically stable form that also ensures hyperbolicity, we do a *conformal tracless transformation*. In particular, we consider the BSSNOK [236, 28, 50] formulation here, however other formulations are possible. For example, CCZ4 [11] is a variation of the Z4 [42] that has better constraint satisfying properties. Indeed, it is an on-going area of research as the CCZ4 system has recently been derived as first-order system [76].

We now proceed with a brief overview of the BSSNOK formulation. We first define some new variables, specifically

$$\begin{aligned}
\phi &= \frac{1}{12}\ln(\gamma) \quad &(2.43a)\\
K &= \gamma^{ij}K_{ij} \quad &(2.43b)\\
\tilde{\gamma}_{ij} &= e^{-4\phi}\gamma_{ij} \quad &(2.43c)\\
\tilde{A}_{ij} &= e^{-4\phi}\left(K_{ij} - \frac{1}{3}\gamma_{ij}K\right) \quad &(2.43d)\\
\tilde{\Gamma}^i &= \tilde{\gamma}^{jk}\tilde{\Gamma}^i{}_{jk}, \quad &(2.43e)
\end{aligned}$$

where $\tilde{\Gamma}^i{}_{jk}$ are the Christoffel symbols computed from the conformal metric $\tilde{\gamma}_{ij}$. The BSSNOK and gauge equations take then the form:

$$\begin{aligned}
\partial_\perp\phi &= \frac{1}{6}\partial_k\beta^k - \frac{1}{6}\alpha K \quad &(2.44a)\\
\partial_\perp\tilde{\gamma}_{ij} &= -2\alpha\tilde{A}_{ij} - \frac{2}{3}\tilde{\gamma}_{ij}\partial_k\beta^k \quad &(2.44b)\\
\partial_\perp K &= \alpha\left(\tilde{A}_{ij}\tilde{A}^{ij} + \frac{1}{3}K^2\right) - \gamma^{ij}\nabla_i\nabla_j\alpha \quad &(2.44c)\\
&\quad + 4\pi(S^k{}_k + E) &\\
\partial_\perp\tilde{A}_{ij} &= e^{-4\phi}\left[\alpha(R_{ij} - 8\pi S_{ij}) - \nabla_i\nabla_j\alpha\right]^{TF} \quad &(2.44d)\\
&\quad - \frac{2}{3}\tilde{A}_{ij}\partial_k\beta^k + \alpha\left(K\tilde{A}_{ij} - 2\tilde{A}_{ik}\tilde{A}^k{}_j\right) &\\
\partial_\perp\tilde{\Gamma}^i &= \tilde{\gamma}^{kl}\partial_k\partial_l\beta^i + \frac{2}{3}\tilde{\gamma}^{jk}\tilde{\Gamma}^i{}_{jk}\partial_l\beta^l \quad &(2.44e)\\
&\quad + \frac{1}{3}\tilde{\nabla}^i(\partial_k\beta^k) - 2\tilde{A}^{ik}\partial_k\alpha + 2\alpha\tilde{A}^{kl}\tilde{\Gamma}^i{}_{kl} &\\
&\quad + 12\alpha\tilde{A}^{ik}\partial_k\phi - \frac{4}{3}\alpha\tilde{\nabla}^i K - 16\pi\alpha\tilde{\gamma}^{ij}S_j &\\
\partial_t\alpha &= -2\alpha K + \beta^k\partial_k\alpha \quad &(2.44f)\\
\partial_t\beta^i &= \frac{3}{4}B^i + \beta^k\partial_k\beta^i \quad &(2.44g)\\
\partial_t B^i &= \partial_t\tilde{\Gamma}^i - \eta B^i + \beta^k\partial_k B^i, \quad &(2.44h)
\end{aligned}$$

where the operator $\partial_\perp$ stands for $\partial_t - \mathcal{L}_{\boldsymbol{\beta}}$, that is to say the derivative with respect to coordinate time minus the Lie derivative along the shift, and the notation $[\ldots]^{TF}$ is used to indicate terms that are made trace free with respect to the conformal metric. The covariant derivatives ∇ and $\tilde{\nabla}$ are constructed from the physical and covariant three metric, respectively, and $\eta \sim 1/M$ (M being the mass of the system).

The three dimensional Ricci tensor R_{ij} is split in two parts, $R_{ij} = \tilde{R}^{\phi}_{ij} + \tilde{R}_{ij}$, where the first involves the conformal factor ϕ and the second the derivatives of the conformal metric $\tilde{\gamma}_{ij}$:

$$\begin{aligned}\tilde{R}^{\phi}_{ij} &= \phi^{-2}[\phi\left(\tilde{\nabla}_i\tilde{\nabla}_j\phi + \tilde{\gamma}_{ij}\tilde{\nabla}^k\tilde{\nabla}_k\phi\right) \\ &\quad - 2\tilde{\gamma}_{ij}\tilde{\nabla}^k\phi\tilde{\nabla}_k\phi] \end{aligned} \tag{2.45a}$$

$$\begin{aligned}\tilde{R}_{ij} &= -\frac{1}{2}\tilde{\gamma}^{lm}\partial_l\partial_m\tilde{\gamma}_{ij} + \tilde{\gamma}_{k(i}\partial_{j)}\tilde{\Gamma}^k \\ &\quad + \tilde{\Gamma}^k\tilde{\Gamma}_{(ij)k} + \tilde{\gamma}^{lm}\left[2\tilde{\Gamma}^k{}_{l(i}\tilde{\Gamma}_{j)km} + \tilde{\Gamma}^k{}_{im}\tilde{\Gamma}_{kjl}\right].\end{aligned} \tag{2.45b}$$

In integrating these equations a constrained approach is used, i.e., we enforce the constraints $\det\tilde{\gamma}_{ij} = 1$ and $\mathrm{tr}\tilde{A}_{ij} = 0$ at every step.

The spacetime evolution is taken care of by the `McLachlan` code [48] to evolve the spacetime variables in the BSSNOK formulation. `McLachlan` approximates the equations using standard central finite-difference operators of fourth-order accuracy [236, 28, 50], with upwinding of the shift advection terms and Kreiss-Oliger dissipation [134] to ensure stability. The gauge conditions are the standard "1+log" and "Gamma driver" choices (see e.g., [29])

2.4 General relativistic hydrodynamics

Until now, we have focused only on the evolution and structure of the left-hand side of the Einstein equations, the spacetime. As such we have left the energy-momentum tensor $T_{\mu\nu}$ unspecified. However, in order to study the evolution of neutron stars, which are composed are a source of energy-momentum, we must now specify a form of this tensor.

A fundamental approach that could be used to define this tensor would be to use kinetic theory and build up the energy-momentum tensor from distribution functions. Such a fundamental approach is possible [213] and we shall see in Section 2.6 that this method of deriving equations of motion is preferred in the evolution of neutrinos. However, a more traditional approach that is found in many textbooks, e.g., [227, 70, 54], is to consider the energy-momentum tensor in the rest-frame of the fluid.

To define the energy-momentum tensor in the rest frame, we make the assumption that the underlying fluid that can be used to model neutron stars is that of a *perfect fluid*. A perfect fluid has no heat transport and no viscosity and the pressure is assumed to isotropic. It can be shown that under these assumptions the energy-momentum tensor for a perfect fluid can be written as

$$T_{\mu\nu} := \rho \left(1 + \epsilon + \frac{p}{\rho}\right) \, u_\mu u_\nu + p \, g_{\mu\nu} \, . \tag{2.46}$$

Here we define

$$u^\mu := \frac{dx^\mu}{d\tau} , \tag{2.47}$$

as the four velocity of the perfect fluid with position x^μ and proper time τ. Another connection that we enforce is that the 4-velocity is timelike,

$$u^\mu u_\mu = -1. \tag{2.48}$$

Additionally, ρ is the rest-mass density, p is the pressure, and ϵ is the specific internal energy. The rest-mass density ρ is, in principle, defined as

$$\rho := \sum_i m_i n_i \, , \tag{2.49}$$

where i represents the particle species, m_i the rest-mass, and n_i the number density. In practice, this quantity reduces to

$$\rho = m_b n_b \, , \tag{2.50}$$

where m_b is the mass of baryons and n_b is the number density of baryons. The reason for this split is that protons and neutrons are the dominant species of particles in the fluid even though other species, such as electrons, are present. Additionally, sometimes another simplifying consideration is to take protons and neutrons to have the same mass and denote the combination as the "baryonic" mass with a value of $m_b \sim 930\,\mathrm{MeV}$.

It is also useful to define two additional useful quantities: the *total energy density*

$$e := \rho(c^2 + \epsilon) \, , \tag{2.51}$$

and the *specific enthalpy*

$$h := \frac{e + p}{\rho} \, . \tag{2.52}$$

The factor of c^2 has been readded in the definition of the total energy to emphasise the origin from the rest mass.

It is a natural question to ask how justified it is to model a neutron star as a perfect fluid. Putting aside concerns of physical issues with constructing non-perfect fluids in general relativity [213], the important factor is whether the dynamical timescale is shorter or longer than the heat or viscous timescales. The dynamical timescale of gravitational systems is given by

$$\tau_{\rm dyn} \sim (G\bar{\rho})^{-1/2}\,, \tag{2.53}$$

and in the case of neutron stars, we take the average density to be the nuclear saturation density $\rho_{\rm nuc} \sim 2.3 \times 10^{14}\,{\rm g/cm^3}$ which leads to a dynamical time scale of

$$\tau_{\rm dyn} \sim 2 \times 10^{-4}\,{\rm s}\,. \tag{2.54}$$

In comparison, and will be further discussed in Chapter 5, the viscous and heat timescales can be on the order of $10^8\,{\rm s}$, although with neutrinos these timescales can be reduced but still remain larger than $\tau_{\rm dyn}$ and this simplifying assumption is justified. Additionally, there are is no implicit preferred directional processes in the merger of neutron stars, so the assumption of isotropic pressure is valid.

Once an energy-momentum tensor has been selected, we can proceed in deriving the equations of motion. As a consequence of the Bianchi identities, we have that the covariant derivative of the energy-momentum tensor is conserved

$$\nabla_\mu T^{\mu\nu} = 0\,. \tag{2.55}$$

In addition to the conservation of energy-momentum another equation must be added, to represent the conservation of rest-mass. This reads as a simple conservation law of the rest-mass density flux as

$$\nabla_\mu(\rho u^\mu) = 0\,. \tag{2.56}$$

Taken together, equations (2.55) and (2.56) are the governing equations of relativistic hydrodynamics. Plugging in the definition of a perfect fluid Eq. (2.46) and doing some basic manipulation, yields the following set of equations

$$u^\mu \nabla_\mu \rho + \rho \nabla_\mu u^\mu = 0\,, \tag{2.57}$$

$$u^\mu \nabla_\mu u_\nu + \frac{1}{\rho h} h^\mu{}_\nu \nabla_\mu p = 0\,, \tag{2.58}$$

$$u^\mu \nabla_\mu e + \rho h \nabla_\mu u^\mu = 0, \tag{2.59}$$

where $h^\mu{}_\nu = g_{\mu\nu} + u_\mu u_\nu$ is the projection tensor.

However there is still additional information that needs to be added. There are 6 unknown quantities are u_i, ρ, ϵ, p^2 but only 5 equations. Thus in order to close the system, an additional piece of information must be given. This is the *equation of state* and relates the thermodynamic variables to each other. We shall discuss

---

[2] Recall that $u_\mu u^\mu = -1$ hence u_μ has 3 independent components instead of 4.

equations of state in Section 2.5 in more detail and for now we simply take it as given that the pressure is given as a function of the thermodynamic variables

$$p = p(\rho, \epsilon)\,. \tag{2.60}$$

Unfortunately, as it currently stands Eqs. 2.57 - 2.59 are not in a form that amenable to numerical methods. In order to so, these equations must be written in *conservative* form in which the well-developed theory of hyperbolic methods [145, 29, 224, 213, 233] may be applied. An system of equations is in conservative form when it takes the following structure

$$\partial_t \mathbf{U} + \partial_i \mathbf{F}^i = \mathbf{S}(\mathbf{U})\,, \tag{2.61}$$

where $\mathbf{U}$ are the vector of unknowns, $\mathbf{F}^i$ are the fluxes, and $\mathbf{S}$ are the source terms which may depend on the unknowns. Integrating over Eq. 2.61 and applying the divergence theorem leads to the classic result of conservation of the given quantity, in the limit of source terms vanishing.

It can be shown [24] that the Eqs. 2.57 -2.59 can be written in conservative form by defining the conserved quantities as

$$\mathbf{U} := \begin{pmatrix} D \\ S_j \\ E \end{pmatrix} = \begin{pmatrix} \rho W \\ \rho h W^2 v_j \\ \rho h W^2 - p \end{pmatrix}\,, \tag{2.62}$$

the fluxes as

$$\mathbf{F}^i := \begin{pmatrix} \alpha v^i D - \beta^i D \\ \alpha S^i{}_j - \beta^i S_j \\ \alpha S^i - \beta^i E \end{pmatrix}\,, \tag{2.63}$$

and source terms as

$$\mathbf{S} := \sqrt{\gamma} \begin{pmatrix} 0 \\ \frac{1}{2}\alpha S^{ik}\partial_j \gamma_{ik} + S_i \partial_j \beta^i - E\partial_j \alpha \\ \alpha S^{ij} K_{ij} - S^j \partial_j \alpha \end{pmatrix}\,, \tag{2.64}$$

where we have introduced some additional definitions of the 3-velocity v^i,

$$v^i := \frac{1}{\alpha}\left(\frac{u^i}{u^t} + \beta^i\right)\,, \tag{2.65}$$

and the Lorentz factor W

$$W := \frac{1}{\sqrt{1 - v^i v_i}} = \alpha u^t\,, \tag{2.66}$$

and all other quantities are defined as in Section 2.2. This formulation is known as the *Valencia formulation* due to significant work originating from Valenica, Spain.

With this formulation, the equations of hydrodynamics have been converted into a form that makes them amenable to numerical methods. The numerical scheme used to solve the hydrodynamics evolution equations is a finite-volume method applied to the above flux-conservative formulation. To solve this scheme, we use the code `WhiskyTHC` code [202, 204] which implements the above equations into the EinsteinToolkit. `WhiskyTHC` makes use of a fifth-order MP5 [253] reconstruction operator, the HLLE Riemann solver [111] and the positivity-preserving limiter of Ref. [115, 204]. Additionally, the refluxing technique [38] is used to minimize numerical spurious losses or gains of mass at the interface between refinement levels. Although this specific system has been used, an interesting alternative approach has recently been developed that uses entropy as a method to solve the hydrodynamics equations [108].

2.5 Equation of State

In order to solve Eqs. 2.57-2.59, one additional equation must be specified, the equation of state (EOS). The equation of state is derived independently of the evolution equations and must be provided. For example, the simplest equation of state, that also have been used sigificantly in numerical relativity, is that of an ideal gas. It can be shown that the EOS for this simple case takes the form of a polytrope, i.e.,

$$p(\rho) = K\rho^{\gamma}\,, \tag{2.67}$$

where K is the polytropic constant and Γ is the polytropic index. For example, it can be shown that for a degenerate non-relativistic electronic fluid, the polytropic index is $\Gamma = 5/3$ [213]. Building from this simple description, piecewise polytropes are also used, which consist of multiple polytropes with different polytropic indices and are matched at the boundaries.

In general, the equation of state depends on more thermodynamical variables such as the rest-mass density or temperature, which are difficult to model with simplistic treatments such as the polytropic EOS. Currently, the most general form of EOS used in numerical relativity are those that have a temperature-dependence whereas polytropes are "cold" i.e., $T = 0$, although hybrid EOSs that have a thermal component can also be used. The use of a temperature-dependent equation of state is essential because in order to include neutrino effects, the composition and temperature of the fluid are required.

So in order to close the system of equations (2.68) and (2.69) an equation of state (EOS) of the form $p = p(\rho, \epsilon, Y_e)$ is required, where ρ is the rest-mass density, ϵ is the specific internal energy, and Y_e is the electron fraction.

In this thesis, temperature-dependent equations of state are used, spanning a wide range in stiffness. From the stiffest to the softest, these EOSs are: (i) DD2 [269]; (ii) LS220 [140] with compressibility parameter $K = 220\,\mathrm{MeV}$; SFHO [249]. Note that recent calculations in Ref. [261] have shown that the LS220 EOS does not satisfy constraints stemming from a lower bound on the energy per nucleon provided by the unitary-gas approximation. This result disfavours the LS220 as a viable model for the microphysics of neutron stars, but since this EOS is also one of the most well-studied in numerical applications, we include it in our study since it provides a useful comparison with the literature. Additionally, the DD2 and SFHO EOSs include additional light nuclei that are not included in the LS220 and these change the neutrino interactions [250].

2.6 Neutrinos

In the previous sections, the physics that would be simulated is a somewhat simplified view of neutron stars as it lacks any type of microphysics. In the context of mergers, there are two important sources of microphysics that must be added in, each with their own complications. The two types of microphysics are electromagnetic fields and neutrino transport. The inclusion of electromagnetic fields yields the theory of general relativistic magnetohydrodynamics (GRMHD) [213]. In this work we do not include any magnetic fields. Instead, the focus is on the influence of neutrino microphysics in the post-merger evolution of a neutron star. Neutrinos change the composition of the material and play an important role determining the initial conditions under which nucleosynthesis takes place.

In terms of dynamical evolution, neutrinos play a relatively minor role as during the post-merger phase they remain trapped until $\mathcal{O}(100\,\mathrm{ms})$ after merger when the diffusive timescale from the trapped regions starts to cool the star [193], although a further refinement in the context of viscous dissipation will be given in Chapter. 5. Instead, neutrinos play an important role in material ejected by the merger where neutrinos are free-streaming. Here, weak interactions significantly change the composition of the ejecta depending on the rest-mass density and the temperature, as will be discussed in detail in Chapter 6.

In the idealised case, neutrino transport would be governed by a Boltzmann equation. However, this equation is a 7D dimensional equation in, 4 terms for the spacetime position and 3 for the momentum, and too computationally infeasible for inclusion in current numerical relativity codes. Instead, a simplification must be used. The scheme we consider here is the simplest scheme a so-called grey leakage scheme [95]. Grey schemes integrate over the energy and assume that the neutrinos have an average energy. Spectral schemes (i.e., non-grey) have been used in numerical relativity however only with Newtonian-based codes [194]. Alternative approaches to leakage schemes are so-called moment-based schemes, such M0 [201] or M1 [235].

To take into account neutrinos in a leakage schemes, changes in energy due to neutrino are approximated by neutrino emission source terms. These source terms are derived from the theory of weak interactions and cause the baryon number to change. Typically, baryon number is conserved, however when neutrinos are included, a source term must be added to the conservation equation because beta decay can convert neutrons and protons into electrons and neutrinos (and vice-versa). This change modifies the continuity equation and can be written as

$$\nabla_\alpha(n_e\, u^\alpha) = R\,, \tag{2.68}$$

where n_e is the electron-number density and where R is the net lepton number emission/absorption rate per unit volume in the fluid rest-frame, which is a function of input neutrino interactions which depend on the thermodynamical properties such as rest-mass density. Likewise, the conservation of energy and momentum now becomes, with the introduction of sources

$$\nabla_\beta T^{\alpha\beta} = Q u^\alpha\,, \tag{2.69}$$

and Q is the net neutrino cooling/heating rate per unit volume in the fluid rest-frame [201]. A detailed discussion on the computations of Q and R within the `WhiskyTHC` code employed here is contained in Refs. [95, 201] which include numerical implementation details of the leakage scheme and the interactions included.

Chapter 3

On the use of tracer particles in simulations of binary neutron stars

In order to study the effects of macro- and microphysics in the post-merger dynamics in binary neutron star mergers, this chapter is dedicated to the discussion of the method developed in order to study these regimes in a novel way that hereto has been unused in grid-based numerical relativity simulations[1]. The techniques derived in this chapter will be used in the remaining chapters so explore macroscopic and microscopic effects in the post-merger of a binary neutron star merger.

3.1 Introduction

The question of what astrophysical process produces the heavy elements have been a topic of extensive discussion since it was first suggested in the 1970s [139] that r-process would be produced in the merger of compact objects. Prior to the detection of GW170817, the site that had already received significant interest was the possibility that BNS mergers would be the most likely progenitors of the heavy elements in the universe [139, 146, 260, 37, 259, 220, 228, 201]. The detection of gravitational waves from GW170817 along with the follow-up kilonova appear now to have completely confirmed this prediction and will be discussed further in Chapter 6. As such, a detailed method to study the ejected material is required.

During the initial post-merger stages of a binary neutron star merger, a significant amount of material, known as *dynamical ejecta*, is ejected due to tidal interactions and from various numerical simulations is on the order of $10^{-2} - 10^{-4}\,M_{\odot}$ [114, 31, 201, 68, 69] and this material exists in an environment that is

---

[1] This chapter is based on the work of [45] where I was the first author. All figures in this chapter have been reproduced from [45]. My contribution to the work of [45] was to run all the simulations, analyse all the data, generate all the figures, and write all the text of the paper.

very conducive towards rapid process neutron capture, r-process, nucleosynthesis [146, 223, 16, 171, 214].

A neutron rich environment is required for r-process reactions to occur and thus this limits the potential astrophysical sites that could produce the r-process elements and mostly restricting it to compact objects. The paradigm, for many years, was thought that core collapse supernova (CCSN) were the source of the heavy elements in our universe [217, 163]. However, recent recent improvements in the simulations of CCSN have shown that although CCSN eject sufficient amounts of r-process rich material, the environment around the explosion does not appear to be sufficiently neutron-rich enough to reproduce the observations of the abundances observed in the solar system [15]. Furthermore, recent observations of metallicity in ultra-faint dwarf galaxies, specifically that of Reticulum II disfavours CCSN and instead point towards BNS mergers as being the primary source of r-process [120]. Specifically, to explain the yields of barium and europium measured in this ultra-faint dwarf galaxy would require approximately ~ 2000 supernovas would be required whereas a single neutron star merger would be sufficient.

In the context of numerical simulations, and prior to GW170817, BNS merger simulations have been significantly improved with neutrino microphysics and have further provided numerical evidence that supports the BNS merger scenario as being the main progenitor of r-process as the ejecta from the mergers is very neutron rich [23]. Furthermore, as this ejected material expands, it was conjectured, and definitively verified with GW170817, that the material would undergo radioactive decay and could potentially create an electromagnetic counterpart, the so-called "kilonova" [146, 258, 168]. With the detection of GW170817, a kilonova was observed and hence, there is vested interest in accurately studying the composition, evolution and outflow from a BNS merger and the different types of mechanisms that can cause the fluid to undergo nucleosynthesis.

From extensive numerical simulations, four types of ejection channels have been classified: dynamical ejecta [209, 214, 137, 216, 31], neutrino-driven winds [67, 194, 272, 123, 228, 164, 163, 124, 229, 182], magnetically driven winds [237, 131, 245, 211, 59], and viscous evolution of the accretion disc [103, 128]. All these ejection channel classifications have different ejecta properties in total amount of ejected material, electron fraction compositions, velocities, and so on, which can produce different nucleosynthetic signatures and different light curves emitted from a kilonova, [222, 196, 107, 194, 272, 123, 228, 201, 124, 229, 258, 168] and a discussion of the results of such a calculation will be done in Chapter 6.

An essential piece of physical information needed in order to study the nucleosynthesis produced from these different categories of ejecta is that of the thermodynamic history of the ejecta, i.e., the temperature, entropy, and electron fraction, of a fluid element is required. By following the fluid through a simulation, a time series of every quantity is produced and then can be used as the input for nuclear-reaction networks to determine the abundances of the different elements [163]. However, the timescales required for the nuclear reactions to occur is on the order of seconds to days, and these timescales are far beyond the current capabilities of numerical-relativity codes, which can run at most a few tens of milliseconds after the merger in full 3D and at most a few seconds assuming axisymmetry. As such, this presents a problem on how to evolve and solve the two physical process simultaneously.

In the ideal case, a nuclear-reaction network would be solved simultaneously with the fluid evolution in the simulation, however currently this is numerically infeasible due to the vast timescales required for the evolution of the nuclear network - potentially reaching several years of simulated time - so all nuclear reactions must be treated in a post-processing step. Furthermore, the different classifications of ejecta mechanisms have different timescales over which they dominate, ranging from $\sim\,10\,\mathrm{ms}$ for dynamical ejecta, to $\sim\,1\,\mathrm{s}$ for the viscous ejecta in the disk. This difference in timescales requires different numerical models and physical assumptions to be made and thus to overcome these technical issues and various approaches have been used by numerous groups to study these systems in detail.

One approach is to use Newtonian codes, eschewing general relativity completely [82, 163]. An advantage of Newtonian codes is that they are computationally and mathematically much simpler and can be run for longer times. Hence, they have been used to study the long-term evolution of the fluid as it outflows, such as that required by the neutrino driven winds – which has timescales of $\sim\,100\,\mathrm{ms}$ [163] – and the viscous forces of the accretion disk [82]. These codes also study the nucleosynthesis produced from the ejecta and the fluid history is recorded by tracer particles (hereafter simply "tracers"). Another approach is to use smoothed particle hydrodynamics (SPH) [196, 220, 107, 170, 163] instead of grid-based codes. One major advantage here is that it allows for exact evolution of the fluid's thermodynamic properties because the fluid itself is made of interacting particles. While this approach is beneficial for the nucleosynthesis analysis, normally it does not provide solutions in full general relativity. Furthermore this approach cannot be evolved for the long term as the Newtonian codes can. Finally, for grid-based codes which fully solve the Einstein equations, there are two approaches that have been used to follow the thermodynamic history of the ejecta. The first is that of tracers which passively follow the fluid as it evolves recording the properties of the fluid as it evolves [272], providing a history of the fluid lines. The second is to use a spherical surface that the fluid passes through and use that as the initial conditions for the ejecta; assuming the fluid to be undergoing adiabatic expansion, it is then possible to extrapolate the dynamics to long timescales [201]. While both methods can successfully reproduce the r-process, [272, 201, 44], there is a benefit in using the former over the latter. The second method, in fact, is simpler to implement but it does not allow for the history of the fluid element to be recorded. With the thermodynamical history of the fluid element, the tracers are able to be input into radiative-transfer codes that allow for the calculation of kilonova light curves [107]. Thus, it is important that the tracers accurately represent the underlying fluid.

Besides the study of the ejected matter, another area of research in which the use of tracers is particularly beneficial is the evolution of the binary merger product (BMP), that is, of the metastable object that forms after a binary neutron merger. Significant work recently has gone into understanding the nature of the stability of this BMP [23] and tracers provide a novel way of interpreting the resulting behaviour of the BMP that is otherwise inaccessible to only studying the fluid evolution [110, 8].

Although simple in principle, the use of tracers in numerical relativity is far from settled. As observational quantities can be computed from tracer data, it is critical to ensure that the tracers used accurately represent the underlying fluid. As such, many issues such as the effects of placements of the tracers and of assigning tracers mass have not been adequately discussed or settled. Furthermore, tracers are an inherently particle-based idea while the most advanced GR simulations use a grid-based code. Thus relating how tracers properly relate to the underlying fluid requires special care which we discuss in detail. In this Chapter, I present and implement the first detailed discussion of the use tracers in numerical-relativity simulations. Focus is paid to two explicit areas in particular: *unbound material* in the form of dynamical ejecta, and *bound material* in the core of a BMP formed from the merger of two neutron stars.

More specifically, when considering unbound matter the question of how well the tracers match the underlying material is essential as it has important implications for kilonova modelling cf. Chapter 6. To investigate this question, I have evaluated four different placement schemes that could be used to initially distribute the tracers and how well their predictions match those obtained when using information from the actual fluid flow. Contradicting our naive expectations that the best placements are those that are correlated with the rest-mass density distribution or that follow the fluid that is marked unbound, it is shown that the most effective method to initially distribute tracers is to simply *uniformly* sample across the rest-mass density distribution as this leads to the closest matching with the hydrodynamical information on the unbound material flowing across the computational domain.

In contrast, the question of *bound material* represents a different goal as detailed thermodynamical evolution of the tracers is not required. Here, the goal is to simply sufficiently follow as many tracers as possible to ensure a good sampling of the evolution of the fluid within the merger remanent. Here, I have show that tracers can provide insight into the stability of the BMP as they can be used to track the evolution of fluid elements or to calculate the evolution of quantities conserved along streamlines that would otherwise be inaccessible in a grid-based code [110, 127] which will be used in Chapters 4 and 5. Such a method of investigating the evolution of a fluid has not been fully explored and here I introduce the power of this method to answering complicated physical problems with simple physical answers.

This chapter is organised as follows: in Sec. 3.2 I review the mathematical and numerical setup employed to solve the equations of relativistic hydrodynamics but also those describing the motion of the tracers and their analysis. Section 3.3 is instead dedicated to the study of the dynamics of unbound material and to the discussion of the various placement schemes that we have considered. The results in this section should be contrasted with those presented in Sec. 3.4 for bound material, where we analyse tracers in the core of an HMNS produced by a BNS merger. Finally, in Sec. 3.5 I summarise our results and discuss how these results will be applied to the work of Chapters 4-6.

3.2 Mathematical and numerical setup

3.2.1 Relativistic hydrodynamics and neutrino transport

Although already discussed extensively in Chapter 2, I will repeat the basics of the simulation set-up to make this discussion as self-contained as possible and also remind the most salient features that are required for the evolution of the tracers.

Recalling this, Einstein's theory of general relativity can be written as

$$R_{\mu\nu} - \frac{1}{2}Rg_{\mu\nu} = 8\pi T_{\mu\nu} \,. \tag{3.1}$$

In order to solve the above equations, we use the 3+1 decomposition

$$ds^2 = -(\alpha^2 - \beta_i\beta^i)dt^2 + 2\beta_i dx^i dt + \gamma_{ij}dx^i dx^j, \tag{3.2}$$

where α is the lapse, β_i is the shift vector, and γ_{ij} is the 3-metric cf. Section 2.2. To evolve the spacetime, we then decompose the spacetime into a conformal-traceless 3+1 formulation known as the BSSNOK formulation of the Einstein equations cf. Section 2.3. This decomposition deals with the spacetime, but to simulate BNS mergers, we require a description for the underlying matter. To do so, we model the neutron stars as perfect fluids, where the energy-momentum tensor is given by

$$T_{\mu\nu} := (e + p)\, u_\mu u_\nu + p\, g_{\mu\nu} \,, \tag{3.3}$$

where $u^\mu := dx^\mu/d\tau$ is the four velocity of the fluid with position x^μ and proper time τ, e is the energy density, and p is the pressure.

In order to close the system of equations (2.68) and (2.69) an equation of state (EOS) of the form $p = p(\rho, \epsilon, Y_e)$ is required, where ρ is the rest-mass density, ϵ is the specific internal energy, and Y_e is the electron fraction. The EOSs we use are the LS220 EOS of [140] with a nuclear compressibility parameter $K = 220\,\mathrm{MeV}$ and the DD2 EOS [269]. These EOSs have been used extensively in numerous simulations, e.g., [95, 110, 201, 23] and provide useful test cases, although LS220 is ruled out [261] on theoretical grounds, it has been extensively used in numerical relativity simulations and thus provides a standard template to test against.

On the computational side, I solve the spacetime equations numerically using the `Mclachlan` code [49] which is part of the `Einstein Toolkit` [153]. The hydrodynamics are solved using the `WhiskyTHC` code [203, 204]. `WhiskyTHC` implements finite-volume and finite-difference with high-resolution shock-capturing methods.

3.2.2 Initial data and grid setup

As discussed in the introduction, there are two types of material behaviour to capture depending on whether our analysis focuses on unbound or bound material. However, in both cases, the BNSs are considered to be irrotational and were computed using the multi-domain spectral-method code `LORENE` [104] under the assumption of a conformally flat spacetime metric and employing the EOS at beta-equilibrium. These assumptions are justified for this study as the influence of rotation only adds another physical parameter that is a free parameter and unnecessarily adds complication.

For the study of the *unbound material*, quasi-circular initial data – at least four orbits – with an initial gravitational mass of $M = 1.35\,M_\odot$ and initial separation of $45\,\mathrm{km}$ with the LS220 EOS was produced. This set-up reflects a standard of initial data used in more complicated simulations done in numerical relativity. In contrast, for the bound material, again quasi-circular initial data with a gravitational mass of $M = 1.35 M_\odot$ and initial separation of $45\,\mathrm{km}$ is chosen, but with the DD2 EOS instead of the LS220. The reason for choosing a different EOS is that DD2 is stiffer than LS220 and collapses to a black hole at a later time allowing sufficiently long timescales to investigate the structure of the core before collapse.

Because the fluid that becomes unbound is located far away from the merger site, e.g., at distances $\gtrsim 300\,\mathrm{km}$ from the centre of the grid, a higher resolution is desirable to better capture the fluid. For this reason, a resolution of $\Delta h_5 = 0.15\,M_\odot \approx 220\,\mathrm{m}$ for the finest refinement level was used for the unbound material evolution and π-symmetry imposed. π-symmetry is useful in numerical relativity simulations as only half the domain is required to be evolved and thus saves on computational cost. However, as shall be discussed in Chapter 4, it can hide the evolution of odd-degree modes that can influence the evolution of the post-merger object. For the bound material, resolution is not as important for investigating some aspects of the fluid properties, see, e.g., [110], but for completeness $\Delta h_5 = 0.15\,M_\odot \approx 220\,\mathrm{m}$ was also used for the finest refinement level but with no π-symmetry to ensure that the one-arm stability is allowed to develop [200]. Both simulations had five refinement levels, reflection symmetries, and an outer boundary of $512\,M_\odot \approx 760\,\mathrm{km}$.

3.2.3 Tracer evolution

As discussed in the introduction, the thermodynamical history of the fluid element is required and in order to follow the evolution of the fluid and obtain this information, tracers are placed in the fluid which are able to record the properties of the fluid at a given point. These tracers are massless – a point which requires a more extensive discussion see Sec 3.2.4 – and are passively advected through the equation [87, 175]

$$\frac{d\vec{\boldsymbol{x}}}{dt} = \tilde{\vec{\boldsymbol{v}}}\,, \tag{3.4}$$

where the velocity vector $\tilde{\vec{\boldsymbol{v}}}$ refers to the three-velocity of the fluid with respect to the coordinates. Although this equation seems simple, it is important not to mix up the definitions of the different values. The position vector $\vec{\boldsymbol{x}}$ refers to the coordinates of the tracers while $\tilde{\vec{\boldsymbol{v}}}$ refers to the velocity of the fluid and the fluid velocity is evolved through the Einstein equations and are specified at every step. In the 3+1 formalism this velocity is related to the fluid velocity through

$$\tilde{\vec{\boldsymbol{v}}} := \alpha\vec{\boldsymbol{v}} - \vec{\boldsymbol{\beta}}\,, \tag{3.5}$$

with α the lapse, $\vec{\boldsymbol{v}}$ the three-velocity of the fluid, and $\vec{\boldsymbol{\beta}}$ the shift vector. To solve Eq. (3.4), a simple forward Euler scheme is used where the Δt is equal to the time-step of the finest grid. Although this scheme is simple, it is sufficient for the purposes of evolution of the tracers as higher order schemes do not provide additional accuracy as the evolution is not bound by the time-step, but instead the velocity of the fluid. Indeed, a comparison with a higher-order Adams-Bashforth time-stepping scheme yielded no significant improvement in the results and only required more computation time. Thus a simple forward Euler scheme is chosen.

In the simulation, this equation must be solved for each individual tracer and thus the number of tracers is a specified user-parameter denoted by N_t. Here, the value is set to $N_t = 10^5$ throughout. As we shall see in Chapter 6, the total number of tracers required for nucleosynthesis is only on the order of ~ 1000.

One potential computational issue is that the tracers do not interact and are considered point particles they can, in principle, occupy the same coordinates. In practice, however, this does not happen in the simulations performed as the velocity is sufficiently different at every point so that numerically it is challenging to achieve this. Furthermore, as the tracers pass through the grid, the value of various variables is recorded satisfying the requirement of recording the thermodynamical evolution. Specifically, the most important quantities for nucleosynthesis are (ρ, T, Y_e), which are evolved through the main evolution code. In addition to these quantities, other properties of the fluid are recorded, such as the position, fluid-velocity, and so on. In what follows, any time a quantity of the tracers is referenced, it has been recorded like the other thermodynamical quantities. As a final technical point, note that since the variables are computed only on the grid points, as it typical in a grid-based code, and in general the tracers will not be on the grid points, the desired properties are interpolated to the (x, y, z) position of the tracer using the default interpolator of the EinsteinToolkit.

3.2.4 Tracer mass flux

The overall goal of the tracers, in the context of unbound material, is to obtain the thermodynamical evolution of the tracers that can be used as input for the nuclear network. For a given trajectory, the values produced from the tracers are used as the initial data for the evolution of the r-process, which is evolved for the thousands of potential reactions that come into play. After a sufficient simulated time, the final abundance curve is produced for a given tracer. This is repeated for all the different tracers which will result in different final abundances depending on the initial input. In order to produce a final abundance, the individual tracers must be weighed in some way.

To do this, a “mass” must be associated to each tracers. In contrast to SPH codes, where the tracers explicitly represent the underlying fluid and can have a mass, the tracers we employ are *massless* and attention needs to be paid when wanting to assign a ”mass“ to an individual tracer. In some fully general-relativistic works, e.g., Ref. [175], tracers have been assigned an associated mass; this concept, however, is potentially misleading. First, since tracers play only a passive role without a coupling to the fluid besides that of following the advection equation (3.4), assigning a mass to the tracers breaks these assumptions. This is because if a tracer has a mass, it, in principle, will contribute to the energy-momentum tensor as it represents a source of energy-momentum. In our formulation of the right-hand side of the Einstein equation, contributions due to point sources are not considered at all and thus having tracers with mass will not be properly evolved. Furthermore, although the amount of material is ejected is rather small, on the order of less than 1% of the total mass, the highly complicated nonlinear nature of the Einstein equation means that small perturbations can have drastic effects at later times. Thus assigning the tracer mass without including them properly in the energy-momentum tensor is physically inconsistent.

Second, if one does want to assign a mass to a tracer, the question arises to what mass should be assigned. One method involves the tracer mass being initially associated with a mass based on its surroundings. A huge problem with this method is that then at later times this mass cannot represent the same mass it did initially since the underlying properties will have changed. For example, in this viewpoint, the tracer is considered a hollow sphere and the mass is simply the volume times the density within this sphere. Now if the initial mass is calculated from the rest-mass density where the tracer is initially at, say in the crust where densities are on the order of $\sim\ 10^{10}\,\mathrm{g/cm^3}$ then at a later time the density will have decreased significantly as is want to do with unbound material. For example a few hundred kilometres from the centre of the merger, the density has decreased by about 6 orders of magnitude and clearly does not represent the same mass as it did before.

Finally, if one did want to use the above scheme with its problems, in order to calculate a mass from a density, some volume has to be specified and tracers represent idealised point particles and thus don't have any volume. Overall, the issue is trying to assign methods that are explicit in SPH codes to grid based codes where such methods are not clear.

Despite having made these remarks, and since nucleosynthesis calculations require masses to weight the different abundance curves, a scheme to assign a "mass" with the tracers is necessary. A simple method around this mass association is to use the idea of flux through a surface. A flux through a surface is a well-defined quantity both mathematically and physically and doesn't rely on any assumptions made. To this end, the flux of the tracers is calculated through a given 2-sphere of coordinate radius R, which we take to be $200\,M_\odot \approx 295\,\mathrm{km}$ [201, 44]. Although this distance seems arbitrary, it turns out that the distributions of the thermodynamical quantities is relatively independent of radius and will be discussed in more detail in Chapter 6. So for now, a representative radius of $295\,\mathrm{km}$ is sufficient.

Following standard definitions in many branches of physics, "tracer mass current" at a given iteration i can be defined as

$$\vec{\boldsymbol{j}}_i := \vec{\boldsymbol{j}}(\vec{\boldsymbol{x}}, t_i) = \rho W(\alpha\vec{\boldsymbol{v}} - \vec{\boldsymbol{\beta}}) = \sum_j W_j(\vec{\boldsymbol{x}}, t)\rho_j(\vec{\boldsymbol{x}}, t)\,\vec{\boldsymbol{v}}_j(\vec{\boldsymbol{x}}, t)\,, \tag{3.6}$$

where we sum over the tracers that cross through a surface of a given radius during that iteration. The justification for this definition is well-motivated by other physics. In standard fluid mechanics, the flux is typically defined as a density times a velocity. In general relativity, a similar definition can be made, but in order to make the expression relativistically consistent, the rest-mass density is not used but instead the rest-mass density times the Lorentz factor is required. A simplification can immediately be made, effectively removing the effects of general relativity, transforming the expression into a more familiar special relativity expression. This can be done because we evaluate this flux far from the BMP, and the space-time geometry is approximately flat, i.e., $\alpha \simeq 1, \vec{\boldsymbol{\beta}} \simeq 0$, so that the final special-relativistic expression (3.6) provides a good approximation. As the information about the velocity, Lorentz factor, and the rest-mass density are recorded, this quantity is well defined for each tracer and thus an associated current with the tracers crossing the surface can be made. Integrating this current over the surface gives a mass-flux and integrating this over time gives a mass. Explicitly, this defines a "tracer mass flux" as

$$\dot{M}_i(t) = \oint \vec{\boldsymbol{j}}_i \cdot \vec{\boldsymbol{n}} \sqrt{\gamma}\, dS = \oint \vec{\boldsymbol{j}}_i \cdot \vec{\boldsymbol{n}}\, dS\,, \tag{3.7}$$

where the surface element on a sphere is taken to be $dS = r^2 \sin\theta d\theta d\phi$ and again the special relativity expression is taken since the integral is evaluated sufficiently far away from the BMP and spacetime is to good approximation flat. Then a simple differential equation for the "tracer mass" is obtained in the form of

$$\frac{dM_{\rm tr}}{dt} = \dot{M} = \sum_i \dot{M}_i \tag{3.8}$$

This equation can be integrated to obtain a mass associated with the tracers. We stress that this "mass" is only valid as the tracers pass through the surface and does not represent the true mass unbound that would be measured when calculating the flux of the underlying fluid through a sphere. In Sec. 3.3.4 we will compare the mass flux computed via the tracers, i.e., Eq. (3.8), with the corresponding quantity computed using standard hydrodynamical quantities, e.g., the rest-mass current, and demonstrate that this method can reasonably well approximate that of the "exact" answer from the underlying fluid. In contrast, for the bound material, we are only interested in following the streamlines of the fluid, which is the most fluid dynamical role that passively advected tracers play. In this case, the mass of the tracers is irrelevant.

3.3 Tracing unbound material

We start our discussion on the use of tracers by considering the case in which they are employed to describe the dynamics of matter that is gravitationally *unbound*. For the case considered here, this material is the dynamical ejecta, i.e., ejecta that is launched in the first few milliseconds of the merger due to tidal interactions. Although this is the only case studied here, due to computational limitations, a priori there is no reason that the tracer method will not also apply to situations such as neutrino-driven wind ejecta.

In merger simulations, a grid must be created and due to computational limitations, must have a finite size. This presents a computational issue as matter that ultimately undergoes r-process nucleosynthesis is material that becomes "unbound" which is sufficiently far away from the merger. Physically, this ejecta has velocities that are roughly $\sim 0.2c$ cf. Chapter 6, and thus over the time period of seconds will distances that are many orders larger than the width of the computational grid boundary of $512\,M_{\odot}$. Thus a criterion to determine what material becomes "unbound" is required.

The simplest criteria that can be derived is known as the *geodesic criterion* and corresponds to tracers reaching infinity with no kinetic energy. This means that a tracer is considered to be unbound when the corresponding fluid element has the covariant time component of the four-velocity $u_t \leq -1$, which corresponds to considering tracers as moving on geodesics and reaching infinity with zero energy [213]. To see the motivation for such a justification, sufficiently far away from the merger remanent, the spacetime becomes Minkowski, as discussed above, and thus in this limit the covariant time component can be approximated as

$$u_t \approx -1 - \phi - \frac{1}{2}v^2 \,. \tag{3.9}$$

In the simplest case, the tracer is unbound when it reaches infinity with zero velocity and is gravitationally unbound so the condition for reaching infinity with these quantities is

$$u_{t,\mathrm{inf}} = -1 \,. \tag{3.10}$$

It is possible for a tracer to have greater than zero velocity so this simple limit sets the bound. It is important to note that this interpretation is only valid sufficiently far away from the merger product and it is possible for tracers within the merger product to satisfy the geodesic criterion and are physically not unbound at all so by itself, the geodesic criterion at a single point in time alone is not sufficient to determine if a tracer is unbound. To avoid this issue, every tracer records the value of the underlying fluid's u_t at that point and it is then determined in a post-processing stage whether or not the tracer should be counted for comparison with the fluid quantities. This decision is done by checking that the tracer satisfies the geodesic criterion at all times, after it becomes unbound since it is possible for the tracer to become unbound, then undergo shock heating and become rebound. Finally, due to the high velocity of the ejecta, tracers can easily reach the boundary of the grid and, in this case, the tracer properties are set to atmosphere values and dealt with in a post-processing step.

In addition to the geodesic criterion, other criteria could be used, such as the Bernoulli criterion $hu_t \leq -1$, which has been explored, for instance, in Ref. [128]. Here however, only the geodesic criterion is used of the geodesic criterion as it is sufficiently robust, does not require any tuning and makes minimal assumptions. A more detailed discussion of the influence of boundness criterion on ejecta can be found in Chapter 6.

3.3.1 Initial placement

An often neglected aspect of the treatment of tracers is, namely, their initial placement. Despite this being a very important step, as it can significantly influence the overall results recorded by the tracers, a detailed study of the influence on the initial placement has hereto not been done.

The final goal here is to accurately capture the essential properties of the underlying fluid in the tracers. In order to properly represent the underlying fluid, we need to ensure that we are sampling the fluid in a sufficiently accurate manner. The important first step is to ensure that when we initially place the tracers, we are sampling the material that is most likely to become unbound. However, different placements of the tracers initially can potentially lead to different representative properties. One potential placement scheme, which was followed in Refs. [164, 175], is to place more tracers where there is higher rest-mass density. This process is done randomly with more tracers being placed at higher densities and fewer at lower densities. Foucart et al. [87] have successfully used tracers to measure fluid properties but no discussion is made on the initial placement procedure. Finally, Wanajo et al. [272] have used tracers in their study of r-process nucleosynthesis, focussing however only on the (x, y), (y, z), and (x, z) planes; also in this case no discussion is made on the impact of the placement of the tracers on their conclusions. Thus how effective tracers are with respect to the underlying fluid and how their results would change if they change the initial placement has been unexplored. In what follows we discuss three different placement schemes and the corresponding dynamics.

Before deciding *where* to place the tracers, we must decide *when* they should be first distributed. Luckily, when studying BNS merger, the most natural selection of placement time is straightforward: at the merger. Prior to the merger, in fact, there is no mass outflow, beyond some small spurious outflow due to initial conditions and the inevitable and tenuous mass loss at the stellar surface. Another timing option is to let the simulation evolve for a few milliseconds after merger, which is when much of the dynamical ejecta is produced, and then place the tracers to best capture this material. Once this optimal time is fixed, we need a way

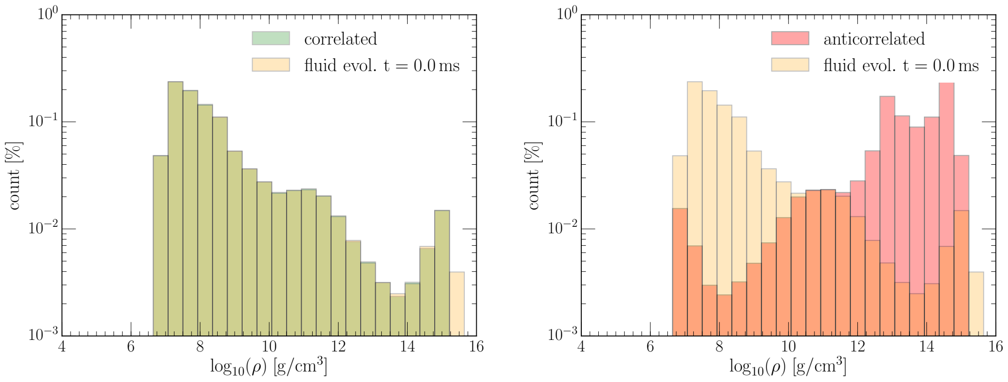

Figure 3.1: Histograms showing the distribution of the underlying rest-mass density of the fluid (light-yellow shade) compared with the initial placement of the tracers for the "correlated" (green) and the "anticorrelated" (red). The histograms are normalised with respect to the total number of cells for the fluid and 10^5 for the tracers. The placement is done at merger.

to distribute the tracers. A priori, there is no obvious "best choice" for what the correct initial placement of tracers is. However, since we are also interested in using the tracer flux to get a representative mass, choosing a scheme that is based on an initial rest-mass density distribution does have merit. Furthermore, it is reasonable to expect that low rest-mass density material around the merging stars are going to be good candidates for material that will become unbound. Conversely, we do not expect material at the high densities in the core of the merger product to be ejected in contrast with the schemes of [164, 175]. Material inside the neutron star that is between these two extremes can still be ejected due to the complicated merging process, which can eject material from within the neutron star.

In light of these considerations, at the chosen time during the simulation we fix a Cartesian box surrounding the BMP and place tracers at the grid points within this box, distributed according to a scheme that is weighted with some probability distribution. In practice we have considered four different options that we discuss in detail below.

Tracers correlated/anticorrelated

To begin, the most natural probability distribution, namely, placing tracers using a distribution function which is directly correlated to the rest-mass density distribution at merger is investigated. In other words, within the fixed box that is used to determine where the tracers are placed, the number of cells within a given rest-mass density range are counted, then normalised by the total number of cells, giving a distribution of how many cells have a given rest-mass. From this number, that percentage of tracers is distributed randomly over cells with that given density range, making sure that no more than one tracer is assigned to a given cell.

This procedure is illustrated in both panels of Fig. 3.1. Here the light-yellow shaded distribution represents the underlying rest-mass density distribution produced by the fluid evolution and is calculated directly from the grid data. For this initial data, the fluid rest-mass density ranges from $\sim 10^{15}\,\mathrm{g/cm^3}$ in the core out to $\sim 10^7\,\mathrm{g/cm^3}$ in the material around BMP, which represents approximately $20\,\%$ of the rest-mass density cells. The reason for this sudden drop is that in our simulations there is an "atmosphere" set at $\sim 6 \times 10^3\,\mathrm{g/cm^3}$ [203, 204] which corresponds to the bottom of the equation of state table. In an ideal case, the rest-mass density around the surface of the neutron star would be vacuum, but computationally this presents immense challenges as the surface of the star would decrease a discontinuous drop from higher rest-mass densities to vacuum which poses numerical challenges. This is avoided by adding an "atmosphere" which smooths out this discontinuity. As such, there is some material present outside the neutron star that is evolved, albeit at significantly lower densities than the neutron star itself. The rest-mass density of this atmosphere is at least three orders of magnitude smaller than the neutron star, so this cut-off ensures that no tracers are placed at the (unphysical) atmospheric rest-mass densities.

The left panel of Fig. 3.1 compares the rest-mass distribution computed from the fluid evolution with the one adopted for the tracers, to which it is *"correlated"* within a rest-mass density range (light-green shade). More specifically, the lower rest-mass density is set to the same as the fluid while the upper rest-mass density is taken to be $10^{15}\,\mathrm{g/cm^3}$. We then select 10^5 cells randomly from the underlying fluid bins. The variations between the "correlated" distribution and that of the fluid are very small and are negligible, with the only difference occurring just below $10^{14}\,\mathrm{g/cm^3}$ where the fewest number of fluid cells with that rest-mass density exist due to being near the core of the neutron star where material is already unlikely to become unbound.

In contrast, this distribution should be compared with the one obtained when the tracer distribution is *"anticorrelated"* with the rest-mass density and that is shown in the right panel of Fig. 3.1 (light-red shade). Effectively, this is the reverse of the correlated distribution. However subtleties arise when trying to associate tracers to all the cells because at higher densities, there are simply not sufficiently enough cells to use. This means in practice all higher rest-mass densities cells are first filled and then randomly the lower densities are filled densities, thus resulting in an almost reflected distribution from the underlying distribution. It is not a perfect reflection due to the aforementioned point as tracers are placed at every cell at higher rest-mass densities, leading to a flattening of the distribution in the this region. At lower densities, on the other hand, there is an increase in the distribution which is due to the random selection.

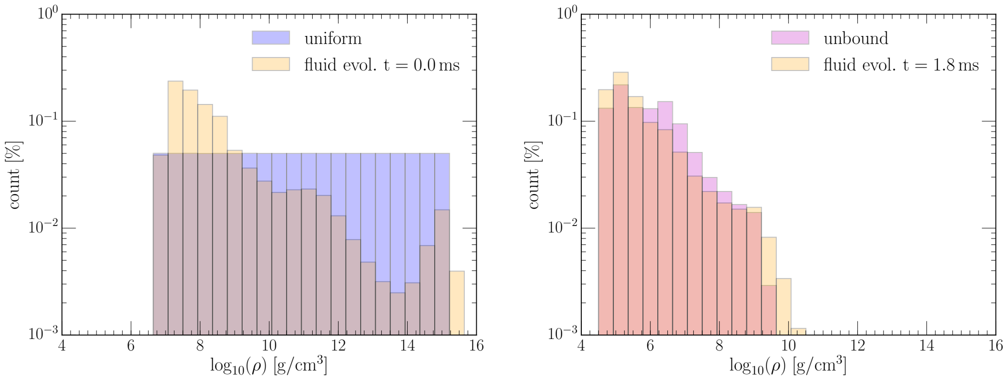

Figure 3.2: *Left:* Histograms showing the distribution of the underlying rest-mass density of the fluid (light-yellow shade) compared with the initial placement of the tracers for the uniform (blue). The histograms are normalised with respect to the total number of cells for the fluid and 10^5 for the tracers. The placement is done at merger. *Right:* The same as in the left panel but showing the distribution of the underlying rest-mass density of the fluid (light-yellow shade) compared with the placement of the tracers for the u_t placement scheme (purple). The histograms are normalised with respect to the total number of cells for the fluid and 10^5 for the tracers. The placement is made $1.8\,\mathrm{ms}$ after the merger.

Tracers uniformly distributed

The third placement to be considered is that of a uniform distribution. In this case, the rest-mass density range is distributed evenly into 20 bins with tracers in them. Doing this procedure results in a distribution that does not follow the underlying rest-mass density distribution at all, but instead places an equal number of tracers at all densities. The resulting distribution is shown in the left panel of Fig. 3.2 (light-blue shade) and when comparing with the underlying fluid (light-yellow shade) it can clearly be observed that this placement oversamples the higher densities (i.e., $\gtrsim 10^{10}\,\mathrm{g/cm^3}$) while it undersamples the lower densities (i.e., $\lesssim 10^8\,\mathrm{g/cm^3}$).

Tracers following unbound matter

The last placement that has been considered is different from the previous three in at least two important aspects. Firstly, the time of placement is completely different from the others. To wit, tracers were not placed until just before the first dynamical outflow is about to pass through a radius of $200\,M_\odot$ radius. This radius is chosen because it is the radius through which the tracer-flux is computed. Additionally, at this radius, a detector is placed that can capture the outgoing flow [201]. For this particular set-up, the time after merger for this criteria to be satisfied was approximately $1.8\,\mathrm{ms}$. It is at this time the dynamical ejecta are close to, but have not passed the $200M_{\odot}$ radius.

The second major difference is that instead of placing the tracers based on the rest-mass density, they are placed based on u_t and only placed into cells where $u_t \leq -1$, i.e., at that time the cell represented unbound material. Then, from all these flagged cells, 10^5 tracers are randomly placed at these number of cells where the geodesic criterion is satisfied. The resulting distribution is shown in the right panel of Fig. 3.2 (light-purple shade) and it is interesting to note that even though the tracers were distributed based on u_t, the distribution still has approximately the same structure as that of the evolved fluid[2]. The main differences when comparing with the underlying fluid are that the tracer distribution overshoots the rest-mass density between $10^6 - 10^8\,\mathrm{g/cm^3}$ and does not place tracers at higher densities of $10^{10}\,\mathrm{g/cm^3}$. This is likely due to the fact that higher rest-mass density material is closer to the BMP and less likely to be unbound. Also note that the underlying fluid distribution densities extend above rest-mass densities of $10^{10}\,\mathrm{g/cm^3}$ but do not appear in the right panel of Fig. 3.2 because the latter maintains the same dynamic range of the other three panels in Figs. 3.1 and 3.2.

3.3.2 Three-dimensional dynamics of unbound tracers

As previously discussed, an important aspect of material that undergoes nucleosynthesis is that it is unbound, i.e., it will escape from the merger and form the heavy elements. To ensure that the ejected has had sufficient time to become unbound a all the simulations presented here have been run for at least $10\,\mathrm{ms}$ after merger. By this time, when using the geodesic criterion, in fact, there is essentially no flux of unbound material or of tracers[3] through a 2-sphere of radius $200\,M_{\odot}$. Furthermore, $10\,\mathrm{ms}$ is also a sufficient time for the tracers and the fluid to reach the outer boundary of the computational domain when they are, as previously discussed, dealt with in a post-processing step.

In order to get a feel for the spatial distributions of the various placements Fig. 3.3 displays a visualisation of the tracers for the four different placement schemes discussed above (from top to bottom: “correlated”, “anticorrelated”, “uniform”, and “unbound”) at three different times corresponding roughly to when the unbound material passes through spheres of radii $200,\ 300,\ 500\,M_{\odot}$ (i.e., $t \sim 2, 3,$ and $7\,\mathrm{ms}$ after the merger, respectively). On the (x, y), (y, z), and (x, z) planes are the shown the values of the rest-mass density using the colourbar in the

---

[2] Note that the distribution coming from the fluid evolution is different than that on the left panel of Fig. 3.2 since it refers to a different time in the simulation.

[3] This is not necessarily the case when using the Bernoulli criterion, which is less restrictive and allows for mass being ejected also at later times as will be discussed in Chapter 6.

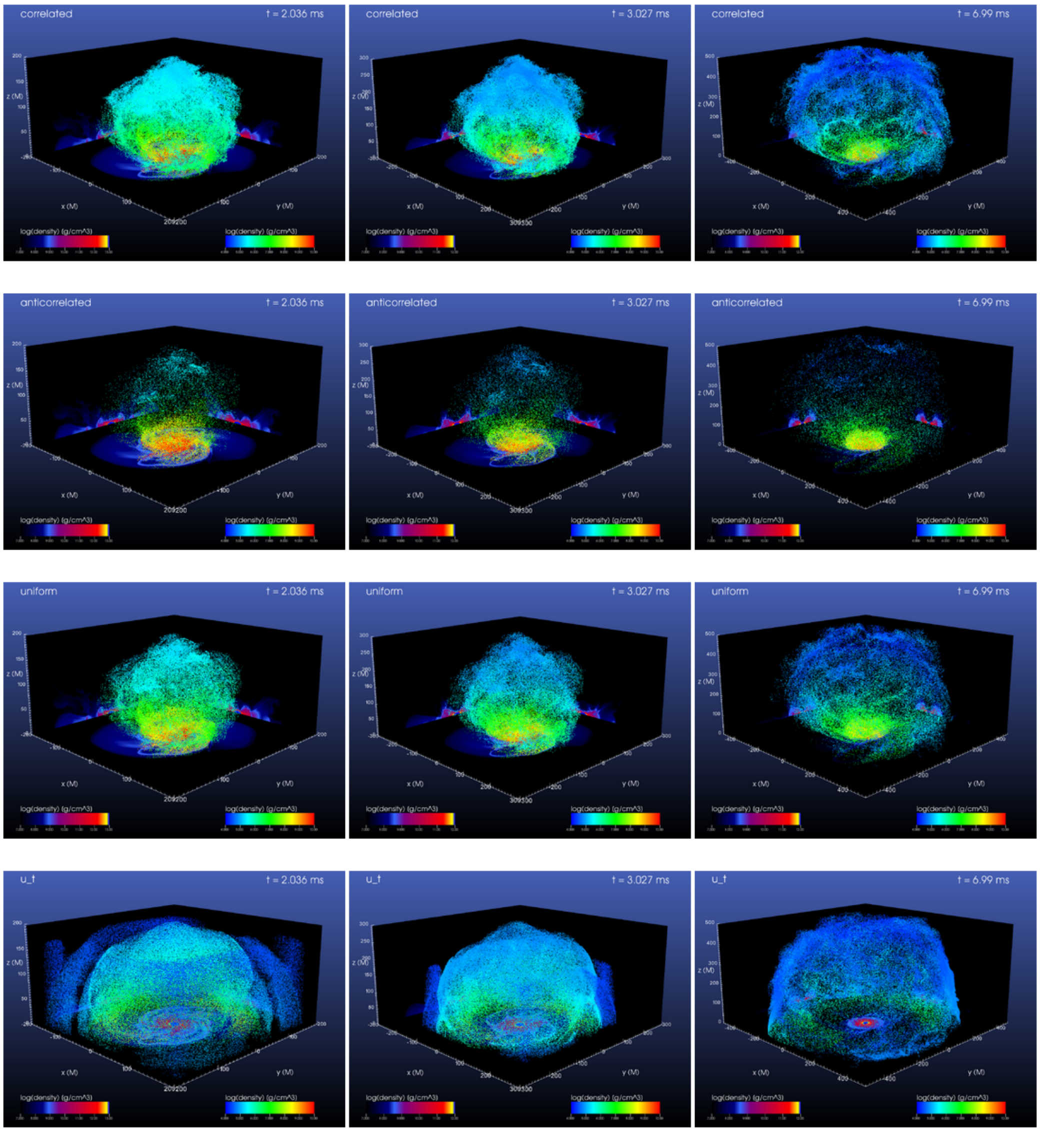

Figure 3.3: Visualisation of the tracers for four different placement schemes (top to bottom) at three different times (left to right). From top to bottom: “correlated”, “anticorrelated”, “uniform”, and “unbound”. From left to right to $\sim 2, 3, 7\,\mathrm{ms}$ after merger. On the (x, y), (y, z), and (x, z) planes are the shown the values of the rest-mass density using the colourbar in the left lower corner. A colourbar on the right lower corner is also used to visualise the rest-mass density of the fluid elements hosting the tracers. Note the different colour scales for the fluid and the tracers.

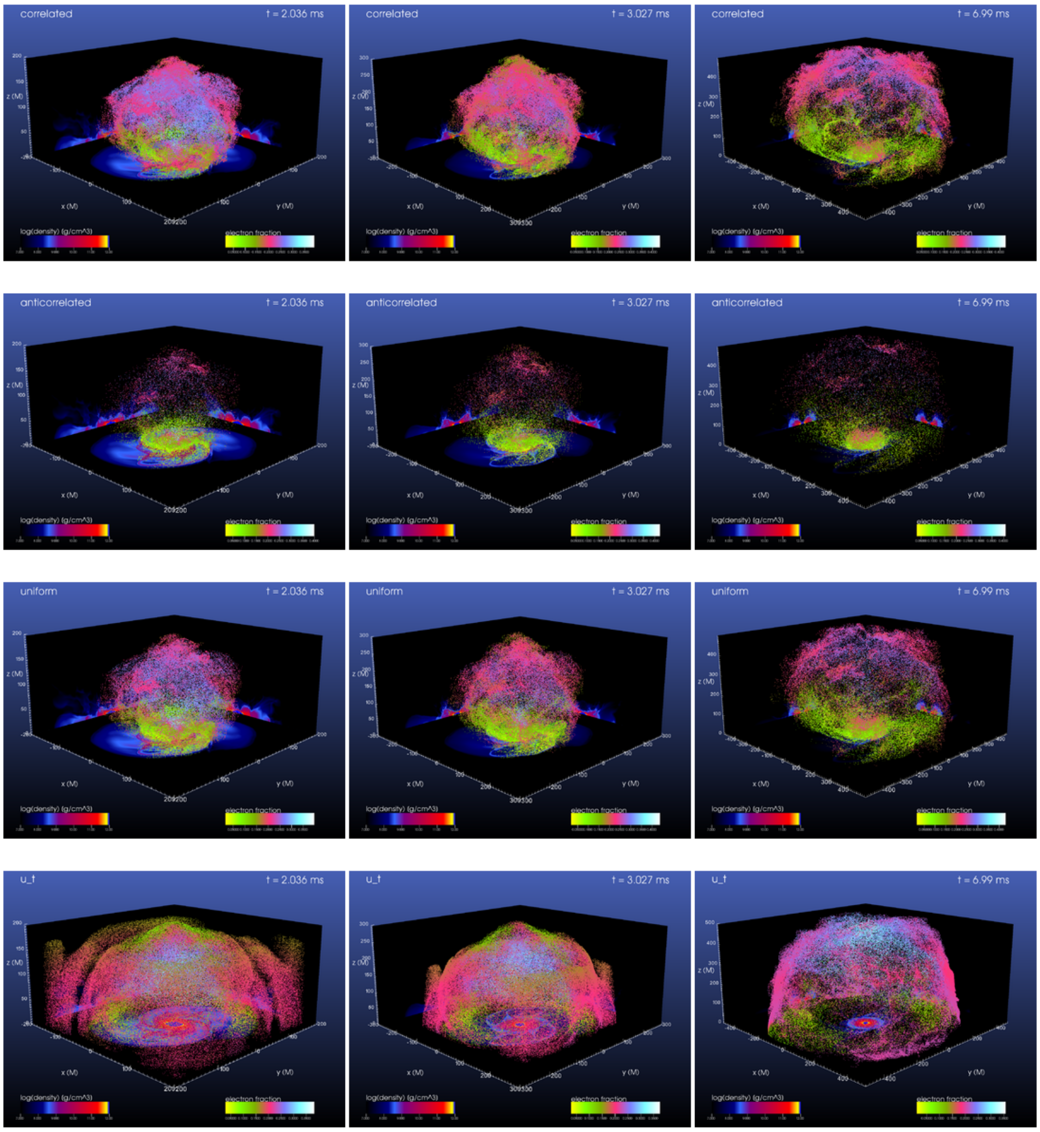

Figure 3.4: Visualisation of the tracers for four different placement schemes (top to bottom) at three different times (left to right). From top to bottom: “correlated”, “anticorrelated”, “uniform”, and “unbound”. From left to right to $\sim 2, 3, 7\,\mathrm{ms}$ after merger. On the (x, y), (y, z), and (x, z) planes are the shown the values of the rest-mass density using the colourbar in the left lower corner. A colourbar on the right lower corner is also used to visualise the electron fraction Y_e of the fluid elements hosting the tracers.

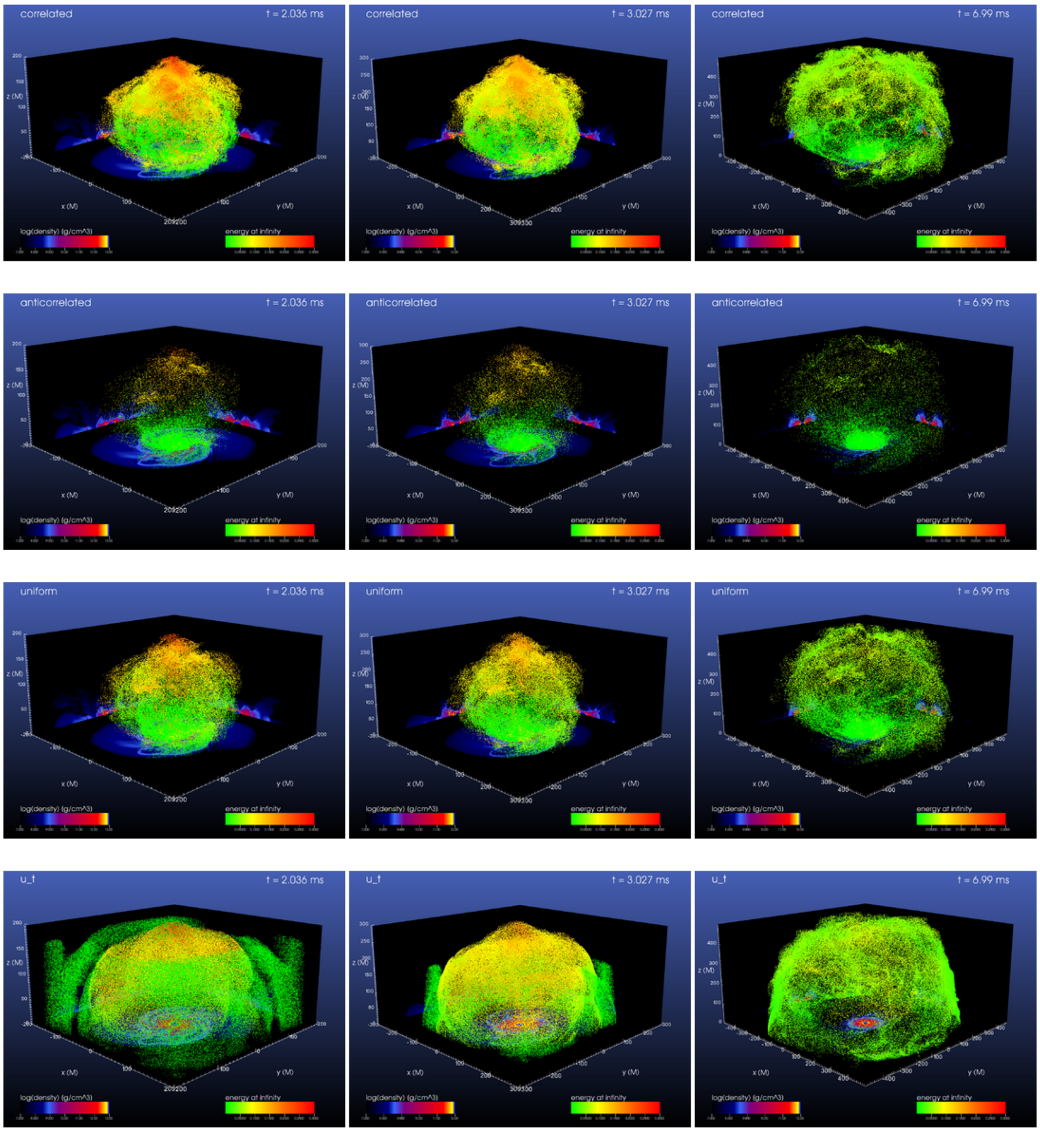

Figure 3.5: Visualisation of the tracers for four different placement schemes (top to bottom) at three different times (left to right). From top to bottom: “correlated”, “anticorrelated”, “uniform”, and “unbound”. From left to right to $\sim 2, 3, 7\,\mathrm{ms}$ after merger. On the (x, y), $(y, z$, and (x, z) planes are the shown the values of the rest-mass density using the colourbar in the left lower corner. A colourbar on the right lower corner is also used to visualise the kinetic energy at infinity, $K := -u_t - 1$.

left lower corner. A colourbar on the right lower corner is also used to visualise the rest-mass density of the fluid elements hosting the tracers. Note the different colour scales for the fluid and the tracers.

For the case of "correlated" tracers (first row), it is evident that there is a presence of a large number of tracers at high latitudes, which correspond to those initial tracers that are at low rest-mass density which mostly originate from near the surface of the neutron star. This is to be contrasted with the dynamics of "uncorrelated" tracers (second row), which shows the anticorrelated placement which has significantly fewer tracers at higher latitudes and closer to the BMP, simply as a result of having undersampled the fluid elements at low rest-mass densities, i.e., those near the surface, and oversampled those at high rest-mass density, i.e., those near the core. Unsurprisingly, the "uniform" tracers strikes a balance between the two (third row). Finally, the case of "unbound" tracers (fourth row) shows a very different structure, where it is possible to clearly distinguish the different "waves" of matter ejected dynamically (left and central columns) and where an almost spherically "dome" develops over the BMP product and which is not present in the other placements. Note that this should not be interpreted as an indication that the mass outflow is spherically symmetric as the tracers in this case are not a faithful description of the rest-mass density as the tracers do not represent mass. Although it may appear that there is more, recall that in the tracer-flux description above that the tracer-flux involves the rest-mass density so though there appear to more tracers, the total mass-flux they represent is lower. Indeed, this picture is clear when using the colourbar to track the actual rest-mass density of the fluid and it is possible to note that high rest-mass density material (coloured red) is ejected mostly near the equatorial plane, while low rest-mass density material (coloured blue) is ejected at higher latitudes. This also implies, importantly, that the ejected material has a strong angular dependence and we be explored further in Chapter 6. This is particularly important in view of the previous studies of nucleosynthesis with tracers carried out in Ref. [272], where the tracers were analysed only on the (x, y), (y, z), and (x, z) planes, and of the fact that the angular dependence of the tracers can change the potential observed properties (see Refs. [164, 163] for an extended discussion). The snapshots in Fig. 3.3 demonstrate that there is significant material that lies outside these planes; indeed, as we will further discuss in Sec. 3.3.4, about $50\,\%$ of the mass ejected lies within 10 degrees of the orbital plane, while the remaining $50\,\%$ occurs at higher angles from the equator.

Figure 3.4 is similar to Fig. 3.3 but we use the colourbar to represent the value of the electron fraction Y_e carried by the various tracers. The importance of Y_e in terms of nucleosynthesis is that lower electron fractions will produce the heavier elements, while higher electron fraction produces the lighter elements. An intuitive way to view this is that a lower electron fraction means a higher density of neutrons being available which means that heavier elements are more able to form as the r-process has more material to react with, while the opposite picture happens for higher values of the electron fraction.

In all placements, a similar distribution of the electron fraction is visible, with low Y_e values near the equator and increasingly high values near the poles. For all distributions, this increase in Y_e is correlated with a decrease in the rest-mass density. Thus despite having potentially high-Y_e ejecta in the polar regions, it is associated with only a modest amount of ejected matter. Overall, the snapshots indicate that there will be a strong angular dependence of the r-process nucleosynthesis; a detailed discussion of this will be presented in an Chapter 6 and how this distributions agrees with neutrino interactions.

The final figure, Fig. 3.5, is similar to the two previous ones but refers now to the kinetic energy at infinity, i.e., $K := -u_t - 1$, so that $K \geq 0$ corresponds to $u_t \leq -1$. Clearly, all snapshots show that, independently of the placement criterion chosen, the material near the equator is just unbound, but, as the latitude increases, the material becomes more unbound, increasing to a maximum at the poles. Similarly, at late times, we can see that all the high-energy material has already been ejected in the violent dynamics accompanying the early postmerger and that and most values of K are close to zero.

In summary, when analysed in a combined manner the three-dimensional dynamics of the unbound tracers shown in Figs. 3.3–3.5 reveals that the ejected matter near the poles has lower densities, but larger values of electron fraction and kinetic energy, and such a picture has implications for the detection and observation of kilonova as will be discussed in Chapter 6.

3.3.3 Distribution dynamics of unbound tracers

Another useful feature of the tracers is that they can answer questions about the evolution of the fluid flow that are not able to be answered in regular grid-based codes. To this, a key assumption often made in studying the outflow material in r-process nucleosynthesis and in kilonova modelling [146, 107], is that the unbound material is expanding adiabatically, i.e., that the internal energy remains constant. In addition, the material is assumed to expand radially, so that the rest-mass density decreases in time as $\sim t^{-3}$. While all reasonable, our use of tracers allows the testing of these assumptions as the direct thermodynamical history of the tracer is recorded. This is done in Fig. 3.6 by reporting the time evolution of the distribution functions of representative quantities, i.e., the rest-mass density, the radial position, the specific entropy[4]. In these plots, the worldlines of the various tracers

---

[4] A diagram showing the evolution of the distribution function of the radial position of the various tracers effectively represents a spacetime diagram, thus offering the opportunity to visualise

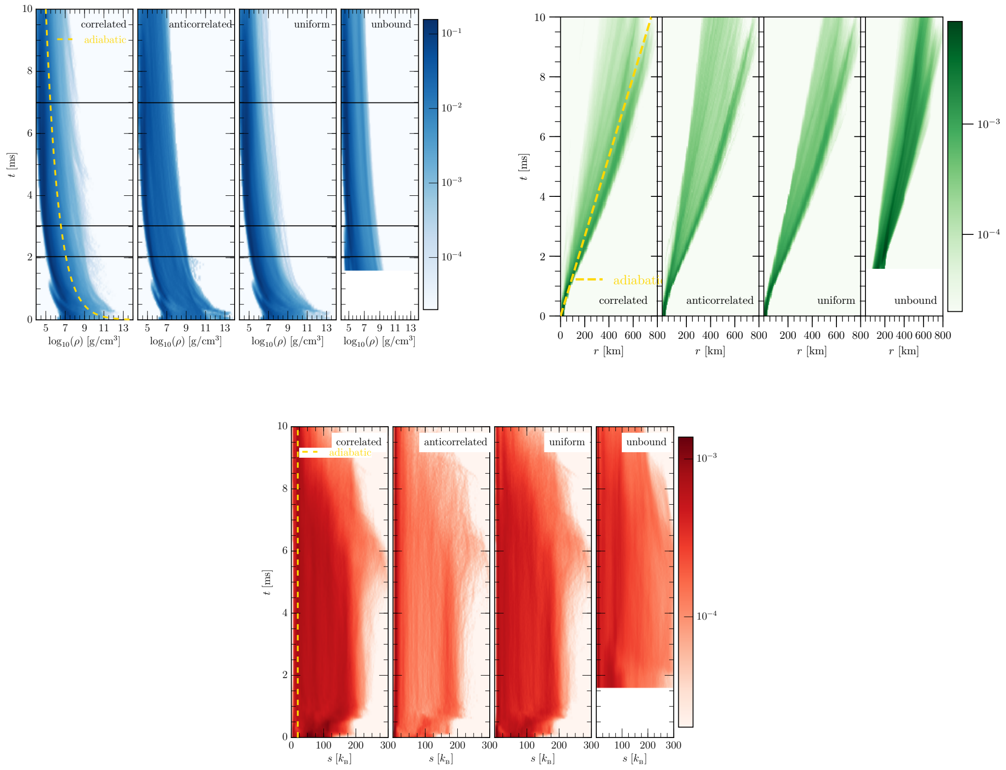

Figure 3.6: Evolution of the distribution functions for three representative quantities: the rest-mass density, the radial position and the specific entropy. From left to right are the “correlated”, “anticorrelated”, “uniform”, and “unbound” placements. The yellow lines represent the adiabatic expansion for each of the plotted quantities. Note that the “unbound” placement starts $1.8\,\mathrm{ms}$ after the merger. Horizontal black lines correspond to the times shown in Figs. 3.3–3.5.

are marked with small dots whose colour marks the corresponding fraction; as a result, a dark/light trajectory will indicate that a large/small number of tracers with the corresponding quantity having the reported values at a given time.

In the top left panel of Fig. 3.6 the evolution diagram of the evolution of rest-mass density, with the dashed-gold curve representing adiabatic expansion, $\rho \sim t^{-3}$ is displayed. The four sub-panels distinguish the various criteria adopted for the initial placement, while the horizontal black lines correspond to the times shown in Figs. 3.3–3.5. In all cases, the general trend of the adiabatic expansion can be seen very clearly and involves both tracers with high rest-mass density and tracers with low rest-mass density. However, it is important to note that while the general trend is for an adiabatic expansion, not all tracers follow this behaviour. For example, in the case of "correlated" tracers, the panel shows that there is a small fraction of tracers (light blue) corresponding to higher rest-mass densities that does not always follow the adiabatic expansion prior. Another feature is the number of tracers that reach close to atmospheric values and that eventually represents a large fraction of the total number (dark blue). In all placements considered there is a clear gradient of colours with increasing rest-mass density. An exception to this behaviour is offered by the case of "anticorrelated" tracers, where the fraction gradient is not as strong. This is a manifestation of the initial placement scheme: there are more tracers at high rest-mass densities and of those that become unbound, they represent a significant fraction of the unbound material.

Similarly, in the top right panel of Fig. 3.6 shows a standard spacetime diagram of the radial distance from the origin of the tracers; note that the "unbound" placement starts $1.8\,\mathrm{ms}$ after the merger as discussed above. In the adiabatic approximation, the expansion radius r should scale linearly with time, i.e., $r \sim t$, and the figure shows clearly that most tracers do follow a very close to radial ejection. In addition, we can see the wide distribution of the tracers. Our domain is approximately $750\,\mathrm{km}$ wide from the origin in each direction and the tracers have a radial distance ranging from $300\,\mathrm{km}$ up to $800\,\mathrm{km}$ at any given time. This spatial distribution has been discussed in terms of the neutrino-drive wind ejecta [163] but has not been explored in the dynamical ejecta case in general relativity and will be discussed further in Chapter 6.

Finally, in the bottom panel of Fig. 3.6 the evolution of the distribution function for the specific entropy is displayed.For an adiabatic expansion, they distribution functions would simply be represented by a vertical line for each tracer. The panel clearly allows for the verification of this assumption and it can be noted that indeed many of the tracers obey this adiabatic expansion, but not all. For example, it is clear that at high entropies the tracers do not expand adiabatically and that tracers can actually increase their entropy, for instance as a result of ad-

---

the (radial) worldlines of the tracers.

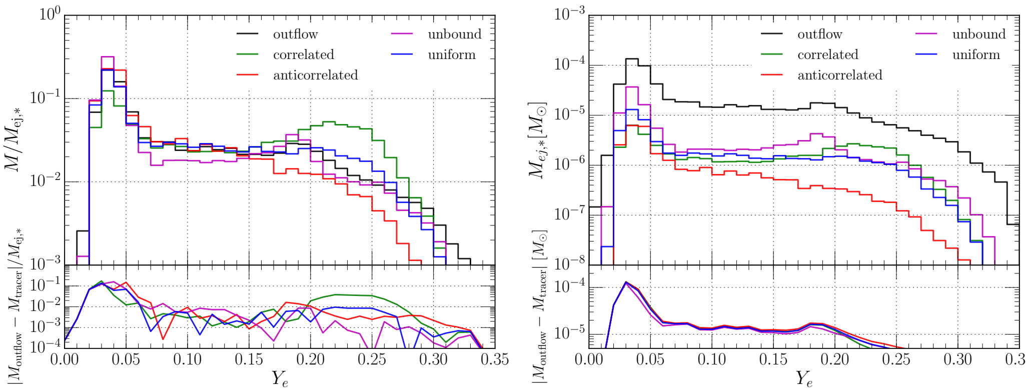

Figure 3.7: *Left panel:* Comparison between the distributions in electron fraction as computed with the tracer mass-fluxes through the surface at $200\,M_\odot$ as computed with the different placement schemes (coloured lines) and the outflow (black line). Because the ejected masses are different in the various cases, all curves have been normalised to the masses of their respective total values. Shown in the bottom part is the relative error, which is smaller for the uniform distribution placement. *Right panel:* The same as in the left but when the distributions are absolute and not normalised.

ditional shocks with the outgoing matter. Hence, this panel illustrates that the assumptions made that the ejected matter follows an adiabatic flow is a very valid approximation for much of the unbound material, but in order to have the most robust input data for the nuclear network, one needs to have the full history of the fluid element. This is in contrast with the analysis of [201], where the unbound material was expanded adiabatically from the surface of the outflow sphere.

3.3.4 Tracer and fluid information

In the previous sections it was shown how different choices of the initial placement of the tracers can lead to different dynamics of the tracers and hence to different measurable quantities, for example in the electron fraction. However, these experiments are merely qualitative and do not provide a quantitative method of determining which method is the "best". A quantitative method needs to be determined which will demonstrate which of these possible choices should be the recommended one in numerical simulations in order to most accurately represent the underlying fluid. To answer this question and hence determine the efficacy of the different placements, the tracer flux is compared with the mass-flux of the underlying fluid. In this comparison, the tracer distributions of the most important thermodynamical and physical quantities, i.e., electron fraction, entropy, energy at infinity, angular distribution of the mass flux, are compared with the corresponding distributions from the underlying fluid evolution which is hereafter referred to the latter as the (fluid) “outflow”. As in the previous discussions, the computation of the distributions are done through the fluxes of a fluid across a spherical detector at $200M_{\odot}$ from the origin and consider only material that is unbound according to the geodesic criterion, $u_t \leq -1$.

Perhaps the most important quantity of all thermodynamical quantities is the electron fraction Y_e, which measures how neutron rich the material is. In addition to determining the elements created through r-process, the value also has important implications for the signal observed from a kilonova, see Chapter 6 for a detailed discussion. It is for these reasons that the electron fraction is the quantity which will be used to determine which placement best matches that of the underlying fluid. In Fig. 3.7 the distributions of the electron fraction using the different placement prescriptions (marked with lines of different colour) along with the distribution obtained with the fluid “outflow” (black) are plotted. Also plotted in the bottom panel is the error between each of the tracer prescriptions with that of the “outflow”. In the left panel, in particular, all curves are normalised to the amount of rest-mass ejected in the various cases, $M_{\mathrm{ej},*}$, so that the integral of the various distributions is unity. In the case of the outflow, the normalisation mass is the total amount of ejected material while in the case of the tracers, it is the “mass” measured by Eq. 3.8. In the right panel of Fig. 3.7 such a normalisation is not used and the distributions refer to the absolute amount of ejected matter for the different distributions. Here again, the mass of the outflow is the actual measure of ejected material while the tracer mass is only a representative sample.

Overall, the fluid-outflow distribution (black solid line) shows that the electron fraction has a main peak at $Y_e \sim 0.04$ and a secondary one at $Y_e \sim 0.19$. Concentrating on the left panel, clearly the “anticorrelated” and “uniform” placements both give the correct value for the $Y_e \sim 0.04$ peak with a relative error of $\sim 10^{-2}$ and 10^{-3} respectively[5]. On the other hand, the “unbound” (u_t) and the “correlated” placements over- and underestimate it respectively by roughly the same amount of 10^{-1}. In particular, for the secondary peak, the “correlated” placement overestimates the peak significantly with an error of about 50%; a much better agreement is obtained with the “unbound” and “uniform” distributions, with errors that are of a few percent only. In the intermediate electron-fraction range, i.e., for $0.04 \lesssim Y_e \lesssim 0.19$, all placements provide an accurate description, with the only exception of the “unbound” placement, which tends to underestimate the

---

[5] For the purposes of this comparison, the question of whether or not the distribution and physical and what type of r-process material it would produce is relegated to Chapter 6. The only important point is the comparison and not the physical interpretation.

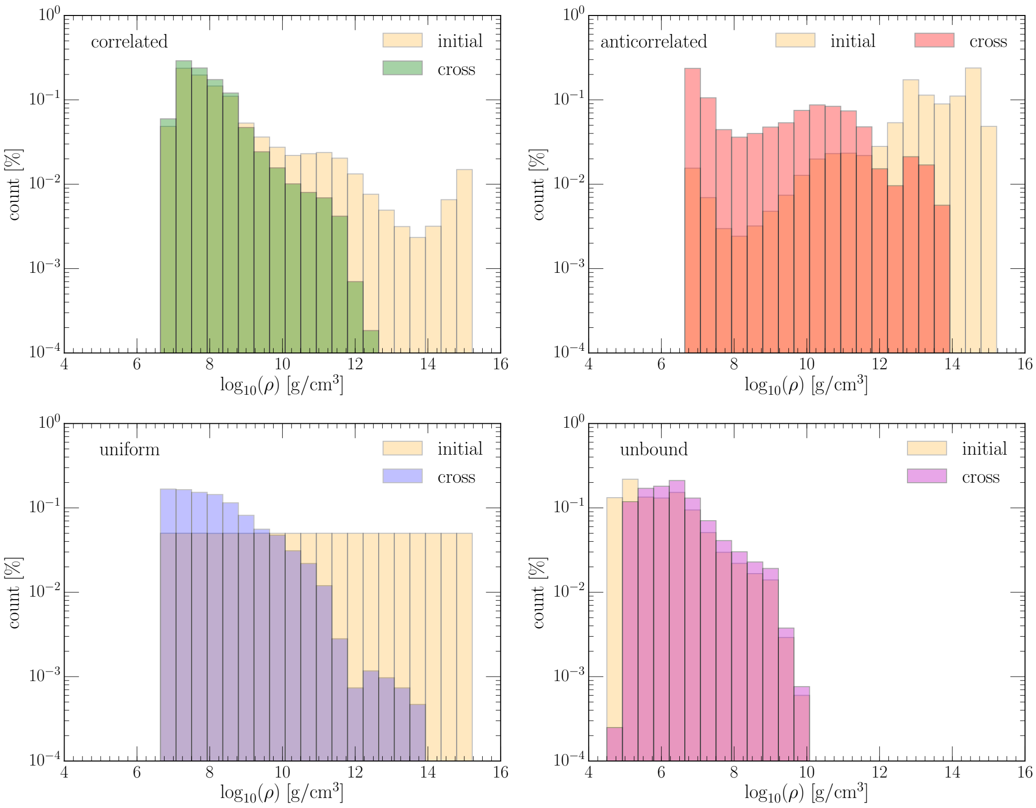

Figure 3.8: Distributions in rest-mass density of the tracers (light-yellow shade) and the corresponding distributions when the tracers cross the $200\,M_\odot$ surface. Shown from left to right are the distributions corresponding to the “correlated”, “anticorrelated”, “uniform”, and “unbound”.

underlying fluid. Hence, all things considered, it can be concluded that the initial tracer placement that provides the best match with the consistent fluid evolution is the *“uniform”* distribution.

This is a somewhat surprising result as one would have naively expected that the “correlated” placement would have provided a more faithful representation of the fluid dynamics since the material that is closest to the surface of the neutron star is the most likely material, a priori, to become unbound and it exists at low densities. In order to appreciate why this is not the case, Fig. 3.8 reports the initial distributions of the rest-mass density of the tracers (light-yellow shade) and the corresponding distributions when the tracers cross the $200\,M_\odot$ surface. In particular, the comparison presented in the top left panel allows one to appreciate that initially there were significantly more tracers at low rest-mass densities for the "correlated" placement, so that there is an effective oversampling at lower rest-mass densities and, consequently, undersampling at high rest-mass densities. Indeed, this is clearly illustrated as there are no tracers that come from above $\sim 10^{12}\,\mathrm{g/cm^3}$ while almost all tracers below $10^{9}\,\mathrm{g/cm^3}$ become unbound. Because the lower densities also have higher values of Y_e, the "correlated" placement defacto leads to an oversampling around $Y_e \sim 0.18$ (hence the second broad peak in the distribution) and to an undersampling at $Y_e \sim 0.05$ (hence the smaller first peak in the distribution).

Not surprisingly, the "anticorrelated" placement suffers of the opposite problem. It undersamples cells at lower rest-mass densities resulting in there being fewer tracers with large values of Y_e. More precisely, the top right panel of Fig. 3.8 shows that there is a significant number of tracers above $10^{12}\,\mathrm{g/cm^3}$, which have low values of Y_e, thus yield a good agreement with the first peak. However, at lower rest-mass densities, a higher percentage of tracers that become unbound come from lower densities and hence we are effectively and significantly undersampling matter at low densities. For example, only about $1\,\%$ of the initial tracers were placed at the lowest initial rest-mass density of $\sim 10^{7}\,\mathrm{g/cm^3}$, but almost $20\,\%$ of the tracers that are unbound come from these rest-mass densities. Examining the bottom left panel of Fig. 3.8 one can also appreciate that the "uniform" placement distribution is, in a sense, the average of the above two placements. It uniformly samples from all densities and hence has no oversampling or undersampling at high and low rest-mass densities. As shown in Fig. 3.8 tracers that are initially at $10^{14}\,\mathrm{g/cm^3}$ become unbound, as in the case of the "anticorrelated" placement; at the same time, the tracers at low rest-mass densities are unbound, thus making the "uniform" placement be the most effective one, besides being also the simplest to implement.

When considering the "unbound" placement, the bottom right panel of Fig. 3.8 shows that there is a remarkably good match between the initial distribution of the placed tracers and the distribution at detector crossing, especially for medium and high rest-mass densities, which is not surprising given that it focuses on material just before it becomes unbound. Yet, while such a placement nicely reproduces the counts at the two peaks in electron fraction, it also fails to capture the values between the two peaks, as shown in the left panel of Fig. 3.7. This is most likely due to the fact that this placement completely misses some of the material that the other tracer placements otherwise capture. In particular for example, it undersamples the material that is at low rest-mass density, which is well captured by the correlated placement for example. Hence, the behaviour in Figs. 3.7 and 3.8 highlights a potential drawback of the "unbound" placement procedure. This placement, in fact, while it can nicely sample the unbound material, only captures material that is unbound at a given moment and neglects any material that might become unbound and that has not yet become unbound, most notably,

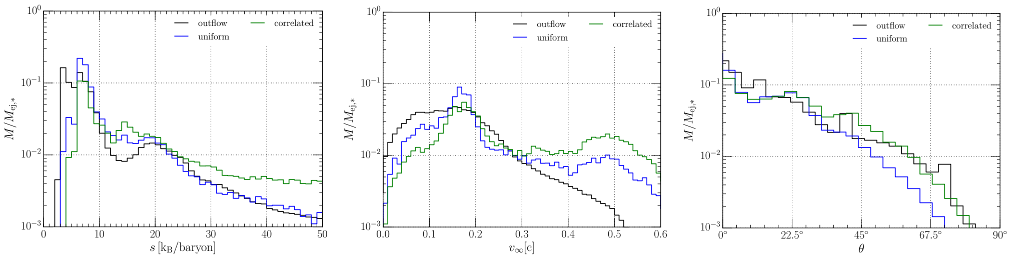

Figure 3.9: Comparison between the distributions in electron fraction as computed with the tracer mass-fluxes through the surface at $200\,M_\odot$ as computed with the different placement schemes (coloured lines) and the outflow (black line). The quantities considered are: the entropy, the velocity at infinity, and the angular distribution; all curves have been normalised to the corresponding total ejected masses (cf. Fig. 3.7).

the very low rest-mass density material. Furthermore, this distribution is highly time-dependent as how close to the crossing-time is necessary is left as a free parameter.

However the electron fraction isn't the only quantity that one can compare. In Fig. 3.9, the thermodynamical and physical quantities similar the one presented in Fig. 3.7 are illustrated. These three quantities are: the specific entropy (left), the velocity at infinity (middle), and the angular distribution (right). Here, only a comparison between the fluid outflow (black line), the "uniform" distribution placement (blue line), and the "correlated" placement (green line) is done as discussed above, it represents the best placement tested. In terms of the distributions, note how the specific-entropy distributions are all rather similar, although the "uniform" placement undersamples at the first peak and does not show a local minimum at around $15\,\mathrm{k_B/baryon}$. The velocity at infinity is another measure of the u_t and here we do not see great agreement at higher values. These higher values correspond to the more energetic tracers, thus indicating that both the "uniform" and the "correlated" placement tend to oversample the highly energetic material. Similar considerations apply to the angular distribution of the ejected, where the two placement schemes show rather similar results, both in agreement with the fluid evolution, even though the tracer mass flux shows slightly more mass at the higher angles. Interestingly, the tracer evolution is also able to reproduce the local maximum at $\sim 45°$ which a numerical artefact of the Cartesian grid and was first mentioned in Ref. [201].

In conclusion, it was found that out of all the initial tracer placements considered, the "uniform" placement results in the best agreement with the underlying fluid based on a comparison with the electron fraction. The reason for this agreement is that "uniform" method samples both high and low rest-mass densities uniformly, avoiding over- or undersampling in these regimes and captures the best of both distributions. Additionally, a priori, the "unbound" distribution sounds like the best method to capture the underlying fluid, it fails to properly reproduce all the measurements and suffers in comparison with the "uniform" method.

3.4 Tracing bound material

In this section, the discussion changes towards the use of tracers in the **bound** case by applying the tracer method to the case in which they are employed to describe the dynamics of matter that is gravitationally bound. Despite already having a complete description of the fluid dynamics as measured by Eulerian observers, i.e., the observer at "infinity", there are a number of reasons why using tracers could be a powerful tool as it represents a shift to a Lagrangian viewpoint, i.e., an observer who "lives" on a fluid element. The most important of such reasons is that tracers following bound fluid elements allow for the disentanglement of the local dynamics of the fluid from the global one, such as in the case of differential rotation. Because both of these dynamics can be complex and operate on different timescales, having the possibility of setting them apart is quite valuable to interpret the results of simulations. As discussed previously, there are several examples of the successful use of tracers in bound material (see, e.g., the interesting analysis of precessing and tilted disk accretion in Ref. [175]), but here the concentrated is focused on the dynamics of the HMNS produced by the merger of a binary system of neutron stars [110] which will be delved into more detail in Chapter 4.

More specifically, the focus of this section is not on dynamical ejecta, but instead on studying the rotational properties of the HMNS produced by the merger of a binary system of neutron stars. When two neutron stars merger, the merger remanent is a metastable object which can survive for some time before ultimately collapsing to a black hole. For every equation of state, there exists a maximum mass above which the neutron star will promptly collapse to a black hole. However, to derive this maximum mass, the assumption is made that the star is non-rotating. With the exception of perfectly head-on collisions, there is some non-zero angular momentum which will be transferred to the merger remanent which results in a rotating object. This rotation adds additional support to prevent collapse and thus larger masses than the non-rotating case are possible. To complicate this picture is that the remanent is subject to violent oscillations and, at the same time, it is subject to a barmode deformation that leads to a copious emission of gravitational waves which makes disentangling the physics of each effect complicated. Hence, a deeper understanding of the distribution of angular momentum and angular velocity can help in determining under what conditions the HMNS will collapse to a black hole in a more realistic case. It is therefore useful to study the angular velocity of the fluid as a first step to decoupling these processes. The angular velocity Ω, is defined as

$$\Omega := \alpha\, v^{\phi} - \beta^{\phi}\,, \tag{3.11}$$

where ϕ refers to the azimuthal direction (see Chapter 4 where a more detailed discussion will be presented). Hereafter focus will be concentrate on the HMNS produced when two identical neutron stars with a (gravitational) mass of $1.35\,M_{\odot}$ and described by the hot DD2 EOS, but a much large sample of binaries will be explored in Chapter 4.

3.4.1 Initial placement

Unlike the case of the dynamical ejecta of the previous sections, selecting the optimal initial placement when studying bound flow is much less problematic since the ultimate goal is not to accurately capture the underlying fluid, but instead ensure that the fluid is well sampled to obtain tracers in all regions. Thus as long as it is clear as to what region of the fluid that is to be studied, then placing tracers is mostly a matter of deciding a good time for the seeding and employing a sufficiently large number of tracers so that all parts of the flow are properly represented. For the case of angular velocity, the motion in the core of the HMNS needs to be tracked thus it is straightforward to set the time of the merger as the time for the tracer seeding as this is the time when the HMNS forms. Furthermore, for the spatial placement no probability distribution associated with the rest-mass density is required but instead simply placing a single tracer in each of the fluid cells that are mark to be within a certain region of the computational domain, namely, the core of the HMNS. In practice, using $\sim\ 10^5$ tracers is more than sufficient to ensure that every cell within the core had a tracer in it. With this placement scheme of the 10^5 initially placed tracers, approximately 6000 remained on the (x, y) plane for the entire simulation run time, thus allowing the study of the fine details of the fluid motion on this plane to be done.

3.4.2 Dynamics of the HMNS

In Fig. 3.10 a representative time is plotted, approximately $\sim\ 5.5\,\mathrm{ms}$ after the merger and of the evolution of the rest-mass density (left) and the angular velocity (right). In the top panel the frame of an observer at infinity (Eulerian) is chosen, while in the bottom the "corotating frame" is chosen. Here a corotating frame is a frame defined to be rotating at a frequency that is half of the instantaneous gravitational-wave frequency, Ω_{GW} where here $\Omega_{\mathrm{GW}}/2\ =\ 1291\,\mathrm{Hz}$. The tracers plotted here are just a representative of the $\sim\ 6000$ tracers that remain in the (x, y)

plane throughout the entire evolution. For each tracer, a small filled circle is used to report the position at the given time, and the solid lines of decreasing size are the position at two previous times separated by $\sim 0.3\ \mathrm{ms}$. The "tails" that are produced in this manner provide a simple way to visualise the tracer streamlines and hence the evolution of the fluid as it rotates around the core. Also, the number of tracers is sufficient to completely cover the core and all key features are represented by numerous tracers, however only representative ones are plotted to illustrate the rich evolution of the feature that is difficult to observe without the streamlines.

The benefit of tracers is immediate and clarifies and illustrates the evolution of the fluid when in the corotating frame. In the top panel of Fig. 3.10, the evolution of the tracers in the Eulerian frame is a complete mess. Given a time series it would be possible to observe the $l = m = 2$ bar deformation that forms, but the evolution of the tracers do not illustrate this feature. Contrast this to the corotating frame plotted in the bottom left panel of Fig. 3.10. Here the underlying rest-mass density clearly exhibits an $l = m = 2$ deformation and the tracers clearly see illustrate that there is a central bar around which the tracers flow. In addition to this bar deformation, there are two vortices that trap fluid (bottom of Fig. 3.10) that are not clear in the Eulerian frame. This pattern can be even more clearly seen in the angular velocity, where these side vortices have higher angular velocity compared with the central bar. Additionally, the tracers illustrate further the structure of the angular velocity distribution. In this panel, white refers to "non-rotating" within the corotating frame, i.e., fluid elements are rotating exactly at the corotating frequency. Blue regions are rotating slower and red regions faster than the corotating respectively. This rotating explains the vortices in the fluid, as in these regions, the fluid is revolving faster than the corotating frequency – and hence move counterclockwise – while other tracers either corotate – hence they appear not to move – or rotate more slowly than the corotation frequency – and hence move clockwise. This behaviour is not possible to determine in the Eulerian frame where everything is rotating and there is no stationary reference to use. This combined use of tracers and the corotating frame demonstrates the ability to visualise features of the core that are otherwise difficult to visualise in an Eulerian picture.

A similarity with the dynamical ejecta, in the case of bound material, is that the tracers record the values of variables along fluid lines. For dynamical ejecta, this is used for r-process, but for the bound material they allow for the computation of quantities that should be conserved along streamlines. For example, it is expected that if fluid is perfect and the flow is isentropic the Bernoulli constant will be conserved [213]. Keeping track of such quantities can be extremely useful to explain a behaviour which would otherwise appear puzzling when only considering the bulk motion of the fluid. As will be shown in Chapter 4, it will be

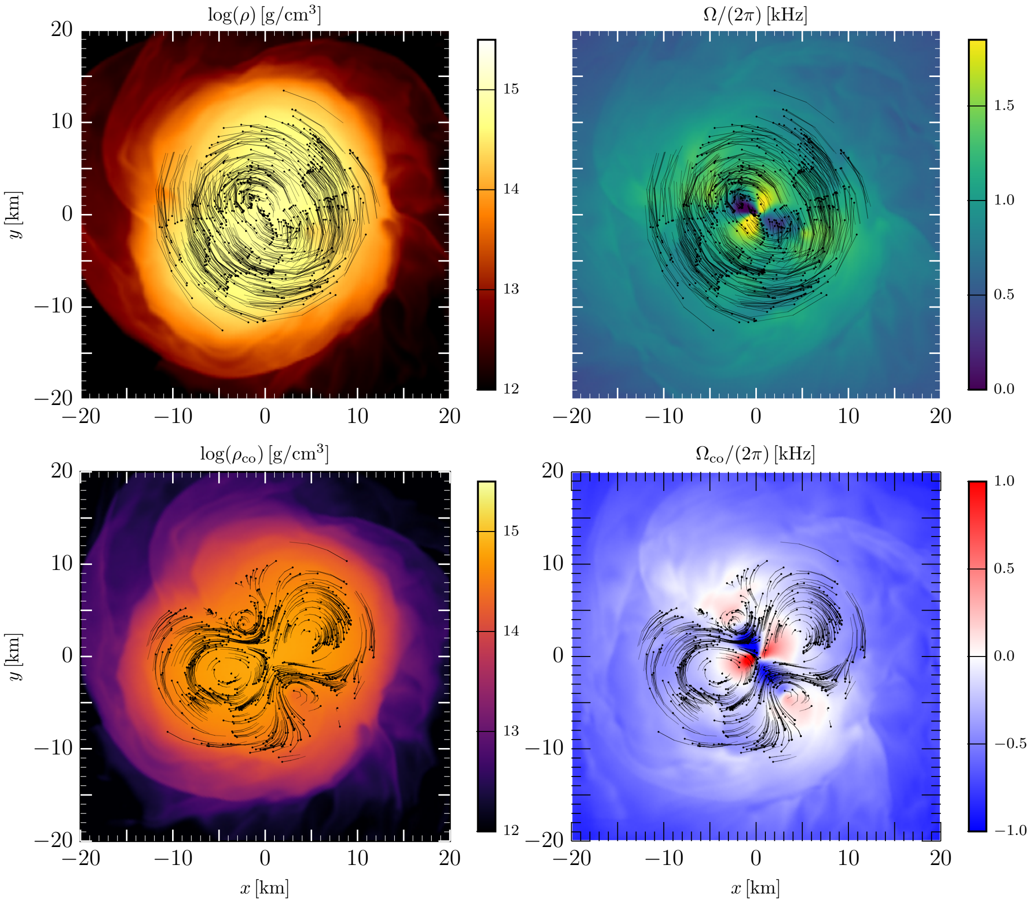

Figure 3.10: Distributions on the (x, y) plane of the rest-mass density (left panels), and of the angular velocity (right panels). The top panels are relative to the Eulerian frame at time $t = 5.5$ ms, while the bottom panels refer to a corotating frame with angular velocity $\Omega_{\rm co} := \Omega - \Omega_{\rm GW}/2$, where $\Omega_{\rm GW} = 2582\,{\rm Hz}$ is the instantaneous gravitational-wave frequency. Also shown are portions of the flowlines of several tracer particles that remain close to the (x, y) plane and for which we show only the final part of the flowlines (i.e., for the last $\simeq 0.285\,{\rm ms}$), using small dots to indicate the particle position at the time indicated in the frame. In addition, the initial parts of the trajectories have increasing transparency so as to highlight the final part of the trajectories.

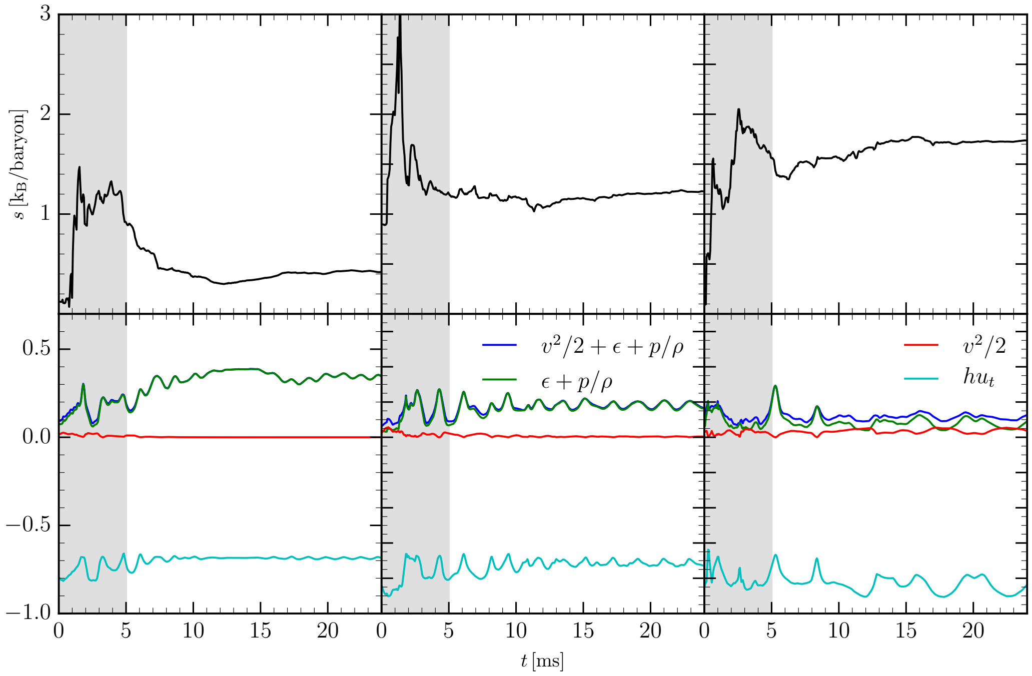

Figure 3.11: *Top panels:* Evolution of the entropy for tracers in the HMNS that are eventually either in the inner core (i.e., $r \lesssim 4$ km; left panel), in the middle core (i.e., $4 \lesssim r \lesssim 6$ km; middle panel), or in the outer core (i.e., $6 \lesssim r \lesssim 8$ km; right panel). *Bottom panels:* evolution of the Bernoulli constant hu_t (light blue line), the classical Bernoulli constant $v^2/2 + \epsilon + p/\rho$ (blue line) and its main contributions: $\epsilon + p/\rho$ (green line) and the kinetic term $v^2/2$ (red line). The grey-shaded area refers to the postmerger transient when the HMNS is far from an equilibrium.

shown that the dependence of the angular velocity depends inversely on the rest-mass density, through the Bernoulli constant. This conjecture explains why the rest-mass density and angular velocity profiles have a clear 90 degree phase difference (cf. left and right panels of Fig. 3.10). This assertion, however, is difficult to verify without tracers and the streamlines they can be provide.

Recall that in relativistic hydrodynamics a perfect fluid with four-velocity $\boldsymbol{u}$, the quantity $h\,(\boldsymbol{u}\cdot\boldsymbol{\xi})$ is Lie-dragged along $\boldsymbol{u}$ [213]

$$L_{\boldsymbol{u}}(h\,\boldsymbol{u}\cdot\boldsymbol{\xi}) = 0\,, \tag{3.12}$$

where $h := (e+p)/\rho$ is the specific enthalpy, $e := \rho(1+\epsilon)$ is the total energy density, and $\boldsymbol{\xi}$ is a Killing vector of the spacetime and also a generator of the symmetry obeyed by the fluid. If spacetime admits a timelike Killing vector so that the fluid motion is stationary, then the quantity $\mathcal{B} := hu_t$ is a constant of the fluid. In its classical limit, Eq. (4.13) becomes

$$\left(1+\epsilon+\frac{p}{\rho}\right)\left(1+\phi+\frac{1}{2}\vec{\boldsymbol{v}}^2\right) = \text{const.}\,, \tag{3.13}$$

where ϕ is the gravitational potential and $\boldsymbol{v}$ is the local fluid velocity. When neglecting higher-order terms and taking the gravitational potential to be independent of time and essentially constant across the HMNS, expression (4.14) further reduces to

$$\left(\frac{1}{2}\vec{\boldsymbol{v}}^2+\epsilon+\frac{p}{\rho}\right) = \text{const.}\,, \tag{3.14}$$

which coincides with the classical expression for the Bernoulli constant [213]. When consider the above simulation, it is clear that during the post-merger phase of a BNS merger there is no timelike Killing vector, however the Bernoulli constant can still be computed using the tracer particles and can be used to measure how well the Bernoulli constant is actually conserved along streamlines in this complicated situation.

This computation is done and illustrated in Figure 4.17 and this example provides a simple example of how the evolution of tracers allows one to quickly and simply perform the analysis of very precise regions of the fluid and can illustrate hidden physical laws that are not evident at first. In particular, the panels in Fig. 4.17 show the time evolution of several quantities relative to three tracers that have been chosen as representative of three areas areas of the HMNS: the inner core (i.e., $r \lesssim 4$ km), the middle core (i.e., $4 \lesssim r \lesssim 6$ km), and the outer core (i.e., $6 \lesssim r \lesssim 8$ km). The top panels, in particular, show the evolution of the specific entropy which, during the violent post-merger phase, undergoes a sudden jump due to heating, but quickly settles to become approximately constant. The bottom panels, instead, shows the evolution of the Bernoulli constant in light blue.

In essence, Fig. 4.17 shows that even though the post-merger phase does not exhibit a timelike Killing vector, the Bernoulli constant stays roughly constant across the interior of the HMNS. This constant behaviour can be used to explain the phase difference between the where the rotation-profile is out-of-phase with the barmode from the rest-mass density, as will be discussed in more detail in Chapter 4.

3.5 Conclusions

In this chapter the basics of tracers, so called massless particles, were investigated for bound and unbound material. Tracers are massless particles that are passively advected and provide an effective way of recording the thermodynamical history of the fluid in grid-based codes. However, while not particularly expensive to compute, the use of tracers requires a judicious initial placement, both in time and space, and especially if the portion of the fluid one is interested in is the one that is gravitationally unbound. This is because different placements can potentially lead to different physical observables and hence to different physical conclusions on the properties of the underlying fluid.

In particular the efficacy of how well the tracers can match the underlying fluid in the context of dynamical ejecta was evaluated by directly comparing results from the fluid itself. More specifically, four different placement schemes that could be used to initially distribute the tracers were evaluated and how well their evolution matches that when compared with information from the actual fluid flow. The four schemes considered were built by constructing distribution functions of the tracers that are either directly *correlated* with the rest-mass density distribution, or *anti-correlated*, or *uniformly* distributed, or, as a final case, independent on the rest-mass density and related instead to the portion of fluid that is *unbound*. Countering naive expectations that a placement that follows the rest-mass density would result in the best tracer evolution or indeed with a placement that picks up the fluid just before it becomes unbound, it was found that the most effective method of placing tracers initially is to *uniformly* sample them across the rest-mass density distribution. The reason for this for this placement is that this leads to the closest matching with the unbound material that is flowing through a detector at roughly $300\,\mathrm{km}$ from the centre of the merger. This match has been compared across a number of physical quantities, such as the unbound rest-mass, the distributions of electron fraction, specific entropy and kinetic energy. Interestingly, the most important reason why a uniform distribution represents the optimal one is that it has the merit of sampling sufficiently from both the high and low rest-mass density regions that are ejected during the merger. Other methods, in fact, tend to either underestimate or overestimate the contributions coming form certain regions of the fluid.

In addition, tracers can be also used for bound material. In particular they allow for a fine analysis of the motion of the fluid in regions that are highly complex, providing information on the properties of the fluid and on the quantities that should be conserved along streamlines if the flow is adiabatic. This was illustrated by considering the motion of tracers in the core of an HMNS produced in the merger of a BNS system. It was shown that tracers provide a novel way to show the evolution of the fluid and display features that are otherwise difficult to observe and analyse. As a representative example, it was shown that the fluid vortices can form in the HMNS where matter is locally trapped and that these vortices are located in regions of low rest-mass density and high fluid velocity, as expected from the conservation of the Bernoulli constant.

The results of this chapter provide the framework for the next three chapters as they discuss particular applications of tracers touched upon briefly here. In particular, in Chapter 4 and Chapter 5 the application of tracers to bound material will be explored further. In Chapter 6, the tracer data as input for radiative-transfer models to calculate the light curves resulting from the corresponding kilonova for unbound dynamical ejecta.

Chapter 4

Rotational properties of hypermassive neutron stars from binary mergers

In this chapter, the tracer method of Chapter 3 is used in the context of bound material in the post-merger phase, focusing specifically on the problem of differential rotation. [1]

4.1 Introduction

Prior to the direct detection GW170817 of gravitational waves from merging neutron stars, the formation of heavy compact objects with large amounts of angular momentum was expected, for example, from the collapse of the iron core in Type-II supernova. When a significant amount of angular momentum is present, the neutron star is prevented from collapse by additional pressure support coming from the rotation. The simplest case of rotation, uniform rotation, while theoretically easy to model, is not an effective way of sustaining large rotation rates – on the order of a few thousand kHz – in realistic stars where the densities vary over several orders of magnitude. Instead, a far easier way of maintaining this support from collapse is by distributing the angular momentum differentially in radius, or "differential rotation". If this differential rotation law is known, by measuring the mass of the object, one can obtain an estimate of how far from or how close to gravitational collapse to a black hole equilibrium configuration is. As such, pro-

---

[1] This chapter is based on the work of [110]. All figures in this chapter have been reproduced from [110]. My contribution to the work of [110] was to run additional simulations – specifically those of the temperature-dependent EOS with tracers –, do data analysis, generate all the figures, write and edit the text of the paper.

viding a rotational law is essential, especially after the detection of GW170817 where, although the post-merger wasn't seen, the prospects of detecting a signal from this part of the merger is likely. Additionally, estimates of the mass from other channels, such as kilonova modelling, can be used to validate models and predictions from a differential rotation law.

Over the past decades, a large number of works have explored this problem in full general relativity, either through the construction of equilibrium configurations [30, 155, 240, 238, 13, 96, 252, 101] or through their dynamical production in core-collapse supernovae [186] or in binary neutron star mergers [23]. Unfortunately, there is a distinct lack of a physically motivated law of differential rotation. In lieu of this, almost all of these previous works have assumed that the rotation law is particularly simple. Specifically, the assumption made is that the angular momentum, $j := hu_\phi$ is constant, where h is the specific enthalpy and u_ϕ the covariant azimuthal component of the four-velocity. One physical advantage of the law is that it satisfies the Rayleigh criterion for local dynamical stability against axisymmetric perturbations, $dj/d\Omega < 0$, where Ω is the angular velocity.

However, perhaps the biggest benefit of the law is that it is analytically simple, with the angular velocity decreasing monotonically from the center of the star and with the degree of differential rotation being regulated by a single dimensionless parameter, normally referred to as $\tilde{A}$. Despite this simplicity, numerous studies have shown that for a given degree of differential rotation, different classes of solutions are possible for a given set of parameters [13, 101] and also potentially reaching as large as four times that of the maximum mass of nonrotating configurations $M_{\rm TOV}$. In contrast, when assuming a uniformly-rotating model, a variance of only 20% is seen [47]. These results have implications for constraining the maximum of a neutron star e.g., [160], and thus an understanding of how differential rotation affects the stability of a hypermassive neutron star can lead to constraints on the equation of state.

However, even with this simplistic law, little work has been done to make suitable generalizations [96] for a wider space of equilibria and general prescriptions for differential rotation. This means that while the $j - \mathrm{constant}$ law of differential rotation has been useful so far to explore the equilibria of differentially rotating compact stars, such as isolated neutron stars, its study in neutron merger simulations is harder to justify where clear violations of a $j - \mathrm{constant}$ law are observed. Numerous studies over the past decade have indeed shown that the formation of a hypermassive neutron star (HMNS), that is, a neutron star whose mass exceeds the maximum mass of a uniformly rotating star, the law of differential rotation is rather different [241, 18, 12, 151, 39, 210, 65]. This means that a law of differential rotation that, while maybe not analytically simple, reflects the results from hydrodynamical simulations.

Some preliminary work in this direction has been undertaken in Refs. [128, 127], where the properties of the angular-velocity distribution in the merged object were analyzed in detail, although only for a very limited number of binaries. These studies agree with earlier simulations of Ref. [238], and these more studies have found that the angular-velocity profile of the HMNS exhibits a slowly rotating core and an envelope that rotates at angular frequencies that scale as $r^{-3/2}$, where r is the radius from the centre. Although irrotational binaries are most likely to be physical, extensions to initial data with rotation has shown similar results [129] suggesting that differential rotation observed in the HMNS is robust.

In contrast to previous studies, here, a more systematic approach is adopted. In particular, a large number of equations of state, masses, and mass ratios are studied. The results of these numerous simulations confirm the more early results of Refs. [238, 128, 127], however, it is exhibited here that the rotation law exhibits "quasi-universality" which has hitherto not been discussed in the context of differential rotation. Quasi-universal relationships have been found in both isolated [276, 191, 248, 112, 71, 55, 47] and in binary systems [276, 165, 254, 212] and are a very powerful tool it allows complicated non-linear simulations to be summarised by a few dimensionless parameters, which themselves are typically functions of a few simple observables such as mass or radius. In the case to be presented here, the angular-velocity distributions found are to be, independently of the EOS, composed of an almost uniformly rotating core and a disk with angular frequencies $\Omega(r) \propto r^{-3/2}$. This disk, which is in the outer regions of the HMNS, plays an important role in longer term evolution – here longer term means longer than the timescale of the simulations, which is on the order of 10s of milliseconds – through accretion and the creation of a torus around a black hole. Both of these physical effects are important within the proto-magnetar model for short gamma-ray bursts [278, 173, 51] and the subsequent extended X-ray emission [211, 59].

This chapter is organized as follows: Section 4.2 is dedicated to a brief overview of the mathematical and numerical setup employed in the simulations, while in Secs. 4.3 and 4.4 the results of the simulations are obtained results obtained when modelling high- and low-mass binaries, respectively with particular focus paid to the distributions of rest-mass density and angular velocity, and illustrates the approach to obtain time and azimuthally averaged profiles. Section 4.5 focuses on the use of tracer particles, introduced in Chapter 3, to disentangle the physically meaningful results from the possible contamination of gauge effects, while Sec. 4.6 discusses the "quasi-universal" features of the angular-velocity profiles and how to correlate them with the properties of the progenitor stars in the binary. Also discussed in Sec. 4.6 is the amount of mass in the disk and the influence of the thermal component of the EOS on the results presented. Finally, Sec. 4.7 provides a discussion in terms of the dynamics of tracers on the conservation of the Bernoulli constant in the quasi equilibrium of the HMNS. Sec. 4.8 provides a discussion of the effects of resolution and symmetries on the lifetime and evolution of the HMNS.

4.2 General Framework

4.2.1 Mathematical and numerical setup

The mathematical and numerical setup used for the simulations reported here is the same discussed in Refs. [254, 256] and presented in greater detail in other papers [18, 19, 21] and in Chapter 2. For completeness a brief review is done here the basic aspects as some of the numerical methods used differ from those in other parts of the thesis.

Like the previous simulations performed, all simulations presented here are performed using the fourth-order finite-differencing code `McLachlan` [49, 153], which is part of the publicly available `Einstein Toolkit` [1]. This code solves a conformal traceless formulation of the Einstein equations [183, 236, 28], with a "$1 + \log$" slicing condition and a "Gamma-driver" shift condition [6, 198]. A difference here, however, is that the simulations were not performed with the code `WhiskyTHC` but instead with the general-relativistic hydrodynamics finite-volume code `Whisky` [20], which has been extensively tested in simulations involving the inspiral and merger of binary neutron stars [18, 19, 209, 22]. All simulations are performed in general relativity using the of energy, momentum and rest mass [213] and are cast in the conservative Valencia formulation [85] cf. Chapter 2. Their numerical solution is obtained employing the Harten-Lax-van Leer-Einfeldt [111] approximate Riemann solver [111] in conjunction with the Piecewise Parabolic Method [61] for the reconstruction of the evolved variables. For the time integration of the coupled set of hydrodynamic and Einstein equations the Method of Lines with an explicit fourth-order Runge-Kutta method is used. All simulations use a CFL number of 0.35 to compute the timestep.

An adaptive mesh refinement (AMR) approach based on the `Carpet` mesh-refinement driver [226] is used to both increase resolution and extend the spatial domain, placing the outer boundary as close as possible to the wave zone. The grid hierarchy consists of six refinement levels with a grid resolution varying from $\Delta h_5 = 0.15\,M_\odot$ (i.e., $\simeq 221\,\mathrm{m}$) for the finest level to $\Delta h_0 = 4.8\,M_\odot$ (i.e., $\simeq 7.1\,\mathrm{km}$) for the coarsest level, whose outer boundary is at $514\,M_\odot$ (i.e., $\simeq 759\,\mathrm{km}$). To reduce computational costs, a reflection symmetry across the $z = 0$ plane and a π-symmetry condition across the $x = 0$ plane has been adopted , although this assumption will be tested in Section 4.8 on the influence this has on the overall results. The initial configuration for the quasi-equilibrium irrotational binary neutron stars has been generated with the use of the `LORENE`-code [104] and an initial coordinate separation of the stellar centers of $45\,\mathrm{km}$ has been used for all binaries. For each EOS considered equal-mass binaries where each star has initial gravitational masses that are either $M = 1.25 M_\odot$ (low-mass binaries; cf. Sec. 4.4) or $1.35 M_\odot$ (high-mass binaries; cf. Sec. 4.3) at infinite separation have been used.

A quantity that is particularly important in the analysis is the angular velocity, Ω, which is defined as the amount of coordinate rotation

$$\Omega := \frac{d\phi}{dt} = \frac{dx^\phi}{dt} = \frac{u^\phi}{u^t}\,, \tag{4.1}$$

where u^ϕ and u^t are components of the four-velocity vector u^μ. The corresponding three-velocity as measured by the same Eulerian observer is then defined as

$$v^i := \frac{\gamma^i_\mu u^\mu}{-n_\mu u^\mu} = \frac{1}{\alpha}\left(\frac{u^i}{u^t} + \beta^i\right)\,, \tag{4.2}$$

where α is the lapse function, β^i is the shift vector, n^μ is the unit timelike vector normal to a constant t hypersurface, and γ_{ij} is the three-dimensional metric. With the above definition the angular velocity within the $3+1$ split can be expressed as

$$\Omega = \alpha\, v^\phi \;-\; \beta^\phi\,, \tag{4.3}$$

where

$$v^\phi = \frac{x v^y - y v^x}{x^2 + y^2 + z^2}\,, \tag{4.4}$$

$$\beta^\phi = \frac{x \beta^y - y \beta^x}{x^2 + y^2 + z^2}\,, \tag{4.5}$$

are the three-velocity and shift vector components as computed from the Cartesian grid with coordinates (x, y, z). Written in this form, one can interpret Ω as consisting of a lapse-corrected part of the ϕ-component of the three-velocity, minus a frame-dragging term provided by the ϕ-component of the shift vector.

4.2.2 Microphysical matter treatment

In order to evolve the binaries, the evolution equations must be closed with an equation of state (EOS). The equation of state provides a relation among the thermodynamical quantities of neuron star matter, for example the rest-mass density and the pressure. Typically, the general independent thermodynamical quantities of an equation of state are the rest-mass density, electron fraction, and the temperature. However, in some cases, a simplified treatment is acceptable. For example, during the inspiral, the neutron star is “cold” and a temperature independent

EOS is sufficient to represent the matter inside of a neutron star. However, as the neutron stars merger, large shocks are formed within the neutron star which are inherently temperature dependent and thus a proper treatment of the neutron star is required, as discussed in Chapter 2. Although ideal, the number of fully consistent thermodynamic EOSs is limited, especially after the detection of GW170817, the parameter space that these tabulated EOSs provide is rather limited. To get around this fact, and in order to study the more extremes of the EOS parameter space, here a simple piecewiese-polytrope set of EOSs is used. Thermal effects are included through the addition of an ideal-fluid component which is able to account for shock heating. This means that the pressure p and the specific internal energy ϵ are therefore composed of a cold nuclear-physics part and of a "thermal" ideal-fluid component[2] [119]

$$p = p_{\rm c} + p_{\rm th}\,, \qquad \epsilon = \epsilon_{\rm c} + \epsilon_{\rm th}\,, \tag{4.6}$$

where p and ϵ are the pressure and specific internal energy, respectively. The cold part $p_{\rm c}, \epsilon_{\rm c}$ are modelled with five different nuclear-physics EOSs. Two of such EOSs, namely APR4 [5] and SLy [72], belong to the class of variational-method EOSs and the underlying particle composition within these models consists mainly of neutrons with little admixtures of protons, electrons and muons. Additionally, two more EOSs, i.e., GNH3 [99] and H4 [100], are built using relativistic mean-field models which include, above a certain rest-mass density, hyperonic particles.

However, a change is made for the fifth and final EOS, namely ALF2 [7]. This EOS is more a model for hybrid stars than for neutron stars because it implements a phase transition to colour-flavor-locked quark matter. Within this model, the hadronic particles begin to deconfine to quark matter above a certain transition rest-mass density $\rho_{\rm trans} = 3\,\rho_{\rm nuc}$, where $\rho_{\rm nuc} := 2.705 \times 10^{14}$ g/cm^3 is the nuclear-matter rest-mass density.

Note that all of the EOSs used in the calculations satisfy the current observational constraint on the observed maximum mass in neutron stars, i.e., $2.01 \pm 0.04 M_{\odot}$ [14], although evidence from GW170817 does rule out some stiffer EOSs [263]. Instead of using the data tables of the various EOSs, it is more suitable to convert them to piecewise polytropes [206]. Each EOS has been parametrized, based on specifying its stiffness in three rest-mass density intervals $i = 2, 3, 4$, measured by the adiabatic index $\Gamma_i = d\,\log \bar{p}_i / d\,\log \bar{\rho}_i$. Additionally, a unique polytrope with $\Gamma_1 = 1.357$ has been added for all of the used EOS to account for the star's low rest-mass density region $\rho \leq \rho_{\rm nuc}$.

---

[2] This class of EOSs is referred in the literature as the so-called "hybrid EOS" [213] and should not be meant to indicate that the star is composed of a hybrid hadron-quark matter present in hybrid stars.

model	EOS	M [$M_\odot$]	R [km]	$M_{\rm ADM}$ [$M_\odot$]	$M_{\rm b}$ [$M_\odot$]	M/R	$f_{\rm orb}$ [Hz]	J	I/M^3
GNH3-M125	GNH3	1.250	13.817	2.4780	1.3464	0.13358	273.29	6.4067	18.890
GNH3-M135	GNH3	1.350	13.777	2.6746	1.4641	0.14468	281.58	7.2766	16.450
H4-M125	H4	1.250	13.533	2.4780	1.3506	0.13638	273.25	6.4058	18.610
H4-M135	H4	1.350	13.550	2.6746	1.4687	0.14711	281.61	7.2770	16.344
ALF2-M125	ALF2	1.250	12.276	2.4779	1.3672	0.15034	273.16	6.4014	16.455
ALF2-M135	ALF2	1.350	12.353	2.6746	1.4877	0.16136	281.42	7.2708	14.581
SLy-M125	SLy	1.250	11.469	2.4779	1.3720	0.16092	273.04	6.3977	14.000
SLy-M135	SLy	1.350	11.465	2.6745	1.4946	0.17386	281.34	7.2663	12.309
APR4-M125	APR4	1.250	11.052	2.4779	1.3783	0.16700	273.05	6.3973	13.226
APR4-M135	APR4	1.350	11.079	2.6746	1.5020	0.17992	281.37	7.2665	11.720
LS220-M132	LS220	1.319	12.775	2.6127	1.4360	0.15108	278.68	6.9891	15.113
LS220-M135	LS220	1.350	12.750	2.6740	1.4733	0.15638	281.29	7.2656	14.112

model	EOS	M [$M_\odot$]	k_2	λ/M^5
GNH3-M125	GNH3	1.250	0.11753	1842.4
GNH3-M135	GNH3	1.350	0.10841	1139.9
H4-M125	H4	1.250	0.12361	1746.5
H4-M135	H4	1.350	0.11483	1111.1
ALF2-M125	ALF2	1.250	0.13049	1132.6
ALF2-M135	ALF2	1.350	0.12037	733.63
SLy-M125	SLy	1.250	0.10266	634.27
SLy-M135	SLy	1.350	0.092993	390.29
APR4-M125	APR4	1.250	0.099787	512.14
APR4-M135	APR4	1.350	0.090990	321.78
LS220-M132	LS220	1.319	0.099289	840.93
LS220-M135	LS220	1.350	0.096575	688.26

Table 4.1: All binaries evolved and their properties. The various columns denote the gravitational mass M of the binary components at infinite separation, the corresponding radius R, the ADM mass $M_{\rm ADM}$ of the binary system at the initial separation, the baryon mass $M_{\rm b}$, the compactness $\mathcal{C} := M/R$, the orbital frequency $f_{\rm orb}$ at the initial separation, the total angular momentum J at the initial separation, the dimensionless moment of inertia I/M^3 at infinite separation, the $\ell = 2$ dimensionless tidal Love number k_2 at infinite separation, and the dimensionless tidal deformability λ/M^5 defined by $\lambda := 2k_2R^5/3$.

The "cold" nuclear-physics contribution to each EOS is obtained after expressing the pressure and specific internal energy $\epsilon_{\rm c}$ in the rest-mass density range $\rho_{i-1} \leq \rho < \rho_i$ as (for details see [32, 34, 255, 256])

$$p_{\rm c} = K_i \rho^{\Gamma_i} \,, \qquad \epsilon_{\rm c} = \epsilon_i + K_i \frac{\rho^{\Gamma_i - 1}}{\Gamma_i - 1} \,. \tag{4.7}$$

For an overall consistency, the rest-mass density ranges used for the piecewise polytropes have been chosen to be the same for the different EOSs ($\rho_2 = 5.012 \times 10^{14}\,{\rm g/cm^3}$ and $\rho_3 = 10^{15}\,{\rm g/cm^3}$). The transition densities ρ_1 to the low rest-mass density polytrope and the EOS-dependent adiabatic indexes Γ_i are summarized in Table 2 of [255]. Due to the implementation of the hadron-quark phase transition, the ALF2 EOS has the largest softening at the rest-mass density boundary ρ_2 ($\Gamma_1 = 4.070$ and $\Gamma_2 = 2.411$). Finally, the "thermal" part of the EOS is given by

$$p_{\rm th} = \rho \epsilon_{\rm th} \left(\Gamma_{\rm th} - 1 \right) \,, \qquad \epsilon_{\rm th} = \epsilon - \epsilon_{\rm c} \,. \tag{4.8}$$

where the last equality in (4.8) is really a definition, since ϵ refers to the computed value of the specific internal energy. In all of the piecewise polytrope simulations used hereafter, a value of $\Gamma_{\rm th} = 2.0$ is taken, but see [255, 256] for an analysis of the effect of different $\Gamma_{\rm th}$ and Sec. 4.6.3 for a discussion of the impact of $\Gamma_{\rm th}$ on the results presented here. Detailed information on all the binaries and their properties is collected in Table 6.1.

Finally, note that in order to verify the hybrid-EOS approach and numerical setup and contrast the results with an alternative one, an additional simulation has been performed using the "hot", i.e., temperature dependent, Lattimer-Swesty (LS220) EOS [140]. For this simulation the hydrodynamic equations are solved employing the `WhiskyTHC` code [203, 204] and the BSSNOK formulation of the Einstein equations [11].

4.3 High-mass binaries

The following sections are devoted to the analysis of the high-mass binary systems. To begin the discussion of the dynamics, a representative binary that is high-mass is chosen, specifically the `ALF2-M135` equation of state. Recall here that high mass means initial data of the form $2 \times 1.35\,M_{\odot}$. To contrast, in the following section, the low-mass case of `ALF2-M125` will be discussed .

The first point to address is that of collapse time. For the EOSs considered here, with the exception of APR4 and LS220, all the high-mass cases collapse to a black hole within the simulation time, as is displayed in Fig. 4.1 which shows the lapse-function approaching zero and the density blowing up for these cases. Note that lapse values close to 1 correspond to a flatter spacetime while those values close to 0 represent very curved space. Similarly, the density suddenly increasing is also a tell-tale sign of a black hole formation. In contrast, the low-mass cases do not collapse at all within the simulation time, cf. 4.7.

Following the bottom panel of Fig. 4.1, prior to the merger – note that merger, $t = 0 := t_{\rm M}$, is defined as the time of the peak gravitational wave emission – , the maximum of the rest-mass density is essentially constant in time. This maximum value of the rest-mass density corresponds to the centre of the neutron star. Likewise, the minimum of the lapse does not change too much prior to the merger. This lack of change is that during the inspiral, the two orbiting neutron stars do not experience significant tidal forces which due to the effects of strong gravity. The differences between the respective values for each EOS is due to the softness or stiffness of a given EOS.

At merger, however, this picture changes. Slightly before merger, tidal effects become more important and the two distinct maxima that are visible correspond to the tidally deformed individual stars. Immediately after merger, there is a "transient" phase –here defined to be $t \in [0, 4]\,{\rm ms}$– where there are strong and irregular fluctuations of the rest-mass density and the lapse. These fluctuations are due to the violet and shock-dominated dynamics right after merger. It is during this phase that the emergence of these two distinct maxima, known as the "double-core" structure, can be see in Fig. 4.3 and result in the maximum and minimum of the rest-mass density and lapse functions no longer corresponding to the central density. A toy model of this phase has been developed in [255] that can be used to illustrate the complicated dynamics of this phase.

Sooner after this initial transient phase, i.e., times with $t \gtrsim 4\,{\rm ms}$, these two maxima merger into a single maximum at the HMNS's centre. This is a robust merging of two maxima into a single "bar" as it appears in other works with different numerical set-ups, EOSs, and masses e.g., [239, 18]. This next phase, known as the "post-transient" phase, there is significant oscillation of both the rest-mass density and the lapse exhibiting an average increasing and decreasing value respectively. Additionally, it is possible to note a continuous decrease in the oscillation frequency, which signals the approaching of the "zero-frequency" limit and hence the quasi-radial stability limit to gravitational collapse [257]. Finally, there is a either a rapid change in the maximum and minimum, which signals a collapse to a black hole, or reaching a "quasi-equilibrium" state where there is little change in either quantity.

4.3.1 Density evolution and gravitational-wave emission

Prior to merger, the central rest-mass density is below nuclear saturation density,i.e., $\rho_{\rm max} \simeq 2.17\,\rho_{\rm nuc}$. This value is below the onset of a quark-hadron

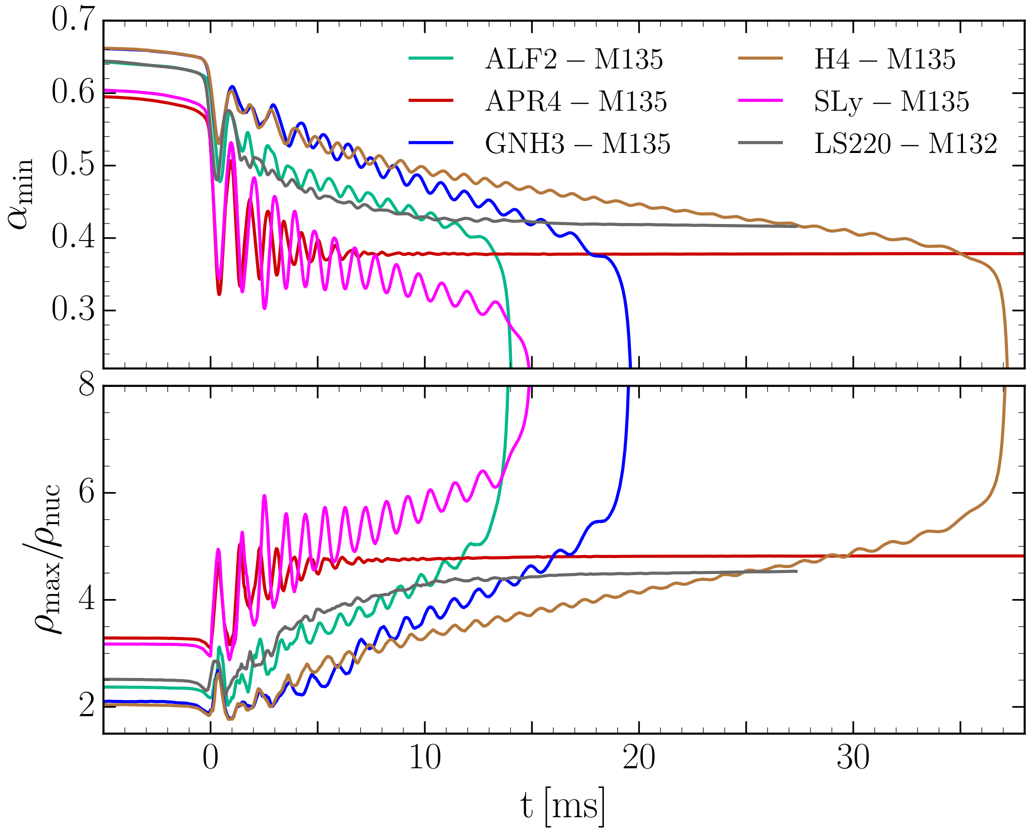

Figure 4.1: Minimum value of the lapse function $\alpha_{\rm min}$ (upper panel) and maximum of the rest-mass density $\rho_{\rm max}$ in units of the nuclear-matter rest-mass density $\rho_{\rm nuc}$ (lower panel) versus time in milliseconds after the merger for the high-mass simulations. All models collapse to a black hole except for the APR4 and LS220 EOSs.

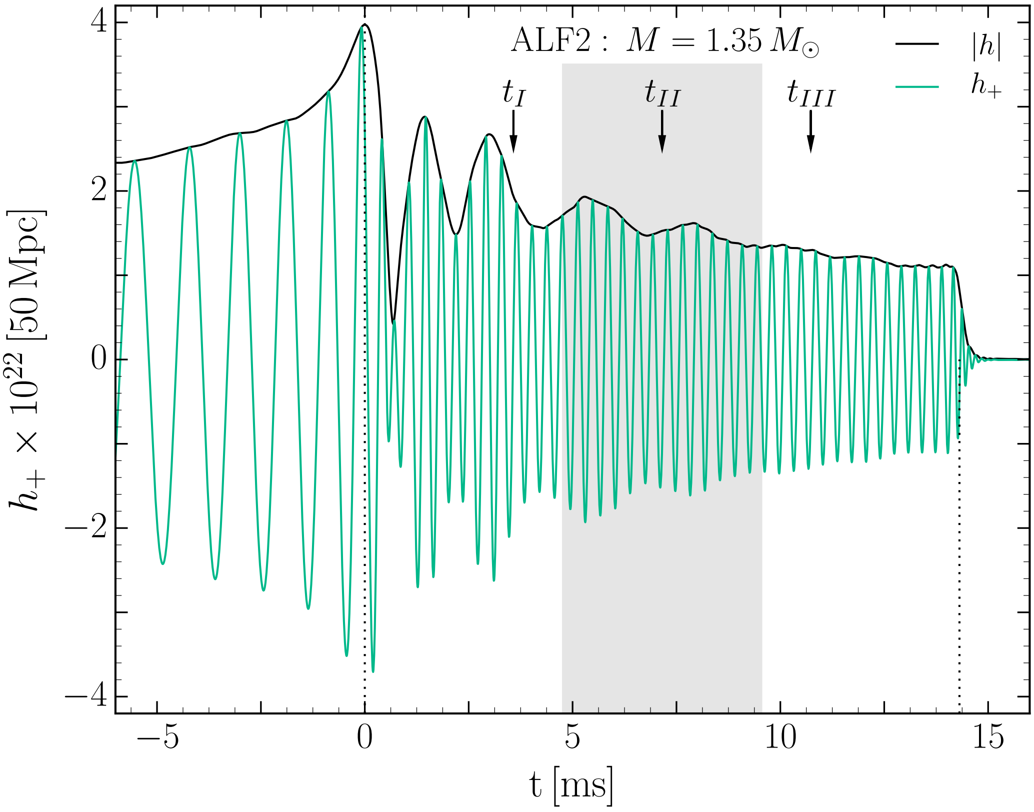

Figure 4.2: Gravitational-wave amplitude $|h|$ (black line) and strain amplitude in the $+$ polarisation h_+ (green line) for the `ALF2-M135` binary at a distance of 50 Mpc. Shaded in gray is the portion where a time average is performed, while the arrows indicate the times when representative distributions of the rest-mass density and angular velocity are shown in Fig. 4.3. Finally, the dotted vertical lines mark the time of merger and the first detection of an apparent horizon.

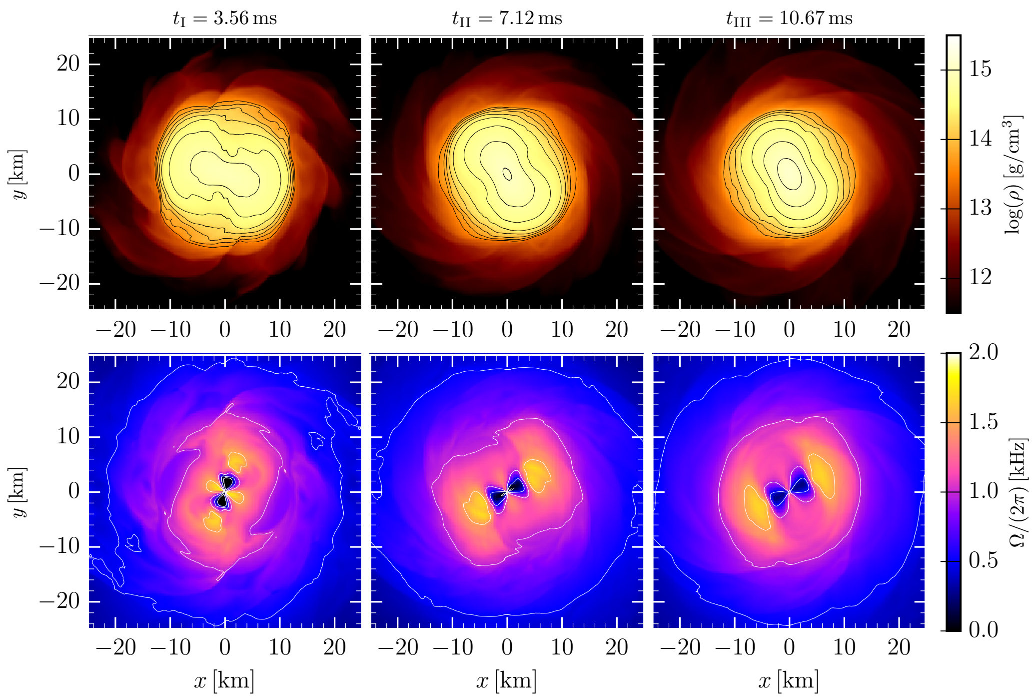

Figure 4.3: Distributions of the rest-mass density (upper row, log scale) and of the fluid angular velocity (lower row) in the (x, y) plane for the `ALF2-M135` binary at three different post-merger times as indicated in Fig. 4.2. The iso-contours have been drawn at $\log(\rho) = 13.6 + 0.2n$ (upper row) and $\Omega = \{0, 0.5, 1.0, 1.5, 2.0\}$ kHz (lower row), $n \in \mathbb{N}$.

phase transition, which occurs at roughly $\rho \sim 3\,\rho_{\rm nuc}$, so all of the matter inside the HMNS is composed of neutrons and mixtures of protons and neutrons [7]. However, during the transient post-merger phase the maximum central densities reaches above this number, for example for the `APR4-M135` model the maximum central density is $5\rho_{\rm nuc}$. However, due to the strongly oscillating nature of this phase, the mixed phase does not remain in the HMNS and confines again to hadronic matter. The exact nature of this evolution can be important when one considers the "strange matter hypothesis" which states that a strange quark-phase is the true ground state of matter. If this is the case, the resulting neutron star could transform into a quark state after certain conditions are met [109, 74, 41, 154] and during this transition, a large amount of energy would be released in the form of neutrinos and gamma-rays [73].

For times after 5 ms, the maximum rest-mass density is constanly above the phase-transition threshold and thus the HMNS will contain an inner region of deconfined mixed-phase matter. However, the HMNS collapes very quickly to a black hole, so even though a pure-quark phase will appear, it will only exist for ashort period of time.

Turning to gravitational waves, the standard is to only consider the $(\ell, m) = (2, 2)$ mode, which has been found to be the most dominant mode [255, 208]), although a discussion on the one-arm stabilities will briefly be discussed in Section 4.8 where other modes may be important. Figure 4.2 shows the gravitational-wave amplitude $|h| := (h_+^2 + h_\times^2)^{1/2}$ and h_+ at a distance of 50 Mpc as a function of time. The absolute maximum of $|h|$ corresponds to the time of merger for all of the different simulation runs, as discussed previously. The last peak of h_+ corresponds approximately to the time when the black hole is formed (i.e., $t_{\rm BH} = 14.16\,{\rm ms}$), which is defined as the time when the apparent horizon is first detected. In order to study the rotation profile of the HMNS, a time-averaging procedure will be required and this is illustrated as the grey region in Fig. 4.2.

The upper row of panels in Fig. 4.3 illustrate the evolution of the HMNS rest-mass density during the post-merger phase. The three different snapshots have been taken at $t = 1/4$, $1/2$ and $3/4\,t_{\rm BH}$. The left panel visualizes the rest-mass density distribution at $t_{\rm I} = t_{\rm BH}/4 \approx 3.6\,{\rm ms}$, shows that the overall rest-mass density of the HMNS is much higher than the rest-mass density at merger time. The double-core structure in the inner area of the HMNS is right on the verge of merging to a single core and the maximum rest-mass density reached, $\rho_{\rm max} \simeq 3.1\rho_{\rm nuc}$, is slightly above the onset of the underlying hadron-quark phase transition. In the central and right upper panels of Fig. 4.3 ($t_{\rm II} = t_{\rm BH}/2 \approx 7.1\,{\rm ms}$ and $t_{\rm III} = 3\,t_{\rm BH}/4 \approx 10.7$ ms) the double-core structure is no longer present. The value of the central rest-mass density maximum $\rho_c \simeq 3.8\,\rho_{\rm nuc}$ at $t_{\rm II}$ is clearly above the onset of the underlying hadron-quark phase transition.

4.3.2 Angular-velocity evolution: 2D slices

In this section, the focus is turned to that of the angular velocity Ω, defined in Eq. (4.3), in the post-merger evolution of the HMNS. In the lower panels of Fig. 4.3, the distribution of Ω in the (x, y) plane is shown for the same times as for the rest-mass density in the upper panels. In the first two milliseconds after the merger the time variation of Ω is very rapid, with two inner maxima placed between the double-core rest-mass density maxima (left lower panel). In the intermediate part of the post-merger (i.e., for $t \in [3\,{\rm ms}, t_{\rm BH}]$), Ω has a roughly time independent global structure in a frame corotating at half the frequency of the gravitational-wave emission, $\Omega_{\rm GW}$ (see Sec. 4.5 for a more detailed discussion). This structure then remains stationary for several milliseconds (right lower panel). Approximately two milliseconds before black hole formation, Ω largely increases

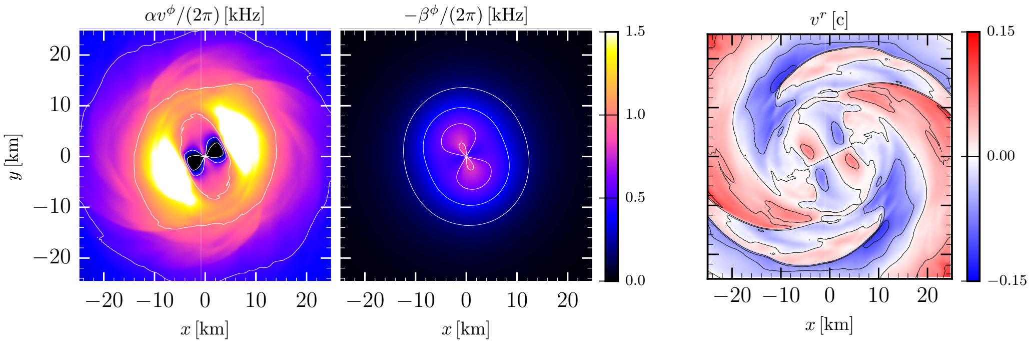

Figure 4.4: Distributions on the (x, y) plane for the `ALF2-M135` binary at $t_{\rm III}$ of the two contributions to the angular velocity Ω. The left and central panels refer to the quantities αv^ϕ and $-\beta^\phi$, respectively [cf. Eq. (4.3)]. The right panel shows instead the distribution of the radial component of the fluid three-velocity v^r.

in the center of the HMNS (not shown in Fig. 4.3).

It is clear that the angular-velocity distribution exhibits an $m = 2$ mode, known as a "bar" mode. It is an $m = 2$ mode since odd modes are not present due to π-symmetry and the $m = 0$ mode is a constant. The two maxima rotate with the same frequency of $\simeq 1.4\,\mathrm{kHz}$ around the centre of the HMNS, cf. upper middle panel of Fig. 4.3, with a radial distance of about $\sim 6\,\mathrm{km}$. In contrast, these two maxima are accompanied by two minima minima in the inner regions of the HMNS, where the angular velocity can even become negative, i.e., with the minima counter-rotating relative to the outer layers of the HMNS. The largest gradients in the Ω-profile take place at $\simeq 3\,\mathrm{km}$ from the center.

It is clear by examining both the ρ and Ω distributions that there is a clear phase difference of $\simeq 90$ degrees between the two quantities. This feature is robust and is seen in all simulations presented here. However, until now, no simple explanation for this difference exists. As alluded to in the previous chapter, and as will be shown in more detail in Section 4.7 using tracers, this relationship can be explained by a simple conservation of a Bernoulli-like quantity. Effectively, areas of large rest-mass density are coincide with regions of low velocity and vice-versa.

An important, but somewhat subtle question, is whether the spatial properties of Ω are physical quantities and not a result of the chosen gauge conditions. Recall that Ω is defined in terms of the lapse- and shift-functions which are entirely gauge dependent. Thus it is possible that numerous features of the angular velocity are simple a result of gauge artefacts and would vanish in a different coordinate system. Simulations by [127] have shown that the influence of gauge deformations are small in cases similar to the type being performed here. To double check this fact, the evolution of the relevant components of the three-metric, γ_{rr}, $\gamma_{\phi\phi}$ and $\gamma_{r\phi}$, was examined and exhibited no corresponding structure which would result in the given distribution of the angular velocity.

A second test is to directly examine the components of the angular velocity, specifically the shift component $-\beta^{\phi}$ and the azimuthal fluid velocity αv^{ϕ}, cf. Eq. (4.3), together with the radial component of the three-velocity v^r. These are displayed in Figure 4.4 which shows the equatorial structure of these three quantities at time $t_{\rm III}$. The left panel, in particular, displays αv^{ϕ}, and has almost the same global structure as that shown by Ω (see lower right panel of Fig. 4.3), with the only (obvious) difference that the maximum and minimum amplitudes are smaller. The central panel of Fig. 4.4 shows the shift component β^{ϕ} with the same colorcode, indicating that it not only has a similar spatial structure to the rest-mass density, but it is also considerably smaller, becoming essentially zero in the outer layers of the HMNS (i.e., for $r \gtrsim 15\,{\rm km}$). Both of these facts indicate that the influence of gauge quantities on the values of Ω cannot be responsible for the 90-degrees phase shift, which has instead a rather intuitive explanation given above.

In addition, the right panel of Fig. 4.4 shows the radial component of the three-velocity v^r, with red regions indicating fluid cells with outward radial motion, while blue regions refer to fluid moving inward. Note that at the outer parts of the HMNS (i.e., for $r \gtrsim 15\,{\rm km}$) the flow is mostly outwards along the two dense spiral arms. These will feed the matter ejected dynamically that will eventually lead to the production of heavy elements [272, 201, 44] and will be discussed further in Chapter 6. On the other hand, the distribution of the radial velocity in the inner parts of the HMNS (i.e., for $r \lesssim 10\,{\rm km}$) shows a clear quadrupolar structure produced by the propagation of the $m = 2$ rest-mass density perturbation. To clarify the properties of this structure it is sufficient to imagine an $\ell = m = 2$ tidal wave moving along the surface of an otherwise spherical star. The local velocity will be a $\ell = 2, m = 4$ succession of positive and negative radial velocities as the tidal wave sweeps through the surface. Additional considerations along these lines will be made when discussing the motion of tracer particles in Sec. 4.5 which, since they are comoving with the fluid, are not affected by gauge effects.

In conclusion, the above discussion strongly favours the interpretation that the $m = 2$ distribution of the angular velocity is not due to gauge effects and is a physical effect.

One important final remark is that the results presented so far only focus on the equatorial plane. By examining higher z-planes yields little change in the angular velocity for $z < 8\,{\rm km}$, although the strength of the $m = 2$ deformation decreases. For higher z-values, the angular velocity becomes almost axisymmetric due to a decrease in the rest-mass density and the HMNS blending smoothly with the

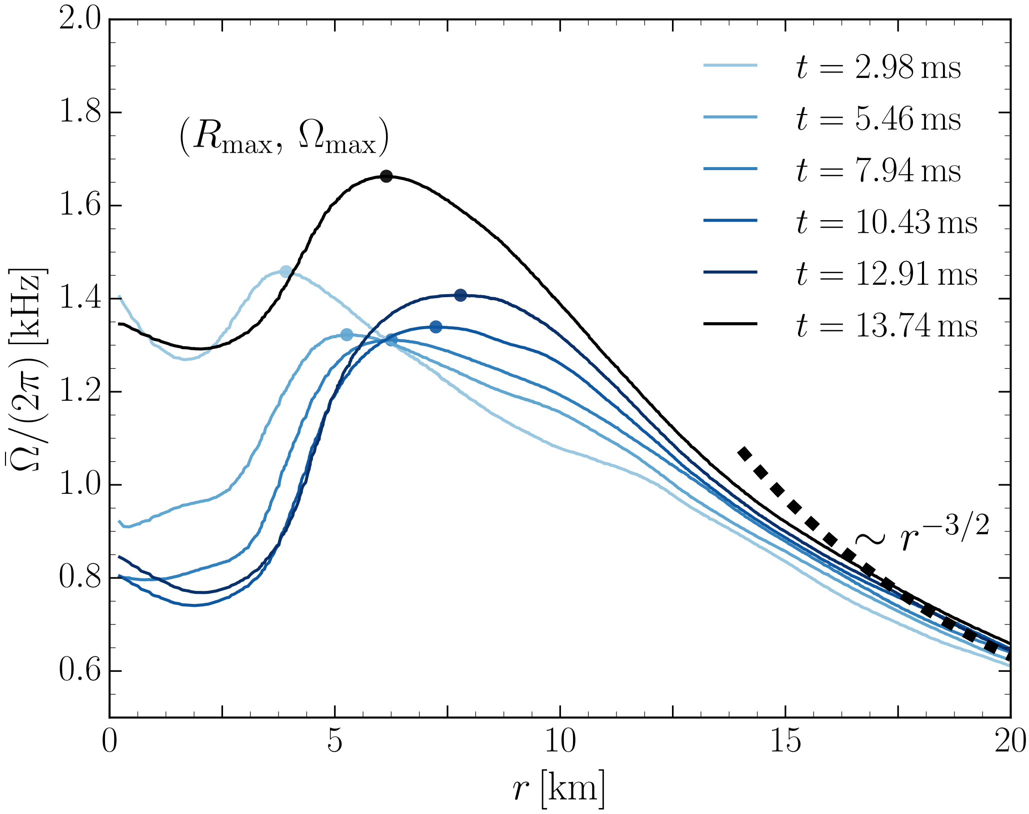

Figure 4.5: Averaged fluid angular velocity $\bar{\Omega}(r)/(2\pi)$ kHz on the equatorial plane for the `ALF2-M135` binary as averaged at different times and with intervals of length $\Delta t = 1\,\mathrm{ms}$. Shown as a thick dashed black line is a reference profile scaling like $r^{-3/2}$.

outward-moving wind of the dynamically ejected material.

4.3.3 Angular-velocity evolution: azimuthal averages

For high-mass binaries, the angular velocity distribution exhibits an $m = 2$ deformation that persists over long time scales, assuming there is no collapse to a black hole. As the spacetime reaches a stationary evolution and the deformation is slowly dissipated away, considering an azimuthal averages reduces the problem to a one-dimensional one and can easily be compared with other angular velocity profiles from different EOSs. As will be shown in Sec. 4.4, this approximation of an azimuthal average gets better as the mass of the system decreases and the

$m = 2$ deformation lessens.

The time- and azimuthally averaged angular velocity is defined as $\bar{\Omega}(r,t)$ as

$$\bar{\Omega}(r,t) := \int_{t-\Delta t/2}^{t+\Delta t/2} \int_{-\pi}^{\pi} \Omega(r,\phi,t')\, d\phi\, dt' \,. \tag{4.9}$$

and its evolution is shown in Fig. 4.5 for the `ALF2-M135` binary. Note that to better illustrate the time dependence, a small time averaging domain ($\Delta t = 1\,\mathrm{ms}$) has been used; the influence of the time-averaging window will discussed more in Section 4.8. Shown are six representative time segments, which span almost the whole HMNS lifetime from merger ($2.98\,\mathrm{ms}$) to gravitational collapse ($13.74\,\mathrm{ms}$).

Shortly after merger, here defined to be $t \lesssim 3\,\mathrm{ms}$, the angular velocity profile exhibits considerable variation due to angular momentum transport from the centre of the neutron star to the outer layers, which is represented by the light-shaded blue lines. Thus transfer results in the inner regions, i.e., between 0 and $5\,\mathrm{km}$, rotating slower and thus their overall angular velocity decreases. As this angular momentum is transferred outwards, these outer regions are more rapidly rotating and this creates the large increase observed around $5\,\mathrm{km}$. As time progresses, the variation amongst the curves e.g., between $7 - 13\,\mathrm{ms}$ decreases as the HMNS is reaching a stationary configuration. This stationary configuration all has similar features with a slowly rotating inner core for $\lesssim 3\,\mathrm{km}$ with about $\Omega \sim 1$ kHz and then this sharp increase to almost $\Omega \sim$ 1.5kHz between 7-8 km. At larger radii, the angular velocity decreases monotonically corresponding to $r^{-3/2}$ for $r \gtrsim 15\,\mathrm{km}$. This is a Keplerian rotation law and will be examined more closely in Sec. 4.6. Finally, the black curve in Fig. 4.5 shows the rotation profile of the HMNS on the merger of collapsing to a Kerr black hole ($t \simeq 13.7\,\mathrm{ms}$) and can therefore be taken as the stationary azimuthally averaged angular-velocity profile. About two milliseconds before black-hole formation, the angular-velocity profile increases and the position of the maximum moves inwards as a result of angular-momentum conservation.

4.3.4 Temperature evolution

Until now, the focus has been strictly on the rest-mass density and the angular velocity and now the focus is turned to a new quantity, specifically that of the fluid temperature and the influence temperature has on the rotation law. The influence of temperature has previously been studied in [127] using the Shen, Horowitz, and Teige EOS [231, 232] and agree generally with the results presented here, even though only one EOS was studied. To make a more quantitative comparison, a comparison with the `LS220-M132` run will be made, which uses temperature-dependent EOS and uses the `WhiskyTHC` code [203, 204] in contrast with the previous simulations.

Figure 4.6 illustrates the equatorial distributions of the temperature at $t = 6.71\,\mathrm{ms}$ (left panel) and at $t = 23.83\,\mathrm{ms}$ (right panel) in a "corotating frame", that is, in a frame that is rotating at a frequency that is half of the instantaneous gravitational-wave frequency. Note that the difference in the collapse time with the previous of `ALF2-M135` does not survive this long. In both simulations, two "hot spots" are observed to be formed in the early post-merger phase (see left panel of Fig. 4.6) which remain stable for approximately 12 ms. Although not present in this figure – they will be presented in more detail in Sec. 4.5 – the fluid lines from the tracer analysis indicate that these hot spots are vortices around which the fluid elements rotate. Indeed, when comparing with Fig. 4.3 this temperature distribution follows exactly that of the angular velocity of that simulation. For example the position of the maxima of the temperature distribution agrees with the position of the maxima of the angular velocity. An intuitive explanation of this is that in these regions, fluid velocity is higher and experiences the largest shear and compression which result increases in the local temperature. In detail, this relationship has regions of smaller pressure/rest-mass density coinciding with regions of larger temperature which can be verified by comparing the left panel of Fig. 5.4, with the temperature in the left panel of Fig. 4.6, which are illustrated at the same time.

In addition to the hot spots, the temperature distribution shows local increases along the edges of the $m = 2$ density perturbation (again where the fluid shear is largest in the corotating frame) and along the spiral arms, where outward moving material is ejected dynamically from the HMNS. In these regions, the effects of neutrinos will be important as the neutrino interactions are heavily temperature-dependent. As time passes, the hot spots disappear as the HMNS reaches a stationary state cf. the right panel of Fig. 4.6. However at this point, one slight difference is that the high-temperature region is not in the centre of the HMNS, which is slowly rotating and colder, but in an annular region around $8\,\mathrm{km}$ from the centre where the angular velocity varies more rapidly.

In conclusion the effects of temperature have a minimal impact on the overall rotation profile and angular velocity distributions, barring minor qualitative differences such as the precise location of the maxima of the rest-mass density or the angular velocity. Also note that although only the `ALF2-M135` and `LS220-M132` binaries were compared, the overall picture holds across all simulations. Indeed, as will be shown in Sec. 4.6, when considering quasi-universal relations, the non-effect of temperature will be more evident.

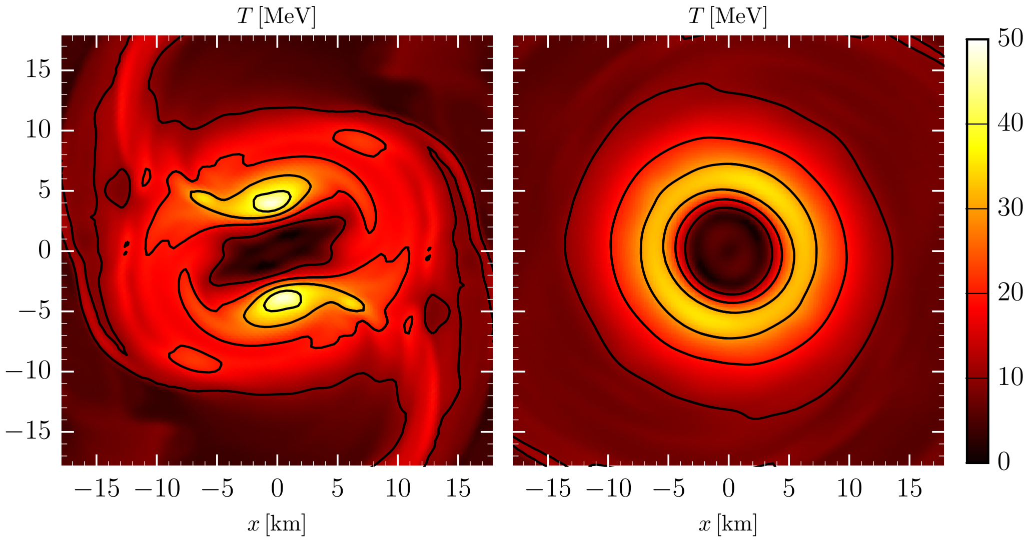

Figure 4.6: Distributions on the (x, y) plane and in a corotating frame of the temperature for the `LS220-M132` binary at $t = 6.71\,\mathrm{ms}$ (left panel) and at $t = 23.83\,\mathrm{ms}$ (right panel). The isocontours correspond to $T = \{10, 20, 30, 40, 50\}$ MeV. Note the presence in the left panel of two hot spots, which do not coincide with the maximum rest-mass density (see also Fig. 5.4, which reports other quantities relative to this binary).

4.4 Low-mass binaries

In the previous sections, attention was paid to the high-mass binaries. Now the case of the low-mass binaries is addressed. Again, the ALF2 EOS is chosen as the representative binary, denoted by `ALF2-M125`. For the low mass case, the total mass of the system is $2 \times 1.25\,M_{\odot}$ and only the equal mass case is examined. In analogy with Fig. 4.1 Fig. 4.7 illustrates the evolution of the minimum value of the lapse function and of the maximum rest-mass density for the five EOSs. None of the resulting HMNS collapses to a black hole within the simulated time range because of the smaller initial masses of the binaries although they will likely collapse on timescales of $\sim$100 ms [18, 209]. It is also interesting to note that the post-merger oscillations in the maximum rest-mass density are all suppressed within about 10-15 ms from the merger, with stiffer EOSs (e.g., GNH3) requiring more time than the softer ones (e.g., APR4).

In Fig. 4.8 the emitted gravitational waves waves of the late inspiral, merger, and post-merger are displayed and can be contrasted with that of the binary shown in Fig. 4.2. Here the maximum amplitude at the merger is comparable of that with the high-mass run, but by about $10\,\mathrm{ms}$ after the merger, the difference is at most of 20$\%$ of that in the inspiral. This is due to the rapid disappearance of the non-axisymmetric deformation of the rest-mass density in the HMNS, which attains an almost axisymmetric distribution within $\simeq 20\,\mathrm{ms}$ after the merger (see upper panels in Fig. 4.9). The three different times indicated in Fig. 4.8 refer to $t = 1/4$, $1/2$ and $t = 3t_{\rm fin}/4$, where $t_{\rm fin} = 40.38\,\mathrm{ms}$ is the time when the simulation is terminated.

Figure 4.9 reports the distributions on the equatorial plane of the rest-mass density (upper panels) and of the angular velocity (lower panels) at the three different times indicated in Fig. 4.8. This figure should be compared with Fig. 4.3, which refers to a high-mass binary of the same (ALF2) EOS. Note that for $t \lesssim 16\,\mathrm{ms}$, the rotation profile (see lower left panel in Fig. 4.9) shows the same qualitative structure as for the high-mass case, even though the overall values of Ω are somewhat lower (note the different color scale in Figs. 4.3 and 4.9). Although in a weaker form, the low-mass binary also shows the 90-degree shift between the $m = 2$ deformation in the rest-mass density and in the angular velocity, which was discussed in Sec. 4.3.2 in terms of the manifestation of the Bernoulli theorem, cf. Eq. (4.13)].

Furthermore, for $t \gtrsim 16\,\mathrm{ms}$ (see middle and right panels in Fig. 4.9) the rest-mass density and the rotation profile have reached a stationary state in which a small $m = 2$ perturbation is still present, but is subdominant when compared to the overall axial symmetry. The inner part of the HMNS ($r \leq 6\,\mathrm{km}$) is where the rest-mass density is the largest, but is also rotating rather slowly ($\Omega \simeq 0.5\,\mathrm{kHz}$); this region is much broader than in the high-mass binary and the sharp transition to

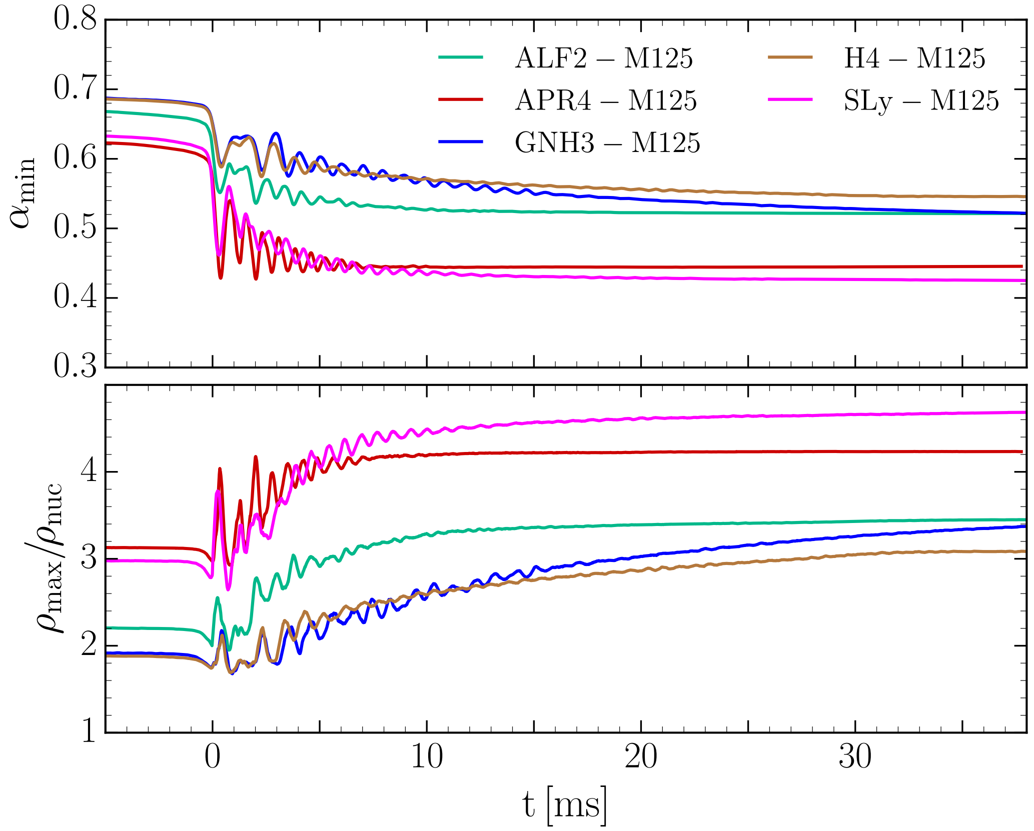

Figure 4.7: Minimum value of the lapse function $\alpha_{\rm min}$ (upper panel) and maximum of the rest-mass density $\rho_{\rm max}$ in units of $\rho_{\rm nuc}$ (lower panel) versus time in milliseconds after the merger for the low-mass simulations; this figure should be contrasted with Fig. 4.1.

a $r^{-3/2}$ outer profile takes place at a larger radius ($6.5 \lesssim r \lesssim 8.5$ km). The panels on the right column of Fig. 4.9 clearly indicate that at later times the HMNS has reached a high degree of axial symmetry, although not a complete one, since gravitational waves are still being emitted (cf. Fig. 4.8).

Similar to the discussion of that at the end of Sec. 4.3 for the high-mass binaries, the analysis was only carried out in the equatorial plane. When examining higher values of the z-plane, a qualitatively similar picture emerges with little variation in the rest-mass density and the angular-velocity profiles up to about $z \lesssim 9\,\mathrm{km}$. At higher values in the z-plane, the densities are comparable to that of the outflowing material and the angular velocity increases in the central regions, where it has the largest values.

In conclusion, most of the properties of the higher-mass binaries apply to the case of the `ALF2-M125` with only differences being qualitative. Furthermore, this comparison extends to the other EOSs considered and thus this case can be considered representative.

4.5 Tracer particles evolution

As discussed in Sec. 4.3, the influence of gauge effects on the simulation are an important consideration and it must be insured that the angular velocity is physical and not simply due to gauge effects. In that section, examination of the metric coefficients and the components of the lapse- and shift-functions were examined and demonstrated how the fields considered are physical. However the strongest evidence is that of the tracers,i.e., massless particles that are advected with the fluid, introduced in Chapter 3. To do a detailed analysis, the binary selected is `LS220-M132`, which was, as previously discussed evolved with the `WhiskyTHC` code [203, 204].

Firstly, the upper panels of Fig. 5.4 report, for the `LS220-M132` binary and at time $t = 6.7\,\mathrm{ms}$, the rest-mass density ρ (left panel), the angular velocity Ω in the corotating frame (middle panel) and in the Eulerian frame (right panel), i.e., an observer at infinity. Similarly, the bottom row of panels in Fig. 5.4 shows the same quantities, but for a later time of $t = 23.8\,\mathrm{ms}$. The times shown are representative ones but the dynamics for this EOS is qualitatively very similar to those presented in Secs. 4.3 and 4.4. The only difference is that although the binary `LS220-M132` belongs to the high-mass class, its evolution does not lead to a collapse to a black hole over the timescale during which the simulations have been carried out, i.e., $\sim 27.3\,\mathrm{ms}$ after merger.

Also shown in Fig. 5.4 are the flowlines of several tracer particles that remain close to the (x, y) plane (i.e., with small velocity in the z direction). More specifically, only the final part of the flowlines (i.e., for the last $\simeq 0.285\,\mathrm{ms}$) are

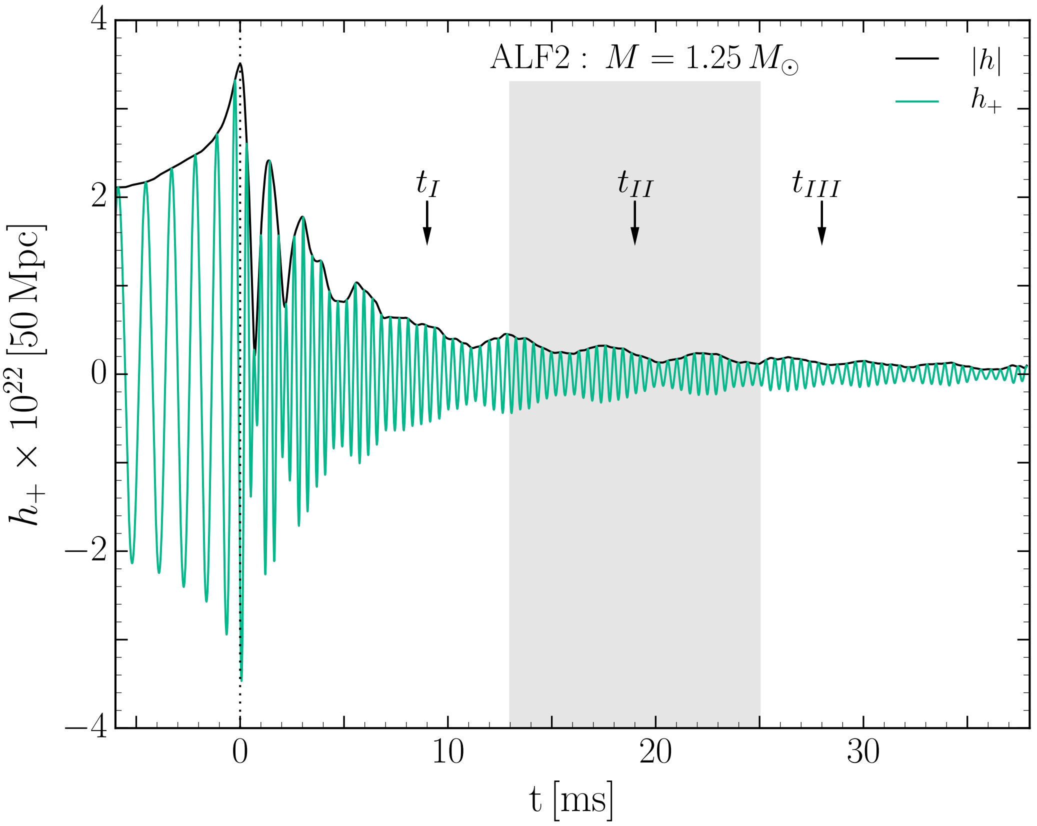

Figure 4.8: Gravitational-wave amplitude $|h|$ (black line) and strain amplitude in the $+$ polarisation h_+ (green line) for the `ALF2-M125` binary at a distance of 50 Mpc. Shaded in gray is the portion where a time average is performed, while the arrows indicate the times when representative distributions of the rest-mass density and angular velocity are shown in Fig. 4.9. Finally, the dotted vertical line marks the time of merger. This figure should be contrasted with the equivalent one, Fig. 4.2, for the high-mass binaries.

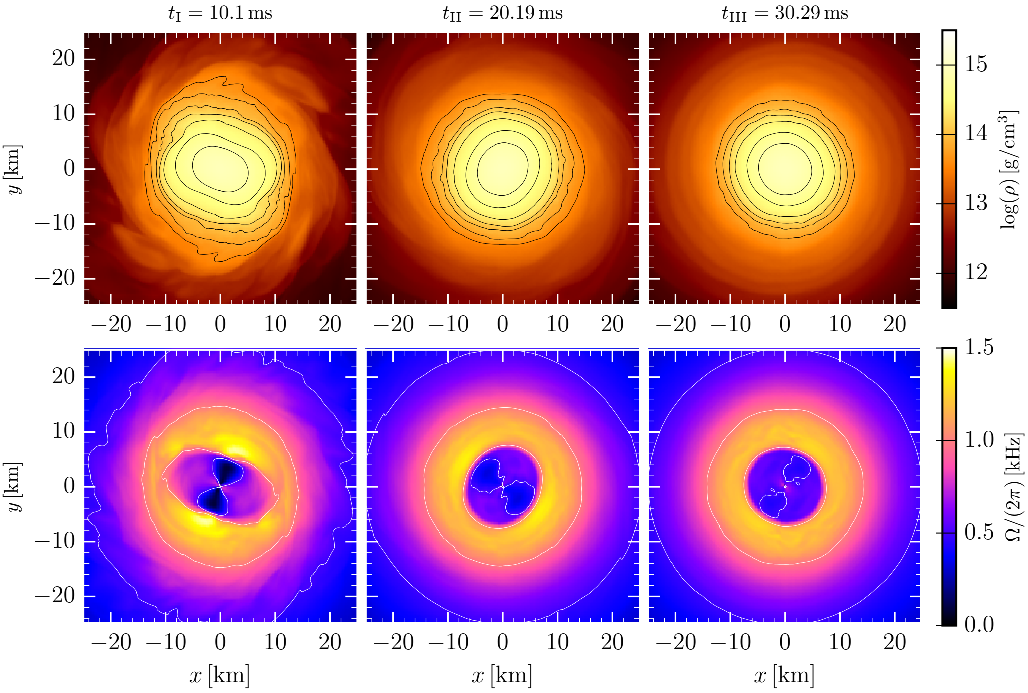

Figure 4.9: Distributions of the rest-mass density (upper row, log scale) and of the fluid angular velocity (lower row) in the (x, y) plane for the `ALF2-M125` binary at three different post-merger times as indicated in Fig. 4.8. The iso-contours have been drawn at $\log(\rho) = 13.6 + 0.2n$ (upper row) and $\Omega = \{0, 0.5, 1.0, 1.5, 2.0\}$ kHz (lower row), $n \in \mathbb{N}$.

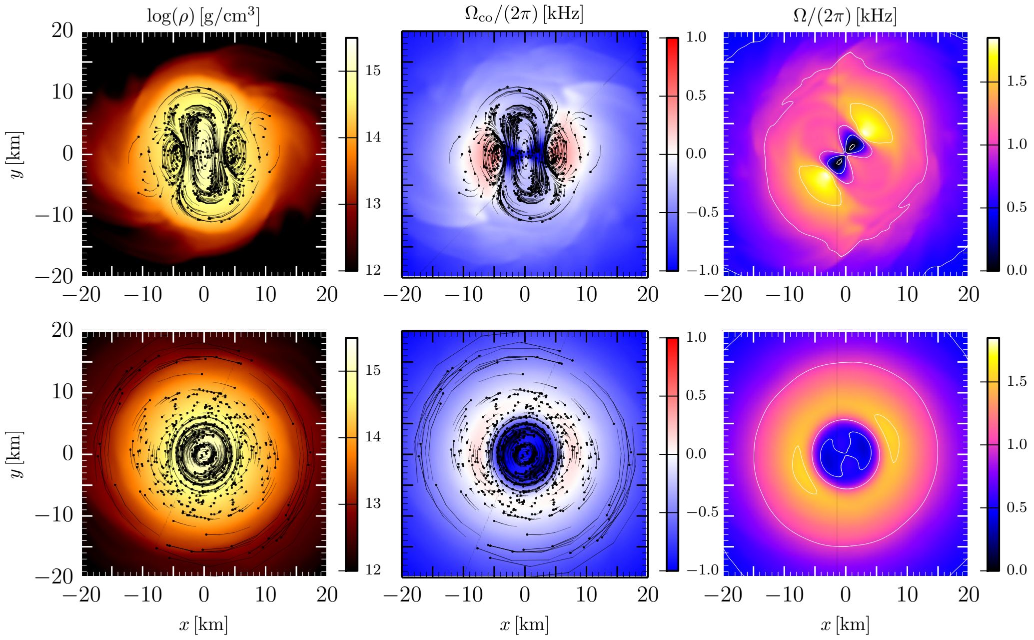

Figure 4.10: Distributions on the (x, y) plane and in the corotating frame of the rest-mass density (left panels), and of the angular velocity (middle panels) for the `LS220-M132` binary, where $\Omega_{\rm co} := \Omega - \Omega_{\rm f}$ where $\Omega_{\rm f} = 1.368$ kHz (top), $1.425\,{\rm kHz}$ (bottom). Shown instead in the right panels is the distribution of the angular velocity, Ω, in the Eulerian frame. The top row refers to $t = 6.71\,{\rm ms}$, while the bottom one to $t = 23.83\,{\rm ms}$. Also shown are portions of the flowlines of several tracer particles that remain close to the (x, y) plane and for which is only shown in the final part of the flowlines (i.e., for the last $\simeq 0.285\,{\rm ms}$), using small dots to indicate the particle position at the time indicated in the frame. In addition, the initial parts of the trajectories have increasing transparency so as to highlight the final part of the trajectories.

visualised, using small dots to indicate the particle position at the time indicated in the frame. Furthermore, the initial parts of the trajectories have increasing transparency so as to highlight the final part of the trajectories. This approach has at least two advantages. First, it provides a measure of the linear velocity (faster tracers leave longer tracks); second, the presence of the filled dots and the increasing transparency allow one to read-off the direction of motion.

The top panels in Fig. 5.4 show the dynamics of the fluid in the inner parts of the HMNS and highlight that two distinct regions can be identified. The first region is in the core of the HMNS, where there is an ellipsoidal structure orthogonal to the angular-velocity distribution. Within this ellipsoid, fluid elements essentially move clockwise along isobaric surfaces, with linear velocities that are rather small in the inner regions. In addition to this ellipsoidal motion, the tracers also show the presence of two small "vortices", i.e., regions of increased vorticity in this frame, which also coincide with the regions of highest angular velocity, and which border the areas where velocity drops almost to zero (in this frame). Note that it appears that the tracers that are "trapped" in these vortices where they remain without traversing the boundary to the central ellipsoid and where they have an inverse sense of rotation (counter-clockwise). Stated differently, the vorticity distribution in the corotating frame would show two islands of vorticity with different signs, referring to clock and counterclockwise rotation. Tracers in one region do not migrate to the other region. This is mostly the result of using a corotating frame in a flow that is differentially rotating. It is quite intuitive, in fact, that if Ω is positive but not uniform, the transformation to a corotating frame amounts to a net subtraction of a positive amount of angular velocity, hence leading to areas of now negative angular velocity. This becomes more apparent when considering the corresponding picture in the Eulerian frame, as shown in the right panels of Fig. 5.4.

The bottom panels of Fig. 5.4, on the other hand, refer to a much later stage of the HMNS evolution (i.e., $t = 23.83\,\mathrm{ms}$) and clearly show that by this time the HMNS has attained an almost axisymmetric structure, combined with a much smaller $m = 2$ perturbation. As discussed in the previous cases, also here the rotational profile of the HMNS contains an inner area with $r \lesssim 5\,\mathrm{km}$ which is rotating slowly and almost uniformly at $\Omega \approx 0.5\,\mathrm{kHz}$, followed by a sharp increase at $5 \lesssim r \lesssim 7\,\mathrm{km}$ reaching a maximum value $\Omega \approx 1.5\,\mathrm{kHz}$ at $r \approx 8\,\mathrm{km}$ and decreasing continuously for $r \gtrsim 8\,\mathrm{km}$[3]. Since this behaviour follows the one described previously for hybrid EOSs, it suggests that both the rest-mass density and the

---

[3] Note that the angular-velocity distribution in the lower central panel of Fig. 5.4 refers to the corotating frame and that this frame is rotating at half the angular frequency of the emitted gravitational waves, $\Omega_{\rm GW}$. Because the maximum of the angular velocity $\Omega_{\rm max}$ is of the order of $\Omega_{\rm GW}/2$ (cf. left panel of Fig. 4.13), the ring structure in this panel is approximately at zero angular velocity.

angular-velocity distributions are preserved when using a fully three-dimensional EOS and radiative losses are taken into account. In turn, this confirms that an analysis carried out with piecewise polytropes and a thermal component does not introduce a bias in the results.

The tracers in the lower panels of Fig. 5.4 further illustrate the axisymmetric nature of the flow, with the fluid moving along essentially circular orbits that are tangent to isobaric surfaces. The quasi-circularity is shown in the spacetime diagram reported in Fig. 4.11, where the worldlines of selected tracers in the relevant region of the HMNS and after passing them through a running-average window of $5\,\mathrm{ms}$ to remove the high-frequency jitter are shown. Note that after the transient period, where angular momentum is transferred out and particles move to lower rest-mass density regions, the tracers remain at essentially constant radial coordinates.

It is interesting to note that because the angular velocity refers to the corotating frame and because this frame is rotating at half the gravitational-wave frequency ($\Omega_{_{\rm GW}}/2 \approx \Omega_2/2 \approx \Omega_{\rm max}$, see Fig. 4.13 of Section 4.6), tracers in the inner and outer regions of the HMNS will be both rotating clockwise while tracers belonging to the intermediate regions are almost at rest (white regions). Only those tracers that are trapped in the vortices are moving counter-clockwise (light red regions).

To recap, the analysis of the motion of tracer particles discussed in this section indicates that the angular-velocity distributions presented so far are not contaminated by gauge effects, but rather reflect physically meaningful quantities. The angular-velocity Ω is defined directly in terms of the lapse and shift, which are gauge-dependent quantities and could potentially change the behaviour of the angular-velocity depending on the gauge selected. The evolution of the tracers are comoving with the fluid elements [45] and thus they follow the fluid evolution. As shown, they exhibit behaviour as predicted by the gauge-dependent quantities and illustrate the robustness of the results to the choice of gauge. An additional use of the tracers, explained in detail in Section 4.7, will further illustrate the origin of the phase offset demonstrated in Fig. 4.3.

4.6 “Quasi-universal” behaviour

4.6.1 Averaged profiles

When taking the time- and azimuthally averaged profiles of the angular velocity, plotting them with different EOSs and masses, reveals an interesting and informative result. In order to ensure a fair comparison, as discussed in Sec. 4.3.3, the time averages are performed across a time interval Δt, cf. Eq. (4.9), centered around $t_{\rm fin}/2$ and with extent $t_{\rm fin}/3$, where $t_{\rm fin}$ corresponds either to the time of

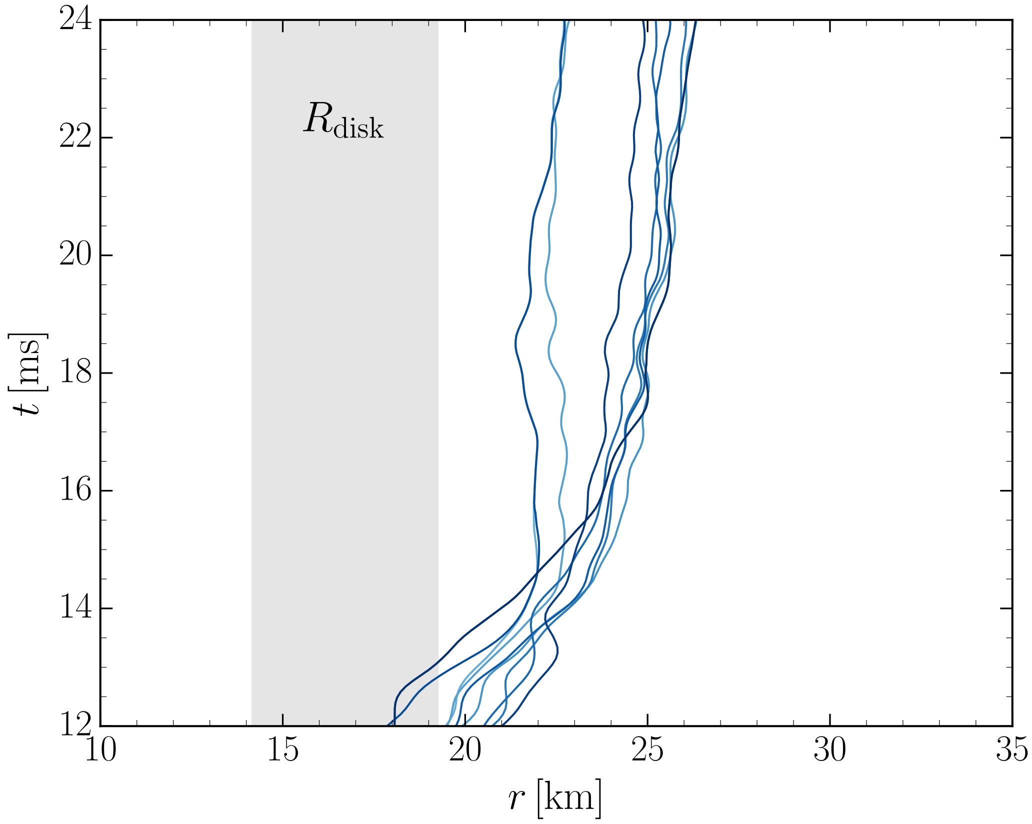

Figure 4.11: Worldlines of selected tracers in the outer regions of the HMNS where the angular frequencies scale like $r^{-3/2}$. Note how in these regions the tracers remain at essentially constant radial coordinates; the gray-shaded area shows the region where $\Omega(r) \propto r^{-3/2}$ (see Sec. 4.6.1 for a definition and discussion).

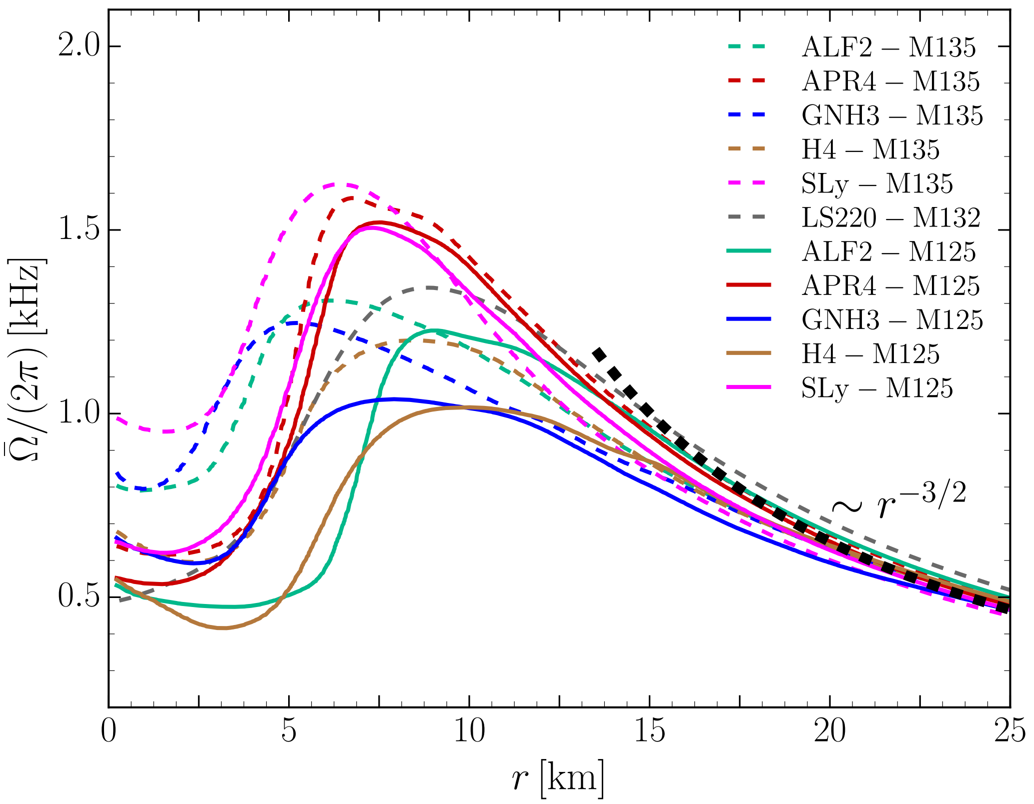

Figure 4.12: Comparison of the time- and azimuthally averaged rotation profiles for different EOSs. Solid curves show the profiles for high-mass runs ($M = 1.35 M_{\odot}$), whereas dashed curves refer to low-mass simulations ($M = 1.25 M_{\odot}$). Shown as a thick dashed black line is a reference profile scaling like $r^{-3/2}$.

black-hole formation (in the case of high-mass binaries) or to the final time of the simulation (in the case of low-mass binaries). As will be discussed in Section 4.8 the influence of the resolution on the lifetime of the HMNS and the time-intervals on the time-averaging will be shown to be minimal. Using this procedure ensures that all simulations have the same well-defined criteria for choosing the integration time. The exact width of this window will change for different binaries, but it ensures that all angular velocity calculations will have the same proportion of HMNS lifetime relative to the total lifetime. Finally, these time intervals have been indicated with gray-shaded regions in Figs. 4.2 and 4.8, respectively

To this end, Figure 4.12 illustrates the results of the time- and azimuthally averaged angular velocity profiles for the different simulated binaries. As can be seen in Fig. 4.12, there appears to be a relationship between all the different curves that depends weakly on the EOS and thus is labelled “quasi-universal”. In more detail, each angular velocity profile exhibits a slowly rotating and almost completely uniform inner core. This is followed by a transition to a more rapidly rotating outer region, narrowly taking place roughly between $3 - 4\,\mathrm{km}$. This sharp increase in the rotation rate leads to large shear forces that cause the local temperature to increase cf. Fig. 4.6. After this rapidly rotating region, the rotation profile starts decreasing as $r^{-3/2}$ in the outer regions of the star and also regions outside of the star. This differential rotation profile is rather different from the one normally considered in the literature, i.e., the $j - \mathrm{constant}$ law that has been explored in the past both in equilibrium configurations [240, 238, 13, 96, 252, 101] and in dynamical ones [17, 158, 53, 62, 98, 131, 90, 125, 244, 245, 152].

Although this general picture is rather robust across all EOSs and hence is “quasi-universal”, there are some small differences that do arise with the variation of the composition. Specifically, the size of slowly rotating inner core depends on both the EOS and on the initial mass of the stars with a trend towards larger rotating inner cores for the larger initial masses and the opposite for the smaller masses. For example, for the high-mass run of the GNH3 and SLy EOS the slowly rotating core is rather small ($r \lesssim 4\,\mathrm{km}$) while for the low-mass run of the ALF2 EOS it extends up to $r \lesssim 7\,\mathrm{km}$. In terms of the maximum rotation rate, there is a weak dependence on the EOS, with the general trend being towards softer EOSs having a larger maximum in comparison with stiffer EOSs. This is likely due to the softer EOS resulting in a more compact object which will result in a faster spinning object in comparison with a less compact object.

Following the previous approaches of [32, 34, 255, 256, 212], a method to relate how to relate the “quasi-universal” features of the averaged angular-velocity profiles with some of the properties of the merging neutron stars, such as the mass and radius, when they are at infinite separation is considered. As discussed previously, observations of merging neutron stars, such as GW170817, can provide information on the properties of the neutron star. Often times, however, the information obtained from analysing the signal does not come in the form of a single quantity like the mass or radius, but often in terms of a combined quantity such as the compactness or the tidal Love number. These quantities themselves do not uniquely determine any particular EOS or mass as many different EOSs can lead to similar results. However, the power of these combinations is that they often occur in “universal” or “quasi-universal” relationships which allows constraints to be placed on data, even with limited information.

Such correlations from the above simulations are summarised in Fig. 4.13. The first quantity to consider is that of how the maximum angular velocity angular velocity Ω_{max} of the averaged profiles relates to the angular frequency corresponding to the largest peaks of the post-merger power spectral density $\Omega_2 := 2\pi f_2$ (left

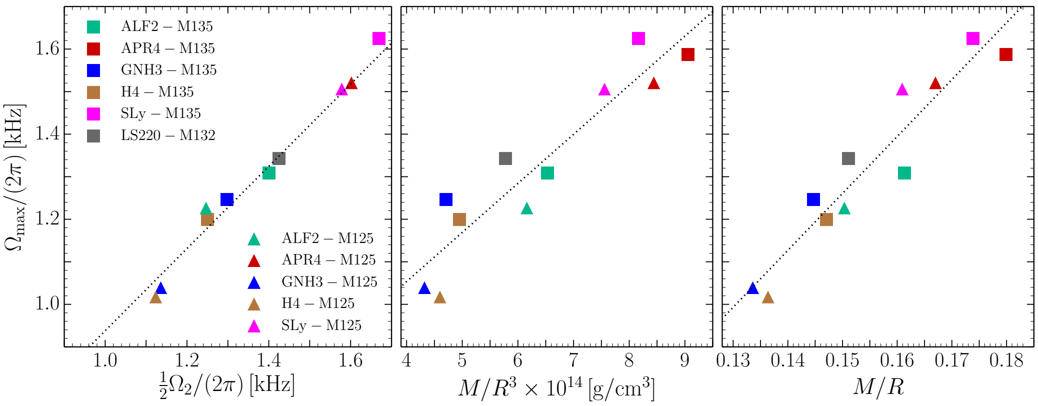

Figure 4.13: Left panel: maximum value $\Omega_{\rm max}$ of the time- and azimuthally averaged rotation profiles (see Fig. 4.12) as a function of (half of) the main gravitational-wave frequency of the emitted by the HMNS Ω_2. Middle panel: $\Omega_{\rm max}$ as a function of the average rest-mass density $\bar{\rho} := M/R^3$ relative to the initial stellar models. Right panel: $\Omega_{\rm max}$ as a function of the initial stellar compactness $\mathcal{C} := M/R$.

panel of Fig. 4.13) [255, 256, 212] where f_2 is defined to be a peak in the power spectral density and is also typically the strongest peak frequency.

Physically, this f_2-frequency is customarily interpreted as twice the spinning frequency of the $m = 2$-deformed HMNS [251, 255] and is therefore not surprising that it should tightly correlate with the maximum angular frequency of the averaged angular-velocity profiles as the $m = 2$ mode is the dominant source of the gravitational waves. Another interesting feature of the value of $\Omega_{\rm max}$ displayed in Fig. 4.13 is that not vary significantly with time and is thus the value of $\Omega_{\rm max}$ remains relatively constant till the end of the simulation despite the $m = 2$ deformation being washed out or negligible. This means that even though the HMNS has almost reached an axisymmetric configuration, the gravitational-wave frequency $\Omega_{\rm GW} \simeq \Omega_2$ can still be used to measure the maximum angular velocity of the fluid. Additionally, the correlation shown between $\Omega_{\rm max}$ and Ω_2 confirmations that the measurements of the angular-velocity distributions discussed in Sec. 4.3 is physically meaningful. This is because Ω_2 is defined in terms of the gravitational waves, which are a gauge-independent, and thus a correlation between the two is unlikely to be due to gauge-dependent quantity.

In the central and right panels of Fig. 4.13 are the correlations of $\Omega_{\rm max}$ with the average rest-mass density $\bar{\rho} := M/R^3$ and the stellar compactness $\mathcal{C} := M/R$, where these quantities are defined from the initial data values. In this case as well, the correlation between the two quantities is linear. This has a straight forward interpretation because stiffer EOSs – which will have a smaller compactness – have HMNSs that have comparatively larger radii and thus smaller average densities which in turn means smaller angular velocities are required to attain a quasi-stationary hydrostatic equilibrium and the opposite holds for the softer EOS case. This logic also extends to the same EOS but with different initial masses as the lower mass binaries will have comparatively smaller average densities which explains why the triangles have systematically lower averaged maximum angular velocities, cf. central panel of Fig. 4.13. Finally, a similar line of reasoning applies for the stellar compactness displayed in the right panel of Fig. 4.13.

As previously mentioned, Fig. 4.12 shows that the fluid flow in the outer regions of the HMNS, i.e., for $r \gtrsim 15\,\mathrm{km}$, exhibits a profile scaling like $r^{-3/2}$. To explain this behaviour, consider the spacetime around a Kerr black hole, which describes a rotating black hole. Outside this Kerr black hole, a fluid particle following a geodesic on the equatorial plane will have orbital angular frequencies given by Kepler's expression [213]

$$\Omega_{\mathrm{Kep}}(r) = \frac{\sqrt{M}}{\sqrt{r^3} + a\sqrt{M}}\,, \tag{4.10}$$

where $a := J/M$ is the spin parameter of the Kerr black hole, J is the total angular momentum, and M is the total gravitational mass. Of course this approximation is not strictly valid as the object considered here is a HMNS and not a Kerr black hole, and the spacetime metrics will differ – indeed the lower-mass binaries do not even collapse – and furthermore the motion of the fluid elements in the simulation are not completely geodetic, but this simplified picture provides a clear physical model of the behaviour outside the HMNS.

Within this model, the following quantity can be defined

$$\chi(r) := \Omega^2(r) r^3\,, \tag{4.11}$$

which would tend asymptotically to the mass of the black hole if $\Omega = \Omega_{\mathrm{Kep}}$, if the motion was a geodetic one, and if this was a Kerr spacetime. Thus $\chi(r)$ provides a measure of how "Kerr-like" the material is behaving. An advantage of this quantity is that it can be used to define where flow starts having angular frequencies scaling like $r^{-3/2}$.

This dependence is shown in Fig. 4.14, which plots the behaviour of $\chi(r)$ for the binaries simulated. Clearly, all of the profiles converge to a rather constant value for large radii, thus indicating that the low rest-mass density regions of the HMNS exhibit a flow with angular frequencies scaling like $r^{-3/2}$. To define the region where the flow does this transition, the scale height of χ, $\chi'/\chi := (d\chi/dr)/\chi$, is used. To define the appropriate limit, consider a flow with $\Omega(r) \propto$

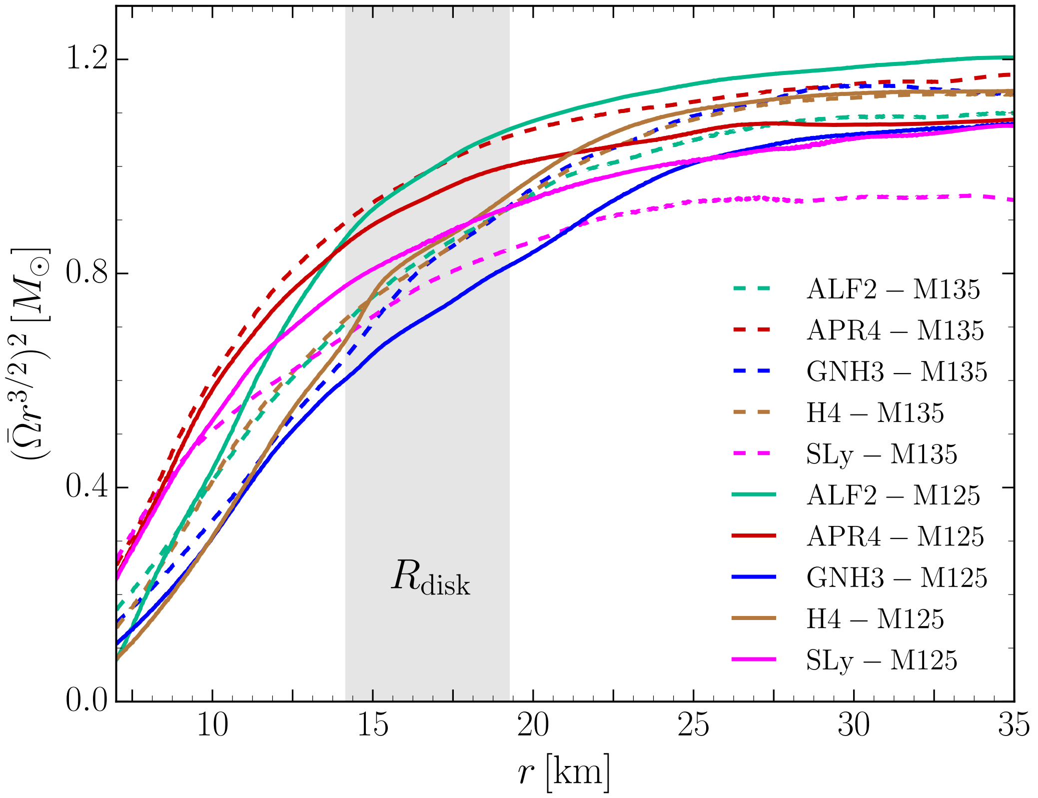

Figure 4.14: Radial dependence of the quantity $\chi(r) := \bar{\Omega}^2 r^3$ for all of the simulated binaries. Note that all profiles reach an almost constant value for $r \gtrsim 25\,\mathrm{km}$. The gray-shaded area shows the region where the flow starts to having angular frequencies scaling like $r^{-3/2}$; see Table 4.2 for the exact values of $R_{\rm disk}$ for the various EOSs.

$r^{-3/2}$, which implies that χ'/χ will be zero. Thus the region where the disk is said to begin is thus defined when the monotonically decreasing function χ'/χ reaches a sufficiently small value, is chosen to be $\chi'/\chi \leq 0.05$.

There are two important reasons for having a disk form in the outer regions of the HMNS. Firstly, when the core of the HMNS eventually collapses to a rotating black hole, the presence of mass around the outside of the black hole will ensure that the black hole is not "naked" [161] and is instead surrounded by a torus which can potentially lead to the formation of a relativistic jet. The formation of such a jet will be discussed in the subsequent section. The second reason is that a flow with $\Omega \propto r^{-3/2}$ satisfies the Rayleigh stability criterion for rotating fluids against axisymmetric perturbations. [4] and thus the differentially rotating disk surrounding the will likely only accrete onto the uniformly rotating core of the HMNS on a dissipative timescale. Thus it is possible that the disk will not affect the long-term stability required in the proto-magnetar model for short gamma-ray bursts [278, 173, 51] and the subsequent extended X-ray emission [211].

4.6.2 Mass in the disk

The distribution of rest mass in the HMNS is of great astrophysical importance as it regulates the amount of mass that is ejected in the merger and that can subsequently feed r-process nucleosynthesis and an electromagnetic counterpart to the merger via the radioactive decay of by-products of the r-process, i.e., via a kilonova [147, 135, 171, 214, 126, 25, 259, 220, 107, 149, 201, 44]). In addition, as mentioned in the previous section, the knowledge of the rest-mass distribution in the HMNS, and in particular of the portion of it in the disk, is important to determine how much of the HMNS will "survive" the process of gravitational collapse of the HMNS to a black hole and end up in building a torus around the black hole.

To this end, the rest-mass distribution has been computed as a function of the radial distance from the origin as

$$M_{\rm b}(\tilde{r}) := \int_0^{2\pi} \int_0^{\pi} \int_0^{\tilde{r}} \sqrt{\gamma}\, W \rho\, r^2 \sin(\theta)\, dr\, d\theta\, d\phi\,, \tag{4.12}$$

with $W = \alpha u^t$ being the Lorentz factor and the other quantities defined as previously. This quantity is illustrated in Figure 4.15 which shows the radial dependence of the total rest mass in the HMNSs when normalised with the total initial rest mass $2\,M_{\rm b,0}$. For both the high- and low-mass binaries, the distributions refer to times which are in the middle of the averaging intervals in Figs. 4.2 and 4.8,

---

[4] Recall that this classical-physics criterion can also be seen as requiring that the specific angular momentum $j = \Omega(r) r^2$ increases outwards for a stably rotating fluid configuration.

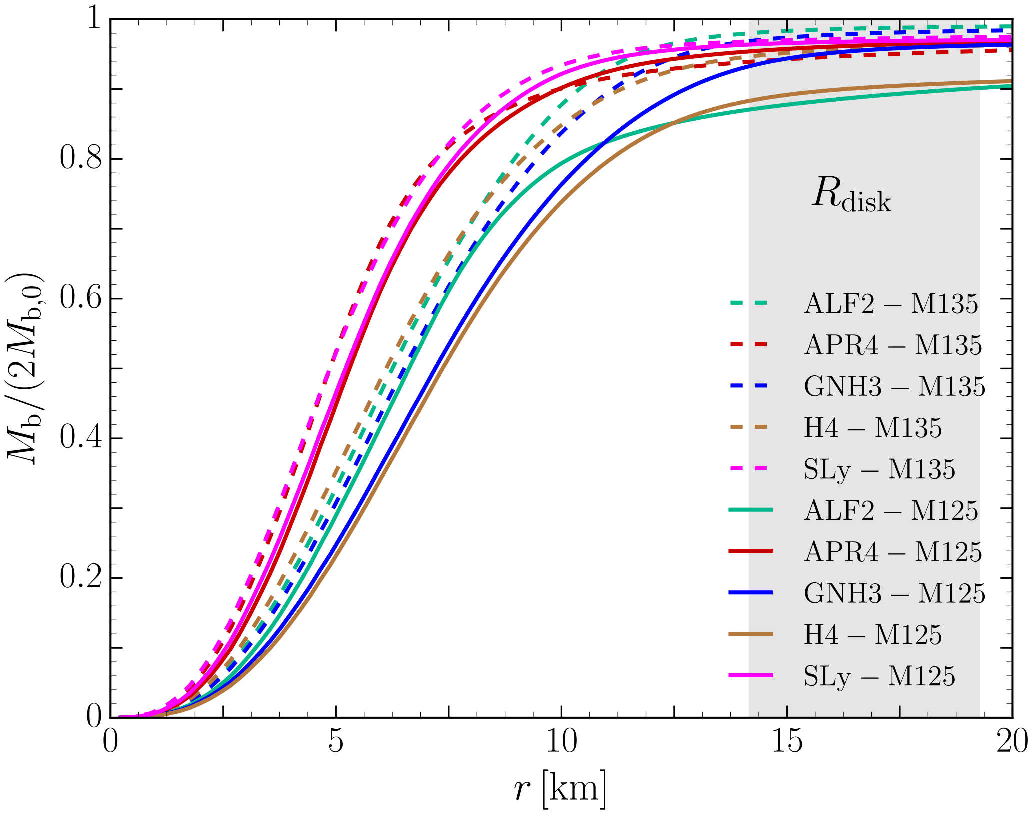

Figure 4.15: Integrated rest mass $M_{\rm b}(r)$ as function of the radial coordinate and normalised with the total initial rest mass. The gray shaded area shows the region where the disk starts; see Table 4.2 for the exact values of $R_{\rm disk}$ for the various EOSs.

model	$R_{\Omega_{\rm max}}$ [km]	$\Omega_{\rm max}$ [kHz]	$M_{\rm b,\Omega_{\rm max}}$ [$M_\odot$]	$M_{\rm b,\Omega_{\rm max}}/(2\,M_{\rm b,0})$ [%]	$R_{\rm disk}$ [km]	$M_{\rm b,disk}$ [$M_\odot$]	$M_{\rm b,disk}/(2\,M_{\rm b,0})$ [%]
`GNH3-M125`	7.92	1.04	1.56	57.89	18.96	0.10	3.79
`GNH3-M135`	5.19	1.25	0.97	33.12	19.27	0.05	1.65
`H4-M125`	9.98	1.02	1.99	73.70	17.08	0.26	9.66
`H4-M135`	8.36	1.20	2.18	74.20	17.07	0.12	4.10
`ALF2-M125`	9.04	1.23	2.04	74.49	15.71	0.32	11.73
`ALF2-M135`	6.20	1.31	1.46	49.35	16.39	0.04	1.35
`SLy-M125`	7.31	1.51	2.13	77.44	14.15	0.10	3.63
`SLy-M135`	6.43	1.63	2.16	72.17	15.05	0.09	3.01
`APR4-M125`	7.57	1.52	2.15	78.49	14.56	0.12	4.43
`APR4-M135`	6.76	1.59	2.30	76.40	14.70	0.18	5.85

Table 4.2: Summary of the HMNS properties. The various columns denote the radial position $R_{\Omega_{\rm max}}$ of the maximum of the averaged angular-velocity profiles $\Omega_{\rm max}$, the total rest mass inside $R_{\Omega_{\rm max}}$, i.e., $M_{\rm b,\Omega_{\rm max}} := M_{\rm b}(R_{\Omega_{\rm max}})$, the radial position $R_{\rm disk}$ where the disk starts, and the total rest mass outside $R_{\rm disk}$, i.e., $M_{\rm b,disk} := 2\,M_{\rm b,0} - M_{\rm b}(R_{\rm disk})$.

i.e., at $t = t_{\rm BH}/2$ for the high-mass binaries and at $t = t_{\rm fin}/2$ for the low-mass binaries.

Independent of the EOS and initial mass, all the rest-mass distributions indicate that the rest mass $M_{\rm b}(r)$ does not change significantly for $r \gtrsim 15\,{\rm km}$, so that the missing amount of rest mass is the one that has been ejected dynamically soon after the merger. However, it is important to note that largest majority of this ejected matter is gravitationally bound and only a very small fraction of it will be ejected *and* unbound [272, 201, 44].

Additionally in Figure 4.15 shows a somewhat expected result, namely, that binaries with softer EOSs have considerably more compact rest-mass distributions, reaching 80% of the total within only $r \lesssim 7.5\,{\rm km}$, quite independently of the initial mass of the binary. By contrast, binaries with stiffer EOSs (e.g., GNH3 or H4) have less compact distributions, reaching 80% of the total only for $r \lesssim 10\,{\rm km}$, and a bit less for low-mass binaries.

Another useful measure of the rest-mass distribution is that of the mass in the disk, which is defined to be the rest mass confined in the region of the HMNS in the disk. More specifically, if $R_{\rm disk}$ is the radial location (on the equatorial plane) where the disk starts,i.e., where $\chi'/\chi \leq 0.05$, then the rest mass in the disk is defined as $M_{\rm b,disk} := 2\,M_{\rm b,0} - M_{\rm b}\,(R_{\rm disk})$.

In addition, another definition of mass that can be considered is that of the mass that is inside the maximum value of the averaged angular-velocity profile. This is computed by first defining $R_{\Omega_{\rm max}}$ as the location where the angular-velocity profile reaches its maximum. Then, since $R_{\Omega_{\rm max}} < R_{\rm disk}$, the mass inside $R_{\Omega_{\rm max}}$

can be calculated using the same expression as (4.12). This concept of mass is referred to as $M_{b,\Omega_{\max}}$.

All these results are summarised in Table 4.2 for all of the binaries simulated. Overall, the table illustrates that the mass outside $R_{\Omega_{\max}}$ and the mass outside $R_{\rm disk}$ are rather similar (the former being slightly larger since since $R_{\Omega_{\max}} \lesssim R_{\rm disk}$) and can be quite large, being almost $0.3\,M_{\odot}$ for some of the soft-EOS low-mass binaries and of the order of $0.1\,M_{\odot}$ for the other binaries. Finally, an important consideration is that of long-term angular-momentum transport and neutrino radiation. These physical effects will change quantitatively these values, but they should not be expected to change the qualitative picture that low-mass soft-EOS binaries will have comparatively larger disks.

4.6.3 Influence of the thermal component

This next section is dedicated to assessing the impact of the thermal component of the EOS on the results presented so far. The influence of the thermal component was briefly discussed in Sec. 4.5 and here a more in-depth discussion will be presented. Recall, that with the exception of the LS220 EOS, all of the EOSs simulated do not have a nuclear-physics thermal component and that thermal effects are accounted for via a hybrid EOS in which an ideal-fluid contribution is added to the total pressure, recall Sec. 4.2.2 for details. The choice of the adiabatic index $\Gamma_{\rm th}$ is somewhat arbitrary (the only mathematical constraint being that $1 \leq \Gamma_{\rm th} \leq 2$, but see discussion in [213]). Since the value of $\Gamma_{\rm th}$ regulates the amount of thermal pressure produced after merger and hence, to some extent, the equilibrium properties of the HMNS, it is important to investigate the effects on the rest-mass density and angular-velocity distributions.

The effects of the different Gammas are shown in Fig. 4.16 for the `ALF2-M125` binary. Note that although only a single case is shown, the results are similar for other binaries. Indicated with green (black) solid, dashed and dotted lines is the averaged angular velocity (rest-mass density) profiles for $\Gamma_{\rm th} = 2.0, 1.8$ and 1.6, respectively. The curves are obtained after averaging in the azimuthal direction and over a time interval $[1/3\,t_{\rm fin}, 2/3\,t_{\rm fin}]$. Figure 4.16 illustrates that a larger value of $\Gamma_{\rm th}$ yields a larger pressure support and hence prevents the matter in the HMNS to reach large values of compression. This explains why the maximum rest-mass density is larger for smaller values of the thermal adiabatic index (see black lines). In turn, since a larger pressure support implies that the HMNS is less compact (compressed) and since the angular momentum is essentially the same for the binaries with different $\Gamma_{\rm th}$ considered here, it is not surprising that the maximum value of the averaged angular velocity increases as the contribution of the thermal component is decreased (see green lines).

What is possibly more important to note is that the changes induced by the

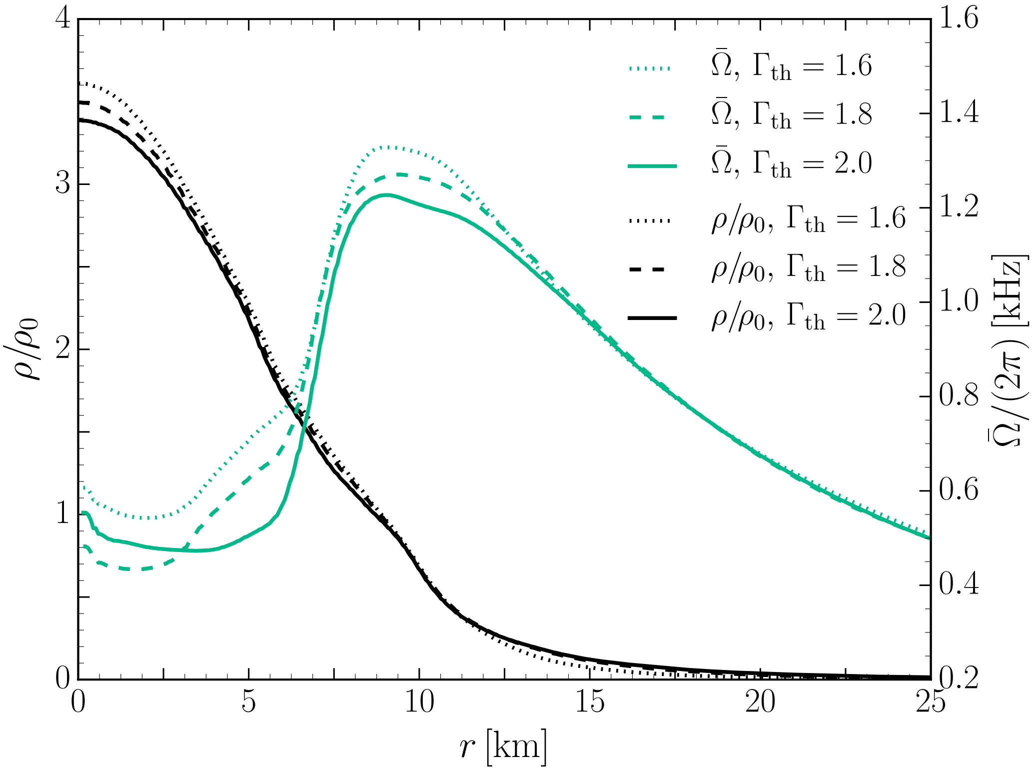

Figure 4.16: Time- and azimuthally averaged rest-mass density profiles (black lines) and angular-velocity profiles (green lines) of the `ALF2-M125` binary for different values of the thermal adiabatic index $\Gamma_{\rm th}$. The time and azimuthal averages have been performed in the same manner as in Fig. 4.12.

different values of $\Gamma_{\rm th}$ are quantitative only and also rather small, i.e., with relative variations of $\lesssim 10\%$ in the angular velocity. The qualitative behaviour, however, remains unchanged, most notably, in the disk, thus removing the influence of the thermal component of the EOS as a potential bias in previous the analysis.

4.7 On the Bernoulli constant

As discussed in section 4.3.2, the evident $\pi/2$ phase difference in the distribution of the angular velocity and of the density, so that areas of low pressure (rest-mass density) are accompanied by regions of large velocity, can be explained in terms of the manifestation of the Bernoulli theorem. To illustrate this observation, a rather idealised description of the quasi-stationary equilibrium of the HMNS and a series of assumptions that will simplify the mathematical treatment and hopefully improve the physical understanding.

Recall that in relativistic hydrodynamics and for a perfect fluid with four-velocity $\boldsymbol{u}$, the quantity $h\,(\boldsymbol{u}\cdot\boldsymbol{\xi})$ is Lie-dragged along $\boldsymbol{u}$ [213]

$$\mathscr{L}_{\boldsymbol{u}}(h\,\boldsymbol{u}\cdot\boldsymbol{\xi}) = 0\,, \tag{4.13}$$

where $h := (e+p)/\rho$ is the specific enthalpy, $e := \rho(1+\epsilon)$ is the total energy density, and $\boldsymbol{\xi}$ is a Killing vector of the spacetime and also a generator of the symmetry obeyed by the fluid. A direct consequence of Eq. (4.13) is that in the case in which the spacetime admits a timelike Killing vector, then the quantity $\mathcal{B} := hu_t$ is a constant of the fluid; this is the general-relativistic extension of the classical Bernoulli theorem.

Of course, the assumption of a stationary spacetime during the evolution of the HMNS is not true and the HMNS is emitting gravitational waves, which are the most evident manifestation of a non-stationary spacetime. Yet, because at least energetically these modulations of the spacetime are small when compared with the total bulk (kinetic) energy of the system, it can be considered the assumption not to be unreasonable even though it is evidently not strictly true.

In its classical limit, Eq. (4.13) becomes

$$\left(1+\epsilon+\frac{p}{\rho}\right)\left(1+\phi+\frac{1}{2}\vec{\boldsymbol{v}}^2\right) = \text{const.}\,, \tag{4.14}$$

where ϕ is the gravitational potential and where $\boldsymbol{v}$ is the local fluid velocity. When neglecting higher-order terms, expression (4.14) further reduces to

$$\left(\frac{1}{2}\vec{\boldsymbol{v}}^2+\phi+\epsilon+\frac{p}{\rho}\right) = \text{const.}\,, \tag{4.15}$$

which coincides with the classical expression for the Bernoulli constant [213]. Next, to translate into a classical Newtonian language with the assumption on the existence of a timelike Killing vector, the gravitational potential is taken to be independent of time and essentially constant across the HMNS, so that Bernoulli's theorem effectively reduces to the well-known condition that, along a fluidline,

$$\left(\frac{1}{2}\vec{\boldsymbol{v}}^2+\epsilon+\frac{p}{\rho}\right) = \text{const.}\,. \tag{4.16}$$

To validate whether or not the classical Bernoulli constant (4.16) is actually a constant along a fluidline, the Bernoulli constant has been calculated for a number of tracer particles and shown for three representative fluidlines in Fig. 4.17 for the `LS220-M132` binary. These tracers have been selected because they are originally in the equatorial plane and have an essentially zero velocity in the vertical

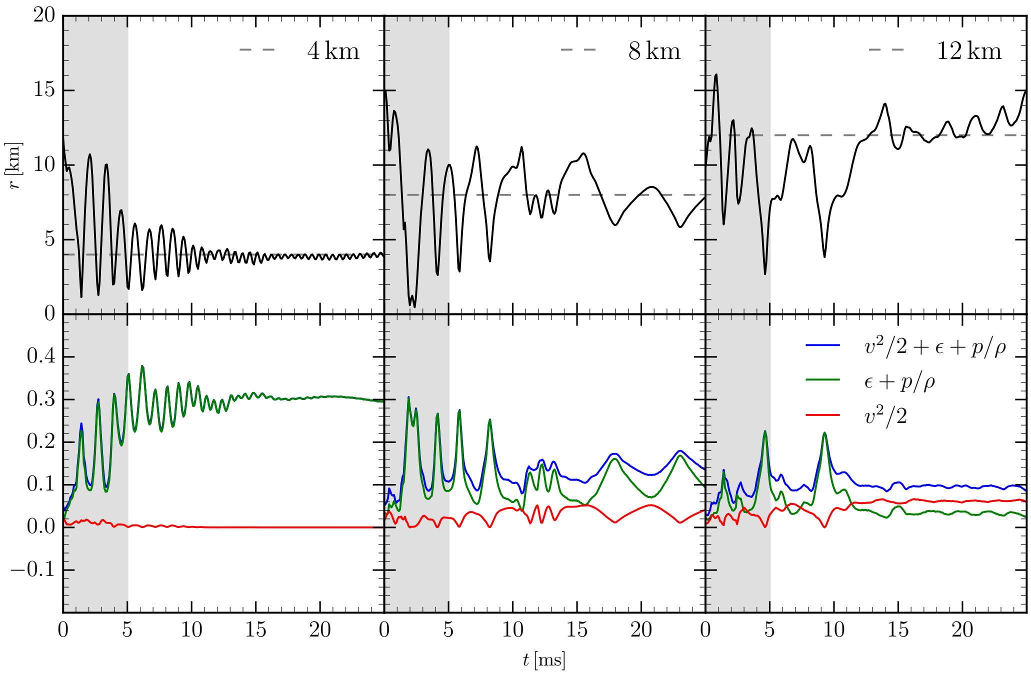

Figure 4.17: *Top panels:* evolution of the radial positions for tracers in the `LS220-M132` binary that are eventually either in the inner regions of the HMNS (left panel), or at some distance from the rotation axis (central panel), or in outer regions of the HMNS (right panel). *Bottom panels:* evolution of the classical Bernoulli constant (4.16) relative to these tracers (blue solid lines), and its main contributions. The gray-shaded area refers to the post-merger transient when the HMNS is far from an equilibrium.

rotation, hence representing particles that are genuinely moving in the equatorial plane. The three panels in the top row of Fig. 4.17 show the evolution of the radial positions for tracers that at the end of the simulation are either in the inner regions of the HMNS [i.e., $r(t = t_{\rm fin}) = 4\,{\rm km}$, left panel], or at some distance from the rotation axis [i.e., $r(t = t_{\rm fin}) = 8\,{\rm km}$, central panel], or in outer regions of the HMNS [i.e., $r(t = t_{\rm fin}) = 12\,{\rm km}$, right panel]. The gray-shaded area refers to the post-merger transient when the HMNS is far from an equilibrium. Note that these selected particles can experience large excursions from their original positions (shown as dashed horizontal lines) due to the complex motion around the core per Fig. 5.4, but that on average they do not stride too far away.

The panels in the bottom row of Fig. 4.17 show instead the values of the classical Bernoulli constant (4.16) relative to the corresponding tracers in the top row (blue solid lines), but also the two main quantities contributing to it, namely: $\epsilon + p/\rho$ (green solid lines)[5] and $v^2/2$ (red solid lines). While the values of (4.16) are strictly not constant in time (especially in transient post-merger phase indicated with the gray-shaded areas), they also do not vary significantly around the initial values. More importantly, it is very clear that there is a phase opposition in the evolution of the pressure term $\epsilon + p/\rho$ and of the kinetic term $v^2/2$, so that large values of the former correspond to low values of the latter and viceversa. This is exactly what one would expect in the presence of a fluid satisfying Bernoulli's theorem, hence supporting the explanation of the phase difference in the distribution of angular velocity, recalling that $v \sim \Omega r$, and density being a result of the conservation of the Bernoulli quantity $\mathcal{B} = h\,u_t$. All that has been discussed above for the three representative tracers holds true for all others that are taken in the neighborhood of the equatorial plane.

4.8 Time-averaging, symmetries, and resolutions

Finally, this last section, the impact that the time-averaging techniques, the use of a π-symmetry and the chosen spatial resolution are evaluated for the influence they have on the robustness of the presented results. Recall that all the simulations reported here have used six refinement levels and a rather high spatial resolution, namely, $\Delta h_5 = 0.15\,M_\odot \approx 221\,{\rm km}$ on the finest refinement level. Furthermore, to reduce computational costs, a a reflection symmetry across the $z = 0$ plane and for most simulations a π-symmetry condition across the $x = 0$ plane has been employed.

---

[5] Note that $\epsilon \simeq p/\rho$ at all times and hence they are not shown separately.

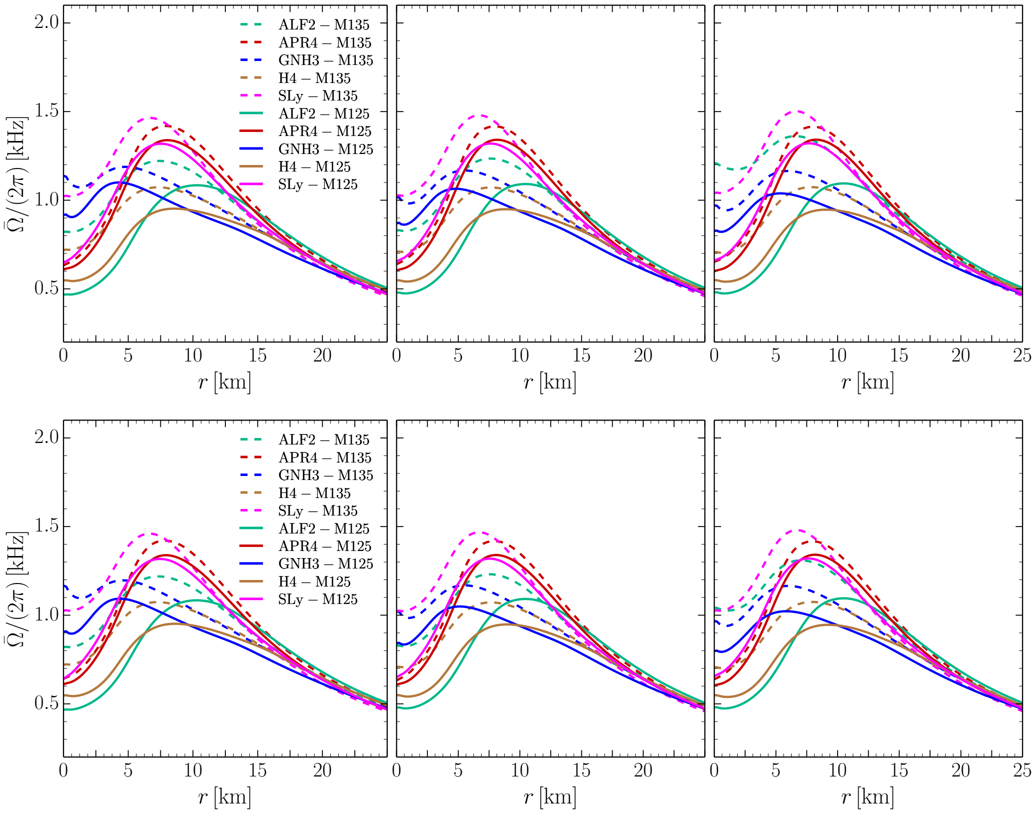

Figure 4.18: Comparison of different averaging techniques for the time- and azimuthally averaged angular-velocity profiles for different EOSs. The beginning of the averaging window has been fixed at $6\,\mathrm{ms}$. *Top panels:* For all EOSs and masses, the different panels refer to different lengths of the window, namely, $5,\ 7,\ 9\,\mathrm{ms}$, so that the from left to right the data refer to time windows $[6\,,11]$, $[6\,,13]$ and $[6\,,15]\,\mathrm{ms}$, respectively. *Bottom panels:* The same as above but when the averaging window is not the same for the different EOSs and masses but is determined by the gravitational-wave frequency $f_2 = \Omega_2/(2\pi)$. As a result, from left to right the averaging windows are: $[12,\ 18,\ 24] \times 1/f_2$, respectively.

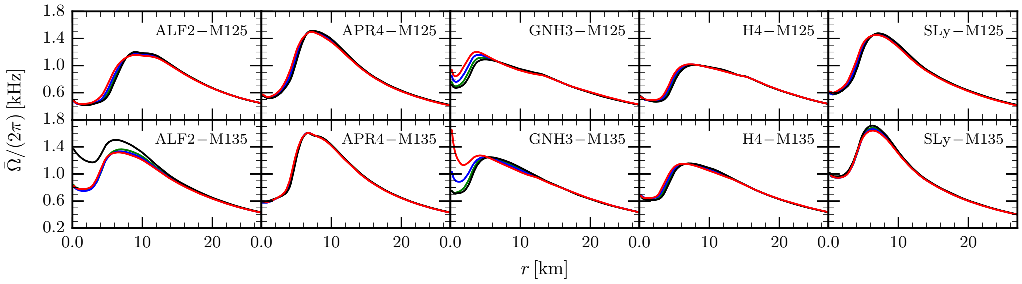

Figure 4.19: Averaged angular-velocity profiles when the averaging windows is set to be $7\,\mathrm{ms}$ for all EOSs and masses, but where the initial averaging time is varied and set to be 5 (red line), 6 (blue line), 7 (green line), and $8\,\mathrm{ms}$ (black line), respectively. The four lines refer to averaging windows given by $[5, 12]$, $[6, 13]$, $[7, 14]$, and $[8, 15]\,\mathrm{ms}$, respectively; note that the top part of each panel refers to the low-mass binary, while the bottom one to the high-mass one.

Impact of time-averaging techniques

The choice of the origin and length of the time-averaging window has been guided by two principal considerations: avoiding the initial post-merger phase and avoiding the phase briefly preceding the collapse to a black hole. Avoiding the initial post-merger phase is important because the HMNS is rapidly changing in its attempt to reach an equilibrium; the matter dynamics in this phase is quite irregular, as can be seen in the gravitational waves [212], and differs significantly from the evolution at later times when the system reaches a more equilibrium state. On the other hand, avoiding the stage preceding the collapse to a black hole is important because again in such a stage the dynamics is far from equilibrium and any information on the angular velocity does not reflect a quasi-stationary solution.

Within these constraints, there are two free parameters available to produce the time averages: the initial time of the averaging window and its width. Recall that in the previous section a time-averaging centered about $t_{\rm fin}/2$ with a width of $t_{\rm fin}/3$ where $t_{\rm fin}$ is chosen as the time to collapse to a black hole in the high-mass cases and the end of the simulation in the low-mass cases. These values ensure that the above mentioned considerations are realised and have no influence on the angular-velocity profiles. Although these constraints may appear restrictive, the effect of different times and how they influence the averaging procedure is considered next.

To this end, several initial and final values of the averaging procedure have been chosen and plotted in Fig. 4.18. More precisely, the top panels of Fig. 4.18 report the angular-velocity profiles when the initial time of the averaging window is taken to be $6\,\mathrm{ms}$ after the merger, independently of the EOS and mass of the binary. Furthermore, the different panels from left to right refer to different lengths of the window, namely, $5,\ 7,\ 9\,\mathrm{ms}$, so that the windows data refer to time windows $[6\,,11]$, $[6\,,13]$ and $[6\,,15]\,\mathrm{ms}$, respectively. Clearly, independent of the window length, the qualitative features are essentially identical, exhibiting a slowly rotating core, followed by an increase to a maximum, followed by a decrease to a flow with $\Omega(r) \propto r^{-3/2}$.

The bottom panels of Fig. 4.18, on the other hand, show similar information in that the initial time is still fixed to $6\,\mathrm{ms}$, but the averaging window is not the same for the different EOSs and masses. Rather, it is determined by the gravitational-wave frequency $f_2 = \Omega_2/(2\pi)$, which is related to the maximum of the angular velocity $\Omega_{\max}$ (cf. Fig. 4.13). In this way, each binary will have an average window which is set to be a multiple of the spinning frequency of the HMNS. In practice the averaging window has been set to be $\Delta t = [12,\ 18,\ 24] \times 1/f_2$ in the panels from left to right, respectively. Also in this case, the qualitative behaviour of the various angular-velocity profiles is the same and the differences are of a few percent at most.

As a final variant of the possible way of performing the time averages, reported in Fig. 4.19 is the angular-velocity profiles when the averaging windows is set to be $7\,\mathrm{ms}$ for all EOSs and masses, but where the initial averaging time is varied and set to be $5,\ 6,\ 7$ and $8\,\mathrm{ms}$, respectively. As a result, the four lines reported in each panel refer to averaging windows given by $[5, 12]$, $[6, 13]$, $[7, 14]$, and $[8, 15]\,\mathrm{ms}$, respectively; note that the top part of each panel refers to the low-mass binary, while the bottom one to the high-mass binary. Also when considering this different technique it emerges rather clearly that the averaging procedure has little influence on the angular-velocity distribution. However, two exceptions are also equally clear and for obvious reasons. The first one is offered by the binary `ALF2-M135` case, whose HMNS collapses at approximately $15\,\mathrm{ms}$ (cf. Fig. 4.2) and whose "late-time" averaging window is obviously spoiled by the large increase in Ω occurring before the collapse. The second exception is given instead by the binary `GNH3-M135`, which has instead a long-lasting transient post-merger phase, with the two stellar cores still clearly visible. Also in this, the "early-time" averaging is not representative of a quasi-stationary stage. Excluding these two obvious pathological averaging windows, the maximum angular-velocity changes by 5% at most for all masses and EOSs.

Impact of π-symmetry

Next to be considered is the impact of having imposed a π-symmetry in the simulations. While this is a perfectly reasonable option in view of the considerable savings in computational costs, it does not allow the development of an $m = 1$

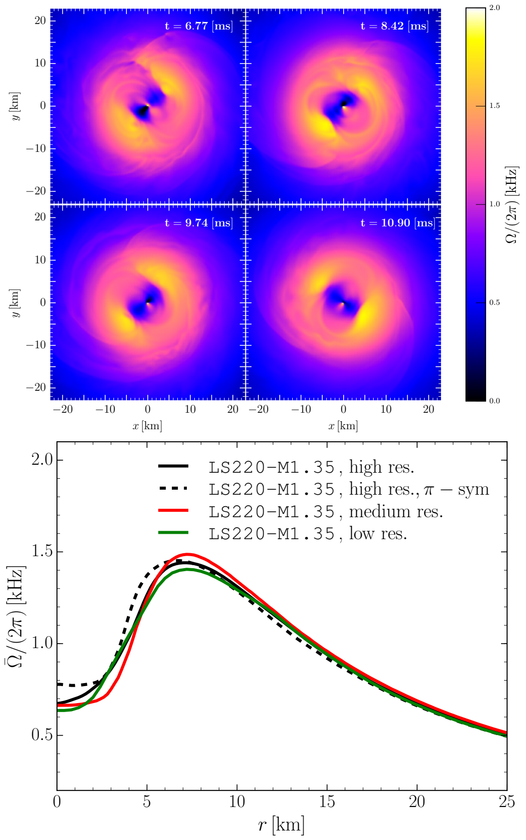

Figure 4.20: *Left panel:* angular velocity distribution on the equatorial plane at four representative times for a binary with the LS220 EOS evolved without π-symmetry; note the appearance of an $m = 1$ deformation in addition to the larger $m = 2$ deformation. *Right panel:* corresponding azimuthal and time-averaged profile for the same binary with π-symmetry (black dashed line) and without (black solid line) at a resolution of $\Delta x = 0.15$. Additionally, low resolution runs of $\Delta x = 0.20$ (red solid line) and $\Delta x = 0.25$ (green solid line) are shown. All resolutions exhibit the same behaviour already discussed above.

instability that has been reported by a number of groups [77, 200, 143]. While the gravitational-wave signal associated with the instability is always smaller than the dominant one coming from the $m = 2$ deformations in the HMNS, so that its observation by current generation detectors is unlikely and will require third-generation detectors [200], it is useful to verify whether the presence of the one-arm instability would leave an imprint on the angular-velocity profiles despite the azimuthal average.

Thus, to test the influence of symmetry on the result, an additional simulation was conducted using an equal-mass binary with the LS220 EOS and a gravitational mass of $2 \times 1.350\, M_{\odot}$ (cf. binary `LS220-M135` in Table 6.1), evolved with and without π-symmetry to investigate the exact influence of the instability on the rotation profiles. The corresponding angular-velocity distribution on the equatorial plane for the simulation without the π-symmetry is shown in the left panel of Fig. 4.20 at four representative times after the merger and when the HMNS has reached a quasi-stationary state. Comparing such a panel with the bottom rows of Figs. 4.3 and 4.9, where the π-symmetry is imposed, highlights the presence of a small $m = 1$ deformation. The right panel of Fig. 4.20, on the other hand, reports the corresponding azimuthal and time-averaged profile for two simulations. The black dashed line refers to the π-symmetric run, while the black solid line to the run without π-symmetry; in both cases the average is done between $t = 5\,\mathrm{ms}$ and $t = 12\,\mathrm{ms}$.

Clearly, no sign of the $m = 1$ deformation is present, as one would expect from an averaging process; rather, the angular velocity shows similar quantitative behaviour with and without the use of π-symmetry. The greatest difference is in the very centre of the HMNS where the angular velocity is higher with π-symmetry than without. The maximum angular velocity is 1% larger with π-symmetry and the location of the maximum is slightly shifted to larger radii. Both runs exhibit quasi-circular orbits at larger radii. Thus the conclusion is that that in the very interior of the HMNS, the use of π-symmetry plays a small role, but also that outside a core region of $\simeq 5\,\mathrm{km}$ the influence is minimal and does not affect the conclusions.

Impact of grid resolution

Since the stability properties of the HMNS phase depend on the resolution (see [19] where this was first investigated systematically), the determination of its lifetime against gravitational collapse requires a systematic and very careful resolution study. At the same time, because of the development of large shocks, the convergence order after the merger is inevitably very low i.e., of order unity or less. In fact, different resolutions would mostly produce phase differences in the dynamics of the fluid and spacetime variables, hence with only a small impact on the results that are expressed in terms of time and azimuthal averages.

Notwithstanding these considerations, it is reasonable to ask how significant are the changes in the angular-velocity profiles when the simulations are performed at different resolutions. The simulations considered here were first published in Ref. [256] where the influence of the resolution on the dynamics of the HMNS by using three different resolutions for a binary described by an ideal-fluid EOS was described. As remarked in [256], the rather high resolution employed in these simulations on the finest refinement level, i.e., $\Delta h_5 = 0.15\,M_\odot$, provides a description of the HMNS which is very close to that obtained with an even higher resolution of $\Delta h_5 = 0.125\,M_\odot$.

The results of the present resolution study are summarized in the right panel of Fig. 4.20 for the `LS220-M135` binary. More specifically, in the right panel of Fig. 4.20 the averaged angular velocity for the binary `LS220-M135` for three different resolutions on the finest refinement level, i.e., $\Delta h_5 = 0.15, 0.20, 0.25\,M_\odot \approx 221, 295, 369\,\mathrm{m}$ is plotted. These three times are denoted as “high”, “medium” and “low resolution”, respectively. All simulations do not use a π-symmetry, except where noted. Also although a resolution of $\Delta x = 0.25\,M_\odot$ may appear coarse, it is routinely used in numerical-relativity simulations of binary neutron stars (see, e.g., [65, 156, 81]) and has been shown to be high enough to provide physically robust results (see [65] for an extensive discussion).

Clearly, at all resolutions the profile of the angular-velocity is similar, namely, showing a slowly rotating core, rising to a maximum around $8\,\mathrm{km}$ before decreasing to a $r^{-3/2}$ profile. The largest differences between resolution are in the centre of the HMNS, where the rest-mass densities are the highest and the metric functions show the largest gradients. Despite this, all resolutions reach a maximum angular-velocity at around $8\,\mathrm{km}$ with a variation with resolution that is at most 5%. This small variance demonstrates the robustness of the maximum angular-velocity and illustrates that quasi-universal relations proposed in Sec. 4.6 are a robust feature of the HMNS.

4.9 Conclusions

The long-term stability of astrophysical compact objects is an important aspect of their evolution to understand in order to confirm physical theories. The formation of these compact objects can arise from different channels, such as Type-II core collapse supernovae or from the merger of binary neutron stars. These rotating objects possess large amounts of angular momentum and their stability cannot be attributed to uniform rotation alone, but instead require a differentially rotating object. However, the exact nature of this differential rotation remains unknown and if it is discovered, if it is a “universal” law or dependent of the system considered.

Previous work on the study of rotation in the HMNS has focused mainly on two categories: analytical and numerical. The analytical studies assume a differential rotation law of a certain form, known as the $j-$ constant law in which the angular velocity decreases monotonically away from the centre of the star and the amount of rotation is controlled by a singular dimensionless parameter. The alternative approach is that of the numerical simulation, where no law of differential rotation is assumed by is instead extracted numerically from the evolved simulation. General features have emerged here, such as a slowly rotating core and an envelope that rotates at frequencies scaling like $r^{-3/2}$. This empirical result is clearly very different from what is expected when using a $j-\mathrm{constant}$ law of differential rotation.

To shed some light on these differences, and to obtain a comprehensive picture of the rotational properties of HMNSs from binary neutron-star mergers, a large number of numerical simulations in full general relativity of binary neutron stars described with various EOSs and masses has been carried out. These simulations confirm the preliminary results in Refs. [238, 128, 127], but, more importantly, demonstrate that the angular-velocity distribution have only a modest dependence on the EOS, thus exhibiting the traits of “quasi-universality”. More specifically, the EOS-independent angular-velocity distributions found here are characterized by an almost uniformly rotating core and a disk. The rest mass contained in such disk can be quite large, ranging from $\simeq 0.03\,M_{\odot}$ in the case of high-mass binaries with stiff EOSs, up to $\simeq 0.2\,M_{\odot}$ for low-mass binaries with soft EOSs. In these numerical simulations there is also a puzzling, at first, result that there is a phase difference between the distributions of the rest-mass density and the angular velocity. However, there is a simple explanation in terms of a Bernoulli-like constant that can easily be shown to hold using tracers in bound material.

Even though the work presented here is extensive, there are some important technical points that must be made. Firstly, the binaries that were simulated here were all equal mass. Studies of non-equal mass binaries have shown that this isn’t a big issue [58] as these cases exhibit similar angular velocity profiles, but an extensive study is required. Second, the effects of neutrinos is not taken into account in all simulations, except for the fully temperature-dependent LS220 EOS. From this run, in comparison with the others, it is clear that neutrinos do not play an important in the differential rotation law. This is because the neutrino-diffusion timescale is at least one order of magnitude larger than the one considered here [193] Third, the simulations here have neglected magnetic fields, even though magnetic fields are very likely to play a role in post-merger dynamics, especially in light of GW170817. This is because magnetic fields can transfer angular momentum from the inner regions to the outer regions which would affect the rotation law considered here. However, this transfer will take place on an Alfvén timescale, which is much longer than the one considered here. In this sense, the quasi-universal behaviour reported here should be taken as representative of the first few tens of milliseconds after the merger and studied with magnetic fields [58] indicate that the results should remain valid also in the presence of magnetic fields and at least within $\sim 40\,\mathrm{ms}$ after merger.

In conclusion, the use of tracers developed in Chapter 3 provides a unique tool to study the evolution of post-merger effects in bound material and can be used to visualise complicated flow that is otherwise inaccessible to other, more standard techniques. This use of tracers will be further used in the next chapter to investigate the effects of shear and bulk viscosity in the post-merger evolution of a binary neutron star merger.

Chapter 5

On the importance of viscous dissipation and heat conduction in binary neutron-star mergers

In this chapter, the tracer method of Chapter 3 is now applied to the problem of dissipative effects in the post-merger evolution of a binary neutron star.[1] As discussed in Chapter 2 the assumption of a perfect fluid is made in numerical relativity, however a closer examiniation of the conditions this assumption can be made with the user of tracers.

5.1 Introduction

With the detection of GW170817, the need for increasingly more accurate numerical relativity simulations is needed. Improvement lies not only in the computational and numerical side, but also increasing the accuracy of the physical models themselves. For example, as introduced in Chapter 2, the fluid composition of a neutron star is taken to be a perfect fluid, i.e., one without dissipation or shear effects. Almost all present simulations, with a few exceptions [75, 234], of neutron-star mergers make this assumption and hence neglect the transport properties of the material, assuming that they are too small to operate on dynamical timescales [40].

In this chapter, this assumption of perfect fluid behaviour is challenged by exploring the impact of viscosity and thermal transport after merger, exploiting results of simulation discussed in Chapter 4 and using the tracers introduced in

---

[1] This chapter is based on the work of [9]. All figures in this chapter have been reproduced from [9]. My contribution to this work was to run the numerical relativity simulations, do the data analysis, generate the figures, and write parts of the text.

Chapter 3. As mentioned previously, enormous progress [241, 18, 12, 151, 39] has been made in the modelling of neutron stars although the extensions beyond the perfect fluid model are limited. During the post-merger phase, the post-merger object is metastable to gravitational collapse over tens of milliseconds cf. Chapter 4 and is subject to many different physical scales. For example, in the inner region of this object, $\sim 10\,\mathrm{km}$ across, can reach several times nuclear-matter saturation (number) density $n_0 \approx 0.16\,\mathrm{fm}^{-3}$ and temperatures of tens of MeV, which, as will be shown below, allow for the possibility of shear and thermal effects to be important. Thus estimates of the timescales of transport and dissipation processes for a typical post-merger scenario are calculated and it is shown that such effects are likely to be important in future simulations.

5.2 Thermal equilibration

The first process to investigate is to establish whether or not the effects of heat diffusion is important. To this end, consider a region of size z that is hotter than its surrounding with a temperature difference of ΔT. Suppose now that the material in this region has a specific heat per unit volume c_V and thermal conductivity κ. This means that the extra thermal energy in this region is easily approximated by

$$E_{\mathrm{th}} \sim c_V z_{\mathrm{typ}}^3 \Delta T, \tag{5.1}$$

up to some numerical constant pre-factor depending on the geometry. Additionally, the heat conduction rate is simply

$$W_{\mathrm{th}} \sim \kappa \Delta T z_{\mathrm{typ}}, \tag{5.2}$$

assuming a smooth temperature distribution. By dividing these two scales give the timescale of thermal equilibrium time,

$$\tau_\kappa \equiv E_{\mathrm{th}}/W_{\mathrm{th}} \sim c_V z_{\mathrm{typ}}^2/\kappa, \tag{5.3}$$

which is the timescale required to dissipation all the extra thermal energy. In order to estimate this quantity in neutron stars, the values of c_V and κ must be determined. It can be shown that the specific heat is typically dominated by neutron, yield $c_V \approx 1.0\, m_n^* n_n^{1/3}\, T$, assuming a Fermi liquid of neutron density n_n with Landau effective mass m_n^* [144]. The thermal conductivity is written as

$$\kappa \propto \sum_i \kappa_i \propto \sum_i n_i v_i \lambda_i. \tag{5.4}$$

where n_i is the number density, v_i the characteristic speed, and λ_i is the mean free path of the ith species respectively. The terms that dominate are those that have large mean free paths and high densities so although neutrons are rather abundant, they are strongly interacting and hence have a very small mean free path. Thus the particles that dominate the thermal conducitivity are electrons and neutrinos. Although neutrinos are very important in the evolution of a neutron star, below a few MeV, the neutrino mean free path becomes longer than the merger region [23, 207], so neutrinos become free streaming and thus escape the system and cannot contribute to the sum and hence the only option is the electrons. It can be shown that thermal conductivity of electrons is temperature-independent $\kappa_e \approx 1.5\, n_e^{2/3}/\alpha$ (Eq. (40) of [243]), where n_e is the electron number density and $\alpha \approx 1/137$. Plugging all these numbers into the approximation for the timescale yields a lower bound for the thermal equilibration time in the electron dominated regime

$$\begin{aligned} \tau_\kappa^{(e)} &= 5 \times 10^8\,\mathrm{s} \\ &\times \left(\frac{0.1}{x_p}\right)^{\frac{2}{3}} \left(\frac{m_n^*}{0.8\, m_n}\right) \left(\frac{n_0}{n_B}\right)^{\frac{1}{3}} \left(\frac{z_{\mathrm{typ}}}{1\,\mathrm{km}}\right)^2 \left(\frac{T}{1\ \mathrm{MeV}}\right), \end{aligned} \tag{5.5}$$

where n_B is the baryon number density, n_0 nuclear saturation density and $x_p \equiv n_e/n_B$ is the proton fraction. Clearly, this timescale is far too large to have an impact on the $\sim 10\,\mathrm{ms}$ timescale of post-merger processes [23].

The previous section assumed that the electrons were dominating at lower temperatures. However at higher temperatures i.e., $T \gtrsim 10$ MeV, neutrinos become trapped for nucleon density $n \gtrsim n_0$, and thus the neutrino mean free path, which at high density depends strongly on in-medium corrections [207, 215], becomes smaller than the star. Electron neutrinos form a degenerate Fermi gas with a Fermi momentum $p_{F,\nu}$ of about half that of the electrons. Their mean free path is longer than that of the electrons, so they dominate the thermal conductivity [102], which is given by $\kappa_\nu \approx 0.33\, n_\nu^{2/3}/(G_F^2 (m_n^*)^2 n_e^{1/3} T)$, where $G_F \equiv 1/(293\ \mathrm{MeV})^2$ is the Fermi coupling. Again, plugging in these scales yields the timescale for thermal transport via neutrinos

$$\begin{aligned} \tau_\kappa^{(\nu)} &\approx 0.7\,\mathrm{s} \\ &\times \left(\frac{0.1}{x_p}\right)^{\frac{1}{3}} \left(\frac{m_n^*}{0.8\, m_n}\right)^3 \left(\frac{\mu_e}{2\,\mu_\nu}\right)^2 \left(\frac{z_{\mathrm{typ}}}{1\,\mathrm{km}}\right)^2 \left(\frac{T}{10\,\mathrm{MeV}}\right)^2. \end{aligned} \tag{5.6}$$

Thus, in contrast to that of electron-dominated equilibration, the neutrino-driven thermal transport is within the timescale of the lifetime of a neutron star merger. For example, if the length scales are on the order of $0.1\,\mathrm{km}$, this timescale is on the order of a few tens of milliseconds which is within the simulation time of an HMNS evolution.

5.3 Shear dissipation

The next effect to consider is that of shear dissipation. To measure this effect, consider the shear-viscosity timescale. To define this timescale, consider a fluid of rest-mass density ρ flowing in the x direction at velocity v_x, having kinetic energy per unit volume

$$e_{\text{kin}} = \frac{1}{2}\rho v_x^2, \tag{5.7}$$

If the fluid has shear viscosity η, then the energy dissipated per unit time and unit volume is

$$w_{\text{shear}} \approx \eta \left(\frac{dv_x}{dz}\right)^2 , \tag{5.8}$$

and the time needed for shear viscosity to dissipate a significant fraction of the kinetic energy is again

$$\tau_\eta \equiv e_{\text{kin}}/w_{\text{shear}}. \tag{5.9}$$

Assuming that the low is fairly uniform, with the velocity varying by a factor of order unity over a distance z_{typ} in the z direction, so $dv_x/dz \approx v_x/z_{\text{typ}}$ gives

$$\tau_\eta \approx \frac{\rho z_{\text{typ}}^2}{2\eta}. \tag{5.10}$$

To evaluate this timescale, again there are two regimes to consider, the electron-dominated and the neutrino-dominated. Considering first the electron-dominated regime ($T \lesssim 10$ MeV), the dominant transverse contribution from [242] [Eq. (2.4) in [159]] with the damping scale $q_t^2 \equiv 4\alpha p_{F,e}^2/\pi$, yield

$$\eta_e \approx 0.2 \, \frac{n_e^{14/9}}{\alpha^{5/3}\, T^{5/3}}. \tag{5.11}$$

Plugging this and representative values into the timescale yields

$$\tau_\eta^{(e)} \approx 1.6 \times 10^8 \,\text{s} \left(\frac{z_{\text{typ}}}{1\,\text{km}}\right)^2 \left(\frac{T}{1\text{ MeV}}\right)^{\frac{5}{3}} \left(\frac{n_0}{n_B}\right)^{\frac{5}{9}} \left(\frac{0.1}{x_p}\right)^{\frac{14}{9}} , \tag{5.12}$$

which, like the thermal dissipation from the previous section is too long compared to the lifetime of the HMNS.

Now, considering the high-temperature, neutrino-dominated regime ($T \gtrsim 10$ MeV) neutrinos produce a much larger shear viscosity [102]

$$\eta_\nu \approx 0.46\, n_\nu^{4/3} / \left(G_F^2 (m_n^*)^2 n_e^{1/3} T^2\right) \tag{5.13}$$

which plugging into the timescale equation yields

$$\tau_\eta^{(\nu)} \approx 54\,\mathrm{s}\,\left(\frac{0.1}{x_p}\right)\left(\frac{m_n^*}{0.8\,m_n}\right)^2\left(\frac{\mu_e}{2\,\mu_\nu}\right)^4\left(\frac{z_{\mathrm{typ}}}{1\,\mathrm{km}}\right)^2\left(\frac{T}{10\,\mathrm{MeV}}\right)^2 . \tag{5.14}$$

Again, this timescale is significantly longer than the lifetime of a HMNS. However, like eq. (5.6), this result depends only weakly on the density, via the proton fraction x_p, the effective mass m_n^* and the ratio μ_e/μ_ν which in realistic simulations do not vary more than an order of magnitude. A more dominant effect is that of the typical length scale, z_{typ} which can reasonably have values of $0.01\,\mathrm{km}$ in simulations due to turbulence or high-order non-axisymmetric instabilities [130, 77, 200, 143].

5.4 Bulk viscosity

To investigate the potential of influence of this bulk viscosity an "averaged" bulk viscosity $\bar{\zeta}$ is defined, which is a measurement of the response to a periodic compression-rarefaction cycle. In nuclear matter, dissipation arises because the rate of beta equilibration of the proton fraction via Urca processes occurs on the same timescale, so that the proton fraction lags behind the applied pressure. Thus if the oscillations after the merger are roughly periodic the dissipation induced by density variations occurring on a timescale t_{dens} can be estimated by using the bulk viscosity evaluated at frequency $f = 1/t_{\mathrm{dens}}$, which can be measured by tracers. The extremal points of the bulk viscosity are largest when the internal equilibration rate matches the frequency of the oscillation. Furthermore, because the equilibration rate is sensitive to the temperature, the bulk viscosity shows a resonant maximum as a function of temperature (e.g., Fig. 7 in [10]). For oscillations with a timescale t_{dens}, the resonant maximum value is [10]

$$\bar{\zeta}_{\mathrm{max}} \equiv Y_\zeta\,\bar{n}\,t_{\mathrm{dens}}\,, \qquad\qquad Y_\zeta \equiv C^2/(4\pi B\bar{n})\,, \tag{5.15}$$

where $B \equiv -(1/\bar{n})\,(\partial\delta\mu/\partial x_p)|_n$ and $C \equiv \bar{n}\,(\partial\delta\mu/\partial n)|_{x_p}$ are the nuclear susceptibilities with respect to baryon density and proton fraction, where the chemical potential $\delta\mu \equiv \mu_n - \mu_p - \mu_e$ characterises, in the absence of neutrino trapping, the degree to which the system is out of beta equilibrium. This maximum value $\bar{\zeta}_{\mathrm{max}}$ depends only on properties of the EOS and is *independent* of the flavor re-equilibration rate. Changing the re-equilibration rate moves the curve in Fig. 7 in [10] "horizontally", changing the temperature at which the maximum value is attained.

Note that the maximum bulk viscosity is a monotonically increasing function of number density and Fig. 5.1 shows the prefactor Y_ζ for nuclear matter obeying

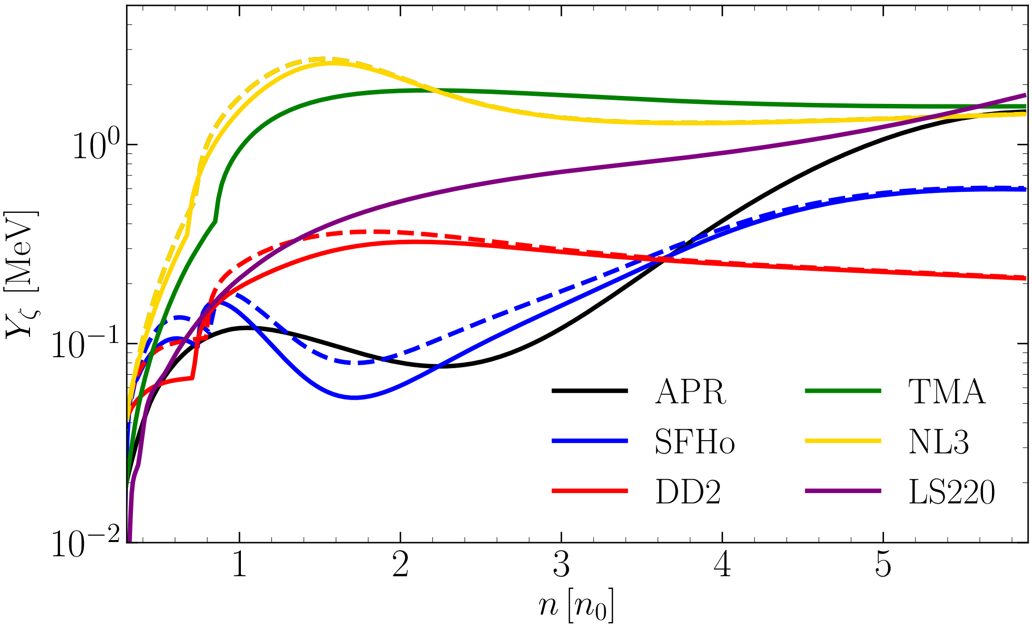

Figure 5.1: Density dependence of the maximum-bulk-viscosity prefactor Y_ζ [Eq. (5.15)] for various EOSs. Solid lines are for cold matter ($T = 0.1$ MeV) while dashed lines are for hot matter ($T = 10$ MeV). For LS220 only a single curve at $T = 1$ MeV is given due to numerical issues in the EOS table.

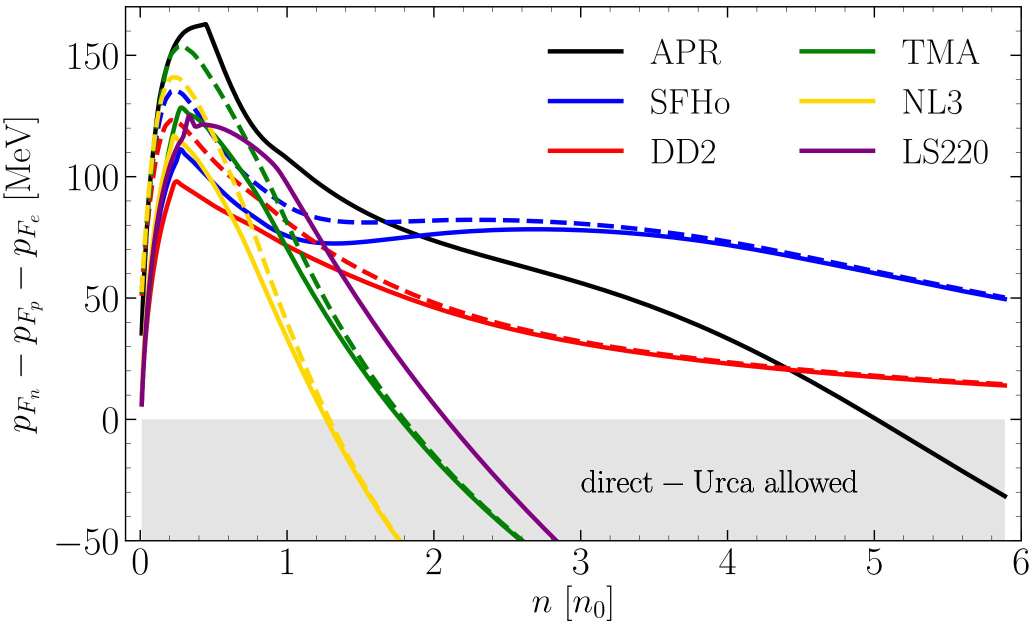

Figure 5.2: Momentum difference relevant to the direct-Urca channel as a function of density, for the EOSs shown in Fig. 5.1. For negative values, direct-Urca processes are allowed (gray-shaded area).

various EOSs, all of which can sustain a $2\,M_\odot$ neutron star [66, 14]. Whereas APR [5] is a cold EOS and is included here for comparison, for all the others a "hot" EOSs calculated using a model of nuclei and interacting nucleons in statistical equilibrium [113] is used. In addition to the LS220 [140], used for the simulations below, these EOSs range from the moderately soft SHFo [249] through the increasingly stiff DD2 [249, 84] and TMA [113], to the extremely stiff NL3.

Next consider the temperature $T_{\zeta\text{max}}$ at which bulk viscosity reaches its resonant maximum. For small-amplitude oscillations [10]

$$T_{\zeta\text{max}} = (2\pi f/(\tilde{\Gamma}B))^{1/\delta}, \tag{5.16}$$

where $\tilde{\Gamma}$ is the prefactor in the equilibration rate, $\Gamma = \tilde{\Gamma}T^{\delta}\delta\mu$. For modified-Urca processes, $\delta = 6$, so $1/\delta$ is small, making $T_{\zeta\text{max}}$ insensitive to details of the EOS. As a result, over the entire relevant frequency range, i.e., from a few tenths to several kHz, a flavor equilibration via nuclear modified-Urca "nmU" processes is observed with temperatures

$$T^{\text{nmU}}_{\zeta\text{max}} \approx 4 - 7\,\text{MeV} \approx 5 - 8 \times 10^{10}\,\text{K}\,, \tag{5.17}$$

which are well within the range of temperatures expected for dense matter in the post-merger [23, 68, 110].

It is also possible that flavor re-equilibration might occur via direct-Urca reactions instead. These reactions are orders of magnitude faster than modified-Urca processes, yielding much lower bulk viscosities at $T \sim 5\ \mathrm{MeV}$, since the resonant maximum of bulk viscosity would have moved to lower temperatures (Fig. 7 in [10]). In neutrino-transparent matter at $T = 0$, direct-Urca processes are allowed when $\Delta p_F \equiv p_{F,n} - p_{F,p} - p_{F,e} < 0$. In Fig. 5.2 the kinematic constraint as a function of density for the same EOSs in Fig. 5.1 is plotted. For softer EOSs (e.g., SFHo, DD2) direct-Urca processes are never possible at $T = 0$; however, for APR the direct-Urca channel opens at $n > 5\,n_0$. For even stiffer EOSs (LS220, NL3, TMA) it already opens around twice saturation density, yet these EOSs have been challenged by nuclear physics constraints [261]. These considerations suggest that the amount of bulk-viscous damping will be a sensitive indicator of whether the EOS allows direct Urca processes at the densities and temperatures prevalent in neutron star mergers. A more precise connection with the EOS will require calculations of the beta equilibration rate that incorporate the effects of temperature, strong interactions, and the gradual opening of phase space above the direct Urca threshold.

The next step is to estimate the dissipation time for compression oscillations. It can be shown that the energy density for a baryon number-density oscillation of amplitude Δn around average density $\bar{n}$ is $\mathcal{E}_{\mathrm{comp}} \approx K\bar{n}(\Delta n/\bar{n})^2/18$ [132], where K is the nuclear compressibility at that density. If the compression varies on a timescale t_{dens}, then, in a material with bulk viscosity $\bar{\zeta}$, the dissipated power per unit volume is [225] $(d\mathcal{E}/dt)_{\mathrm{bulk}} \approx 2\pi^2\bar{\zeta}\,(\Delta n/\bar{n})^2/t_{\mathrm{dens}}^2$. Hence, the time required for bulk viscosity to have a significant impact on the oscillations of the system is

$$\tau_\zeta \equiv \mathcal{E}_{\mathrm{comp}}/\left(d\mathcal{E}/dt\right)_{\mathrm{bulk}} \approx K\bar{n}\,t_{\mathrm{dens}}^2/(36\pi^2\,\bar{\zeta})\,. \tag{5.18}$$

Expecting bulk viscosity to reach its maximum value $\bar{\zeta}_{\max}$ Eq. (5.15) at typical neutron-star merger temperatures Eq. (5.17), Eq. (5.15) and Eq. (5.18) yield that when the direct-Urca channel is not open, the minimum timescale for bulk viscosity to impact the oscillations is

$$\tau_\zeta^{\min} \approx 3\,\mathrm{ms}\left(\frac{t_{\mathrm{dens}}}{1\,\mathrm{ms}}\right)\left(\frac{K}{250\ \mathrm{MeV}}\right)\left(\frac{0.25\,\mathrm{MeV}}{Y_\zeta}\right)\,. \tag{5.19}$$

Stated differently, under conditions of maximum bulk viscosity, the damping timescale is a few times larger than the typical timescale t_{dens} of density variations.

This timescale is well within the initial postmerger phase and potentially will have observational effects. This is because during the first few milliseconds of the

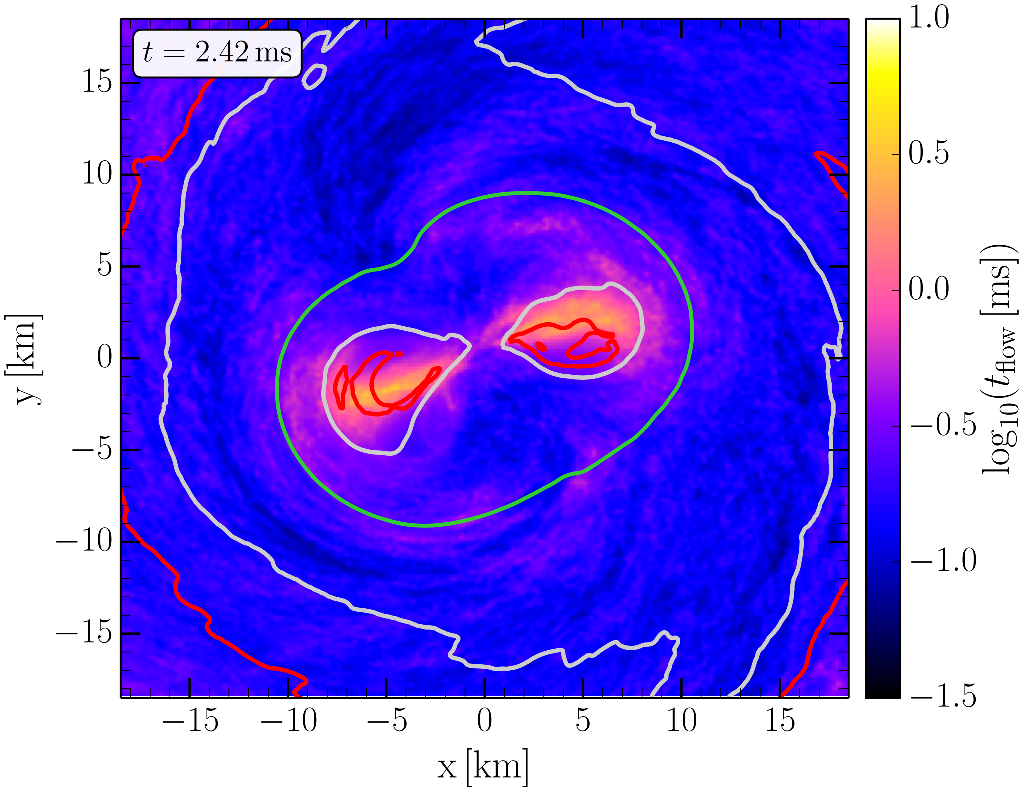

Figure 5.3: The flow timescale t_{flow} obtained from a numerical-relativity simulation of two $1.35\,M_{\odot}$ neutron stars [110]. The red (4 MeV) and gray (7 MeV) contours show the boundaries of the temperature range in which the bulk viscosity roughly takes its maximum value, while the green contour shows the inner region where the rest-mass density exceeds nuclear saturation density.

merger, there is a strong emission of gravitational waves coming from the high-density material, see also the discussion in Chapter 4. During this initial post-merger phase characteristic frequencies f_1 and f_3 appear in the gravitational-wave spectrum [254, 256, 212], and if bulk viscous damping is present, i.e., there are high density oscillations occurring on millisecond timescales with temperatures of a few MeV, these frequencies would differ from the perfect fluid approximation and thus have observable consequences.

In order to test whether such conditions are met in actual simulations, Figs. 5.3 and 5.4 show the results a BNS simulation of a symmetric merger of $M = 2 \times 1.35\, M_{\odot}$, using the LS220 EOS [140], where $t = 0$ is the time of merger [256].

In order to determine the density oscillations, a simple measurement is used through the Lagrangian derivative. The timescale of the flow is thus defined as

$$t_{\text{flow}} \equiv \left\langle \frac{\rho}{D_t \rho} \right\rangle \sim \frac{1}{\langle |\nabla \cdot \vec{v}| \rangle}, \tag{5.20}$$

where $\langle\ \rangle$ represents a time average over a 2 ms time window and where D_t is the Lagrangian time derivative in Newtonian hydrodynamics [213]. In the Newtonian limit, the relativistic continuity equation simplifies to

$$\frac{D\rho}{Dt} + \rho(\nabla \cdot \vec{v}) = 0, \tag{5.21}$$

and immediately leads to the above timescale. The result of this function is shown in Figure 5.3 which uses a colorcode to show the expansion flow timescale. Figure 5.3 reports t_{flow} 2.4 ms after the merger, where the post-merger object is in its violent and shock-dominated transient phase. Inside the green contour, the rest-mass density is above nuclear saturation. The red and gray lines are temperature contours at $4\,\text{MeV}$ and $7\,\text{MeV}$, respectively. Overall, Fig. 5.3 shows that there are significant regions where Eq. (5.19) is a valid estimate of the dissipation time because the density is high and the temperature is in the range that maximizes bulk viscosity [Eq. (5.17)].

This conclusion can also be justified because for a harmonic density oscillation, t_{flow} is related to Eqs. (5.18) and (5.19) by

$$t_{\text{dens}} \sim \frac{\Delta n}{\bar{n}} t_{\text{flow}}. \tag{5.22}$$

In the considered regions $t_{\text{flow}} \sim 0.1 - 1\,\text{ms}$ and $\Delta n/\bar{n} \sim 1$, thus $t_{\text{dens}} \sim t_{\text{flow}}$, is indeed in the millisecond range.

To further confirm this conclusion an additional measurement is displayed in Fig. 5.4, which shows the evolution of various local properties of representative tracer particles along the xy-plane in the inner region of the merger product as defined in Chapter 3. The top panel reports the evolution of the temperature and demonstrates that all tracers pass through the temperature range of large bulk viscosity (dark and light-gray shaded areas, showing the regions of maximum and up to an order of magnitude smaller dissipation) during the first few milliseconds. The top middle panel reports the evolution of the normalized rest-mass density and shows that at early times ($t \lesssim 5\,\mathrm{ms}$) there are variations of order 100% in the rest-mass density on a timescale of milliseconds, confirming that t_{dens} is in that range. The bottom middle panel shows the average of t_{flow} for the tracers, which is in the $0.1 - 1\,\mathrm{ms}$ range, as expected from Fig. 5.3. Finally, the bottom panel of Fig. 5.4 is a spectrogram averaging the power spectral densities of the normalized rest-mass densities in the second panel and showing how, throughout the first 20 ms, the merger product has oscillation with a significant power at frequencies in the kHz range.

Combing Eq. (5.19) with the results shown in Figs. 5.3 and Fig. 5.4, suggest that if direct Urca processes remain suppressed, then significant bulk viscous dissipation may occur on timescales of a few milliseconds, which is fast enough to affect the flow of nuclear material, and hence the emitted gravitational signal. Note a caveat here, which is that the given simulations do not include the effects of bulk viscosity and are only a perfect fluid, so the results simply suggest that the effects may be important and full simulations with a proper viscous treatment are required to accurately quantify the amount of dissipation that would actually be present and its potential impact on the gravitational-wave signal.

5.5 Conclusions

The exact properties of the material that a neutron star are composed of can play a significant role in the post-merger evolution of a neutron star. Here, it was shown that using simple timescale arguments, combined with tracer analysis from a numerical relativity simulation, that effects beyond the perfect approximation are likely important and can, in principle, imprint themselves on the gravitational wave signal through the f_1 and f_3 peaks [33, 251, 254, 212, 157]. An exact understanding of how these effects change the signal is particularly important since from these peaks, information about the EOS can be inferred [60, 43].

Given that additional effects beyond the perfect fluid approximation are required, the question is how to incorporate these effects into numerical simulations in a consistent manner. Unfortunately, this is a technically difficult question and many short comings exist in previous formulations that move beyond a perfect fluid, such as faster-than-light sound speed. Additionally, to be amenable to numerical methods used in numerical relativity, the formulation must be hyperbolic and remains a challenge. Some preliminary discussion of these possible ways

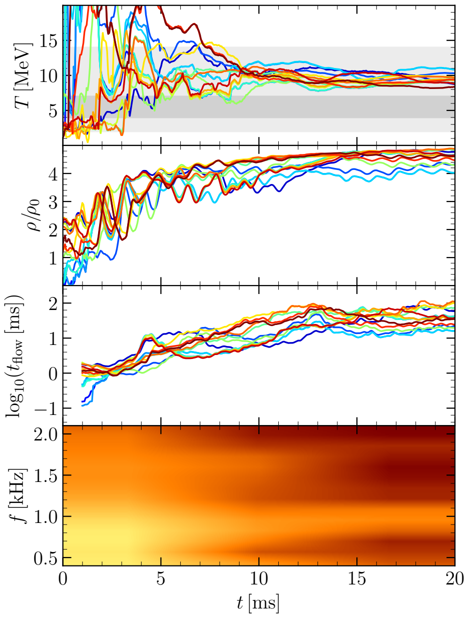

Figure 5.4: Co-moving time variation of physical properties of post-merger material from selected tracers in the same merger as shown in Fig. 5.3. Top panel: temperature [the shaded regions are where bulk viscosity is maximal, see Eq. (5.17)]. Second panel: rest-mass density. Third panel: flow timescale $t_{\rm flow}$. Bottom panel: spectrogram averaging the rest-mass density evolutions in the second panel.

forward can be found in [213].

Chapter 6

On r-process nucleosynthesis from matter ejected in binary neutron star mergers

In this chapter, the tracer method of Chapter 3 is used in the context of unbound material in the post-merger phase. Here, the tracers are used to study the origin of the heavy elements from the merger of merging neutron stars and the resulting kilonova that arises from the radioactive decay of these elements[1].

6.1 Introduction

The detections of gravitational waves from binary neutron stars [263] (BNS) and binary black hole mergers [262, 2, 266] by the LIGO/Virgo Scientific Collaboration has signals the beginning of the era of gravitational-wave astronomy and multi-messenger astronomy. In the coming years, additional detectors such as KAGRA and the Einstein Telescope (ET) [4, 136, 199] are coming online or projected for operation and will allow for a new observational window on the Universe, complementary to the electromagnetic one.

Equally exciting as the detection of gravitational waves, in addition there was a simultaneous detection of an electromagnetic counterpart [264, 148] alongside GW170817. This detection has provided a wealth of activity and provides compelling evidence to many long-standing puzzles such as short gamma-ray bursts (SGRBs) being produced from the merging of neutron stars[78, 184, 210, 36, 263,

---

[1] This chapter is based on the work of [44] where I was the first author. All figures in this chapter have been reproduced from [44]. My contribution to the work of [44] was to run all the simulations, analyse the data, generate all the figures, and write the text of the paper.

264]. Despite only a single neutron star merger being observed so far, more BNS mergers are expected to be observed in the coming years.

One type of electromagnetic counterpart from a merger that has recently received significant attention is that of a kilonova [146, 222, 196, 107, 194, 272, 123, 228, 201, 124, 229, 174, 258, 26, 219, 275]. Simply, a kilonova is an infrared/optical signal powered by the decay of a variety of heavy elements, with dominant contributions coming from the elements near the second r-process peak (i.e., ^{133}I, ^{132}Te and ^{133}Xe), and subdominant ones from the third r-process peak and unstable transuranian elements. Prior to GW170817, it was conjectured that kilonovas would be powered by ejecta from binary neutron star mergers, however evidence was scant with only GRB 130603B [37, 260], GRB 060614 [277, 122] and GRB 050709 [121], being thought to be connected to kilonovae, but even then, there are very large uncertainties in these measurement which had prevented an unambiguous identification. The detection of GW170817 definitively confirms that kilonova can arise from neutron star mergers, although the case of black hole - neutron star mergers remains unobserved, but still another possibility and source of kilonova.

As mentioned, the kilonova is powered by the heavy elements which are formed through a nucleosynthesis process known as r-process. The fundamental concept of r-process has been known for decades [52] but the precise role in astrophysics remained a mystery for quite some time. The problem is is that for matter to undergo r-process nucleosynthesis a very neutron-rich and explosive environment is required which severely restricts and constraints the potential astrophysical sites where the reactions could take place. The two most commonly suggested astrophysical sites core-collapse supernovae and BNS mergers. However, recent simulations of core-collapse supernovae (CCSN) have shown that the environment in the outer layers of the explosion is not neutron-rich enough and have been unable to reproduce the observed solar system abundances of heavy elements [117, 116, 83, 273], although rare forms of CCSN driven by magnetic fields are also a possibility [274, 179, 185], although this scenario requires fine-tuning. In contrast, neutron star mergers are considered an increasingly likely source of heavy elements. In addition to the direct evidence from the detection of a kilonova from GW170817, other recent evidence, such as observations ultrafaint dwarf galaxies [120], have strongly pointed towards BNS mergers being the main site of production of r-process elements.

Furthermore, increasingly sophisticated numerical-relativity simulations with neutrino transport have shown that not only significant amounts of material are ejected (due to a variety of physical processes) in BNS mergers, but the environment in the ejecta provides the necessary conditions to trigger and sustain robust r-process nucleosynthesis. Numerous simulations ranging from Newtonian to full relativistic, with a variety of microphysical treatments, have shown four broad ejection mechanisms. These are: dynamical ejecta [221, 209, 214, 137, 216, 31, 87, 114, 272, 228, 229, 201, 142, 68], neutrino-driven winds [67, 194, 123, 164, 163, 124, 181, 93], magnetically driven winds [237, 131, 245, 211, 59], and viscous evolution of the accretion disk [35, 172, 103, 82]. Their typical time scales are approximately $\sim 10\ \mathrm{ms}$ for dynamical ejecta, $\sim 100\ \mathrm{ms}$ for magnetically driven or neutrino-driven winds, and $\sim 1\ \mathrm{s}$ for viscous evolution. Due to the high computational cost of performing long-term fully relativistic simulations, mostly dynamical ejecta have been studied in full relativity, while other mechanisms have been the subject of mostly Newtonian simulations.

In this chapter, the investigation of dynamical ejecta from neutron star mergers is undertaken. This is done through a number of high-resolution numerical-relativity simulations of BNS mergers which investigate the effects of the neutron-star initial masses, mass ratios and most importantly the microphysical equation of state (EOS) on the resulting r-process nucleosynthesis. To this end, three fully temperature-dependent EOSs spanning a wide range of stiffness as measured from the stellar compactness, i.e., the ratio of the mass and radius of the corresponding nonrotating models are considered. For each EOS, three equal-mass initial setups covering a realistic range of initial BNS masses is evaluated with additional unequal mass cases.

To follow the evolution of the fluid, a combination of techniques are used, namely outflow detectors and passively advected fluid tracers, which were introduced in Chapter 3. This data is then used as input for the nuclear networks, which is done in a post-processing step using a complete nuclear reaction network [274, 133] to obtain the final r-process abundances. Additionally kilonova light curves are also computed using the model outlined in Ref. [107].

This chapter is structured as follows: in Sec. 6.2, the mathematical and numerical methods employed are introduced, together with the initial BNS configurations that are evolved. Section 6.3, instead, summarizes the main properties of the physical models and numerical techniques that are employed to study the BNS evolution as well as to recover the heavy-element abundances. Sections 6.4–6.5.4 present the results and findings of the simulations in terms of the mass ejected, the electron fraction, the specific entropy, and the ejecta velocity. Similarly, Secs. 6.7.4–6.8 reports the estimates of the kilonova light curves and their detectability, together with the constraints on the merger rates of BNSs.

6.2 Physical setup and initial data

In this chapter, unlike in previous chapters, both equal and unequal-mass mergers with quasi-circular orbits are considered. The initial data is constructed from three different initial EOSs, spanning a wide range in stiffness. These are, respectively,

Model	EOS	q	M_1 $[M_\odot]$	M_2 $[M_\odot]$	R_1 $[\,\mathrm{km}]$	R_2 $[\,\mathrm{km}]$	M_{ADM} $[M_\odot]$
`DD2-M1.25`	**DD2**	1.0	1.25	1.25	13.20	13.20	2.48
`DD2-M1.35`	**DD2**	1.0	1.35	1.35	13.23	13.23	2.68
`DD2-M1.45`	**DD2**	1.0	1.45	1.45	13.25	13.25	2.87
`DD2-q09`	**DD2**	0.9	1.22	1.35	13.19	13.23	2.55
`LS220-M1.25`	**LS220**	1.0	1.25	1.25	12.80	12.80	2.48
`LS220-M1.35`	**LS220**	1.0	1.35	1.35	12.75	12.75	2.67
`LS220-M1.45`	**LS220**	1.0	1.45	1.45	12.67	12.67	2.87
`LS220-q09`	**LS220**	0.9	1.21	1.35	12.81	12.75	2.61
`SFHO-M1.25`	**SFHO**	1.0	1.25	1.25	11.97	11.97	2.48
`SFHO-M1.35`	**SFHO**	1.0	1.35	1.35	11.92	11.92	2.68
`SFHO-M1.45`	**SFHO**	1.0	1.45	1.45	11.87	11.87	2.87
`SFHO-q09`	**SFHO**	0.9	1.22	1.35	11.97	11.92	2.55

Model	$M_{\mathrm{b},1}$ $[M_\odot]$	$M_{\mathrm{b},2}$ $[M_\odot]$	M_{TOV} $[M_\odot]$	R_{TOV} $[\,\mathrm{km}]$	$\mathcal{C}_1$ -	$\mathcal{C}_2$ -	J $[M_\odot^2]$
`DD2-M1.25`	1.35	1.35	2.42	11.90	0.140	0.140	6.40
`DD2-M1.35`	1.47	1.47	2.42	11.90	0.151	0.151	7.31
`DD2-M1.45`	1.59	1.59	2.42	11.90	0.161	0.161	8.19
`DD2-q09`	1.31	1.47	2.42	11.90	0.136	0.151	6.68
`LS220-M1.25`	1.36	1.36	2.04	10.65	0.144	0.144	6.42
`LS220-M1.35`	1.47	1.47	2.04	10.65	0.156	0.156	7.26
`LS220-M1.45`	1.60	1.60	2.04	10.65	0.169	0.169	8.20
`LS220-q09`	1.32	1.47	2.04	10.65	0.140	0.156	6.98
`SFHO-M1.25`	1.36	1.36	2.06	10.31	0.155	0.155	6.40
`SFHO-M1.35`	1.48	1.48	2.06	10.31	0.167	0.167	7.28
`SFHO-M1.45`	1.61	1.61	2.06	10.31	0.181	0.181	8.20
`SFHO-q09`	1.32	1.48	2.06	10.31	0.150	0.167	6.67

Table 6.1: Summary of the properties of the systems under consideration. The columns denote, respectively: the EOS; the gravitational mass ratio $q := M_1/M_2$ at infinite separation; the gravitational masses $M_{1,2}$ of the two stars at infinite separation; the stars' radii $R_{1,2}$ at infinite separation; the ADM mass M_{ADM} of the system; the baryon masses $M_{\mathrm{b},1,2}$; the maximum mass of a non-rotating model of the given EOS M_{TOV}; the radius of the maximum mass non-rotating model of the given EOS R_{TOV}; the compactnesses $\mathcal{C}_{1,2} := M_{1,2}/R_{1,2}$; the total angular momentum J at the initial separation.

from stiffest to softest: : (i) DD2 [269]; (ii) LS220 [140] with compressibility parameter $K = \mathrm{MeV}$; SFHO [249]. Note that recent calculations in Ref. [261] have shown that the LS220 EOS does not satisfy constraints stemming from a lower bound on the energy per nucleon provided by the unitary-gas approximation. This result disfavours the LS220 as a viable model for the microphysics of neutron stars, but since this EOS is also one of the most well-studied in numerical applications – as it was used as the prototypical EOS in the previous chapters – it is included in this study since it provides a useful comparison with the literature. Additionally, the DD2 and SFHO EOSs include additional light nuclei that are not included in the LS220 and these change the neutrino interactions [250] and the effects of which will be seen later.

For each EOS, there are three different equal-mass setups, with neutron-star gravitational masses of $1.25, 1.35$ and $1.45\,M_{\odot}$, respectively; and one unequal-mass system, with star masses of 1.2 and $1.35\,M_{\odot}$, resulting in a mass ratio $q = 0.9$ and a total ADM mass of the system which is intermediate between the two lightest equal-mass configurations for the same EOS. The stars' initial separation is chosen to be $45\,\mathrm{km}$, resulting in an inspiral phase of approximately $\sim$ 3 orbits. Table 6.1 summarizes the properties of each system. The stars initial states are computed at neutrinoless beta equilibrium, i.e., at zero neutrino chemical potential, thus setting the initial values of the electron fraction. The initial data for every binary was constructed using the `LORENE` pseudo-spectral elliptic solver [105] and refers to irrotational binaries in quasi-circular orbit.

6.3 Methods

Here, the methods used to evolve the simulations are briefly discussed. In terms of the evolution code, the same set-up described in Chapter 3 is used here. However, there are some additional technical details that must be discussed.

6.3.1 Tracer particles and outflow detectors

To follow the flow of ejected material two different techniques are used. The first technique is the use of tracer particles [272, 127, 175, 45], i.e., massless particles passively advected with the fluid as introduced in Chapter 3. Here a total of $2 \cdot 10^5$ tracers are placed with a uniform distribution in the density interval $10^7\,\mathrm{g/cm^3} \lesssim \rho \lesssim 10^{15}\,\mathrm{g/cm^3}$ at the time of merger. Fluid properties are interpolated at the tracers location, providing a detailed account of the evolution of the associated fluid element. From here, a "tracer mass" can be associated to the otherwise massless tracers by locally integrating a mass flux through a sphere of given radius. Combining this mass with the history of the evolution of the tracer particle provides the initial input for the nuclear-reaction network discussed in Sec. 6.3.3.

The second technique employed to follow the ejected material is the use of so-called outflow detectors, i.e., spherical surfaces placed at a fixed coordinate radius around the center of the computational domain. These detectors are able to measure the flux of the fluid through their surface and record the various hydrodynamical and thermodynamical quantities as a function of time. In the simulations here, a total of nine detectors set at radii between 100 and $500\,M_{\odot}$ with a separation of $50\,M_{\odot}$ were used. Each detector has a resolution of 55 points in the polar and 96 points in the azimuthal direction, and the detector located at a radius of $200M_{\odot} \approx 300\,\mathrm{km}$ is the fiducial one. As the fluid passes through a detector spherical surface, hydrodynamical and thermodynamical variables are interpolated onto it, allowing the measurement of the entire evolution of the fluid in all angular directions. Note that the total ejected mass is calculated by integrating the unbound mass flux over the surface of the detector, in contrast to, e.g., Ref. [114], where the rest-mass density of all unbound fluid elements is integrated over the whole computational domain (see Sec. 6.5.1 for further details).

6.3.2 Selection of unbound material

Although initially discussed in Chapter 3, the selection criteria will be repeated here for brevity. Regardless of whether tracer particles or outflow detectors are used, it is necessary to define a criterion to identify gravitationally unbound material, which will not accrete back onto the merger remnant and can be considered ejected from the system.

The difficulty in determining gravitationally unbound material arises mostly due to the finite size of the grid and ejecta can only be followed to the edge of the computational domain, which is still relatively close to the BNS merger product, and can still be influenced by its gravitational potential. In the context of r-process, this is a setback because the evolution of the nuclear network can be on the order of simulated years which is significantly larger than a domain in a numerical relativity can allow. Part of this problem could be alleviated by using a larger grid, but this comes at greater computational cost and a few numerical drawbacks ,e.g., poor resolution in an AMR grid, so a smaller grid spacing is used.

As introduced in Chapter 3, a criteria is needed to determine when material is unbound. The criteria most commonly used is that of the *geodesic criterion* [128, 228], i.e., if $u_t \leq -1$, where u_t is the covariant time component of the fluid element 4-velocity. In short, the criterion amounts therefore to imposing that the fluid element should have non-zero velocity at infinity. However, this isn't the only criterion that can be used to select whether or not material becomes unbound. An alternative criterion that has been used is the *Bernoulli criterion* [128]. Here, fluid element is defined to be unbound if $hu_t \leq -1$, where h is the fluid specific enthalpy. A reason for considering this criterion that is the enthalpy encodes some information about the thermodynamics of the fluid element, through the enthalpy, while the geodesic does not. In the case of the dynamical ejecta, the thermodynamical properties are important and hence using a criteria that takes these variables into account is desirable. A more thorough discussion of the influence of changing criteria will be done in Section 6.6.

6.3.3 Nuclear network overview

In order for the r-process to be calculated, the numerous reactions of the chemical elements must be calculated. A detailed introduction to this type of calculate can be found in [150]. The calculations here are done with the complete `WinNet` nuclear reaction network [274, 133]. In this network, over 5800 nuclei between the valley of stability and the neutron-drip line are taken into account. The reaction rates are taken from the compilation of Ref. [205] for the Finite Range Droplet Model (FRDM [177]) and weak-interaction rates including neutrino absorption on nucleons [178, 92] are also considered. Neutron-capture rates for nuclei with atomic number $Z \gtrsim 80$ and neutron-induced fission rates are taken from Ref. [189]. Additionally, beta-delayed fission probabilities from Ref. [188] are also included. The `WinNet` network has a long history and has successfully been used in the generation the abundance curves of heavy elements and agrees with other nuclear-reaction networks [150].

The motivating factor for the introducing the tracers into unbound material is that they record the thermodynamical properties of the fluid element cf. Chapter 3. It is in this nuclear network that these tracers are post-processed. In order to do the nuclear network evolution, every tracer records a time series of the rest-mass density, temperature, specific entropy, and electron fraction are used as initial data for the network. For each of these tracers, the calculations begin when the temperature drops below $T = 10^{10}\,\mathrm{K} = 10\,\mathrm{GK}$. Due to the high temperatures, the initial composition is given by nuclear statistical equilibrium (NSE), and is dominated by nucleons and alpha particles and it is assumed that NSE holds for $T \gtrsim 8$ GK. When the temperature drops below the NSE threshold, the composition is evolved with the full reaction network. As discussed numerous times, the limitations of numerical relativity require that the tracers be extrapolated forward in time to larger scales than can be currently simulated. This is done by following prescriptions for the position, density and temperature evolution given in [94, 133]. Specifically, these extrapolations take the form

$$r(t) = r_0 + v_0 t, \tag{6.1}$$

$$\rho(t) = \rho_0 \left(\frac{t}{t_0}\right)^{-3}, \tag{6.2}$$

$$T(t) = T\left[s, \rho(t), Y_{\rm e}(t)\right] . \tag{6.3}$$

where ρ is the total rest-mass density, r the coordinate radius, v the 3-velocity, s the specific entropy, and $Y_{\rm e} := n_{\rm e}/n_{\rm b}$ the electron fraction. The subscript "0" indicates the last available values from the hydrodynamical simulations, and the temperature is computed from the Helmholtz EOS [267, 268]. As discussed in Chapter 3, this extrapolation is well supported by the tracers.

6.4 Overview of simulations

In the following sections, the main results from the simulation that will be analysed and compared are the following major outflow properties: the mass ejected $M_{\rm ej}$, the electron fraction $Y_{\rm e}$, the specific entropy s, and the ejecta velocity $v_{\rm ej}$.

The variability of these quantities across different EOSs, and thus the r-process, is done through 12 simulations which span a wide range of masses and equations of state. For a given EOS, four different masses parameters were run with 3 equal-mass and 1 unequal-mass case. For each simulation, at least $10\ \rm ms$ after merger was simulated to ensure a sufficient time for the dynamical ejecta to reach $300\,\rm km$, which is where the properties of the dynamical ejecta are measured.

Prior to the merger of each BNS, at least $\sim$ 3 orbits are completed before merger and after these orbits, the merger time is defined to the time at which the gravitational-wave amplitude reaches its first peak [22], i.e., $t = 0$. For all mergers that do not immediately collapse to a black hole, a hypermassive neutron star (HMNS) is formed and exists in a metastable state, supported by differential rotation, as discussed in Chapter 4.

There are only three binaries which collapse to a black hole: `SFHO-M1.35`, `SFHO-M1.45`, and `LS220-M1.45` with the latter two being a prompt collapse. More specifically, for `SFHO-M1.45` the collapse is right at merger and results in very little material being ejected (see discussion in Sec. 6.5.1), while for `LS220-M1.45` the collapse takes place about $\sim 0.5\ \rm ms$ after merger, which is sufficient to allow for material to be ejected. Finally for `SFHO-M1.35`, the collapses to a black hole takes place at $\sim 10\ \rm ms$ after the merger, when the HMNS has lost sufficient angular momentum.

The first result from the simulations is the spatial distributions for the three different equations of state for two quantities, the electron fraction (left panels)

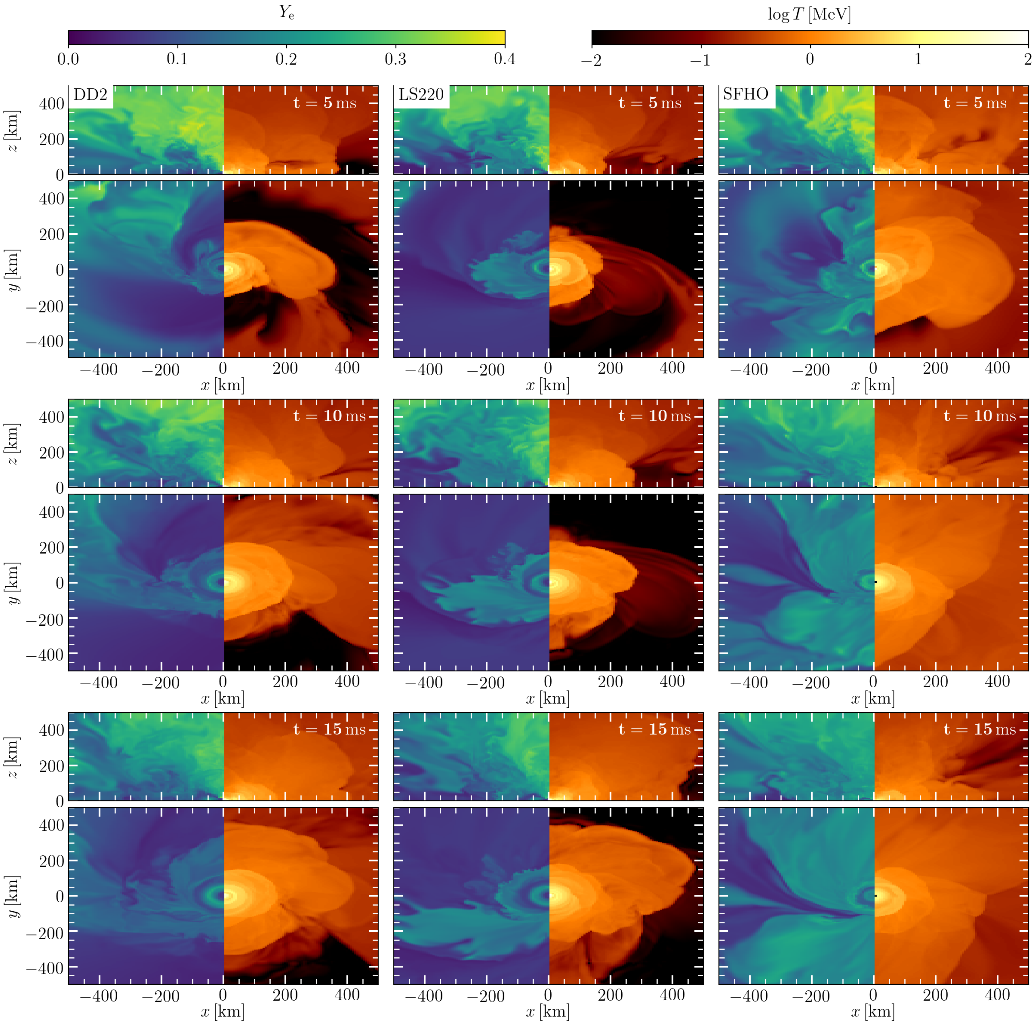

Figure 6.1: Evolution of the electron fraction (left parts of panels) and of the temperature (right parts of panels) on the (x, z) plane (top panels) and on the (x, y) plane (bottom panels), for the different EOSs, namely: DD2, LS220, SFHO, from left to right. All panels refer to binaries with masses of $2 \times 1.35 M_\odot$ and at the same representative times: 5 ms (top row), 10 ms (middle row), and 15 ms (bottom row) after the merger.

and temperature (right panels), illustrated in Fig 6.7.3. From top to bottom, the times correspond to $5, 10, 15$ ms after merger, while the top panels refer to the (x, z)-planes and (x, y)-planes in the bottom panels.

As expected, the figure illustrates the two different sources of dynamical ejecta: tidal forces and shock heating. Tidal forces arise from tidal interactions during merging and eject material primarily along the orbital plane and are a manifestation of gravitational interactions. In comparison, shock heating, is approximately spherically symmetric [228] and depends on the thermal properties of the fluid. These two distinct mechanisms are illustrated in Fig. 6.7.3 where the planar region shows lower Y_{e} and denser material, while the polar regions have higher Y_{e} and less dense material.

Consider first the tidal ejecta. Tidal ejecta tends to have very low electron fraction, i.e., it is very neutron rich. This material becomes unbound immediately during and after the merger and originates from near the surfaces of the star. These tidal tails are visible in the (x, y)-plane at 5 ms (top row) panels of Fig. 6.7.3, where the they have reached the outer regions of the simulation domain beyond $300\,\mathrm{km}$. Additionally, this ejected material also tends to be cooler, with a temperature of around 1 MeV. This can be contrasted with the (x, z)-plane where the Y_{e} reaches much higher values, approximately 0.3, that are do not occur in the (x, y)-plane. The reason for these highers value is due to shock heating, hence this material comes from the other sources of dynamical ejecta. In the polar regions right above the HMNS, no material is ejected tidally –due to the lack of torques along this axis – and thus alllows neutrinos to become free streaming very close to the merger product due to a lack of material that could potentially trap them, cf. the orbital plane. As a result, weak interactions play a more important role here and free neutrons are converted into protons, hence the material becomes less neutron-rich. However, as the angle from the pole decreases, the material becomes more optically thick and more neutron-rich as the neutrino interactions become less strong. This angular dependence is also seen in the temperature profiles as there are higher temperatures near the polar axis when compared with the orbital plane. It is important to note here that although neutrinos are only treated simplistically [95] this broad-brush description is qualitatively similar to more sophisticated approaches such as those using an M1-scheme which lead to an increase in the amount of ejected material in the polar regions [88, 86, 89, 228, 229] and higher Y_{e}.

Examining now the effects of the EOS, it is clear that there is an overall trend present in Fig. 6.7.3. Effectively, the “softer” an EOS is, the hotter the matter tends to be. This is because the softer an EOS is and hence the more compact the object is, a deeper gravitational well forms, which, in turn, allows for the material to become hotter as there more energy available. This dependence is clearest when

Model	$M_{\rm ej}$ $[10^{-3}\,M_\odot]$	$\langle Y_{\rm e}\rangle$ -	$\langle s\rangle$ $[\,{\rm k_B}/{\rm baryon}]$	$\langle v_{\rm ej}\rangle$ $[10^{-1}{\rm c}]$	$\langle v_\infty\rangle$ $[10^{-1}{\rm c}]$
DD2-M1.25	0.96	0.13	13.9	2.3	1.7
DD2-M1.35	0.58	0.14	16.5	2.4	1.8
DD2-M1.45	0.50	0.17	19.2	2.7	2.1
DD2-q09	0.46	0.14	18.5	2.3	1.7
LS220-M1.25	0.61	0.08	10.3	2.2	1.6
LS220-M1.35	0.82	0.10	12.7	2.2	1.5
LS220-M1.45	1.09	0.11	10.5	2.6	2.1
LS220-q09	0.90	0.09	11.9	2.2	1.5
SFHO-M1.25	0.55	0.14	15.6	2.5	2.0
SFHO-M1.35	3.53	0.16	12.7	2.7	2.2
SFHO-M1.45	0.01	0.24	35.9	3.1	2.6
SFHO-q09	0.76	0.16	18.8	2.4	1.8

Model	$t_{H,\rm peak}$ [days]	$L_{\rm peak}$ $[10^{40}\,{\rm erg/s}]$	$m_{J,\rm peak}$ [AB]	$m_{H,\rm peak}$ [AB]	$m_{K,\rm peak}$ [AB]
DD2-M1.25	0.50	2.24	-12.6	-12.5	-12.4
DD2-M1.35	0.50	2.44	-12.7	-12.7	-12.5
DD2-M1.45	0.50	2.89	-12.9	-12.9	-12.5
DD2-q09	0.53	2.34	-12.7	-12.6	-12.4
LS220-M1.25	0.53	2.24	-12.6	-12.6	-12.4
LS220-M1.35	0.51	2.00	-12.5	-12.4	-12.2
LS220-M1.45	0.48	2.62	-12.8	-12.7	-12.5
LS220-q09	0.50	1.94	-12.4	-12.3	-12.1
SFHO-M1.25	0.47	2.54	-12.8	-12.7	-12.5
SFHO-M1.35	0.53	3.36	-13.2	-13.2	-13.0
SFHO-M1.45	0.16	0.86	-11.1	-10.9	-10.5
SFHO-q09	0.60	2.92	-12.0	-13.0	-12.9

Table 6.2: Summary of the mass-averaged quantities of Sec. 6.5 and kilonova observational quantities of Sec. 6.7.4 computed from the simulations. The columns are, respectively: $M_{\rm ej}$ the dynamical mass ejecta measured at $300\,{\rm km}$, $\langle Y_{\rm e}\rangle$ the mass-averaged electron fraction, $\langle s\rangle$ the mass-averaged entropy, $v_{\rm ej}$ the mass-averaged velocity of the ejecta, $\langle v_\infty\rangle$ the velocity of the ejecta at infinity using Eq. (6.6), $t_{H,\rm peak}$ the peak time in the H-band of the kilonova signal, $L_{\rm peak}$ the peak luminosity of the kilonova, $m_{X,\rm peak}$ the peak absolute magnitude in the $X = J, H, K$ bands respectively.

comparing the softer SFHO and the stiffer LS220 EOSs (left and right columns)[2], where the temperature in the (x, y)-plane is much hotter for the SFHO than the LS220, as expected. As a result, because neutrino interactions depend on the temperature, the electron fraction is also higher the softer an EOS is. Again this is most clear when examining the fluid properties on the (x, y)-plane of the SFHO and LS220 simulations, where the data referring to the LS220 EOS is much more neutron-rich when compared with the SFHO.

6.5 Matter-outflow properties

6.5.1 Ejected-mass

An important quantity needed in all the following analysis is that of the total amount of ejected material originating from dynamical ejecta. This total mass has implications for the amount of r-process created, the type of signal a kilonova would produce, and constraints on the rates of neutron star mergers. In Sec. 6.3.1, the total ejected mass is defined as using outflow detectors which measure the flux of unbound material at a given radius. To do this measurement, the detector chosen will be placed at a radius of $M_{\odot} \approx 300\,\mathrm{km}$ and will be used as the fiducial detector to do the measurements. To compute the total mass ejected, the flux of the rest-mass density through the detector's spherical surface is computed and then integrated over the whole sphere. This gives the total mass-flux which can be integrated over time to provide a measurement of the total dynamically ejected material M_{ej}. In this calculation, only the flux associated to unbound fluid elements contributes to the integral. Explicitly, for a detector at a given radial distance, the total ejected mass is given by

$$M_{\mathrm{ej}}(t) := \int_0^t \int_{\Omega} \rho_* W(\alpha v^r - \beta^r)\sqrt{\gamma}_{\Omega} \mathrm{d}\Omega \mathrm{d}t' \,, \tag{6.4}$$

where $\sqrt{\gamma}_{\Omega}$ is the surface element on the detector (i.e., the square root of the 2-metric induced on the detector by the spacetime 4-metric); the term $\rho_* W(\alpha v^r - \beta^r)$ is the flux of mass through the sphere, expressed in terms of the 3+1 quantities: the lapse function α, the shift vector β^i, and the fluid 3-velocity v^i, the Lorentz factor $W := (1-v^i v_i)^{-1/2}$ and the fraction of the rest-mass density that is unbound ρ_*, i.e., of fluid elements that do satisfy the geodesic criterion. The integral of the mass flux can then be integrated in time beginning at merger, i.e., $t = 0$ and ending at T_f, the time at the end of the simulation.

---

[2] As discussed in Sec. 6.2, the inclusion of light nuclei changes the composition, but not the temperature.

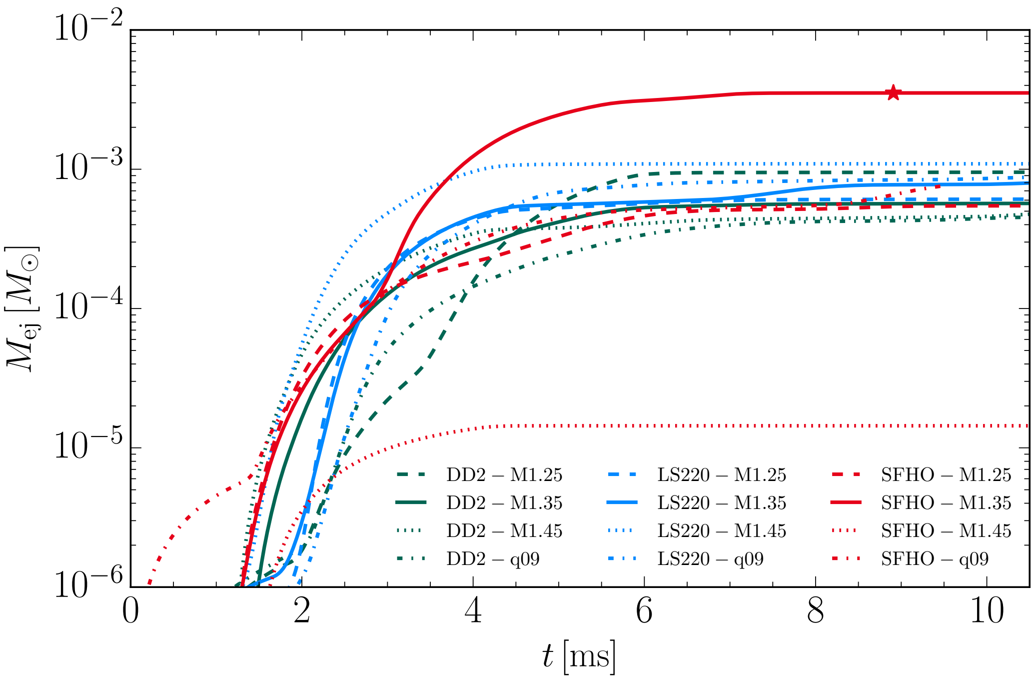

Figure 6.2: Evolution of the dynamically ejected unbound mass $M_{\rm ej}$ as measured through a detector at radius $300\,{\rm km}$ when using the geodesic criterion and for the various binaries considered. The star denotes the time of black-hole formation for model `SFHO-M1.35`. Binaries `LS220-M1.45` and `SFHO-M1.35` collapse shortly after merger and are not visible in the plot.

The results of this calculation are reported in Figure 6.2 for the different EOSs. Here, the colour coding scheme is LS220 (blue), DD2 (green), and SFHO (red) for the EOSs and the different lines styles correspond to different masses and mass ratios[3]. The results of Fig. 6.2 are also summarised in Table 6.2, where $M_{\rm ej}$ refers to the mass ejected $t = 10\ {\rm ms}$ after merger.

The results of the different EOSs and masses demonstrates that there is a very similar universal behaviour independent of the simulation set-up. Initially, there is a large ejection of material, due to tidal interactions and shock heating, and this ejecta reaches the detector approximately $1\ {\rm ms}$ after merger and continues for about $4-5\ {\rm ms}$. After this point, the apparent amount of material that becomes

---

[3] Unless specified otherwise, hereafter the same colour scheme to refer to the various EOSs will used throughout: simulations with the LS220 EOS are shown in blue, DD2 in green, and SFHO in red. Furthermore, the different masses are defined as follows, $1.25M_\odot$ is dashed, $1.35M_\odot$ is solid, $1.45M_\odot$ is dotted, and $q = 0.9$ is dash-dotted.

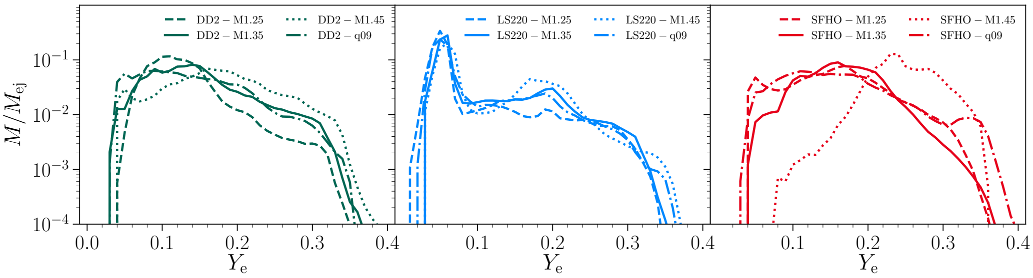

Figure 6.3: Distributions of the ejected mass fraction as function of the electron fraction $Y_{\rm e}$, as measured by a detector at radius $300\,{\rm km}$. The range of $Y_{\rm e}$ is divided into bins of width 0.01. The histograms are normalized over the total ejected mass $M_{\rm ej}$. The left panel refers to the DD2 EOS simulations, the middle one to the LS220 EOS and the right one to the SFHO EOS; different line types mark binaries with different masses and mass ratios.

approaches zero. However, this is simply a consequence of the criteria used to select the unbound material and will be shown in Section 6.6 that when considering another criteria more ejecta becomes unbound at later times.

A number that is almost independent for the simulations is the total amount of ejecta. As can be seen in Figure 6.2, the total amount of ejecta ranges between $0.5 - 1 \times 10^{-3} M_{\odot}$, with two table exceptions. The first is the binary `SFHO-M1.45`, which collapses immediately to a black hole and results in very little material ejected (almost an order of magnitude less), as most is accreted onto the black hole. Conversely, the binary `SFHO-M1.35` model ejects a significant amount of material when compared with the other models. Also this binary collapses to a black hole around $9\ {\rm ms}$ (see star symbol in Fig. 6.2). The reason for this increase in the amount of ejected material is due to the SFHO being a rather soft EOS, in relation to DD2 and LS220. A softer EOS creates more compact stars – the material is “softer” and can be compressed into a smaller area – which means high temperatures can be reached due to a stronger gravitational well, which in turn can cause higher temperatures and shock heating leading to a more forceful dynamical mass ejection.

The measurement given here is simply one method to measure the total amount of ejected material. However, it is not the only method of doing this measurement. For example it is possible to evaluate an integral of the rest-mass density over the entire computational domain, with a threshold on only unbound material [114, 228, 142, 69]. Mathematically, this is defined as i.e.,

$$M_{\rm ej}(t) = \int \rho_* W \sqrt{\gamma} {\rm d}^3 x. \tag{6.5}$$

To check the veracity of the masses measured in this study, Eq. 6.5 was computed for the `LS220-M1.35` model. Evaluating this integral yields a $M_{\rm ej}(t)$ that is highly time dependent and is no longer a monotonically increasing function of time, which is the only possibility for the Eq. 6.4 as it is a cumulative integral. Instead, this integral reaches a maximum of $M_{\rm ej} = 0.80 \times 10^{-3} M_\odot$ which is similar to the outflow detector measurement. Qualitatively, this measurement differs only by $4\,\%$ with that obtained via Eq. (6.4), demonstrating the robustness of the mass ejection method and that the $300\ {\rm km}$ measurement radius is the most robust choice. Although it appears that Eq. 6.5 would be a better measurement, it has some major downsides. Due to the finite size of the domain, material that reaches the outer boundaries, and hence "removed" from the simulation due to boundary conditions, will no longer be countered, which explains the non-monotonic behaviour. Furthermore, there is a question of when to evaluate Eq. 6.5 to get a proper measurement of the total mass of the system. Here, this was chosen as $\sim 3\ {\rm ms}$ after merger where it reaches a maximum and this is well before the material has had a chance to reach the outer domain of the simulation. With this choice, however, there is some level of arbitrariness in the evaluation of the integral as to what time is the most appropriate to report. Although the maximum appears to be the most natural, in cases where there is more ejecta at later times, earlier ejecta will not be counted in this summation as it has left the domain. This arbitrariness does not arise with the flux-integral method (6.4), which is integrated over all time, but instead the arbitrariness is selected in the radius chosen to measure. Using detectors further out finds that the difference between the sphere at $300\,{\rm km}$ and a sphere at $740\,{\rm km}$ is about 30% irrespective of EOS. Although the sphere further away has a slightly higher ejected mass, the properties of the fluid are very close to atmosphere at these radii and should be avoided so $300\,{\rm km}$ is a good compromise.

It is important to note that the measured values of the ejected masses are systematically smaller than those reported in Ref. [228] for the same masses and EOS. While this discrepancy appears troubling, it is most likely due to the neutrino treatment employed here. In Refs. [228, 229], a more-sophisticated M1-scheme with heating is implemented which can allow for material to be more energetic and hence to become more easily unbound [88]. On the other hand, the measurements here agree with those of Ref. [142], where a similar leakage approach was employed. The M0-scheme of Ref. [201] is insufficient t explain this difference in the ejected mass which suggests that a detailed study of the influence of neutrino schemes is required.

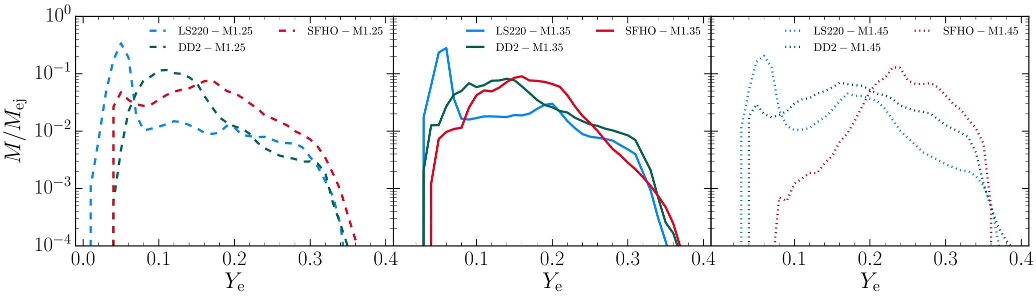

Figure 6.4: Distributions of the ejected mass fraction as function of the electron fraction $Y_{\rm e}$, as measured by a detector at radius $300\,{\rm km}$. This is the same as Fig. 6.3, except that the curves are here grouped by mass configuration rather than EOS so as to highlight the dependence on the latter. For clarity, unequal-mass binaries are not shown.

6.5.2 Electron-fraction distributions

To begin looking at the distributions, the first quantity is that of the electron fraction. This is a very important ingredient in determining the r-process nucleosynthesis yields since $Y_{\rm e}$ is effectively a measure of how many free neutrons are available. Typically, low-$Y_{\rm e}$ environments, i.e., with more free neutrons, favour a robust r-process and yield a higher fraction of heavier elements while in high-$Y_{\rm e}$ regimes, i.e., with less free neutrons, the production of very heavy elements tends to be suppressed. Differences in $Y_{\rm e}$ also correspond to potential differences in the properties of the resulting kilonova signal, due to the efficient production (or lack thereof) of high-opacity elements such as lanthanides. In particular, the so-called “blue” kilonovae (i.e., peaking at higher frequencies, in the optical band) are possible in environments with $Y_{\rm e} \gtrsim 0.25$ and “red” kilonovae (peaking in the infrared) in environments with $Y_{\rm e} \lesssim 0.25$ [174, 168]. The effect on the kilonova light curve will be discussed in Section 6.7.4.

Figure 6.3 plots the histograms of the mass distribution of the ejected matter over the electron fraction for all 12 simulations, as computed from the data relative to the fiducial detector at radius $300\,{\rm km}$. Here, different panels refer to different EOSs, while the various lines refer to the different binaries evolved with the same colour and ordering scheme introduced above. To calculate the above histogram, each patch on the outflow detector sphere measures the local electron fraction value is and the mass flux, from which the ejected mass is determined. These values are then integrated over time up to T_f to produce the mass ejected along with the corresponding $Y_{\rm e}$; the resulting $Y_{\rm e}$ range is divided into bins of width 0.01

and the unbound mass of each patch at each time is assigned to a bin according to its corresponding value of Y_e, thereby generating the histograms shown in Fig. 6.3.

Irrespective of the EOS and mass configuration of the runs, common qualitative features emerge. For all EOSs, the ejected mass is distributed in a range of Y_e varying from approximately 0.04 up to 0.4, peaking at $Y_\mathrm{e} \lesssim 0.2$. The only exception is the `SFHO-M1.45` model, which ejects little material due to black hole formation and whose distribution peaks at higher values of Y_e. This spread of the electron fraction over a wide range is due to the inclusion of a neutrino treatment, which causes the number of electrons to change due to weak interactions. Failure to take such interaction into account would result in a very different distribution, sharply peaked at very low values of Y_e, i.e., pure neutron matter (see, e.g., Ref. [201]).

More in detail, the LS220 runs (left panel) exhibit very similar distributions for all mass configurations, peaking at approximately $Y_\mathrm{e} = 0.05$ with a secondary peak at $Y_\mathrm{e} \approx 0.2$ before sharply dropping off at electron fraction values of $Y_\mathrm{e} \gtrsim 0.3$. The distributions of the DD2 (middle panel) also all exhibit a similar behaviour, with a sharp increasing at $Y_\mathrm{e} \sim 0.05$ before broadening out with a sharp drop around $Y_\mathrm{e} \sim 0.3$. Finally, the distributions of the SFHO runs (right panel) exhibit a somewhat different behaviour, although spanning a similarly broad range in Y_e. The main differences in this case are the tail of the distribution at higher values of the electron fraction. In all cases, most of the ejected matter is found at low values of the electron fraction, i.e., it is very neutron-rich, which suggests a robust r-process in all of the cases considered here.

This conclusion is also supported by Table 6.2, where the average values $\langle Y_\mathrm{e} \rangle$ of the electron fraction are reported for all 12 runs. The averages are computed over the mass/electron fraction histograms of Fig. 6.3. As can be seen in all simulations, the average value of the electron fraction in the ejecta is approximately 0.15 or lower, indicating on average a very neutron-rich environment. The only exception is model `SFHO-M1.45` where $\langle Y_\mathrm{e} \rangle = 0.24$.

In Fig. 6.4, to help the comparison of the results across different EOSs the distributions are arranged according to the total mass of the BNS (the unequal-mass cases are excluded) instead of EOS in Fig. 6.3. In all panels, there is a noticeable trend in the distributions of Y_e, which is most evident in the $1.25 M_\odot$-case (left panel), where $\langle Y_\mathrm{e} \rangle = 0.08$, 0.13, and 0.14 for LS220, DD2, and SFHO EOSs, respectively. This increase in Y_e is expected when considering that neutrino interactions depend strongly on the temperature. The average entropy (see Sec. 6.5.3) of these simulations is 10.3, 13.9, and $15.6\ \mathrm{k_B/baryon}$ respectively. Entropy is related to temperature and the higher the entropy, the higher the average temperature, cf. Fig. 6.3, and hence more free neutrons are converted into neutrinos through positron capture, increasing Y_e.

This effect is also related to the compactness of the object, albeit this relation

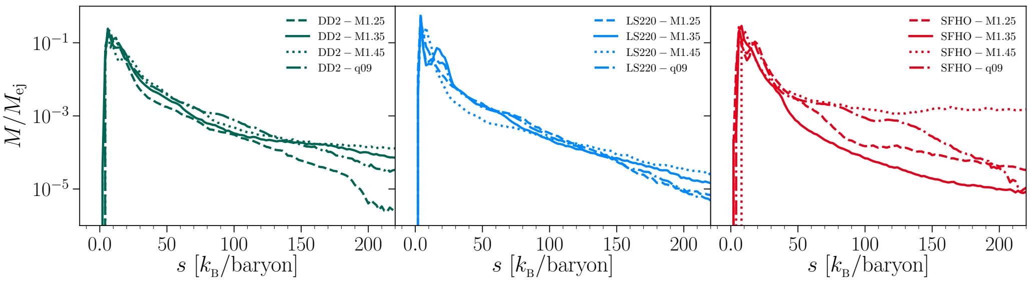

Figure 6.5: The same as in Fig. 6.3 but for the specific entropy s. The range of s is divided into bins of width $2\ \mathrm{k_B/baryon}$ and the histograms are normalized over the total ejected mass.

should be treated carefully. SFHO is the softest EOS, which leads to the most compact objects. This results in higher temperatures during the merger, which causes an increase in the neutrino reactions, which decreases the number of neutrons and as expected has the highest average $Y_{\rm e}$. In contrast, from Table 6.1 one would expect that because LS220 is more compact than DD2, LS220 should have a higher average $Y_{\rm e}$ and entropy when the opposite is this the case. This difference is due to compactness being a property calculated for cold beta-equilibrium where the effects of composition are minimal. As discussed in Sec. 6.2, the LS220 does not include light nuclei which can change the composition and the neutrino interactions so this seemingly non-monotonic relation between compactness and average $Y_{\rm e}$ arises from different constructions of the EOS. When comparing DD2 and SFHO and excluding LS220, there is a clear monotonic relationship between $\mathcal{C}$ and $Y_{\rm e}$.

When comparing the results of the above simulations with that of simulations with similar initial data, there is a disagreement with computed values of the electron fraction. For example, for the `DD2-M1.35` model with the measured value of $\langle Y_{\rm e}\rangle = 0.14$, the authors of Ref. [228] report $\langle Y_{\rm e}\rangle = 0.29$ with an M1-scheme independent of resolution and $\langle Y_{\rm e}\rangle = 0.26$ with a leakage scheme with a resolution of 200 m. However, a similar distribution in $Y_{\rm e}$ is observed in Refs. [187, 142], which use a similar leakage scheme to the one used here.

6.5.3 Specific-entropy distributions

The next thermodynamic quantity to be considered is the distribution of the ejected material over the entropy per baryon s. The specific entropy is important in r-process nucleosynthesis as it impacts the neutron-to-seed ratio, with high initial neutron-to-seed ratios favouring the production of heavy nuclei during the r-process nucleosynthesis even at relatively high electron fractions. In particular, in radiative environments such as those accompanying the ejected matter, the specific entropy will scale with the temperature as $s \propto T^3$, so that the shock-heated (and hotter) part of the dynamical ejecta will exhibit higher entropies. In turn, because the seed nuclei will be photodissociated at high temperatures, a higher specific entropy will increase the neutron-to-seed ratio and thus r-process nucleosynthesis. In contrast, the cold, tidal dynamic ejecta, and which dominates the unbound matter in Newtonian simulations, (see, e.g., Refs. [91, 221, 218]) usually exhibit low entropy, but extremely neutron-rich material [133]. The distributions of the specific entropy computed with the same procedure as the electron fraction distribution in the previous section, is shown in Fig. 6.5, while the average values $\langle s\rangle$ are reported in Table 6.2.

Again, many EOS-independent qualitative features are observed. First, for all EOSs, the mass distribution peaks at $s \approx 2\ \mathrm{k_B/baryon}$, while a fast decay is visible towards higher entropies. In the case of the binaries with the DD2 EOS (middle panel), the qualitative behaviour of different mass configurations is similar up to approximately $s \simeq 100\ \mathrm{k_B/baryon}$. At larger entropies, the `DD2-M1.25` binary has a more rapid drop-off and there is very little material that reaches higher entropies. In comparison, the remaining models exhibit similar behaviour with a flattening of the curve at higher entropies. The average entropy value is in all four cases $\langle s\rangle \approx 15\ \mathrm{k_B/baryon}$. Second, all of binaries with the LS220 EOS (left panel), show a very similar qualitative behaviour among themselves and strong analogies with the DD2 binaries. In particular, the distributions show a rapid increase in entropy at around $2\ \mathrm{k_B/baryon}$ (for the $1.45 M_\odot$ binary this peak is at around $8\ \mathrm{k_B/baryon}$ and is 4 times smaller), with an additional second peak at $20\ \mathrm{k_B/baryon}$ for the $1.35 M_\odot$ case that is not present in the other masses. For all masses, there is a rapid decrease in specific entropy, with average entropies that are slightly lower than the DD2 and SFHO binaries and with a smaller spread between the values, being approximately $s \sim 11\ \mathrm{k_B/baryon}$.

Finally, the simulations with binaries having the SFHO EOS (right panel) show a similar qualitative behaviour with the other runs, at least at low entropies. The distributions peak at about $5\ \mathrm{k_B/baryon}$ and a rapid drop follows, although different binaries show different fall-offs at around $50\ \mathrm{k_B/baryon}$. In the `SFHO-M1.25` case, the distribution begins to decrease less rapidly at higher entropies while the `SFHO-M1.35` model shows the fastest decrease. This is in contrast to the DD2 and LS220 simulations (where the specific entropies correlate with the initial masses of the stars) and is reflected in the average values of the specific entropy, with the `SFHO-M1.25` model having $\langle s\rangle = 15.6\ \mathrm{k_B/baryon}$, while `SFHO-M1.35` a smaller value of $\langle s\rangle = 12.7\ \mathrm{k_B/baryon}$. Lastly, The average specific entropy of the `SFHO-M1.35` binary is almost twice as large, likely due

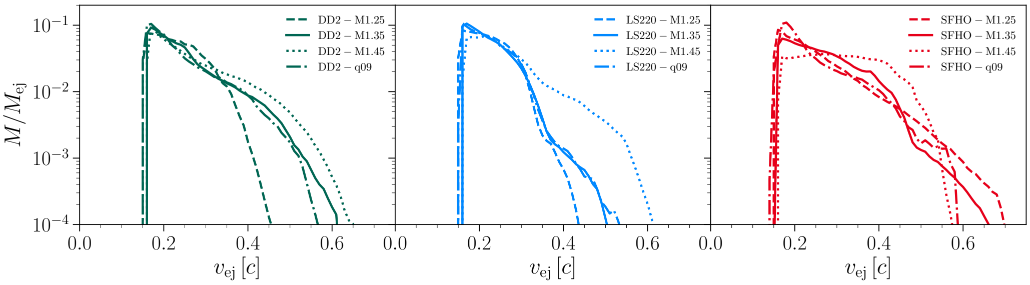

Figure 6.6: The same as in Fig. 6.3 but for the ejecta velocity $v_{\rm ej}$. The range of $v_{\rm ej}$ is divided into bins of width 0.05 and the histograms are normalized over the total ejected mass.

to the fact that the small amount of ejected matter has been efficiently heated on account of its rarefaction. While somewhat puzzling, this non-monotonic behaviour of the specific entropy with the SFHO binaries is likely due to the comparative softness of this EOS, which enhances the nonlinearity associated with shock-heating effects.

Indeed, as with the electron-fraction distributions, the average entropy tends to increases with the softness of the EOS[4], being the highest for the softest EOS, i.e., SFHO. For example, concentrating on the $1.25 M_\odot$ binaries, $\langle s \rangle = 10.3,\ 13.9,\ 15.6\ \mathrm{k_B/baryon}$, for the LS220, DD2, SFHO EOSs, respectively. This dependence is not particularly surprising as softer EOSs produce a higher temperature and the temperature is directly related to the specific entropy. This relation holds for almost all cases, even when including the low-mass ejecta of `SFHO-M1.45`; the only exception is offered by the `SFHO-M1.35` binary, where this discrepancy is likely due to there being at least 5 times as much ejecta as the other binaries.

6.5.4 Ejection-velocity distributions

Figure 6.6 reports the velocity distributions of the ejecta computed in full analogy with the electron-fraction or specific-entropy distributions presented in the previous two sections. Note that unlike, e.g., Ref. [201], here the velocity of the ejected material $v_{\rm ej}$ as measured in the simulation and that of the ejecta at spatial infinity $v_{\rm inf}$ are distinguished. In particular, $v_{\rm ej}$ is computed directly from the Lorentz factor W, i.e., $v_{\rm ej} = [(W^2 - 1)/W^2]^{1/2}$, where it is assumed that the detectors are are sufficiently far away from the merger product so that the Minkowski metric

---

[4] Taking into consideration the caveats at the end of Section 6.5.2.

holds. As discussed in Chapter 3, this is a rather good approximation since it was shown there that the ejected matter moves essentially radially and there is only a subdominant velocity component in the angular directions, hence $v^2 \approx v_r^2$, which enables the computation of $v_{\rm ej} \simeq v^r$ from W. An obvious consequence of distinguishing between $v_{\rm ej}$ and $v_{\rm inf}$ is that the values of the ejecta velocities here are systematically higher than in Ref. [201].

Again, Fig. 6.6 reveals that every simulation exhibits similar qualitative behaviour. The ejecta velocity is never lower than $0.15\,c$; the bulk of the matter has velocities of $v_{\rm ej} \approx 0.25\,c$, and at higher velocities of $v_{\rm ej} \gtrsim 0.6\,c$ the mass distribution quickly drops to zero. Table 6.2 reports the average velocity $\langle v_{\rm ej}\rangle$ for all the runs. A trend clearly emerges from the data, with the higher-mass configurations systematically producing higher-ejecta velocities. More precisely, the ejecta velocity appears to be tightly correlated with the compactness of the neutron stars involved in the merger (cf. Table 6.1). Also in this case, this trend is not particularly surprising since higher-mass configurations result in more compact starts, which in turn experience stronger torques and more efficient shock heating.

In Table 6.2, the column denoted by $\langle v_\infty\rangle$ shows estimates of the ejecta velocity at infinity, which is achieved in the homologous expansion phase. This velocity is used in the approximate model of kilonova emission (see Sec. 6.7.4) and is computed assuming a ballistic radial motion from $r = 300$ km to infinity in the spherically symmetric gravitational field of an object with the same ADM mass of the BNS system under consideration, i.e.,

$$\sqrt{1-\frac{2M_{\rm ADM}}{r}}\frac{1}{\sqrt{1-\langle v_{\rm ej}\rangle^2}} = \frac{1}{\sqrt{1-\langle v_\infty\rangle^2}}\,. \tag{6.6}$$

In the Newtonian limit, $M_{\rm ADM} = M$ and expression (6.6) simply reduces to the familiar energy conservation equation: $\frac{1}{2}\langle v_{\rm ej}\rangle^2 - GM/R = \frac{1}{2}\langle v_\infty\rangle^2$.

6.6 Comparison of criteria for unbound material

As discussed in Sec. 6.3.2, the main criteria used here is that of the geodesic criteria and hence in sections 6.4–6.5.4 only geodesically unbound material is considered. The reason for using such a criteria is that it is simple and doesn't assume anything about the EOS or the material, just that it if it has $u_t \leq -1$ it is unbound. Additionally, it is useful as it sets a lower bound for the total amount of ejecta when considering other more generic criteria. As will be seen below, when considering the Bernoulli criteria, which has the additional benefit of, through the enthalpy h, taking into account things like shock cheating. However, because the enthalpy is always $h \geq 1$ this means that material with the same rest-mass

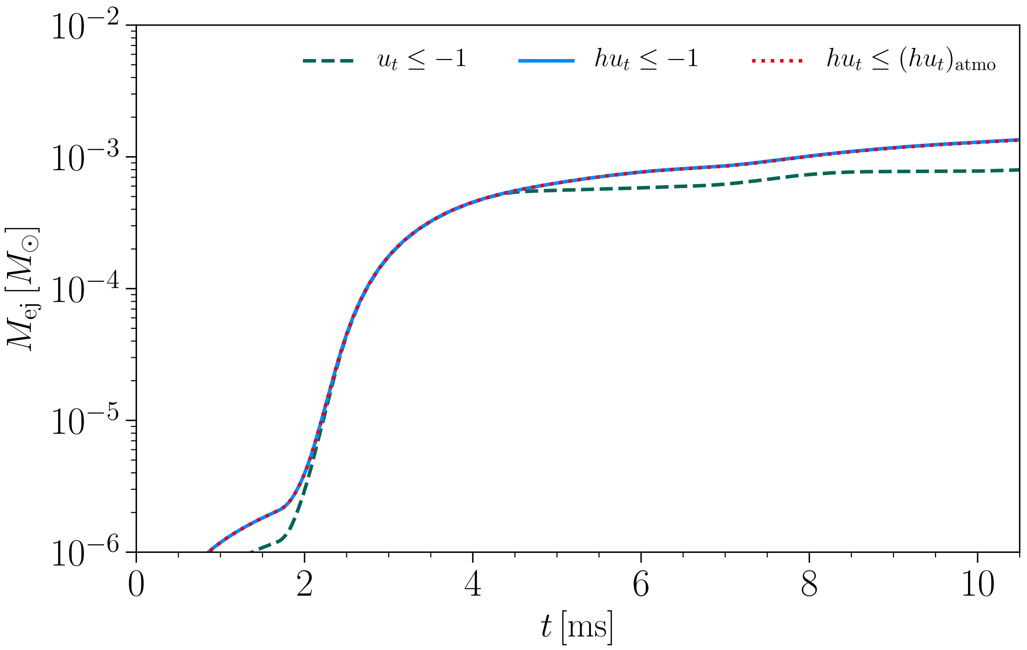

Figure 6.7: Mass ejection according to different unboundness criteria for the `LS220-M1.35` model. In green is the geodesic criterion, blue is the original Bernoulli one, and red is the modified Bernoulli thresholded on the atmosphere value. All values have been measured through a detector at $300\,\mathrm{km}$.

density, temperature, and electron fraction, can be unbound or bound depending on the EOS through the Bernoulli criterion while being unbound according to the geodesic criteria, independent of the EOS. This is a relatively minor trade-off since through the introduction of the enthalpy, the effects of pressure and temperature are taken into account which, intuitively, can make material more unbound.

More explicitly, it follows that

$$|h\, u_t| \geq |u_t|\,, \tag{6.7}$$

and thus the Bernoulli criterion will always result in more material becoming unbound. However, a slight modification of this formula is required. In the above simulations, there is an atmosphere – see discussion in Chapter 2 – which sets a lower bound for the hydrodynamical quantities. As discussed in Sec. 6.5.1 the dynamical ejecta is evaluated at a distance of $300\,\mathrm{km}$ away from the merger remnant to avoid atmospheric effects. But due to the introduction of the enthalpy, it needs to be ensured that the fluid is sufficiently above the atmosphere to avoid unphysical atmosphere values entering the calculations. To achieve this, instead

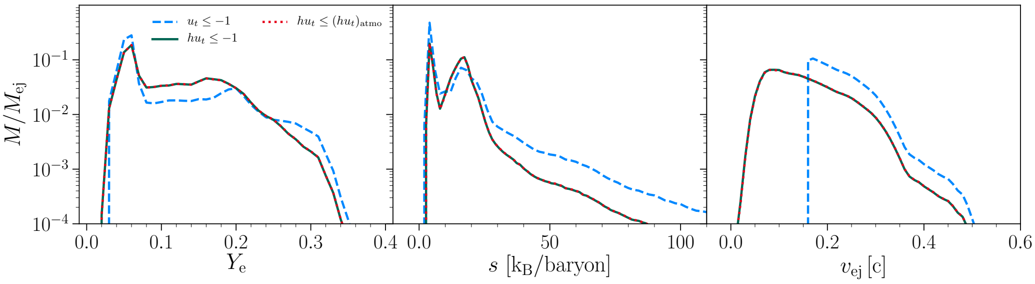

Figure 6.8: Comparison of the mass distribution of electron fraction, specific entropy and ejecta velocity in the ejected matter of the representative model `LS220-M1.35` for the three unboundedness criteria.

of defining unbound elements as satisfying the relation $hu_t \leq -1$, the following modified criterion is considered

$$h\,u_t \leq (h\,u_t)|_{\rm atmo}\,, \tag{6.8}$$

where atmo refers to values set by the atmosphere, which is EOS-dependent. For example, for the LS220 EOS this takes the value[:

$$h\,u_t \leq -1.000163\,, \tag{6.9}$$

instead of -1. Even though this difference is small, the modified constraint does exclude some material from being considered as ejected.

To evaluate the change in quantities that a change in criterion brings, the comparison will be done with the fiducial case of the `LS220-M1.35` model. This compraison is illustrated In Fig. 6.7, where the differences between the three selection criteria in the mass ejection curve are plotted. Overall, the general behaviour for the different criteria is similar, with an ejection phase beginning approximately $2\ \rm ms$ after merger followed by a decrease in the amount of ejected mass. While the geodesic-selected material approaches a constant value, both Bernoulli criteria show a slightly longer increasing phase before settling to a constant. In Table 6.3, the comparison of the ejected material for the three criteria is shown and it is found that by selecting one of the Bernoulli criteria, approximately 2.5 times as much ejected material when compared to the geodesic one is obtained. This increase in the amount of ejecta is similar across all simulations performed: the ejected mass is larger by a factor 1.5 to 4 with the Bernoulli criterion as compared with the geodesic one.

In Fig. 6.8, the mass distribution in the ejecta of the various quantities relevant for r-process nucleosynthesis, again for the representative `LS220-M1.35` model

Criterion	$M_{\rm ej}$ $[10^{-3}\,M_\odot]$	$\langle Y_{\rm e}\rangle$ -	$\langle s\rangle$ $[\,{\rm k_B/baryon}]$	$\langle v_{\rm ej}\rangle$ $[10^{-1}{\rm c}]$
`geodesic`	0.82	0.10	12.3	2.2
`Bernoulli`	2.09	0.11	13.8	1.5
`modified Bernoulli`	2.07	0.11	13.1	1.5

Table 6.3: Average values of the ejected mass, electron fraction, specific entropy and ejecta velocity for different unboundedness criteria in the representative `LS220-M1.35` model.

is plotted. Additionally, the average values are summarized in Table 6.3. For the electron fraction and entropy, there is not so much a drastic change in comparison with the geodesic critera and the overall structure of the distribution between different criteria is similar. In both cases however, there is a slight increase in entropy and $Y_{\rm e}$ which is to be expected. This is because there is more overall ejecta with which to bin and becaues this material tends to be shock heated, i.e., with higher enthalpies, it shifts these averages to higher values. However, even with this change, the effects are minimal and the overall nucleosynthesis process will be essentially unaffected.

Finally, the most striking difference is in the $v_{\rm ej}$ quantity. In the geodesic criteria, interpreted in its Newtonian limit, a fluid element has to have non-zero velocity at infinity to be considered unbound. This implies a lower cutoff in the velocity distribution, as slowly moving elements, even though able to cross a given detector surface, would not be considered unbound. For both Bernoulli criteria this strict requirement is relaxed by the presence of the enthalpy, which acts as a multiplicative factor larger than one. This means that even slowly moving elements, provided they have sufficiently high enthalpy, would be counted as unbound, and so the velocity distribution acquires a lower end tail and its mean is shifted towards lower values.

6.7 r-process nucleosynthesis

6.7.1 Tracer-input comparison

In Chapter 3 the concept of assigning a “mass” to the tracers was introduced. Here, two new additional tracer-selection criteria (together with the unboundness criterion already discussed and which is always enforced) and the corresponding procedures to associate a mass to the tracers are introduced and evaluated based on the final nucleosynthesis yields.

The first criterion, introduced in Sec. 6.3.1, consists of considering all unbound tracers and assigning a mass to each of them following the procedure in Chapter 3. Then, each tracer is put through the nuclear network and a abundance curve is produced. Then when all the tracers have been evaluated in this way, each curve is weighted based on the "mass" that has been assigned to it producing a weighted average of the final abundance. This curve represents the total tracer abundance and to obtain observed values, simply multiplied by the total ejected mass measured by the detectors. For example, in the cases considered here, roughly $40,000$ tracers are unbound and each is put through the nuclear network. The advantage of this method is that every single unbound tracer is used producing very robust statistics, however the trade-off is that it is computationally very expensive. To get around this computational trade-off two alternative weighting schemes are proposed.

The first alternative weighing scheme is to selected the tracers based on the Y_e histograms discussed in Sec. 6.5.2. That is, one tracer from each Y_e bin of width $\Delta Y_\mathrm{e} = 0.01$, is selected, resulting in about 40 tracers for each simulation, a reduction of a factor of a thousand compared with the previous method. The reason for selecting tracers this way is that the electron fraction plays an important role in creating different types of elements, with, for example, higher electron fractions creating lower mass-number elements and thus similarly valued electron fractions will created similar abundance curves. In this approach a mass is then associated to each tracer by assigning to it the mass of the bin it was drawn from taken directly from the outflow detector. This procedure is referred to as the "1D" criterion, since the tracers are drawn from a 1D distribution.

The other criterion to consider is essentially a better improved version of the 1D criterion, except it also smaples in the entropy bins. Thus tracers are selected from every entropy and electron fraction bin, and the associated mass in that bin from the outflow detector is used to assign masses. In this case, this results in roughly 1000 tracers being selected. This criterion is called the "2D" criterion.

The comparison of these three methods of selection are illustrated in Fig. 6.9 which displays the resulting nucleosynthesis yields. Again, the fiducial binary `LS220-M1.35` is used. Additionally, the abundance pattern of the solar system is also plotted (filled circles) . As can be seen, the original approach of considering all unbound tracers reproduces quite well the solar abundances over the whole range of mass numbers considered, as does the 2D criterion. The 1D criterion instead shows significant deviations, especially around the third peak (i.e., $A \simeq 195$) and around the rare-earth peak (i.e., $A \simeq 165$). A posteriori, this is due to the fact that the 1D criterion is systematically biased towards low-entropy tracers, which has a significant impact over the final abundances.

Thus, the 2D criterion is computationally much less expensive than considering all unbound tracers as it allows for a simple and unambiguous definition of the

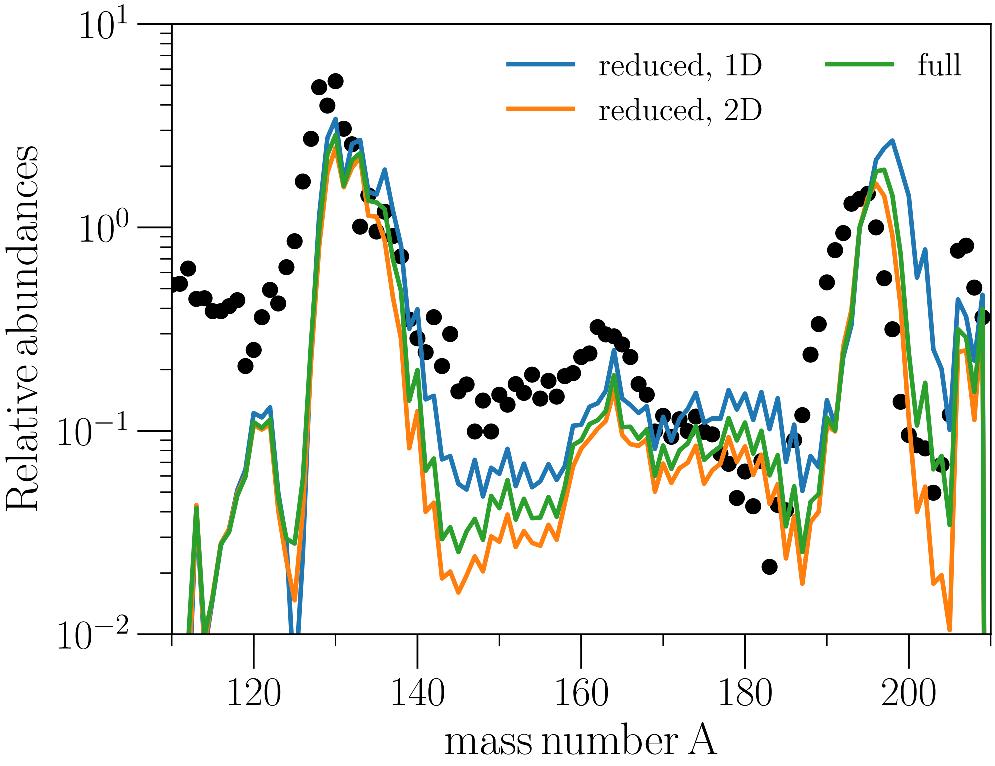

Figure 6.9: Comparison of the relative abundances Y_i of the r-process as function of the mass number A for the three tracer selection criteria. In blue, the abundances produced by the "1D" criterion; in orange the ones produced by the "2D" criterion; in green the abundances obtained considering all unbound tracers. The black filled circles indicate the solar abundances.

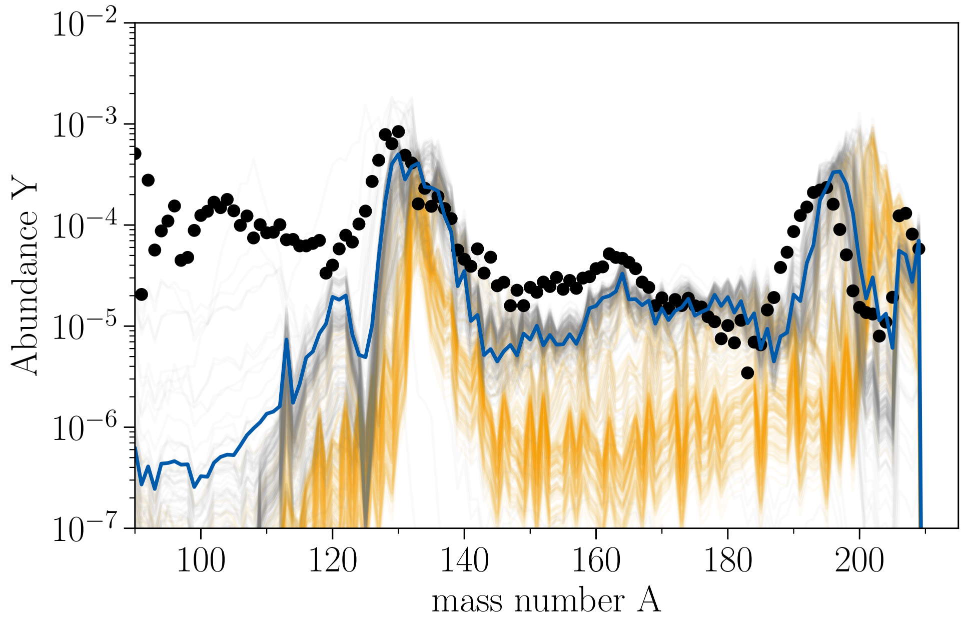

Figure 6.10: Final r-process abundances for all unbound tracers of the `LS220-M.1.35` binary. Gray lines are the yields for individual tracers with low entropies $s < 70\ \mathrm{k_B/baryon}$, and orange lines mark single tracers with high entropies $s \geq 70\ \mathrm{k_B/baryon}$. The mass-integrated nucleosynthesis yields are shown with a blue line, and the black filled circles show the solar abundances.

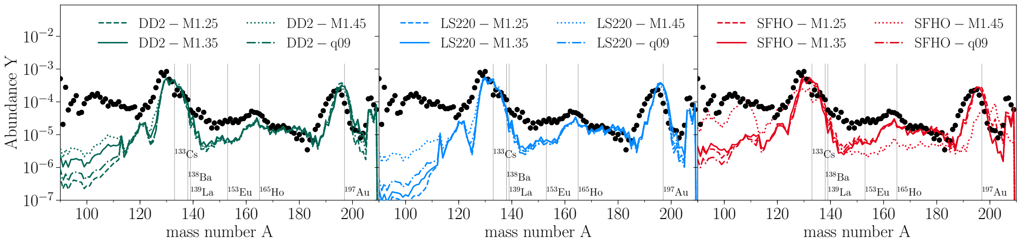

Figure 6.11: Final relative heavy-elements abundances for all the 12 BNS models as a function of mass number A. The abundances are normalized so that the total mass fraction is unity, while the different panels and lines refer to the various EOSs, masses and mass ratios, respectively (see legends). The black filled circles report instead the observed solar abundances, while the vertical lines mark a few representative r-process elements: ^{133}Cs, ^{138}Ba, ^{139}La, ^{153}Eu, ^{165}Ho, ^{197}Au.

tracer mass, and yet it leads to an almost unbiased abundance calculation. In the following, the 2D criterion presented here for tracer selection is adopted and all following results are computed with it, unless otherwise stated.

6.7.2 Heavy-element nucleosynthesis

To illustrate how the different entropies contribute to the overall abundance pattern, Figure 6.10 illustrates the nucleosynthesis results for all $\sim 40{,}000$ unbound tracers of the representative simulation of the `LS220-M.1.35` binary. In particular, the individual tracers with $s < 70\ \mathrm{k_B/baryon}$ are plotted in gray or if $s \geq 70\ \mathrm{k_B/baryon}$, then in orange, respectively, alongside the mass-integrated abundances (blue line). As a consequence of the relatively low electron fractions for most of the ejecta (i.e., with $Y_\mathrm{e} \approx 0.1$; see Fig. 6.3 and Table 6.2), for each tracer, the strong r-process component (from the second to the third r-process peak) is well reproduced.

The entropy distribution also gives rise to specific features in the abundance pattern. For example, the low-entropy component, i.e., $s < 70\ \mathrm{k_B/baryon}$, leads to the pattern that are observed in neutron-rich ejecta of Newtonian simulations. In contrast, the high-entropy (i.e., $s \geq 70\ \mathrm{k_B/baryon}$) part of the ejecta, which carries only about $6\,\%$ of the total ejected mass, has a nucleosynthesis pattern with a shifted second and third peaks. This exhibits diminished abundances in the rare-earth region, and effectively fills the gap between third r-process peak and elements in the lead region. This ejecta is similar to the "fast" ejecta found in Ref. [167]. However in contrast to this work, the ejecta here do not move as fast and their unusual abundance distribution is due to extremely high initial neutron-to-seed ratio with the value of $Y_\mathrm{n}/Y_\mathrm{seed} \gtrsim 1{,}000$. This low seed ratio, combined with comparably low initial densities $\rho \lesssim 10^9\,\mathrm{g/cm^3}$ requires substantially more time to incorporate the neutrons, delaying the freeze-out time (i.e., the time when $Y_\mathrm{n}/Y_\mathrm{seed} = 1$). In fact, the time window for the r-process to occur in this minority of ejected material is $\gtrsim 100\,\mathrm{s}$ instead of $\lesssim 1\,\mathrm{s}$. Moreover, the r-process runs along a path much closer to the valley of stability for these tracers, such that the magic neutron numbers are reached at higher mass numbers, and the abundances settle down for a pattern in between s-process and r-process.

Switching to the general comparison, Figure 6.11 reports the final heavy-elements relative abundances for all of the 12 BNS models outlined in Table 6.1 and shows them as a function of the mass number A. As in previous figures, the different panels refer to the different EOSs considered and the various binaries are represented with lines of different types. Furthermore, The results are normalized to have a total mass fraction of 1 and shown with filled circles are the scaled solar system r-process abundances. Clearly, in all cases, a successful r-process is obtained, leading to the production of the r-process pattern from the second

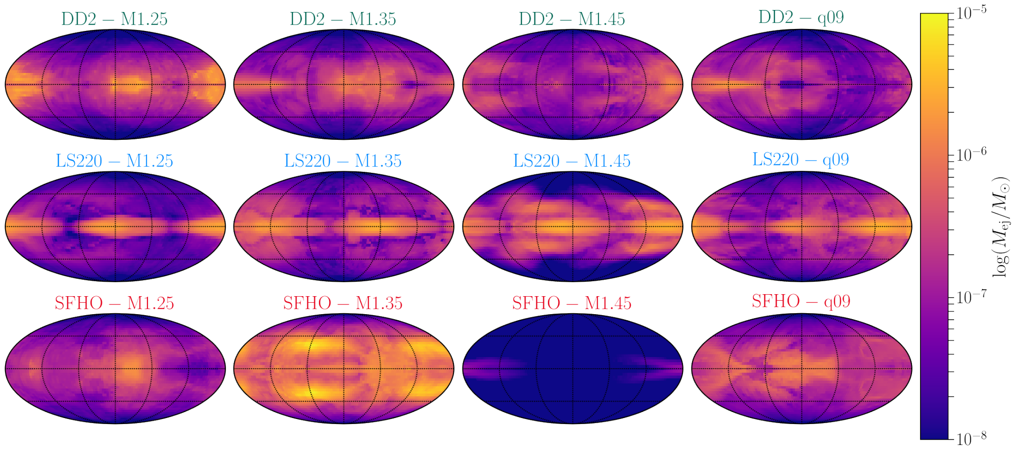

Figure 6.12: Angular distribution of the ejected mass at the final time for the various binaries, with the different rows referring to the different EOSs considered.

(i.e., $A \sim 130$) to the third (i.e., $A \sim 195$) peak.

Although it appears that all practically the same, there are some small differences due to different admixtures arising from different electron fraction distributions discussed in Sec. 6.5.2. For the equal-mass binaries, in particular there is a tendency to slightly enhance the abundances below the second r-process peak with this trend increasing mass of the neutron stars. This is simply due to the more massive BNS systems have a higher electron fraction on average. Furthermore, the contributions from tracers with high initial neutron-to-seed ratios enhance both the second r-process peak and the region with $A \approx 200$ in all cases. This is illustrated most clearly in the `SFHO-M1.45` binary, which immediately collapses to a black hole after merger, and thus ejects very little mass and with a comparatively high electron fraction. As a result, the part of ejected material with low specific entropy leads to nuclei that mainly have mass numbers with $A \lesssim 130$, while the material with high specific entropy – and thus high neutron-to-seed ratios - dominates the final abundances beyond the third r-process peak, leading to an enhanced abundance for $A \gtrsim 200$. The distinctive features observed in the final abundances in the case of the `SFHO-M1.45` binary opens therefore the prospect of using the chemical yields either as a confirmation of the prompt production of a black hole after the merger, or as an indication of this process in the case in which the post-merger gravitational-wave signal is not available.

Perhaps the most evident feature of Fig. 6.11 is the very good and *"robust"* agreement of the various abundance patterns, where by "robust" means a behaviour that is only very weakly dependent on the EOS or the initial neutron-star masses. For example, when considering the second peak at $A \sim 130$, all four different types of initial data predict a similar abundance of $^{133}\mathrm{Cs}$. Although the lanthanides show a slight disagreement with the solar abundances around the mass number $A \sim 145$ (which may be explained by other forms of ejecta, for example from accretion disks [246]), from $^{153}\mathrm{Eu}$ up $^{197}\mathrm{Au}$ in the third r-process peak, there is no disagreement in the final abundances for different initial data and EOSs.

While this agreement might be partly due to the simplified neutrino treatment, this result confirms the robustness of the r-process yields from BNS mergers already noted in the literature. Additionally, it also shows how the uncertainties associated in modelling the microphysics and initial data of BNS mergers have a very limited impact on the nucleosynthesis produced from the merger. However, even though the abundance curves produced are similar, when considering the kilonova, as will be done in Section 6.7.4, there is a large dependence of the kilonova light curves produced from the decaying elements on the parameters and thus allow for a way to distinguish between the different scenarios.

In fact, the spread in the r-process patterns is much less than the one associated to uncertainties in the nuclear-physics modelling of nuclei involved in the r-process, e.g., the choice of the fission fragment distribution [79] or the nuclear-mass model (see, e.g., Refs. [180, 162]) where variations can change the abundance of a given element by an order of magnitude.

6.7.3 Angular distributions of ejected matter

Although tracers are useful for providing detailed calculations of the outflow, directly having outflow detectors allow the detailed study of additional properties of the outflow that do not depend on having a time series. For example, the angular distribution is a quantity which can be evaluated at a given sphere since, roughly, the outflowing material is moving radially cf. Chapter 3. The distribution in itself is interesting, but the exact angular distribution of the ejected matter will have important consequences for the kilonova signal and the exact angular distributions remain well unstudied.

To proceed, the angular distribution of ejected mass is defined in Eq. (6.4), where in, contrast to other spherical integrals, the integration is defined only over the angular patches and not the entire 2-sphere. Thus similarly to Eq. (6.4), the angular averages are defined as

$$\begin{aligned} \langle\chi\rangle := & \int_0^{T_f} \int_{\Delta\Omega} \chi\, \rho_* W(\alpha v^r - \beta^r) S \, d\Omega \, dt \; / \\ & \int_0^{T_f} \int_{\Delta\Omega} \rho_* W(\alpha v^r - \beta^r) S \, d\Omega \, dt \,, \end{aligned} \tag{6.10}$$

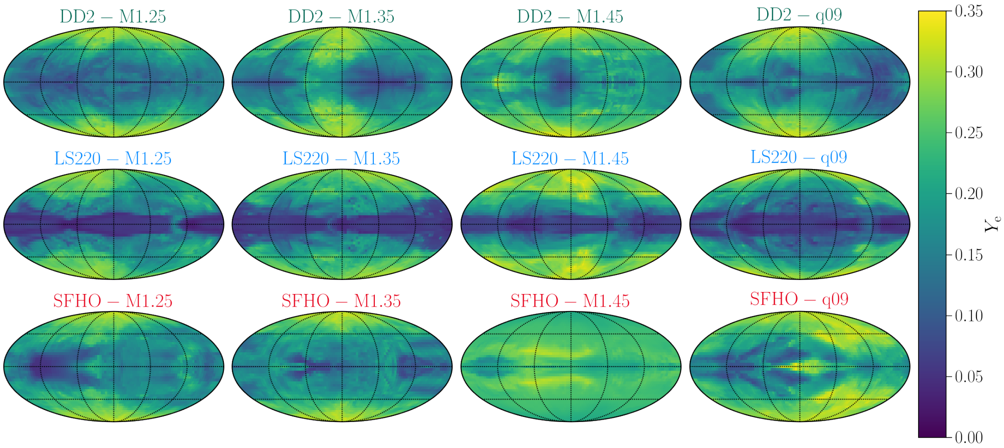

Figure 6.13: The same as in Fig. 6.12 but for the electron fraction.

where χ is any one of Y_e, s or v_{ej} and the $\Delta\Omega$ corresponds to small coordinate patches with approximately 60 points in the θ-direction and 70 points in the ϕ-direction.

This quantity is computed and displayed in Fig. 6.12 for a detector located at $\sim 300\,\mathrm{km}$ for the ejected mass. Immediately, a dependence on equation of state and initial mass can be seen, although general features exist. One example that is immediate note is the binary `SFHO-M1.45`, which immediately collapses to a black hole after the merger and hence has very little ejected material. Even considering this case, the most robust feature that is featured in every EOS and mass is that most mass is ejected along the orbital plane where higher masses correspond to yellower colours and less mass are bluer. This result is consistent with the interpretation that dynamical ejecta can originate from the tidal interactions at merger and as a result, these torques fling material outwards along the plane. In contrast, other sources of ejecta exhibit a somewhat more isotropic structure [23]. Even within this observation, there is still some variation on the exact angular distribution of the mass in the plane and it is not uniform, but exhibits anisotropies due to the disruption flows produced by the tidal torques and this concentrates the emission of matter into rather small regions on the detector surface. The only binary that appears to evade this trend is `SFHO-M1.35`, which has ejected also at latitudes as high as $\sim 45°$ and seems to peak around $\sim 30°$.

Similarly, when comparing with the distribution of the electron fraction Y_e, plotted in Fig. 6.13, the anticorrelation between of Y_e and the mass is evident. As discussed in Sec. 6.5.2, values along the polar axis have higher electron fractions due to more interactions with neutrinos as in this region, there is little mass, and the neutrinos are free streaming. In contrast, along the plane where there is more mass, the electron fraction is lower due to the planar region having "trapped" neutrinos and hence less efficient production of neutrino interactions. This difference also suggests that matter ejected around the poles is less neutron rich (i.e., with $Y_\mathrm{e} \gtrsim 0.25$) and this material may undergo a less robust r-process leading to a suppressed production of lanthanides and thus to a lower opacity. An exact understanding of this angular dependence is important in the context of determining line of site to a merger because a "blue" kilonova, i.e., a signal with a strong optical component, will form along the poles while a "red" kilonova, i.e., a signal with a strong infrared component, will form along the plane [168, 258]. Observations of GW170817 [64] suggest that a more "blue" kilonova was produced and hence suggesting that the system line of sight was closer to the poles than the plane.

To test this hypothesis, the explicit angular distribution of lanthanide mass fraction was computed in the `LS220-M1.35` model. This was done by computing the lanthanide mass fraction for every unbound tracer in the simulation and plotting their location on the 2-sphere, as illustrated in Fig. 6.14. Here the lanthanide mass fraction values have been averaged over patches of angular size $10^\circ \times 10^\circ$. It is clear that near the poles, the lanthanides mass fraction is rather high, i.e., $X_\mathrm{La} \approx 10^{-2}$ which is bluer in the colour scheme. This value is somewhat larger as one would expect of $X_\mathrm{La} \sim 10^{-5}$ for a blue kilonova to be observed [168]. Similar results are obtained in all the other BNS models. Based on this, and in contrast to the results observed in GW170817 [64, 169] where a blue-kilonova scenario is favoured, the kilonova observed is unlikely to have come from dynamical ejecta. However, some care must be taken as despite despite the three orders of magnitude difference between the expected value and the one computed here, there is a bias due to an oversimplified neutrino treatment. More sophisticated treatments, such as in Ref. [89], results in higher values of the electron fraction around the polar regions which will change the fraction of lanthanides produced.

The next quantity to consider is the specific entropy, and similar to the Y_e, there is an anticorrelation with the ejected matter. Higher entropy material is related to higher temperature material, which as illustrated in Fig. occurs at higher angles. One simple way to interpret this is that in higher density regions, shock heating is less effective in comparison to lower density regions. This also explains why the `SFHO-M1.45` model has rather higher specific entropies as little material is ejected and hence is at lower densities where shock heating is more effective at heating up the material.

The final quantity considered is that of the velocity distribution shown in Fig. 6.16. Unlike the other quantities, there is no generic features present in all the models and is highly model dependent. For the low masses and unequal masses, there is an almost isotropic distribution in the velocity. In contrast, the higher masses models, there is an overall higher velocity likely due to a stronger gravita-

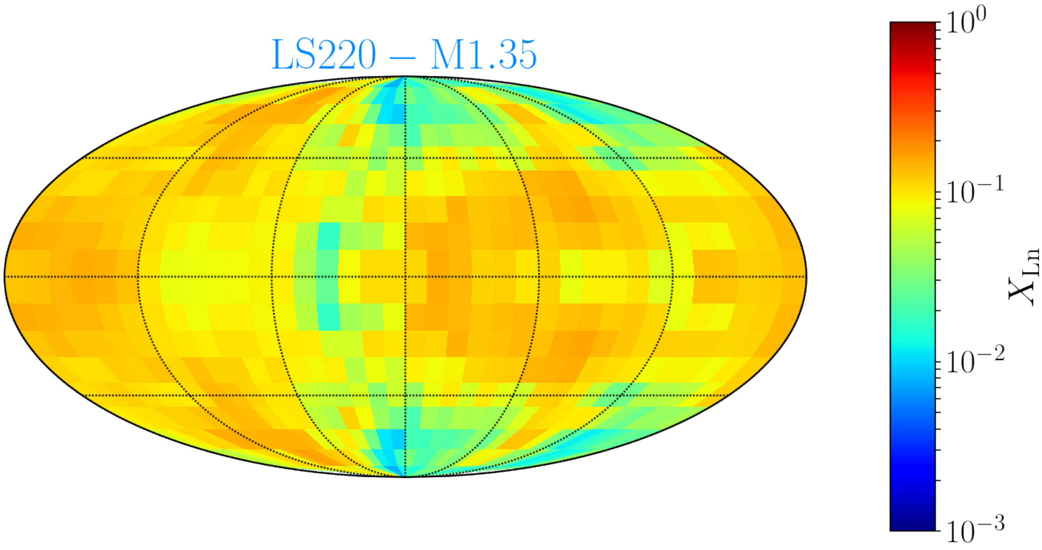

Figure 6.14: Angular distribution of the mass fraction of lanthanides in the representative case of the binary `LS220-M1.35`; the data refers to the final simulation time.

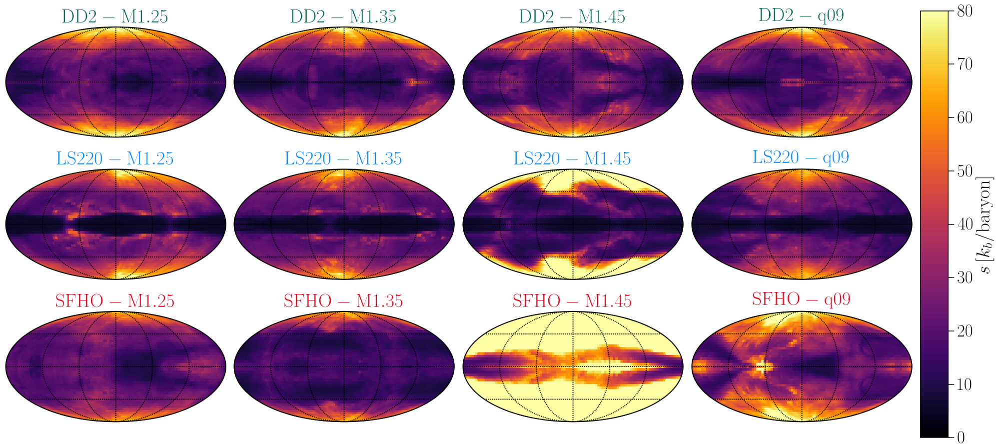

Figure 6.15: The same as in Fig. 6.12 but for the specific entropy averaged over the ejected mass.

tional potential able to ejecta material at a faster velocity outwards.

As discussed in Section 6.6, changing the criteria of the unbound material can produce differences in the average quantities of the different measurable quantities. However, when considering the spatial angular dependence, there is little

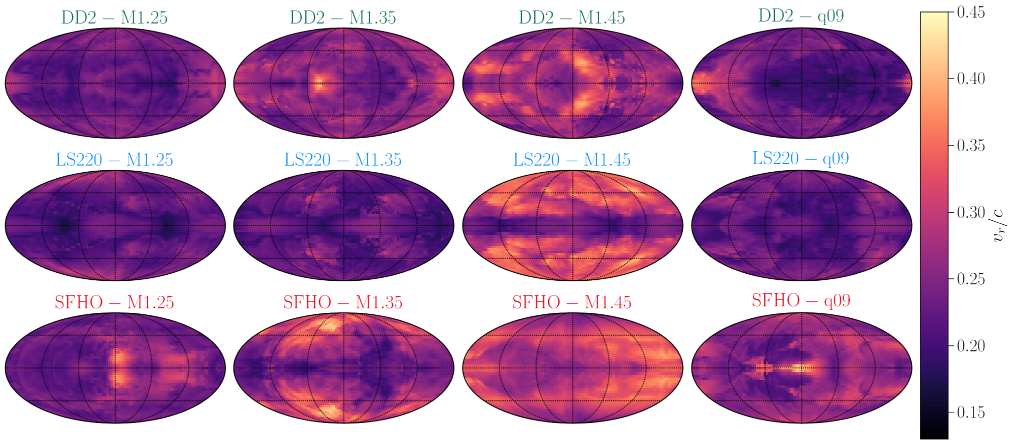

Figure 6.16: The same as in Fig. 6.12 but for the ejecta velocity averaged over the ejected mass.

change in the qualitative picture with the results presented above remaining relatively unchanged for the entropy, ejected mass, and the electron fraction. However, one difference is in the ejected mass where, simply by manner of there being more overall mass, there is more mass at higher altitudes as the Bernoulli criteria takes into account thermodynamical quantities such as entropy, which tends to be higher at higher angles. The biggest change is in the ejected velocities because, as is clearly displayed in Fig. 6.8, there is a significantly lower velocity that is reached by the material. When considering the angular distribution of the velocity, the isotropy of the geodesic case vanishes and becomes more anisotropic.

6.7.4 Kilonova

To access the observability of infrared transients associated with the decay of r-process elements, a simple gray-opacity model of kilonovae is used [107]. A setback of this model is that there is only a small amount of measured dynamical ejecta from the simulations which means that more sophisticated radiative transfer treatments. In the case of more ejecta, they can potentially form a “lanthanides curtain” and typically occur in magnetically [245] and viscously driven wind from an accretion disk, or neutrino-driven wind from the hypermassive neutron star [194]. In contrast, in the model of Ref. [107], the dynamical ejecta is approximated by a homologously expanding spherically symmetric solution [275])

$$\rho(r,t) = \rho_0 (t_0/t)^3 (1 - v^2/v_{\text{max}}^2)^3, \tag{6.11}$$

where $v_{\text{max}} = 2\langle v_\infty \rangle$ is taken from Table 6.2.

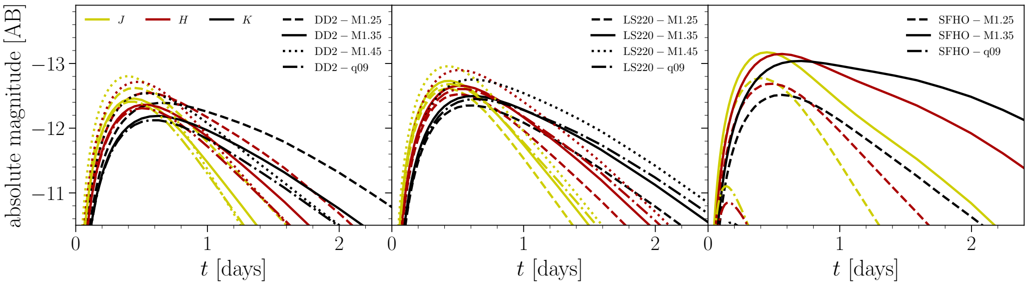

Figure 6.17: Synthetic light curves in the infrared 2MASS J, H and K-bands for all of the binaries considered.

To compute the luminosity, the nuclear heating rate is integrated directly from the nuclear network over a layer of matter from which photons can diffuse out. This is a common technique and has been used in similar models [194, 164, 219]. For the opacities, an effective gray model, i.e., $\kappa = 10\,\mathrm{cm}^2\,\mathrm{g}^{-1}$, is used. Although simple, it has been shown to reproduce reasonably well the infrared luminosity of lanthanide- and actinide-contaminated ejecta [275]. However, there are some drawbacks, specifically how flux in the optical bands is strongly suppressed when detailed opacities of lanthanides are used. Thus, only the infrared magnitudes J, H and K-bands in the Two Micron All Sky Survey (2MASS) [247] are calculated.

The nuclear heating which powers the kilonova for each model is calculated with the nuclear network code `WinNet` [274, 133], cf. Section 6.3.3, using the average electron fraction $\langle Y_\mathrm{e}\rangle$, specific entropy $\langle s\rangle$ and expansion velocity $\langle v_\infty\rangle$ as given in Table 6.2. The nucleosynthesis yields are computed with reaction rates based on the finite-range droplet model (FRDM) [176] only. This is motivated by the fact that nuclear mass models show little discrepancy in the heating rates at epochs around $t \simeq 1$ day [219], where the peak magnitudes for the models is expected.

The resulting peak bolometric luminosities, peak magnitudes in the infrared bands, and the peak epochs in the H-band are presented in Table 6.2, while the light curves in the three infrared bands (different line colors) are shown in Fig. 6.17, with different line types referring to the different binaries.

It is clear that all of the models exhibit similar behaviour, specifically with peaks around half a day in the H-band and a rapidly decreasing in luminosity after one day, reaching a maximum magnitude of -13. Note that these these luminosities are smaller than those normally expected (see, e.g., [258] for a recent review), which peak around magnitude of ~ -15. This is not unexpected as, previously mentioned, the amount of ejecta used in these simulations is rather small while in other simulations the amount of ejecta is normally assumed to be $\sim 10^{-2}\,M_\odot$ which is an order of magnitude then the results observed here. With 3-minute J-band exposure on the VISTA telescope [80], these magnitudes result in a detection horizon of $\sim 100\ \mathrm{Mpc}$, which, in combination with a very short time around the peak, makes these light curves extremely difficult to detect in a follow-up survey. As observed in the follow-ups to GW170817, light curves were observed that originate from a kilonova [263, 64, 169] which suggests that a significant amount of material, on the order of $10^{-2}M_\odot$, became unbound. This suggests that the source of the radioactive decay powering the kilonova is not in the dynamical ejecta, but in other sources such as neutrino drive winds or viscous ejecta [169].

6.8 Constraints on BNS merger rates

Another interesting way to test the amount of ejected material is compare the amount of ejected material with that of the amount of heavy elements observable in the Milky Way galaxy. As the total amount of heavy elements in the Milky Way is known and from the simulations above, the lower bound on the amount of ejected material is given, the required rate to explain the amount of ejected material is easily calculated which in turn gives a predicted neutron star merger rate that can be compared with experimental bounds. Following Ref. [219], Fig. 6.18 plots the constraints on the rate of BNS mergers and the required amount of ejected material needed per merger. More specifically, assuming the total amount of r-process material in the Galaxy is $M_{\rm r,gal} \approx 19{,}000\,M_\odot$ and given a certain merger rate – either per year and galaxy equivalent ($\mathrm{yr}^{-1}\ \mathrm{gal}^{-1}$, bottom horizontal axis) or per year and cubic Gigaparsec ($\mathrm{yr}^{-1}\ \mathrm{Gpc}^{-1}$, top horizontal axis) – the black line shows the amount of ejected material per merger required to explain the observed abundances. Similarly, the red line has the same meaning, but only takes into account elements with $A \gtrsim 130$, with a total galactic mass of $M_{\rm r,gal} \approx 2{,}530 M_\odot$ [166, 219]. The blue-shaded horizontal region indicates the range of dynamically ejected material from BNS mergers in quasi-circular (QC) orbits and covered by the simulations as reported in Table 6.2[5]; the other two shaded horizontal regions report instead the typical abundances coming from the secular ejecta (pink-shaded region) or from the dynamic ejecta relative to mergers of BNSs in eccentric orbits (green-shaded region).

These constraints should be compared with actual measurements of the merger rates as deduced from different experiments and indicated as vertical lines. In particular, shown as the dot-dashed black line is the predicted merger rate of

---

[5] The `SFHO-M1.45` model has been omitted because it is not representative.

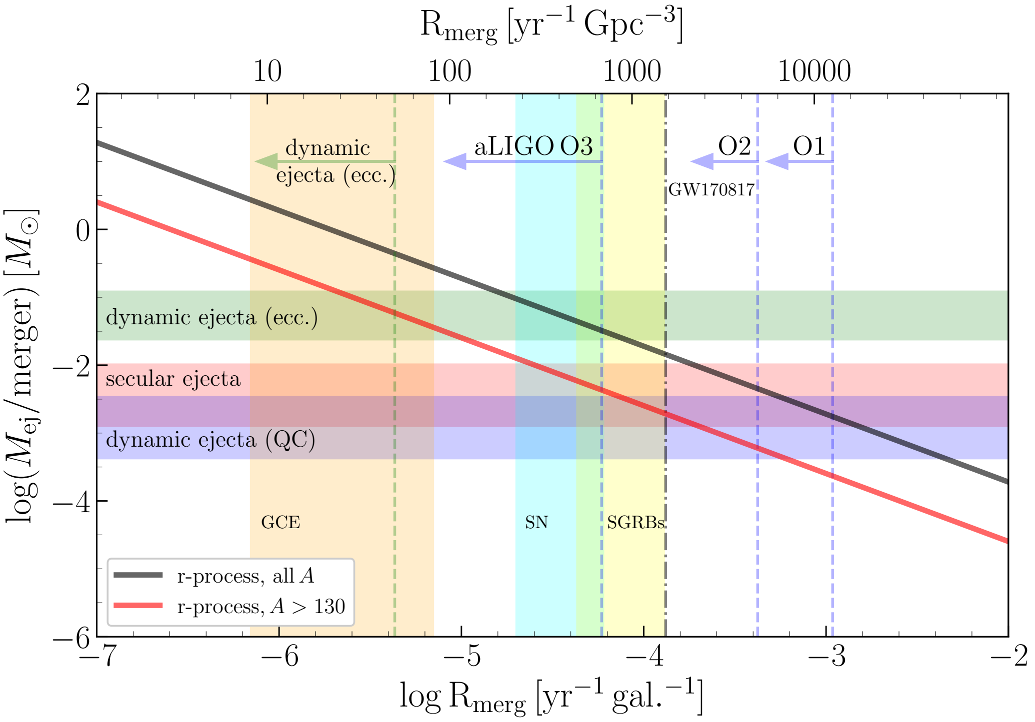

Figure 6.18: Ejected material per merger for a given BNS merger rate required to reproduce the observed mass of all (black) and $A > 130$ (red) r-process elements in the Milky Way. The dark blue-shaded regions correspond to the range of values of ejected mass reported in Table 6.2. The red-shaded region corresponds to ejected masses from other sources of ejecta. The dashed vertical gray lines report the observed, O1, and predicted, O2 and O3, upper bounds on BNS mergers from LIGO. The dot-dashed black line is predicted merger rate from GW170817. The orange, light blue, and yellow shaded regions correspond to observational constraints from galactic chemical evolution (GCE), supernova (SN), and short gamma-ray bursts (SGRBs) population synthesis models as defined in the text.

GW170817 [263], which is computed by simply dividing the number of detected mergers, which till now is only one, by the observing area of the LIGO telescope and the observing run time. This simple calculate yields the vertical line of $1530\mathrm{yr}^{-1}\,\mathrm{Gpc}^{-3}$. In addition to this line, the observed upper bound on BNS mergers observed in the first LIGO operating run O1, and the predicted upper bounds for the planned future runs O2 and O3 [3] are also plotted. Additionally, different population-synthesis models are also displayed corresponding to galactic chemical evolution (GCE) [63], supernova (SN) [57], and SGRBS [195], which are different methods of obtaining an estimation on the rate of neutron star mergers through different channels.

The red line, horizontal-blue shaded region, and GW170817 overlap in Fig. 6.18 which indicates that the measured amount of dynamical ejecta, $\sim 10^{-3}M_{\odot}$, from the presented simulations is sufficient to reproduce the observed r-process mass abundances with $A > 130$ in the Milky Way. Associated with GW170817 was a SGRB [264, 148] and provides strong evidence that SGRBs and neutron star mergers are related. Thus the rate constraint predicted by SGRBS [195] is likely indicative of BNS merger rates and their agreement here provides more evidence on the relationship between the two. This also implies that although there is a lower amount of dynamical ejecta then reported in Newtonian simulations, cf. Sec. 6.5, the frequency of BNSs merger is likely to be sufficiently high to compensate for this. Furthermore, the geodesic criterion that has been employed here is a conservative one and only provides a lower bound on the amount of material ejected; by adopting a different criterion, e.g., the Bernoulli one (see discussion in Section 6.6), the amount of ejected material can increase up to a factor of 4 for the same simulation.

Although it is expected that orbiting neutron star mergers are the dominant source of the neutron star mergers in the universe, there is another more exotic scenario of the source r-process, specifically that of dynamical ejecta from eccentric BNSs mergers. When simulations with this initial data is run, measured ejecta masses from these configurations is in fact much larger [201, 190] by about an order of magnitude or more, and would be sufficient to explain the observed mass values; however these events are likely very rare and current constraints are not well understood [141] so it is difficult to justify these mergers contributing more than a little amount to the total r-process ejecta.

Finally, it is important to take into consideration that the above figure was made with only one channel of unbound material, namely that of dynamical ejecta. There are other channels, such as neutrino driven wind or BH-torus system, where in the latter the mass ejecta can be as high as $0.1\,M_{\odot}$, as estimated semi-analytically in Ref. [97]. This suggests that even if the mass ejected from a single channel is alone insufficient to explain the observed r-process masses, the combination of all ejected material from a BNS merger is likely to so. It is for this reason that the blue-shaded horizontal region only represents a lower bound on the total ejected material and the true value is likely to be higher.

6.9 Conclusions

The simultaneous detection of an electromagnetic counterpart with a gravitational wave from a binary neutron star mergers heralds the beginning of the era of multi-messenger astronomy. Observations now support the picture that material is dynamically ejected from the merger of neutron stars binaries and that such material is neutron-rich and its nucleosynthesis can provide the astrophysical site for the production of heavy elements in the Universe. Furthermore, this simultaneous detection provides confirmation of the long-standing conjecture that the merger of neutron stars is behind the origin of SGRBs [78, 184, 210, 36].

In this chapter, fully general-relativistic simulations of the inspiral and the merger of neutron star was done using a variety of equations of state, initial masses, and mass ratios. For each of these, the r-process nucleosynthesis taking place in the dynamical ejecta was calculated. This calculation was seeded with tracer data introduced in Chapter 6. These tracer particles allow for the following of the fluid and that can be used to extrapolate the fluid properties to the late times needed to run nuclear networks codes. These simulations yield the following three broad conclusions.

First, it was shown that in the cases considered, the r-process nucleosynthesis from BNS mergers is very robust in that it depends only very weakly on the properties of the binary system, such as the EOS, the total mass or the mass. However, one caveat is that a parameter space exploration depending on the EOS is still rather limited, due to the lack of publicly available fully temperature dependent tables and in future work intend to explore it more fully with a larger set of EOSs. Overall, while similar conclusions have been reported before, the confirmation coming from the above study strengthens the evidence that BNS mergers are the site of production of the r-process elements in the galaxy.

Second, two separate methods have been employed to measure the amount of matter ejected dynamically and they both consistently found that it is $\lesssim 10^{-3}\,M_{\odot}$, which is smaller than what usually assumed from other simulations. Importantly, there are a number of factors that need to be considered when measuring the amount of ejected material from merger simulations. For example, the type of neutrino treatment is essential as changes to this treatment changes the way the neutrinos interact with the simulation and thus directly change the amount of ejected material. Other criteria that need to be accounted for include the EOS, the criterion for unboundness, the resolution, and the numerical methods used. Even with all these large sources of error, which is an order of magnitude, dynamical ejecta is still not sufficient to reproduce the amount of ejecta required to explain GW170817, which is on the order of $10^{-2} - 10^{-1}\, M_{\odot}$. It is clear, however, that a more detailed and comprehensive study is needed to understand the uncertainties behind the amount of mass lost by these systems.

Third, to calculate the kilonova, a simplified and gray-opacity model was used. It predicts that the observability of the infrared transients associated to the decay of r-process elements, i.e., of the kilonova emission, to be similar independent of EOS, with emission peaking around $\sim 1/2$ day in the H-band and rapidly decreasing in luminosity after one day, reaching a maximum magnitude of -13. When comparing these predictions with the observations of the kilonova associated with GW170817, there is a clear difference in peak emissions and the amount of ejected material [265] due to a lower amount of dynamical ejecta. This result points to the more likely scenario that there are other sources of ejecta, such as neutrino driven winds or disk ejecta that also contribute to both observations. Thus detailed comparison with the new observations will require more sophisticated calculations with improved neutrino treatments to truly disentangle all the sources of ejecta.

Finally, despite the r-process abundance curves not yielding a way to constrain for example, the equation of state or other BNS parameters, there are features in the kilonova that are related to different parts of the ejecta morphology and can be used to constraint physics this way. In particular, softer EOSs produce higher average electron fractions which has direct observable properties in the type of kilonova produced. And for each of these types of kilonova, there is a strong angular dependence with higher electron fractions around the polar regions and lower along the orbital plane. This is despite that there being less ejecta along the polar axis and more in the plane. This points to a simple homogeneously expanding group of material, often assumed in kilonova modelling, needs to be adjusted to account for this anisotropic distribution.

Chapter 7

Conclusions

The detection of gravitational waves from inspiralling and merging neutron stars heralds a new era of multi-messenger astronomy and numerical relativity. It signals the maturation of the field of numerical relativity from an area of computer experiments to essential aspect of modern relativistic astrophysics. In the coming years, more detections of neutron stars will allow neutron star mergers to be realised as an astrophysics laboratory to explore gravity and nuclear physics at the extremes. In order to study these exciting areas of physics, in this thesis I have introduced the treatment of tracers, massless particles that are passively advected by the fluid, into general relativity and applied it to the macroscopic and microscopic post-merger dynamics of neutron stars.

In particular, in Chapter 3 I developed and implemented the use of tracers in general relativity grid-based codes. Through this method we investigated that the optimal initial placement of tracer should be spread uniformly through the density, which counters initial guesses. Furthermore, using these tracers, a method to assign a "mass" to a tracer was developed. This method of assigning mass is essential in reproducing the abundances of the heavy elements undergoing the r-process as it provides a weight to the contribution of fluid elements to the total abundance curve. Furthermore, tracers allow one to follow the thermodynamical trajectories of the dynamical ejecta, i.e., unbound material, in the merger of binary neutron stars. In contrast, for matter within the core of the neutron star, i.e., bound material, the use of tracers allow a unique representation of the fluid flow that would otherwise be inaccessible.

In Chapter 4 this tracer method was applied to determining the rotation law of the remanent of the merging process. This merger product can have a mass larger than the maximum mass of a non-rotating neutron star because the rotation provides a form of pressure support against collapse. However, the exact form of the rotation of the merger product is still not well understood and is essential in understanding what happens in the post-merger dynamics of a merger. We have shown that the merger product is undergoing differential rotation, i.e., different radii are rotating at different rates. Furthermore, using tracers, we have shown for the first time, that the reason for the bar-mode to be out-of-phase with the rotational profile can be understood as a simple consequence of a Bernoulli-like conservation law.

In Chapter 5 the inclusion of dissipative-like effects in the post-merger dynamics of the neutron star merger was considered. Although neutron stars can be well modelled by a perfect fluid, this assumption depends on effects of the microphysics, for example neutrino transport, being relatively negligible. However, we have shown with the use of tracers that the timescale of neutrino transport effects may be shorter than previous thought and may have an impact on the dynamics of the post-merger remanent as modifications to the perfect fluid assumption must be made.

Finally, in Chapter 6 the tracers were applied to the r-process nucleosynthesis of the heavy elements. The associated kilonova from GW170817 and evidence from dwarf galaxies has suggested that the source of the heavy elements in the universe are produced in the outflow from the merger of neutron stars. This outflow is especially neutron rich and provides an environment for r-process nucleosynthesis to occur. Using the tracers, we were able to follow the thermodynamical histories of the outflow which provide input for a nuclear-network to evolve the trajectories for long periods of time and calculate the abundance of the different elements that would be produced in a merger. It was shown that the abundance curve produced from a merger is in good agreement with the observed solar abundance. Furthermore, using this data, light curves were produced for the signal of a kilonova, which suggests that the dynamical ejecta are dimmer than previously thought. Additionally, it was found that the abundance pattern is essentially independent of the input parameters such as equation of state or initial mass. Related to both of these areas of improvement, is more accurate calculations of the kilonova lightcurves. GW170817 has provided a wealth of observed data must be now understood in the context of numerical relativity and more accurate calculations of lightcurves from ejecta from the mergers is required to explain the observation.

These results set the stage for the future direction of research into numerical relativity. Simulations performed here and observations from GW170817 confirm the need for increasingly sophisticated treatments of microphysics in neutron star mergers, such as in neutrino transport. Such an advancement can come in the form of an updated scheme such as M1 or in advances in computational resources which allow for different solving techniques, such as Monte Carlo, to be used. Another future direction is the improvement of the treatment of the fluid used in simulations. It is clear that although the perfect fluid approximation is good, it is not sufficient to model all the complicated microphysical interactions that occur due to effects such as dissipation or viscosity.

In conclusion, the work described in this thesis, [110, 45, 44, 8] represents my genuine contribution as an author and researcher. I hope that it provides a basic technique that can be used in gaining a clearer understanding of the physics inside and outside of a binary neutron star merger.

Acknowledgements

I want to thank my supervisor Luciano Rezzolla whose expertise and advice have been immense and helped me become a better scientist. I also thank Almudena Arcones for being my second advisor.

I want to thank all the numerous people with whom I have interacted with in the Relativistic Astrophysics group in Frankfurt. They are, in no particular order: Matthias Hanauske, Jens Pappenfort, Hector Olivares, Federico Guercilena, Lukas Weih, Enping Zhou, Marcio de Avellar, Bruno Mundim, Sven Köppel, Yosuke Mizuno, Ziri Younsi, Oliver Porth, Mariafelicia De Laurentis , Elias Most, Cosima Breu, Christian Fromm, Roman Gold, Antonios Nathanail, Kentaro Takami, Filippo Galeazzi, and Antonios Tsokaros. Unfortunately I am terrible at remembering names so if I've probably forgotten people that is entirely unintentional. Special thanks go Jens Papenfort, Elias Most, and Sven Köppel for translating the introduction into German.

Figures in this thesis were produced using `VisIt` [56] and `matplotlib` [118]. Post-processing was done using `numpy` [270].

During this thesis, I was supported by HIC for FAIR and the graduate school HGS-HIRe. The simulations were performed on the SuperMUC cluster at the LRZ in Garching, on the LOEWE cluster in CSC in Frankfurt, and on the HazelHen cluster at the HLRS in Stuttgart. Additional support came from the ERC synergy grant "BlackHoleCam: Imaging the Event Horizon of Black Holes" (Grant No. 610058), by "NewCompStar", COST Action MP1304, by the LOEWE-Program in the Helmholtz International Center (HIC) for FAIR, and by the European Union's Horizon 2020 Research and Innovation Programme (Grant 671698, call FETHPC-1-2014, project ExaHyPE).

Finally, to quote a childhood friend and an influence who has acted as my North Star on more than one occasion, Richard Loat, "I wanna be the very best, like no one ever was. To catch them is my real test, to train them is my cause."

Zusammenfassung

Die Ära der Gravitationswellenastronomie hat begonnen. Sie wurde eingeläutet durch die gleichzeitige Detektion von Gravitationswellen und elektromagnetischen Wellen, ausgesandt bei der Verschmelzung zweier Neutronensterne und gemessen durch die LIGO Scientific Collaboration im August 2017 [263, 264, 148]. Die gleichzeitige Messung bestätigt die seit langem bestehende Vermutung, dass Neutronensternverschmelzungen der Ursprung von kurzen Gammablitzen (engl. short gamma-ray bursts, SGRBs) [184, 78, 210, 27, 36] sowie der Ursprung von schweren Elementen im Universum sind [139, 138, 78].

Es sind aber ebenso aufregende Zeiten für das Gebiet der numerischen Relativitätstheorie. Durch die komplizierte nichtlineare Natur der Einsteingleichungen können Doppelneutronensterne nur numerisch modelliert werden und die Numerische Relativitätstheorie spielt eine zentrale Rolle in der Erklärung dessen, was gemessen wurde, von der Berechnung des Gravitationswellensignals über die Modellierung des Verschmelzungsproduktes bis hin zur Entstehung eines elektromagnetischen Gegenstücks. In den nächsten Jahren wird die numerische Relavitätstheorie im gerade entstehenden Feld der Gravitationswellenanalyse eine essentielle Rolle spielen. In der Erwartung, Gravitationswellen messen zu können, wurde in den letzten zehn Jahren intensiv an der Modellierung von Neutronensternen geforscht. Erhebliche Fortschritte konnten dabei in der Beschreibung der Orbitaldynamik, der Verschmelzung und des Endproduktes gemacht werden[23, 192]. Fortschritte im Bereich der enthaltenen Mikrophysik, wie etwa Neutrinotransport und Magnetfelder, haben zunehmend realistischere Simulationen und eine Fülle an neuer Physik sowohl im gravitativen als auch elektromagnetischen Spektrum hervorgebracht.

Wie GW170817 zeigt, ist das elektromagnetische Spektrum von zwei verschmelzenden Neutronensternen umfangreich. Insbesondere ein elektromagnetisches Gegenstück hat vor Kurzem grosse Aufmerksamkeit auf sich gezogen: die Kilonova [146, 222, 196, 107, 194, 272, 123, 228, 201, 124, 229, 174, 258, 26, 219, 275, 168]. Eine Kilonova ist ein Signal im infraroten/optischen Spektrum, das von dem Zerfall einer Vielzahl von schweren Elementen erzeugt wird, daran beteiligt sind in erster Linie Elemente nahe dem zweiten r-Prozess-Peak (also

^{133}I, ^{132}Te und ^{133}Xe), weiterhin Elemente von dem dritten r-Prozess-Peak sowie ferner instabile transuranische Elemente. Diese Elemente können nach einer BNS-Verschmelzung durch das Einsetzen schnellen Neutroneneinfangs entstehen. Eine Kilonova wurde nach GW170817 beobachtet[263], allerdings wurden vorher bereits potentielle Kilonova-Kandidaten in GRB 130603B [37, 260], GRB 060614 [277, 122] und GRB 050709 [121] beobachtet. Die sehr grossen Messungenauigkeiten haben bis dato allerdings eine eindeutige Identifikation verhindert.

Die Energiequelle einer Kilonova ist der Zerfall von Elementen die während dem r-Prozess erzeugt werden. In der Geschichte unseres Universums ist dieser Prozess für die Erzeugung der Hälfte der Elemente verantwortlich, die schwerer sind als Eisen. Während das zugrundeliegende Konzept seit Jahrzehnten bekannt ist [52], wurde der astrophysikalische Ursprung bislang noch nicht zweifelsfrei festgestellt. Damit Materie r-Prozess-Nukleosynthese unterläuft, wird eine hochexplosive, sehr neutronenreiche Umgebung benötigt. Diese stellt an potentielle astrophysikalische Orte, in denen dieser Prozess ablaufen könnte, enge Grenzen. Zwei mögliche Ursprünge sind dabei in der wissenschaftlichen Community am populärsten: Kernkollaps-Supernovae (engl. core-collapse supernovae, CCSN) sowie BNS-Verschmelzungen. Aktuelle Simulationen von CCSN haben gezeigt, dass die Umgebung in den äusseren Schichten der Explosion nicht ausreichend neutronenreich und damit nicht in der Lage ist, die beobachtete Verteilung der schweren Elemente im Sonnensystem zu erklären [117, 116, 83, 273], auch wenn seltene Formen von CCSN, welche von Magnetfelder dominiert werden, möglich sind [274, 179, 185]. Im Gegensatz dazu werden Neutronensternverschmelzungen als immer wahrscheinlicherer Ursprung von schweren Elementen angesehen. Aktuelle Präzisionsmessungen von Zwerggalaxien [120] weisen stark darauf hin, dass BNS die Hauptproduktionsstätte von r-Prozess-Elementen sind.

Des Weiteren haben anspruchsvolle Neutrinotransportsimulationen kombiniert mit numerischer Relativitätstheorie gezeigt, dass nicht nur signifikante Massenauswürfe (auf Grund verschiedenster physikalischer Prozesse) in BNS-Verschmelzungen vorhanden sind, sondern auch, dass in diesem Szenario eine Umgebung erzeugt wird, in dem stabile r-Prozess Nukleosynthese stattfinden kann. Zahlreiche Simulationen, angefangen von Newtonscher Mechanik bis hin zu voll-relativistisch haben mittels einer Vielzahl von mikrophysikalischen Beschreibungen vier wesentliche Massenauswurfsmechanismen gefunden: Dynamischer Massenauswurf [221, 209, 214, 137, 216, 31, 87, 114, 272, 228, 229, 201, 142, 68], Neutrino-dominierte Winde [67, 194, 123, 164, 163, 124, 181, 93], magnetisch dominierte Winde [237, 131, 245, 211, 59], und viskositätsabhängige Entwicklung von Akkretionsscheiben [35, 172, 103, 82]. Die typischen Zeitskalen hierbei sind $\sim 10\ \mathrm{ms}$ für dynamischen Massenauswurf , $\sim 100\ \mathrm{ms}$ für Neutrino- oder magnetisch dominierten Winde, und $\sim 1\ \mathrm{s}$ für Viskositätseffekte. Auf Grund des relativ hohen Rechenzeitaufwands von Langzeitsimulationen haben sich die meisten vollrelativistischen Simulationen auf dynamischen Massenauswurf beschränkt, während die anderen Mechanismen im wesentlichen nur mittels Newtonscher Mechanik untersucht worden sind.

In dieser Arbeit habe ich eine neue Methode entwickelt, die Testteilchen für die Untersuchung von Problemen mikro- und makrophysikalischer Natur der Dynamiken nach einer BNS-Verschmelzung benutzt, um speziell dynamischen Massenauswurf und r-Prozess-Nukleosynthese zu untersuchen. Obwohl prinzipiell einfach zu beschreiben, hat der Testteilchenansatz subtile technische Probleme die zuerst gelöst werden müssen, bevor man sie in numerischen Simulationen einsetzen kann. Der Einsatz von Testteilchen (engl. Tracers) hat eine lange Geschichte im Bereich der Hydrodynamik, sowohl in der Theorie als auch im Experiment, weil man sie dazu benutzen kann, die Entwicklung einer Flüssigkeit zu verfolgen, die sonst im Experiment schwer zugänglich ist. Ein Beispiel hierfür ist die Entwicklung einer Flüssigkeit in einem Behälter zu der Farbe hinzugegeben wird, die dann als Testteilchen modelliert wird. Damit ist es möglich, Wirbelbildung in geschichteten Flüssigkeiten sichtbar zu machen [46]. Insbesondere bei gitterbasierten Codes ist es schwierig, die Entwicklung einer Flüssigkeit nachzuvollziehen, da das Gitter räumlich fest ist und einem Flüssigkeitselement nicht folgen kann. Die geglättete Teilchen-Hydrodynamik (engl. smoothed-particle hydrodynamics) ist hingegen nicht von diesem Problem betroffen, da hier Flüssigkeitsteilchen direkt entwickelt werden und somit die lokalen Eigenschaften der Flüssigkeit trivial zur Verfügung stehen.

Obwohl die Entwicklung von Testteilchen an sich einfach ist, da sie nur passiv advektiert werden, stehen einer direkten Umsetzung einige Schwierigkeiten im Weg, so zum Beispiel die Tatsache, dass Testteilchen masselos sein müssen, da sie sonst mit der Flüssigkeit wechselwirken würden und somit im Energie-Impuls-Tensor berücksichtigt werden müssten, wodurch sie nicht mehr passiv wären. Es kann in manchen Situationen, wie bei Kilonova Leuchtkurven, dennoch nützlich sein einem Testteilchen eine Masse zuzuweisen. In dieser Arbeit wird daher eine Methode entwickelt einem Testteilchen eine Masse zuzuweisen und damit r-Prozess Nukleosynthese sowie Kilonovaleutchkurven zu berechnen. Hierbei gilt es zu beachten, dass wir diese physikalischen Grössen aus den Eigenschaften des Fluids berechnen wollen und die Testteilchen diese somit hinreichend genau abbilden müssen. Daher muss ein besonderes Augenmerk darauf gelegt werden, die Testteilchen zum Startzeitpunkt korrekt zu platzieren, damit sie auch zu einem späteren Zeitpunkt den Zustand des Fluids noch hinreichend genau repräsentieren. Ich habe herausgefunden, dass der effektivste Weg dazu eine gleichmässige Verteilung in der Dichte darstellt. Wenngleich dieser Ansatz zuerst der Intuition zu widersprechen scheint, da man Material niedriger Dichte, das später ungebunden wird, mit mehr Testteilchen abbilden muss, stellt sich jedoch heraus, dass man dadurch diese Dichte zu hoch gewichtet, während man Material, das aus tieferen Regionen des Gravitationspotentials kommt vernachlässigt.

Ich wende diese neue Testteilchenmethode auf zwei verschiedene Bereiche eines verschmolzenen Doppelneutronensternsystems an: Auf gravitativ gebundene Masse [110, 8] sowie ungebundene Masse [44]. Nach der Verschmelzung zweier Neutronensterne entsteht ein metastabiles Objekt, welches wir einen hypermassiven Neutronenstern nennen – falls kein prompter Kollaps zu einem schwarzen Loch stattfindet. Auf Grund von differentieller Rotation wird der hypermassive Neutronenstern an einem prompten Kollaps zu einem schwarzen Loch gehindert [110]. Physikalisch bedeutet das, dass verschiedene Bereiche des Neutronensterns mit unterschiedlichen Geschwindigkeiten rotieren und dadurch den Neutronenstern stabilisieren. Die Art der differentiellen Rotation von hypermassiven Neutronensternen ist eine noch immer nicht endgültig geklärte Frage, aber aktuelle Simulationen haben gezeigt, dass das einfache Modell eines konstanten Rotationsprofils in numerischen Simulationen nicht anzutreffen ist und eine Modifikation des Rotationsprofils nötig ist. Eine weitere interessante Eigenschaft des Verschmelzungsprodukts ist die Phasendifferenz zwischen der $m = 2$, $l = 2$-Mode (in der Literatur der Form wegen auch Balkenmode, engl. bar mode, genannt) und dem Rotationsgesetz. Es zeigt sich, dass Bereiche höherer Dichte langsamer rotieren und Bereiche niedrigerer Dichte schneller rotieren. In [110] haben wir eine Erklärung für dieses Verhalten gegeben, in dem wir mittels Testteilchen die Entwicklung des inneren Bereichs des Kollisonsproduktes verfolgt haben, in welchem die Masse gebunden bleibt. Da die Testteilchen es ermöglichen Flüssigkeitstrajektorien zu identifizieren, konnten wir zeigen, dass ein Bernoulli-artiges Erhaltungsgesetz gilt, insbesondere ist ein reziproker Zusammenhang eine natürliche Konsequenz der Erhaltungsgrösse. Testteilchen weisen explizit auf diesen Zusammenhang hin, da sie – unserer Ansicht nach zum ersten mal – die Entwicklung von Grössen anhand Fluidtrajektorien in gitterbasierten Simulationen der numerischen Relativitätstheorie ermöglichen.

Als weitere Anwendung der Testteilchen in gravitativ gebundener Masse nutzen wir sie in [8] um den Einfluss von dissipativen Effekten auf das Kollisionsprodukt zu untersuchen. Die verbreiteten Modelle von Neutronensternen nutzen ein perfektes Fluid mit einem isotropischen Druck, welches keinen Wärmetransport oder Dissipationseffekte erlaubt. Auch wenn diese Annahmen in der Regel gerechtfertigt sind, sorgt die Berücksichtigung von Neutrinos dafür, dass die Zeitskalen, die mit diesen Effekten assoziiert werden, sich signifikant verringern und möglicherweise die gleiche Grössenordnung aufweisen wie die Lebenszeit eines hypermassiven Neutronensterns.

Zu guter Letzt wurde die Testteilchenmethode angewandt, um die Entstehung von schweren Elementen in den dynamischen Massenauswürfen zu untersuchen. Um die Nukleosynthese mit einem nukelaren Netzwerk zu berechnen, wird der Zustand eines Fluidelements über die Zeit benötigt. Dieser ist insbesondere für die Anfangsreaktionen im Netzwerk wichtig. Eine bislang verbreitete Methode [201] hat eine adiabatische Extrapolation von einer Kugeloberfläche durchgeführt. Auch wenn diese Methode einfach zu implementieren ist, ist sie dennoch nur eine Näherung, da die Ausdehung des Fluids fast, aber nicht exakt adiabatisch verläuft [45]. Mittels des Testteilchenansatzes waren wir in der Lage, die Geschichte eines Fluidelements nachzuvollziehen – eine Beobachtungsgrösse, die in einem gitterbasierten Code normalerweise nicht zugänglich ist. Da die Testteilchen masselos sind, muss eine Methode entwickelt werden, die den Teilchen eine physikalische Masse assoziiert, sodass die letztlich berechneten Isotopenhäufigkeiten korrekt gewichtet werden können. Unter Berücksichtigung einer Vielzahl von Zustandsgleichungen und Massen konnte eine systematische Untersuchung der dynamischen Massenauswürfen mit Neutrinotransport durchgeführt werden, bei der die Testteilchenmethode eine zentrale Rolle einnahm, um den entstehenden r-Prozess zu untersuchen. Wir haben herausgefunden, dass der Wert des dynamischen Massenauswurfs empfindlich von verschiedenen Parametern abhängt, insbesondere haben wir signifikante systematische Fehler im Hinblick auf die Auflösung identifiziert. Dennoch können wir die Menge des dynamischen Massenauswurfs auf ungefähr $\sim 10^3 M_\odot$ bestimmen, was im Einklang mit den Beobachtungen von GW170817 steht [265].

Die vorliegende Arbeit gliedert sich wie folgt: Kapitel 2 führt den notwendigen mathematischen, physikalischen und numerischen Formalismus ein, der nötig ist um Neutronensternverschmelzungen auf Supercomputern zu berechnen; Kapitel 3 führt die Testteilchenmethode auf gridbasierten Codes ein und diskutiert die optimale Platzierung im Vergleich mit dem zugrundeliegenden Fluid; Kapitel 4 wendet die Testteilchenmethode auf gebundene Masse an und erklärt die beobachtete Phasendifferenz zwischen einer Neutronensternverschmelzung und seiner differentiellen Rotation; Kapitel 5 wendet die Testteilchmethode darüberhinaus auf gebundene Massen an, um den Einfluss von Dissipation auf die Modellierung von Neutronensternverschmelzungen zu untersuchen; Kapitel 6 wendet die Testteilchenmethode zur Untersuchung von ungebundener Masse an, es liefert insbesondere eine umfassende Untersuchung der dynamischen Auswürfe von Neutronensternverschmelzungen, r-Prozess-Isotopenhäufigkeiten und Kilonovalichtkurven; und letztlich Kapitel 7, es beinhaltet einige Zusammenfassungen, Schlussworte und zukünftige Forschungsrichtungen.

CV

Personal
Luke Bovard
Citizenship: Canadian

Education

Ph.D. in Physics
September 2014-Today
Johann-Wolfgang-Goethe Universität, Frankfurt am Main, Germany
Supervisor: Luciano Rezzolla

M.Math in Mathematics
January 2012- December 2013
University of Waterloo, Waterloo, Canada
Supervisor: Michael Waite

B.Sc in Mathematical Physics
September 2007- December 2011
University of Waterloo, Waterloo, Canada

Conferences, workshops, schools
August 2017 - INT Workshop 17-2b, Seattle, USA
July 2017 - MICRA Conference 2017, Lansing, USA
March 2017 - NewCompStar Annual Conference, Warsaw, Poland
January 2017 - Hirschegg 2017, Hirschegg, Austria
October 2016 - Compact objects, EOS, and their nucleosynthesis, Basel, Switzerland
September 2016 - NewCompStar School 2016, Coimbra, Portugal
April 2016 - NewCompStar Annual Conference, Istanbul, Turkey
August 2015 - INT Summer School on Neutron Stars, Seattle, USA

Computer skills
Proficient with Python, C, C++, Fortran, MATLAB, Unix

Personal
Languages: English (native), German (fair), French (fair)

Publications

- M. Hanauske, K. Takami, **L. Bovard**, L. Rezzolla, J. A. Font, F. Galeazzi, and H. Stöcker. *Rotational properties of hypermassive neutron stars from binary mergers.* Phys. Rev. D, 96(4):043004, August 2017.
- **L. Bovard** and L. Rezzolla.
  On the use of tracer particles in simulations of binary neutron stars. Classical and Quantum Gravity, 34(21):215005, 2017.
- M. G. Alford, **L. Bovard**, M. Hanauske , L. Rezzolla, and K. Schwenzer. *Viscous dissipation and heat conduction in binary neutron-star mergers.* Phys. Rev. Lett., 120:041101, Jan 2018.
- **L. Bovard**, D. Martin, F. Guercilena, A. Arcones, L. Rezzolla, and O. Korobkin. *On r-process nucleosynthesis from matter ejected in binary neutron star mergers*. Phys. Rev. D, 96(12): 124005, December 2017.

Bibliography

[1] The Einstein Toolkit Consortium: `einsteintoolkit.org`.

[2] B. P. Abbott, R. Abbott, T. D. Abbott, M. R. Abernathy, F. Acernese, K. Ackley, C. Adams, T. Adams, P. Addesso, R. X. Adhikari, and et al. GW151226: Observation of Gravitational Waves from a 22-Solar-Mass Binary Black Hole Coalescence. *Phys. Rev. Lett.*, 116(24):241103, June 2016.

[3] B. P. Abbott, R. Abbott, T. D. Abbott, M. R. Abernathy, F. Acernese, K. Ackley, C. Adams, T. Adams, P. Addesso, R. X. Adhikari, and et al. Upper Limits on the Rates of Binary Neutron Star and Neutron Star-Black Hole Mergers from Advanced LIGOs First Observing Run. *Astrophys. J. Lett.*, 832:L21, December 2016.

[4] T. Accadia et al. Status of the Virgo project. *Class. Quantum Grav.*, 28(11):114002, June 2011.

[5] A. Akmal, V. R. Pandharipande, and D. G. Ravenhall. Equation of state of nucleon matter and neutron star structure. *Phys. Rev. C*, 58:1804–1828, September 1998.

[6] M. Alcubierre, B. Brügmann, P. Diener, M. Koppitz, D. Pollney, E. Seidel, and R. Takahashi. Gauge conditions for long-term numerical black hole evolutions without excision. *Phys. Rev. D*, 67(8):084023, April 2003.

[7] M. Alford, M. Braby, M. Paris, and S. Reddy. Hybrid Stars that Masquerade as Neutron Stars. *Astrophys. J.*, 629:969–978, August 2005.

[8] M. G. Alford, L. Bovard, M. Hanauske, L. Rezzolla, and K. Schwenzer. On the importance of viscous dissipation and heat conduction in binary neutron-star mergers. *arXiv:1707.09475*, July 2017.

[9] M. G. Alford, L. Bovard, M. Hanauske, L. Rezzolla, and K. Schwenzer. Viscous dissipation and heat conduction in binary neutron-star mergers. *Phys. Rev. Lett.*, 120:041101, Jan 2018.

[10] Mark G. Alford, Simin Mahmoodifar, and Kai Schwenzer. Large amplitude behavior of the bulk viscosity of dense matter. *J. Phys.*, G37:125202, 2010.

[11] D. Alic, C. Bona-Casas, C. Bona, L. Rezzolla, and C. Palenzuela. Conformal and covariant formulation of the Z4 system with constraint-violation damping. *Phys. Rev. D*, 85(6):064040, March 2012.

[12] M. Anderson, E. W. Hirschmann, L. Lehner, S. L. Liebling, P. M. Motl, D. Neilsen, C. Palenzuela, and J. E. Tohline. Simulating binary neutron stars: Dynamics and gravitational waves. *Phys. Rev. D*, 77(2):024006, January 2008.

[13] M. Ansorg, D. Gondek-Rosińska, and L. Villain. On the solution space of differentially rotating neutron stars in general relativity. *Mon. Not. R. Astron. Soc.*, 396:2359–2366, July 2009.

[14] J. Antoniadis, P. C. C. Freire, N. Wex, T. M. Tauris, R. S. Lynch, M. H. van Kerkwijk, M. Kramer, C. Bassa, V. S. Dhillon, T. Driebe, J. W. T. Hessels, V. M. Kaspi, V. I. Kondratiev, N. Langer, T. R. Marsh, M. A. McLaughlin, T. T. Pennucci, S. M. Ransom, I. H. Stairs, J. van Leeuwen, J. P. W. Verbiest, and D. G. Whelan. A Massive Pulsar in a Compact Relativistic Binary. *Science*, 340:448, April 2013.

[15] A. Arcones and F.-K. Thielemann. Neutrino-driven wind simulations and nucleosynthesis of heavy elements. *Journal of Physics G Nuclear Physics*, 40(1):013201, January 2013.

[16] M. Arnould, S. Goriely, and K. Takahashi. The r-process of stellar nucleosynthesis: Astrophysics and nuclear physics achievements and mysteries. *Physics Reports*, 450:97–213, September 2007.

[17] L. Baiotti, R. De Pietri, G. M. Manca, and L. Rezzolla. Accurate simulations of the dynamical bar-mode instability in full general relativity. *Phys. Rev. D*, 75(4):044023, February 2007.

[18] L. Baiotti, B. Giacomazzo, and L. Rezzolla. Accurate evolutions of inspiralling neutron-star binaries: Prompt and delayed collapse to a black hole. *Phys. Rev. D*, 78(8):084033, October 2008.

[19] L. Baiotti, B. Giacomazzo, and L. Rezzolla. Accurate evolutions of inspiralling neutron-star binaries: assessment of the truncation error. *Class. Quantum Grav.*, 26(11):114005, June 2009.

[20] L. Baiotti, I. Hawke, P. J. Montero, F. Löffler, L. Rezzolla, N. Stergioulas, J. A. Font, and E. Seidel. Three-dimensional relativistic simulations of rotating neutron-star collapse to a Kerr black hole. *Phys. Rev. D*, 71(2):024035, January 2005.

[21] L. Baiotti, M. Shibata, and T. Yamamoto. Binary neutron-star mergers with Whisky and SACRA: First quantitative comparison of results from independent general-relativistic hydrodynamics codes. *Phys. Rev. D*, 82(6):064015, September 2010.

[22] Luca Baiotti, Thibault Damour, Bruno Giacomazzo, Alessandro Nagar, and Luciano Rezzolla. Analytic modelling of tidal effects in the relativistic inspiral of binary neutron stars. *Phys. Rev. Lett.*, 105:261101, 2010.

[23] Luca Baiotti and Luciano Rezzolla. Binary neutron-star mergers: a review of Einstein's richest laboratory. *Rept. Prog. Phys.*, 80(9):096901, 2017.

[24] F. Banyuls, J. A. Font, J. M. Ibáñez, J. M. Martí, and J. A. Miralles. Numerical 3+1 general-relativistic hydrodynamics: A local characteristic approach. *Astrophys. J.*, 476:221, 1997.

[25] J. Barnes and D. Kasen. Effect of a High Opacity on the Light Curves of Radioactively Powered Transients from Compact Object Mergers. *Astrophys. J.*, 775:18, September 2013.

[26] J. Barnes, D. Kasen, M.-R. Wu, and G. Martínez-Pinedo. Radioactivity and Thermalization in the Ejecta of Compact Object Mergers and Their Impact on Kilonova Light Curves. *Astrophys. J.*, 829:110, October 2016.

[27] Imre Bartos, Patrick Brady, and Szabolcs Marka. How Gravitational-wave Observations Can Shape the Gamma-ray Burst Paradigm. *Class. Quant. Grav.*, 30:123001, 2013.

[28] T. W. Baumgarte and S. L. Shapiro. Numerical integration of Einstein's field equations. *Phys. Rev. D*, 59(2):024007, January 1999.

[29] T. W. Baumgarte and S. L. Shapiro. *Numerical Relativity: Solving Einstein's Equations on the Computer*. Cambridge University Press, Cambridge, UK, 2010.

[30] T. W. Baumgarte, S. L. Shapiro, and M. Shibata. On the Maximum Mass of Differentially Rotating Neutron Stars. *Astrophys. J. Lett.*, 528:L29–L32, January 2000.

[31] A. Bauswein, S. Goriely, and H.-T. Janka. Systematics of Dynamical Mass Ejection, Nucleosynthesis, and Radioactively Powered Electromagnetic Signals from Neutron-star Mergers. *Astrophys. J.*, 773:78, August 2013.

[32] A. Bauswein and H.-T. Janka. Measuring Neutron-Star Properties via Gravitational Waves from Neutron-Star Mergers. *Phys. Rev. Lett.*, 108(1):011101, January 2012.

[33] A. Bauswein and H.-T. Janka. Measuring Neutron-Star Properties via Gravitational Waves from Neutron-Star Mergers. *Phys. Rev. Lett.*, 108(1):011101, January 2012.

[34] A. Bauswein, H.-T. Janka, K. Hebeler, and A. Schwenk. Equation-of-state dependence of the gravitational-wave signal from the ring-down phase of neutron-star mergers. *Phys. Rev. D*, 86(6):063001, September 2012.

[35] A. M. Beloborodov. Hyper-accreting black holes. In M. Axelsson, editor, *American Institute of Physics Conference Series*, volume 1054 of *American Institute of Physics Conference Series*, pages 51–70, September 2008.

[36] E. Berger. Short-Duration Gamma-Ray Bursts. *Annual Review of Astron. and Astrophys.*, 52:43–105, August 2014.

[37] E. Berger, W. Fong, and R. Chornock. An r-process Kilonova Associated with the Short-hard GRB 130603B. *Astrophys. J.*, 774:L23, September 2013.

[38] Marsha J. Berger and P. Colella. Local adaptive mesh refinement for shock hydrodynamics. *J. Comput. Phys.*, 82:64–84, 1989.

[39] S. Bernuzzi, M. Thierfelder, and B. Brügmann. Accuracy of numerical relativity waveforms from binary neutron star mergers and their comparison with post-Newtonian waveforms. *Phys. Rev. D*, 85(10):104030, May 2012.

[40] L. Bildsten and C. Cutler. Tidal interactions of inspiraling compact binaries. *Astrophys. J.*, 400:175–180, November 1992.

[41] I. Bombaci, D. Logoteta, I. Vidaña, and C. Providência. Quark matter nucleation in neutron stars and astrophysical implications. *European Physical Journal A*, 52:58, March 2016.

[42] C. Bona, T. Ledvinka, C. Palenzuela, and M. Zácek. General-covariant evolution formalism for numerical relativity. *Phys. Rev. D*, 67(10):104005, May 2003.

[43] S. Bose, K. Chakravarti, L. Rezzolla, B. S. Sathyaprakash, and K. Takami. Neutron-star Radius from a Population of Binary Neutron Star Mergers. *arXiv:1705.10850*, May 2017.

[44] L. Bovard, D. Martin, F. Guercilena, A. Arcones, L. Rezzolla, and O. Korobkin. On r-process nucleosynthesis from matter ejected in binary neutron star mergers. *Phys. Rev. D*, 96:124005, December 2017.

[45] L. Bovard and L. Rezzolla. On the use of tracer particles in simulations of binary neutron stars. *Classical and Quantum Gravity*, 34(21):215005, 2017.

[46] L. Bovard and M. L. Waite. Short-wave vortex instability in stratified flow. *ArXiv e-prints*, February 2014.

[47] C. Breu and L. Rezzolla. Maximum mass, moment of inertia and compactness of relativistic stars. *Mon. Not. R. Astron. Soc.*, 459:646–656, June 2016.

[48] David Brown, Peter Diener, Olivier Sarbach, Erik Schnetter, and Manuel Tiglio. Turduckening black holes: an analytical and computational study. *Phys. Rev. D*, 79:044023, 2009.

[49] David Brown, Peter Diener, Olivier Sarbach, Erik Schnetter, and Manuel Tiglio. Turduckening black holes: An analytical and computational study. *Phys. Rev. D*, 79(4):044023, Feb 2009.

[50] David J. Brown. Covariant formulations of Baumgarte, Shapiro, Shibata, and Nakamura and the standard gauge. *Phys. Rev. D*, 79(10):104029, May 2009.

[51] N. Bucciantini, B. D. Metzger, T. A. Thompson, and E. Quataert. Short gamma-ray bursts with extended emission from magnetar birth: jet formation and collimation. *Mon. Not. R. Astron. Soc.*, 419:1537–1545, January 2012.

[52] E. M. Burbidge, G. R. Burbidge, W. A. Fowler, and F. Hoyle. Synthesis of the Elements in Stars. *Rev. Mod. Phys.*, 29:547–650, 1957.

[53] Karen D. Camarda, Peter Anninos, P. Chris Fragile, and Jose A. Font. Dynamical Bar-Mode Instability in Differentially Rotating Magnetized Neutron Stars. *Astrophys. J.*, 707:1610–1622, 2009.

[54] S. M. Carroll. *Spacetime and geometry. An introduction to general relativity*. 2004.

[55] S. Chakrabarti, T. Delsate, N. Gürlebeck, and J. Steinhoff. I-Q Relation for Rapidly Rotating Neutron Stars. *Phys. Rev. Lett.*, 112(20):201102, May 2014.

[56] Hank Childs, Eric Brugger, Brad Whitlock, Jeremy Meredith, Sean Ahern, David Pugmire, Kathleen Biagas, Mark Miller, Cyrus Harrison, Gunther H. Weber, Hari Krishnan, Thomas Fogal, Allen Sanderson, Christoph Garth, E. Wes Bethel, David Camp, Oliver Rübel, Marc Durant, Jean M. Favre, and Paul Navrátil. VisIt: An End-User Tool For Visualizing and Analyzing Very Large Data. In *High Performance Visualization–Enabling Extreme-Scale Scientific Insight*, pages 357–372. Oct 2012.

[57] M. Chruslinska, K. Belczynski, T. Bulik, and W. Gladysz. Constraints on the Formation of Double Neutron Stars from the Observed Eccentricities and Current Limits on Merger Rates. *Acta Astronomica*, 67:37–50, March 2017.

[58] R. Ciolfi, W. Kastaun, B. Giacomazzo, A. Endrizzi, D. M. Siegel, and R. Perna. General relativistic magnetohydrodynamic simulations of binary neutron star mergers forming a long-lived neutron star. *Phys. Rev. D*, 95(6):063016, March 2017.

[59] R. Ciolfi and D. M. Siegel. Short Gamma-Ray Bursts in the "Time-reversal" Scenario. *Astrophys. J.*, 798:L36, January 2015.

[60] J. A. Clark, A. Bauswein, N. Stergioulas, and D. Shoemaker. Observing gravitational waves from the post-merger phase of binary neutron star coalescence. *Class. Quantum Grav.*, 33(8):085003, April 2016.

[61] Phillip Colella and Paul R. Woodward. The piecewise parabolic method (ppm) for gas-dynamical simulations. *Journal of Computational Physics*, 54(1):174–201, 1984.

[62] G. Corvino, L. Rezzolla, S. Bernuzzi, R. De Pietri, and B. Giacomazzo. On the shear instability in relativistic neutron stars. *Class. Quantum Grav.*, 27(11):114104, June 2010.

[63] B. Côté, K. Belczynski, C. L. Fryer, C. Ritter, A. Paul, B. Wehmeyer, and B. W. O'Shea. Advanced LIGO Constraints on Neutron Star Mergers and r-process Sites. *Astrophys. J.*, 836:230, February 2017.

[64] P. S. Cowperthwaite, E. Berger, V. A. Villar, B. D. Metzger, M. Nicholl, R. Chornock, P. K. Blanchard, W. Fong, R. Margutti, M. Soares-Santos,

K. D. Alexander, S. Allam, J. Annis, D. Brout, D. A. Brown, R. E. Butler, H.-Y. Chen, H. T. Diehl, Z. Doctor, M. R. Drout, T. Eftekhari, B. Farr, D. A. Finley, R. J. Foley, J. A. Frieman, C. L. Fryer, J. García-Bellido, M. S. S. Gill, J. Guillochon, K. Herner, D. E. Holz, D. Kasen, R. Kessler, J. Marriner, T. Matheson, E. H. Neilsen, Jr., E. Quataert, A. Palmese, A. Rest, M. Sako, D. M. Scolnic, N. Smith, D. L. Tucker, P. K. G. Williams, E. Balbinot, J. L. Carlin, E. R. Cook, F. Durret, T. S. Li, P. A. A. Lopes, A. C. C. Lourenço, J. L. Marshall, G. E. Medina, J. Muir, R. R. Muñoz, M. Sauseda, D. J. Schlegel, L. F. Secco, A. K. Vivas, W. Wester, A. Zenteno, Y. Zhang, T. M. C. Abbott, M. Banerji, K. Bechtol, A. Benoit-Lévy, E. Bertin, E. Buckley-Geer, D. L. Burke, D. Capozzi, A. Carnero Rosell, M. Carrasco Kind, F. J. Castander, M. Crocce, C. E. Cunha, C. B. D'Andrea, L. N. da Costa, C. Davis, D. L. DePoy, S. Desai, J. P. Dietrich, A. Drlica-Wagner, T. F. Eifler, A. E. Evrard, E. Fernandez, B. Flaugher, P. Fosalba, E. Gaztanaga, D. W. Gerdes, T. Giannantonio, D. A. Goldstein, D. Gruen, R. A. Gruendl, G. Gutierrez, K. Honscheid, B. Jain, D. J. James, T. Jeltema, M. W. G. Johnson, M. D. Johnson, S. Kent, E. Krause, R. Kron, K. Kuehn, N. Nuropatkin, O. Lahav, M. Lima, H. Lin, M. A. G. Maia, M. March, P. Martini, R. G. McMahon, F. Menanteau, C. J. Miller, R. Miquel, J. J. Mohr, E. Neilsen, R. C. Nichol, R. L. C. Ogando, A. A. Plazas, N. Roe, A. K. Romer, A. Roodman, E. S. Rykoff, E. Sanchez, V. Scarpine, R. Schindler, M. Schubnell, I. Sevilla-Noarbe, M. Smith, R. C. Smith, F. Sobreira, E. Suchyta, M. E. C. Swanson, G. Tarle, D. Thomas, R. C. Thomas, M. A. Troxel, V. Vikram, A. R. Walker, R. H. Wechsler, J. Weller, B. Yanny, and J. Zuntz. The Electromagnetic Counterpart of the Binary Neutron Star Merger LIGO/Virgo GW170817. II. UV, Optical, and Near-infrared Light Curves and Comparison to Kilonova Models. *Astrophys. J. Lett.*, 848:L17, October 2017.

[65] R. De Pietri, A. Feo, F. Maione, and F. Löffler. Modeling equal and unequal mass binary neutron star mergers using public codes. *Phys. Rev. D*, 93(6):064047, March 2016.

[66] P. B. Demorest, T. Pennucci, S. M. Ransom, M. S. E. Roberts, and J. W. T. Hessels. A two-solar-mass neutron star measured using Shapiro delay. *Nature*, 467:1081–1083, October 2010.

[67] L. Dessart, C. D. Ott, A. Burrows, S. Rosswog, and E. Livne. Neutrino Signatures and the Neutrino-Driven Wind in Binary Neutron Star Mergers. *Astrophys. J.*, 690:1681–1705, January 2009.

[68] T. Dietrich and M. Ujevic. Modeling dynamical ejecta from binary neutron star mergers and implications for electromagnetic counterparts. *Classical and Quantum Gravity*, 34(10):105014, May 2017.

[69] T. Dietrich, M. Ujevic, W. Tichy, S. Bernuzzi, and B. Brügmann. Gravitational waves and mass ejecta from binary neutron star mergers: Effect of the mass ratio. *Phys. Rev. D*, 95(2):024029, January 2017.

[70] Ray d'Inverno. *Introducing Einstein's Relativity*. Oxford University Press, Oxford, 1992.

[71] D. D. Doneva, S. S. Yazadjiev, N. Stergioulas, and K. D. Kokkotas. Breakdown of I-Love-Q Universality in Rapidly Rotating Relativistic Stars. *Astrophys. J. Letters*, 781:L6, January 2014.

[72] F. Douchin and P. Haensel. A unified equation of state of dense matter and neutron star structure. *Astron. Astrophys.*, 380:151–167, December 2001.

[73] A. Drago and G. Pagliara. Combustion of a hadronic star into a quark star: The turbulent and the diffusive regimes. *Phys. Rev. C*, 92(4):045801, October 2015.

[74] Alessandro Drago and Giuseppe Pagliara. Combustion of a hadronic star into a quark star: The turbulent and the diffusive regimes. *Physical Review C*, 92(4):045801, 2015.

[75] Matthew D. Duez, Yuk Tung Liu, Stuart L. Shapiro, and Branson C. Stephens. General relativistic hydrodynamics with viscosity: Contraction, catastrophic collapse, and disk formation in hypermassive neutron stars. *Phys. Rev. D*, 69:104030, 2004.

[76] M. Dumbser, F. Guercilena, S. Koeppel, L. Rezzolla, and O. Zanotti. A strongly hyperbolic first-order CCZ4 formulation of the Einstein equations and its solution with discontinuous Galerkin schemes. *arXiv:1707.09910*, July 2017.

[77] W. E. East, V. Paschalidis, F. Pretorius, and S. L. Shapiro. Relativistic simulations of eccentric binary neutron star mergers: One-arm spiral instability and effects of neutron star spin. *Phys. Rev. D*, 93(2):024011, January 2016.

[78] D. Eichler, M. Livio, T. Piran, and D. N. Schramm. Nucleosynthesis, neutrino bursts and gamma-rays from coalescing neutron stars. *Nature*, 340:126–128, July 1989.

[79] M. Eichler, A. Arcones, A. Kelic, O. Korobkin, K. Langanke, T. Marketin, G. Martinez-Pinedo, I. Panov, T. Rauscher, S. Rosswog, C. Winteler, N. T. Zinner, and F.-K. Thielemann. The Role of Fission in Neutron Star Mergers and Its Impact on the r-Process Peaks. *Astrophys. J.*, 808:30, July 2015.

[80] J. P. Emerson, W. J. Sutherland, A. M. McPherson, S. C. Craig, G. B. Dalton, and A. K. Ward. The Visible & Infrared Survey Telescope for Astronomy. *The Messenger*, 117:27–32, September 2004.

[81] A. Feo, R. De Pietri, F. Maione, and F. Löffler. Modeling mergers of known galactic systems of binary neutron stars. *Class. Quantum Grav.*, 34(3):034001, February 2017.

[82] R. Fernández and B. D. Metzger. Delayed outflows from black hole accretion tori following neutron star binary coalescence. *Mon. Not. R. Astron. Soc.*, 435:502–517, October 2013.

[83] T. Fischer, S. C. Whitehouse, A. Mezzacappa, F.-K. Thielemann, and M. Liebendörfer. Protoneutron star evolution and the neutrino-driven wind in general relativistic neutrino radiation hydrodynamics simulations. *Astron. Astrophys.*, 517:A80, July 2010.

[84] Tobias Fischer, Matthias Hempel, Irina Sagert, Yudai Suwa, and J¡9f¿rgen Schaffner-Bielich. Symmetry energy impact in simulations of core-collapse supernovae. *Eur. Phys. J.*, A50:46, 2014.

[85] J. A. Font. Numerical hydrodynamics and magnetohydrodynamics in general relativity. *Living Rev. Relativ.*, 6:4; http://www.livingreviews.org/lrr–2008–7, 2008.

[86] F. Foucart, M. Chandra, C. F. Gammie, and E. Quataert. Evolution of accretion discs around a kerr black hole using extended magnetohydrodynamics. *Mon. Not. R. Astron. Soc.*, 456:1332–1345, February 2016.

[87] F. Foucart, M. B. Deaton, M. D. Duez, E. O'Connor, C. D. Ott, R. Haas, L. E. Kidder, H. P. Pfeiffer, M. A. Scheel, and B. Szilagyi. Neutron star-black hole mergers with a nuclear equation of state and neutrino cooling: Dependence in the binary parameters. *Phys. Rev. D*, 90(2):024026, July 2014.

[88] F. Foucart, R. Haas, M. D. Duez, E. O'Connor, C. D. Ott, L. Roberts, L. E. Kidder, J. Lippuner, H. P. Pfeiffer, and M. A. Scheel. Low mass binary neutron star mergers: Gravitational waves and neutrino emission. *Phys. Rev. D*, 93(4):044019, February 2016.

[89] F. Foucart, E. O'Connor, L. Roberts, L. E. Kidder, H. P. Pfeiffer, and M. A. Scheel. Impact of an improved neutrino energy estimate on outflows in neutron star merger simulations. *Phys. Rev. D*, 94(12):123016, December 2016.

[90] L. Franci, R. De Pietri, K. Dionysopoulou, and L. Rezzolla. Bar-mode instability suppression in magnetized relativistic stars. *Journal of Physics Conference Series*, 470(1):012008, December 2013.

[91] C. Freiburghaus, S. Rosswog, and F.-K. Thielemann. R-Process in Neutron Star Mergers. *Astrophys. J. Lett.*, 525:L121–L124, November 1999.

[92] C. Fröhlich, G. Martínez-Pinedo, M. Liebendörfer, F.-K. Thielemann, E. Bravo, W. R. Hix, K. Langanke, and N. T. Zinner. Neutrino-Induced Nucleosynthesis of A>64 Nuclei: The νp Process. *Phys. Rev. Lett.*, 96(14):142502–+, April 2006.

[93] S. Fujibayashi, Y. Sekiguchi, K. Kiuchi, and M. Shibata. Properties of Neutrino-driven Ejecta from the Remnant of Binary Neutron Star Merger : Purely Radiation Hydrodynamics Case. *ArXiv e-prints*, March 2017.

[94] S.-i. Fujimoto, N. Nishimura, and M.-a. Hashimoto. Nucleosynthesis in Magnetically Driven Jets from Collapsars. *Astrophys. J.*, 680:1350–1358, June 2008.

[95] F. Galeazzi, W. Kastaun, L. Rezzolla, and J. A. Font. Implementation of a simplified approach to radiative transfer in general relativity. *Phys. Rev. D*, 88(6):064009, September 2013.

[96] F. Galeazzi, S. Yoshida, and Y. Eriguchi. Differentially-rotating neutron star models with a parametrized rotation profile. *Astron. Astrophys.*, 541:A156, May 2012.

[97] B. Giacomazzo, R. Perna, L. Rezzolla, E. Troja, and D. Lazzati. Compact Binary Progenitors of Short Gamma-Ray Bursts. *Astrophys. J.*, 762:L18, January 2013.

[98] B. Giacomazzo, L. Rezzolla, and N. Stergioulas. Collapse of differentially rotating neutron stars and cosmic censorship. *Phys. Rev. D*, 84(2):024022, July 2011.

[99] N. K. Glendenning. Neutron stars are giant hypernuclei? *Astrophys. J.*, 293:470–493, June 1985.

[100] N. K. Glendenning and S. A. Moszkowski. Reconciliation of neutron-star masses and binding of the lambda in hypernuclei. *Phys. Rev. Lett.*, 67(18):2414–2417, Oct 1991.

[101] D. Gondek-Rosińska, I. Kowalska, L. Villain, M. Ansorg, and M. Kucaba. A New View on the Maximum Mass of Differentially Rotating Neutron Stars. *Astrophys. J.*, 837:58, March 2017.

[102] B. T. Goodwin and C. J. Pethick. Transport properties of degenerate neutrons in dense matter. *Astrophys. J.*, 253:816–838, 1982.

[103] S. Goriely, A. Bauswein, and H.-T. Janka. r-process Nucleosynthesis in Dynamically Ejected Matter of Neutron Star Mergers. *Astrophys. J.*, 738:L32, September 2011.

[104] E. Gourgoulhon, P. Grandclément, K. Taniguchi, J.-A. Marck, and S. Bonazzola. Quasiequilibrium sequences of synchronized and irrotational binary neutron stars in general relativity: Method and tests. *Phys. Rev. D*, 63(6):064029, March 2001.

[105] E. Gourgoulhon, P. Grandclément, K. Taniguchi, J. A. Marck, and S. Bonazzola. Quasiequilibrium sequences of synchronized and irrotational binary neutron stars in general relativity: Method and tests. *Phys. Rev. D*, 63:064029, 2001.

[106] Eric Gourgoulhon. *3+1 Formalism in General Relativity*, volume 846 of *Lecture Notes in Physics, Berlin Springer Verlag*. 2012.

[107] D. Grossman, O. Korobkin, S. Rosswog, and T. Piran. The long-term evolution of neutron star merger remnants - II. Radioactively powered transients. *Mon. Not. R. Astron. Soc.*, 439:757–770, March 2014.

[108] Federico Guercilena, David Radice, and Luciano Rezzolla. Entropy-limited hydrodynamics: a novel approach to relativistic hydrodynamics. *Computational Astrophysics and Cosmology*, 4(1):3, Jul 2017.

[109] P. Haensel, A. Y. Potekhin, and D. G Yakovlev. *Neutron Stars 1*. Springer-Verlag, New York, 1st edition, 2007.

[110] M. Hanauske, K. Takami, L. Bovard, L. Rezzolla, J. A. Font, F. Galeazzi, and H. Stöcker. Rotational properties of hypermassive neutron stars from binary mergers. *Phys. Rev. D*, 96(4):043004, August 2017.

[111] A. Harten, P. D. Lax, and B. van Leer. On upstream differencing and godunov-type schemes for hyperbolic conservation laws. *SIAM Rev.*, 25:35, 1983.

[112] B. Haskell, R. Ciolfi, F. Pannarale, and L. Rezzolla. On the universality of I-Love-Q relations in magnetized neutron stars. *Mon. Not. R. Astron. Soc. Letters*, 438:L71–L75, February 2014.

[113] Matthias Hempel and Jurgen Schaffner-Bielich. Statistical Model for a Complete Supernova Equation of State. *Nucl. Phys.*, A837:210–254, 2010.

[114] K. Hotokezaka, K. Kiuchi, K. Kyutoku, H. Okawa, Y.-i. Sekiguchi, M. Shibata, and K. Taniguchi. Mass ejection from the merger of binary neutron stars. *Phys. Rev. D*, 87(2):024001, January 2013.

[115] X. Y. Hu, N. A. Adams, and C.-W. Shu. Positivity-preserving method for high-order conservative schemes solving compressible Euler equations. *Journal of Computational Physics*, 242:169–180, June 2013.

[116] L. Hüdepohl, B. Müller, H.-T. Janka, A. Marek, and G. G. Raffelt. Erratum: Neutrino signal of electron-capture supernovae from core collapse to cooling [phys. rev. lett. 104, 251101 (2010)]. *Phys. Rev. Lett.*, 105:249901, Dec 2010.

[117] L. Hüdepohl, B. Müller, H.-T. Janka, A. Marek, and G. G. Raffelt. Neutrino signal of electron-capture supernovae from core collapse to cooling. *Phys. Rev. Lett.*, 104:251101, Jun 2010.

[118] J. D. Hunter. Matplotlib: A 2d graphics environment. *Computing In Science & Engineering*, 9(3):90–95, 2007.

[119] H.-Th. Janka, T. Zwerger, and R. Mönchmeyer. Does artificial viscosity destroy prompt type-II supernova explosions? *Astron. Astrophys.*, 268:360–368, February 1993.

[120] A. P. Ji, A. Frebel, A. Chiti, and J. D. Simon. R-process enrichment from a single event in an ancient dwarf galaxy. *Nature*, 531:610–613, March 2016.

[121] Z.-P. Jin, K. Hotokezaka, X. Li, M. Tanaka, P. D'Avanzo, Y.-Z. Fan, S. Covino, D.-M. Wei, and T. Piran. The Macronova in GRB 050709 and the GRB-macronova connection. *Nature Communications*, 7:12898, September 2016.

[122] Z.-P. Jin, X. Li, Z. Cano, S. Covino, Y.-Z. Fan, and D.-M. Wei. The Light Curve of the Macronova Associated with the Long-Short Burst GRB 060614. *Astrophys. J. Lett.*, 811:L22, October 2015.

[123] O. Just, A. Bauswein, R. A. Pulpillo, S. Goriely, and H.-T. Janka. Comprehensive nucleosynthesis analysis for ejecta of compact binary mergers. *Mon. Not. R. Astron. Soc.*, 448:541–567, March 2015.

[124] O. Just, M. Obergaulinger, H.-T. Janka, A. Bauswein, and N. Schwarz. Neutron-star Merger Ejecta as Obstacles to Neutrino-powered Jets of Gamma-Ray Bursts. *Astrophys. J. Lett.*, 816:L30, January 2016.

[125] J. D. Kaplan, C. D. Ott, E. P. O'Connor, K. Kiuchi, L. Roberts, and M. Duez. The Influence of Thermal Pressure on Equilibrium Models of Hypermassive Neutron Star Merger Remnants. *Astrophys. J.*, 790:19, July 2014.

[126] D. Kasen, N. R. Badnell, and J. Barnes. Opacities and Spectra of the r-process Ejecta from Neutron Star Mergers. *Astrophys. J.*, 774:25, September 2013.

[127] W. Kastaun, R. Ciolfi, and B. Giacomazzo. Structure of stable binary neutron star merger remnants: A case study. *Phys. Rev. D*, 94(4):044060, August 2016.

[128] W. Kastaun and F. Galeazzi. Properties of hypermassive neutron stars formed in mergers of spinning binaries. *Phys. Rev. D*, 91(6):064027, March 2015.

[129] W. Kastaun, F. Galeazzi, D. Alic, L. Rezzolla, and J. A. Font. Black hole from merging binary neutron stars: How fast can it spin? *Phys. Rev. D*, 88(2):021501, July 2013.

[130] K. Kiuchi, P. Cerdá-Durán, K. Kyutoku, Y. Sekiguchi, and M. Shibata. Efficient magnetic-field amplification due to the Kelvin-Helmholtz instability in binary neutron star mergers. *Phys. Rev. D*, 92(12):124034, December 2015.

[131] K. Kiuchi, K. Kyutoku, and M. Shibata. Three-dimensional evolution of differentially rotating magnetized neutron stars. *Phys. Rev. D*, 86(6):064008, September 2012.

[132] T. Klahn et al. Constraints on the high-density nuclear equation of state from the phenomenology of compact stars and heavy-ion collisions. *Phys. Rev.*, C74:035802, 2006.

[133] O. Korobkin, S. Rosswog, A. Arcones, and C. Winteler. On the astrophysical robustness of the neutron star merger r-process. *Mon. Not. R. Astron. Soc.*, 426:1940–1949, November 2012.

[134] Heinz Otto Kreiss and Joseph Oliger. *Methods for the approximate solution of time dependent problems*. GARP publication series No. 10, Geneva, 1973.

[135] S. R. Kulkarni. Modeling Supernova-like Explosions Associated with Gamma-ray Bursts with Short Durations. *astro-ph/0510256*, October 2005.

[136] K. Kuroda and LCGT Collaboration. Status of LCGT. *Class. Quantum Grav.*, 27(8):084004, April 2010.

[137] K. Kyutoku, K. Ioka, and M. Shibata. Ultrarelativistic electromagnetic counterpart to binary neutron star mergers. *Mon. Not. R. Astron.Soc.*, 437:L6–L10, January 2014.

[138] J. M. Lattimer, F. Mackie, D. G. Ravenhall, and D. N. Schramm. *Astrophys. J.*, 213:225, 1977.

[139] J. M. Lattimer and D. N. Schramm. Black-hole-neutron-star collisions. *Astrophys. J. Lett.*, 192:L145–L147, September 1974.

[140] James M. Lattimer and F. Douglas Swesty. A generalized equation of state for hot, dense matter. *Nucl. Phys. A*, 535:331–376, 1991.

[141] W. H. Lee, E. Ramirez-Ruiz, and G. van de Ven. Short Gamma-ray Bursts from Dynamically Assembled Compact Binaries in Globular Clusters: Pathways, Rates, Hydrodynamics, and Cosmological Setting. *Astrophys. J.*, 720:953–975, September 2010.

[142] L. Lehner, S. L. Liebling, C. Palenzuela, O. L. Caballero, E. O'Connor, M. Anderson, and D. Neilsen. Unequal mass binary neutron star mergers and multimessenger signals. *Classical and Quantum Gravity*, 33(18):184002, September 2016.

[143] L. Lehner, S. L. Liebling, C. Palenzuela, and P. M. Motl. m =1 instability and gravitational wave signal in binary neutron star mergers. *Phys. Rev. D*, 94(4):043003, August 2016.

[144] K. P. Levenfish and D. G. Yakovlev. Specific heat of neutron star cores with superfluid nucleons. *Astronomy Reports*, 38:247–251, March 1994.

[145] R. J. Leveque. *Finite Volume Methods for Hyperbolic Problems*. Cambridge University Press, New York, 2002.

[146] L.-X. Li and B. Paczyński. Transient Events from Neutron Star Mergers. *Astrophys. J.*, 507:L59–L62, November 1998.

[147] Li-Xin Li and Bohdan Paczynski. Transient events from neutron star mergers. *Astrophys. J.*, 507:L59, 1998.

[148] LIGO Scientific Collaboration, Virgo Collaboration, F. Gamma-Ray Burst Monitor, and INTEGRAL. Gravitational waves and gamma-rays from a binary neutron star merger: Gw170817 and grb 170817a. *Astrophys. J. Lett.*, 848(2):L13, 2017.

[149] J. Lippuner and L. F. Roberts. r-process Lanthanide Production and Heating Rates in Kilonovae. *Astrophys. J.*, 815:82, December 2015.

[150] J. Lippuner and L. F. Roberts. SkyNet: A MODULAR NUCLEAR REACTION NETWORK LIBRARY. 2017.

[151] Yuk Tung Liu, Stuart L. Shapiro, Zachariah B. Etienne, and Keisuke Taniguchi. General relativistic simulations of magnetized binary neutron star mergers. *Phys. Rev. D*, 78:024012, 2008.

[152] F. Löffler, R. De Pietri, A. Feo, F. Maione, and L. Franci. Stiffness effects on the dynamics of the bar-mode instability of neutron stars in full general relativity. *Phys. Rev. D*, 91(6):064057, March 2015.

[153] Frank Löffler, Joshua Faber, Eloisa Bentivegna, Tanja Bode, Peter Diener, Roland Haas, Ian Hinder, Bruno C. Mundim, Christian D. Ott, Erik Schnetter, Gabrielle Allen, Manuela Campanelli, and Pablo Laguna. The Einstein Toolkit: A Community Computational Infrastructure for Relativistic Astrophysics. *Class. Quantum Grav.*, 29(11):115001, 2012.

[154] G. Lugones. From quark drops to quark stars. Some aspects of the role of quark matter in compact stars. *European Physical Journal A*, 52:53, March 2016.

[155] N. D. Lyford, T. W. Baumgarte, and S. L. Shapiro. Effects of Differential Rotation on the Maximum Mass of Neutron Stars. *Astrophys. J.*, 583:410–415, January 2003.

[156] F. Maione, R. De Pietri, A. Feo, and F. Löffler. Binary neutron star merger simulations with different initial orbital frequency and equation of state. *Classical and Quantum Gravity*, 33(17):175009, September 2016.

[157] F. Maione, R. De Pietri, A. Feo, and F. Löffler. Spectral analysis of gravitational waves from binary neutron star merger remnants. *Phys. Rev. D*, 96(6):063011, September 2017.

[158] G. M. Manca, L. Baiotti, R. DePietri, and L. Rezzolla. Dynamical non-axisymmetric instabilities in rotating relativistic stars. *Class. Quantum Grav.*, 24:S171–S186, June 2007.

[159] Cristina Manuel and Laura Tolos. Shear viscosity and the r-mode instability window in superfluid neutron stars. *Phys. Rev.*, D88:043001, 2013.

[160] B. Margalit and B. D. Metzger. Constraining the Maximum Mass of Neutron Stars from Multi-messenger Observations of GW170817. *Astrophys. J. Lett.*, 850:L19, December 2017.

[161] B. Margalit, B. D. Metzger, and A. M. Beloborodov. Does the Collapse of a Supramassive Neutron Star Leave a Debris Disk? *Phys. Rev. Lett.*, 115(17):171101, October 2015.

[162] D. Martin, A. Arcones, W. Nazarewicz, and E. Olsen. Impact of Nuclear Mass Uncertainties on the r Process. *Phys. Rev. Lett.*, 116(12):121101, March 2016.

[163] D. Martin, A. Perego, A. Arcones, O. Korobkin, and F.-K. Thielemann. Nucleosynthesis in the Ejecta of Neutron Star Mergers. *ArXiv e-prints*, September 2015.

[164] D. Martin, A. Perego, A. Arcones, F.-K. Thielemann, O. Korobkin, and S. Rosswog. Neutrino-driven Winds in the Aftermath of a Neutron Star Merger: Nucleosynthesis and Electromagnetic Transients. *Astrophys. J.*, 813:2, November 2015.

[165] A. Maselli, V. Cardoso, V. Ferrari, L. Gualtieri, and P. Pani. Equation-of-state-independent relations in neutron stars. *Phys. Rev. D*, 88(2):023007, July 2013.

[166] P. J. McMillan. Mass models of the Milky Way. *Mon. Not. R. Astron. Soc.*, 414:2446–2457, July 2011.

[167] J. d. J. Mendoza-Temis, M.-R. Wu, K. Langanke, G. Martínez-Pinedo, A. Bauswein, and H.-T. Janka. Nuclear robustness of the r process in neutron-star mergers. *Physical Review C*, 92(5):055805, November 2015.

[168] B. D. Metzger. Kilonovae. *Living Reviews in Relativity*, 20:3, May 2017.

[169] B. D. Metzger. Welcome to the Multi-Messenger Era! Lessons from a Neutron Star Merger and the Landscape Ahead. *ArXiv e-prints*, October 2017.

[170] B. D. Metzger, A. Bauswein, S. Goriely, and D. Kasen. Neutron-powered precursors of kilonovae. *Mon. Not. R. Astron. Soc.*, 446:1115–1120, January 2015.

[171] B. D. Metzger, G. Martínez-Pinedo, S. Darbha, E. Quataert, A. Arcones, D. Kasen, R. Thomas, P. Nugent, I. V. Panov, and N. T. Zinner. Electromagnetic counterparts of compact object mergers powered by the radioactive decay of r-process nuclei. *Mon. Not. R. Astron. Soc.*, 406:2650–2662, August 2010.

[172] B. D. Metzger, A. L. Piro, and E. Quataert. Time-dependent models of accretion discs formed from compact object mergers. *Mon. Not. R. Astron. Soc.*, 390:781–797, October 2008.

[173] B. D. Metzger, E. Quataert, and T. A. Thompson. Short-duration gamma-ray bursts with extended emission from protomagnetar spin-down. *Mon. Not. R. Astron. Soc.*, 385:1455–1460, April 2008.

[174] B. D. Metzger and C. Zivancev. Pair fireball precursors of neutron star mergers. *Mon. Not. R. Astron. Soc.*, 461:4435–4440, October 2016.

[175] V. Mewes, F. Galeazzi, J. A. Font, P. J. Montero, and N. Stergioulas. On the dynamics of tilted black hole-torus systems. *Mon. Not. R. Astron. Soc.*, 461:2480–2489, September 2016.

[176] P. Möller, W. D. Myers, H. Sagawa, and S. Yoshida. New Finite-Range Droplet Mass Model and Equation-of-State Parameters. *Phys. Rev. Lett.*, 108(5):052501, February 2012.

[177] P. Möller, J. R. Nix, W. D. Myers, and W. J. Swiatecki. Nuclear Ground-State Masses and Deformations. *Atomic Data and Nuclear Data Tables*, 59(2):185 – 381, 1995.

[178] P. Möller, B. Pfeiffer, and K.-L. Kratz. New calculations of gross β-decay properties for astrophysical applications: Speeding-up the classical r process. *Physical Review C*, 67(5):055802, May 2003.

[179] P. Mösta, S. Richers, C. D. Ott, R. Haas, A. L. Piro, K. Boydstun, E. Abdikamalov, C. Reisswig, and E. Schnetter. Magnetorotational Core-collapse Supernovae in Three Dimensions. *Astrophys. J. Lett.*, 785:L29, April 2014.

[180] M. R. Mumpower, R. Surman, D.-L. Fang, M. Beard, P. Möller, T. Kawano, and A. Aprahamian. Impact of individual nuclear masses on r -process abundances. *Physical Review C*, 92(3):035807, September 2015.

[181] A. Murguia-Berthier, G. Montes, E. Ramirez-Ruiz, F. De Colle, and W. H. Lee. Necessary Conditions for Short Gamma-Ray Burst Production in Binary Neutron Star Mergers. *Astrophys. J.*, 788:L8, June 2014.

[182] A. Murguia-Berthier, E. Ramirez-Ruiz, G. Montes, F. De Colle, L. Rezzolla, S. Rosswog, K. Takami, A. Perego, and W. H. Lee. The Properties of Short Gamma-Ray Burst Jets Triggered by Neutron Star Mergers. *Astrophys. J. Lett.*, 835:L34, February 2017.

[183] T. Nakamura, K. Oohara, and Y. Kojima. General Relativistic Collapse to Black Holes and Gravitational Waves from Black Holes. *Progress of Theoretical Physics Supplement*, 90:1–218, 1987.

[184] R. Narayan, B. Paczynski, and T. Piran. Gamma-ray bursts as the death throes of massive binary stars. *Astrophys. J. Lett.*, 395:L83–L86, August 1992.

[185] N. Nishimura, H. Sawai, T. Takiwaki, S. Yamada, and F.-K. Thielemann. The Intermediate r-process in Core-collapse Supernovae Driven by the Magneto-rotational Instability. *Astrophys. J. Lett.*, 836:L21, February 2017.

[186] C. D. Ott, A. Burrows, T. A. Thompson, E. Livne, and R. Walder. The Spin Periods and Rotational Profiles of Neutron Stars at Birth. *Astrophys. J. Suppl. Ser.*, 164:130, May 2006.

[187] C. Palenzuela, S. L. Liebling, D. Neilsen, L. Lehner, O. L. Caballero, E. O'Connor, and M. Anderson. Effects of the microphysical equation of state in the mergers of magnetized neutron stars with neutrino cooling. *Phys. Rev. D*, 92(4):044045, August 2015.

[188] I. V. Panov, E. Kolbe, B. Pfeiffer, T. Rauscher, K.-L. Kratz, and F.-K. Thielemann. Calculations of fission rates for r-process nucleosynthesis. *Nuclear Physics A*, 747:633–654, January 2005.

[189] I. V. Panov, I. Y. Korneev, T. Rauscher, G. Martínez-Pinedo, A. Kelić-Heil, N. T. Zinner, and F.-K. Thielemann. Neutron-induced astrophysical reaction rates for translead nuclei. *Astron. Astrophys.*, 513:A61, April 2010.

[190] Ludwig Jens Papenfort, Luciano Rezzolla, and *et al.* Dynamics, mass ejection and nucleosynthesis from dynamical encounters of binary neutron stars. *in preparation*, 2017.

[191] G. Pappas and T. A. Apostolatos. Effectively Universal Behavior of Rotating Neutron Stars in General Relativity Makes Them Even Simpler than Their Newtonian Counterparts. *Phys. Rev. Lett.*, 112(12):121101, March 2014.

[192] V. Paschalidis. General relativistic simulations of compact binary mergers as engines for short gamma-ray bursts. *Classical and Quantum Gravity*, 34(8):084002, April 2017.

[193] V. Paschalidis, Z. B. Etienne, and S. L. Shapiro. Importance of cooling in triggering the collapse of hypermassive neutron stars. *Phys. Rev. D*, 86(6):064032, September 2012.

[194] A. Perego, S. Rosswog, R. M. Cabezón, O. Korobkin, R. Käppeli, A. Arcones, and M. Liebendörfer. Neutrino-driven winds from neutron star merger remnants. *Mon. Not. R. Astron. Soc.*, 443:3134–3156, October 2014.

[195] C. E. Petrillo, A. Dietz, and M. Cavaglià. Compact Object Coalescence Rate Estimation from Short Gamma-Ray Burst Observations. *Astrophys. J.*, 767:140, April 2013.

[196] T. Piran, E. Nakar, and S. Rosswog. The electromagnetic signals of compact binary mergers. *Mon. Not. R. Astron. Soc.*, 430:2121–2136, April 2013.

[197] Eric Poisson. *A Relativist's Toolkit: The Mathematics of Black-Hole Mechanics*. Cambridge University Press, 2004.

[198] D. Pollney, C. Reisswig, L. Rezzolla, B. Szilágyi, M. Ansorg, B. Deris, P. Diener, E. N. Dorband, M. Koppitz, A. Nagar, and E. Schnetter. Recoil velocities from equal-mass binary black-hole mergers: A systematic investigation of spin-orbit aligned configurations. *Phys. Rev. D*, 76(12):124002, December 2007.

[199] Michele Punturo et al. The third generation of gravitational wave observatories and their science reach. *Class. Quantum Grav.*, 27(8):084007, April 2010.

[200] D. Radice, S. Bernuzzi, and C. D. Ott. One-armed spiral instability in neutron star mergers and its detectability in gravitational waves. *Phys. Rev. D*, 94(6):064011, September 2016.

[201] D. Radice, F. Galeazzi, J. Lippuner, L. F. Roberts, C. D. Ott, and L. Rezzolla. Dynamical Mass Ejection from Binary Neutron Star Mergers. *Mon. Not. R. Astron. Soc.*, 460:3255–3271, August 2016.

[202] D. Radice and L. Rezzolla. THC: a new high-order finite-difference high-resolution shock-capturing code for special-relativistic hydrodynamics. *Astron. Astrophys.*, 547:A26, June 2012.

[203] D. Radice, L. Rezzolla, and F. Galeazzi. Beyond second-order convergence in simulations of binary neutron stars in full general-relativity. *Mon. Not. R. Astron. Soc. L.*, 437:L46–L50, June 2014.

[204] D. Radice, L. Rezzolla, and F. Galeazzi. High-order fully general-relativistic hydrodynamics: new approaches and tests. *Class. Quantum Grav.*, 31(7):075012, April 2014.

[205] T. Rauscher and F.-K. Thielemann. Astrophysical Reaction Rates From Statistical Model Calculations. *Atomic Data and Nuclear Data Tables*, 75:1–351, May 2000.

[206] J. S. Read, B. D. Lackey, B. J. Owen, and J. L. Friedman. Constraints on a phenomenologically parametrized neutron-star equation of state. *Phys. Rev. D*, 79(12):124032, June 2009.

[207] Sanjay Reddy, Madappa Prakash, and James M Lattimer. Neutrino interactions in hot and dense matter. *Phys. Rev.*, D58:013009, 1998.

[208] C. Reisswig and D. Pollney. Notes on the integration of numerical relativity waveforms. *Class. Quantum Grav.*, 28:195015, 2011.

[209] L. Rezzolla, L. Baiotti, B. Giacomazzo, D. Link, and J. A. Font. Accurate evolutions of unequal-mass neutron-star binaries: properties of the torus and short GRB engines. *Class. Quantum Grav.*, 27(11):114105, June 2010.

[210] L. Rezzolla, B. Giacomazzo, L. Baiotti, J. Granot, C. Kouveliotou, and M. A. Aloy. The Missing Link: Merging Neutron Stars Naturally Produce Jet-like Structures and Can Power Short Gamma-ray Bursts. *Astrophys. J. Letters*, 732:L6, May 2011.

[211] L. Rezzolla and P. Kumar. A Novel Paradigm for Short Gamma-Ray Bursts With Extended X-Ray Emission. *Astrophys. J.*, 802:95, April 2015.

[212] L. Rezzolla and K. Takami. Gravitational-wave signal from binary neutron stars: A systematic analysis of the spectral properties. *Phys. Rev. D*, 93(12):124051, June 2016.

[213] L. Rezzolla and O. Zanotti. *Relativistic Hydrodynamics*. Oxford University Press, Oxford, UK, 2013.

[214] L. F. Roberts, D. Kasen, W. H. Lee, and E. Ramirez-Ruiz. Electromagnetic Transients Powered by Nuclear Decay in the Tidal Tails of Coalescing Compact Binaries. *Astrophys. J. Lett.*, 736:L21, July 2011.

[215] Luke F. Roberts and Sanjay Reddy. Charged current neutrino interactions in hot and dense matter. *Phys. Rev.*, C95(4):045807, 2017.

[216] S. Rosswog. The dynamic ejecta of compact object mergers and eccentric collisions. *Royal Society of London Philosophical Transactions Series A*, 371:20272, April 2013.

[217] S. Rosswog. The multi-messenger picture of compact binary mergers. *International Journal of Modern Physics D*, 24:1530012–52, February 2015.

[218] S. Rosswog and M. B. Davies. High-resolution calculations of merging neutron stars - I. Model description and hydrodynamic evolution. *Mon. Not. R. Astron. Soc.*, 334:481–497, August 2002.

[219] S. Rosswog, U. Feindt, O. Korobkin, M.-R. Wu, J. Sollerman, A. Goobar, and G. Martinez-Pinedo. Detectability of compact binary merger macronovae. *Classical and Quantum Gravity*, 34(10):104001, May 2017.

[220] S. Rosswog, O. Korobkin, A. Arcones, F.-K. Thielemann, and T. Piran. The long-term evolution of neutron star merger remnants - I. The impact of r-process nucleosynthesis. *Mon. Not. R. Astron. Soc.*, 439:744–756, March 2014.

[221] S. Rosswog, M. Liebendörfer, F.-K. Thielemann, M. B. Davies, W. Benz, and T. Piran. Mass ejection in neutron star mergers. *Astron. Astrophys.*, 341:499–526, January 1999.

[222] S. Rosswog, T. Piran, and E. Nakar. The multimessenger picture of compact object encounters: binary mergers versus dynamical collisions. *Mon. Not. R. Astron. Soc.*, 430:2585–2604, April 2013.

[223] Stephan Rosswog. Mergers of neutron star black hole binaries with small mass ratios: nucleosynthesis, gamma-ray bursts and electromagnetic transients. *Astrophys. J.*, 634:1202, 2005.

[224] Olivier Sarbach and Manuel Tiglio. Continuum and discrete initial-boundary value problems and einstein's field equations. *Living Rev. Relativity*, 15(9), 2012.

[225] R. F. Sawyer. Bulk viscosity of hot neutron-star matter and the maximum rotation rates of neutron stars. *Phys. Rev. D*, 39:3804–3806, June 1989.

[226] E. Schnetter, S. H. Hawley, and I. Hawke. Evolutions in 3D numerical relativity using fixed mesh refinement. *Class. Quantum Grav.*, 21:1465–1488, March 2004.

[227] Bernard F. Schutz. *A first course in general relativity*. Cambridge University Press, 1985.

[228] Y. Sekiguchi, K. Kiuchi, K. Kyutoku, and M. Shibata. Dynamical mass ejection from binary neutron star mergers: Radiation-hydrodynamics study in general relativity. *Phys. Rev. D*, 91(6):064059, March 2015.

[229] Y. Sekiguchi, K. Kiuchi, K. Kyutoku, M. Shibata, and K. Taniguchi. Dynamical mass ejection from the merger of asymmetric binary neutron stars: Radiation-hydrodynamics study in general relativity. *Phys. Rev. D*, 93(12):124046, June 2016.

[230] Stuart L. Shapiro and Saul A. Teukolsky. *Black Holes, White Dwarfs, and Neutron Stars*. John Wiley & Sons, New York, 1983.

[231] G. Shen, C. J. Horowitz, and S. Teige. Equation of state of dense matter from a density dependent relativistic mean field model. *Physical Review C*, 82(1):015806, July 2010.

[232] G. Shen, C. J. Horowitz, and S. Teige. New equation of state for astrophysical simulations. *Physical Review C*, 83(3):035802, March 2011.

[233] M. Shibata. *Numerical Relativity*. World Scientific, Singapore, 2016.

[234] M. Shibata and K. Kiuchi. Gravitational waves from remnant massive neutron stars of binary neutron star merger: Viscous hydrodynamics effects. *arXiv:1705.06142*, May 2017.

[235] M. Shibata, K. Kiuchi, Y. Sekiguchi, and Y. Suwa. Truncated Moment Formalism for Radiation Hydrodynamics in Numerical Relativity. *Progress of Theoretical Physics*, 125:1255–1287, June 2011.

[236] M. Shibata and T. Nakamura. Evolution of three-dimensional gravitational waves: Harmonic slicing case. *Phys. Rev. D*, 52:5428–5444, November 1995.

[237] M. Shibata, Y. Suwa, K. Kiuchi, and K. Ioka. Afterglow of a Binary Neutron Star Merger. *Astrophys. J.l*, 734:L36, June 2011.

[238] M. Shibata and K. Taniguchi. Merger of binary neutron stars to a black hole: Disk mass, short gamma-ray bursts, and quasinormal mode ringing. *Phys. Rev. D*, 73(6):064027, March 2006.

[239] M. Shibata, K. Taniguchi, and K. Uryū. Merger of binary neutron stars of unequal mass in full general relativity. *Phys. Rev. D*, 68(8):084020, October 2003.

[240] M. Shibata, K. Taniguchi, and K. Uryū. Merger of binary neutron stars with realistic equations of state in full general relativity. *Phys. Rev. D*, 71(8):084021, April 2005.

[241] M. Shibata and K. Uryū. Simulation of merging binary neutron stars in full general relativity: Γ=2 case. *Phys. Rev. D*, 61(6):064001, March 2000.

[242] P. S. Shternin and D. G. Yakovlev. Shear viscosity in neutron star cores. *Phys. Rev.*, D78:063006, 2008.

[243] P.S. Shternin and D.G. Yakovlev. Electron-muon heat conduction in neutron star cores via the exchange of transverse plasmons. *Phys.Rev.*, D75:103004, 2007.

[244] D. M. Siegel, R. Ciolfi, A. I. Harte, and L. Rezzolla. Magnetorotational instability in relativistic hypermassive neutron stars. *Phys. Rev. D R*, 87(12):121302, June 2013.

[245] D. M. Siegel, R. Ciolfi, and L. Rezzolla. Magnetically Driven Winds from Differentially Rotating Neutron Stars and X-Ray Afterglows of Short Gamma-Ray Bursts. *Astrophys. J.*, 785:L6, April 2014.

[246] D. M. Siegel and B. D. Metzger. Three-dimensional GRMHD simulations of the remnant accretion disks from neutron star mergers: outflows and r-process nucleosynthesis. *ArXiv e-prints*, May 2017.

[247] M. F. Skrutskie, R. M. Cutri, R. Stiening, M. D. Weinberg, S. Schneider, J. M. Carpenter, C. Beichman, R. Capps, T. Chester, J. Elias, J. Huchra, J. Liebert, C. Lonsdale, D. G. Monet, S. Price, P. Seitzer, T. Jarrett, J. D. Kirkpatrick, J. E. Gizis, E. Howard, T. Evans, J. Fowler, L. Fullmer, R. Hurt, R. Light, E. L. Kopan, K. A. Marsh, H. L. McCallon, R. Tam, S. Van Dyk, and S. Wheelock. The Two Micron All Sky Survey (2MASS). *Astronomical Journal*, 131:1163–1183, February 2006.

[248] L. C. Stein, K. Yagi, and N. Yunes. Three-hair Relations for Rotating Stars: Nonrelativistic Limit. *Astrophys. J.*, 788:15, June 2014.

[249] A. W. Steiner, M. Hempel, and T. Fischer. Core-collapse Supernova Equations of State Based on Neutron Star Observations. *Astrophys. J.*, 774:17, September 2013.

[250] Stellarcollapse. `https://stellarcollapse.org/`.

[251] N. Stergioulas, A. Bauswein, K. Zagkouris, and H.-T. Janka. Gravitational waves and non-axisymmetric oscillation modes in mergers of compact object binaries. *Mon. Not. R. Astron. Soc.*, 418:427–436, November 2011.

[252] A. M. Studzińska, M. Kucaba, D. Gondek-Rosińska, L. Villain, and M. Ansorg. Effect of the equation of state on the maximum mass of differentially rotating neutron stars. *Mon. Not. R. Astron. Soc.*, 463:2667–2679, December 2016.

[253] A. Suresh and H. T. Huynh. Accurate monotonicity-preserving schemes with runge-kutta time stepping. *Journal of Computational Physics*, 136(1):83–99, 1997.

[254] K. Takami, L. Rezzolla, and L. Baiotti. Constraining the Equation of State of Neutron Stars from Binary Mergers. *Phys. Rev. Lett.*, 113(9):091104, August 2014.

[255] K. Takami, L. Rezzolla, and L. Baiotti. Constraining the Equation of State of Neutron Stars from Binary Mergers. *Phys. Rev. Lett.*, 113(9):091104, August 2014.

[256] K. Takami, L. Rezzolla, and L. Baiotti. Spectral properties of the post-merger gravitational-wave signal from binary neutron stars. *Phys. Rev. D*, 91(6):064001, March 2015.

[257] K. Takami, L. Rezzolla, and S. Yoshida. A quasi-radial stability criterion for rotating relativistic stars. *Mon. Not. R. Astron. Soc.*, 416:L1–L5, September 2011.

[258] M. Tanaka. Kilonova/Macronova Emission from Compact Binary Mergers. *Advances in Astronomy*, 2016:634197, 2016.

[259] M. Tanaka and K. Hotokezaka. Radiative Transfer Simulations of Neutron Star Merger Ejecta. *Astrophys. J.*, 775:113, October 2013.

[260] N. R. Tanvir, A. J. Levan, A. S. Fruchter, J. Hjorth, R. A. Hounsell, K. Wiersema, and R. L. Tunnicliffe. A ‘kilonova’ associated with the short-duration γ-ray burst GRB130603B. *Nature*, 500:547–549, August 2013.

[261] I. Tews, J. M. Lattimer, A. Ohnishi, and E. E. Kolomeitsev. Symmetry Parameter Constraints From A Lower Bound On The Neutron-Matter Energy. *ArXiv e-prints*, November 2016.

[262] The LIGO Scientific Collaboration and the Virgo Collaboration. Observation of Gravitational Waves from a Binary Black Hole Merger. *Phys. Rev. Lett.*, 116(6):061102, February 2016.

[263] The LIGO Scientific Collaboration and The Virgo Collaboration. Gw170817: Observation of gravitational waves from a binary neutron star inspiral. *Phys. Rev. Lett.*, 119:161101, Oct 2017.

[264] The LIGO Scientific Collaboration, the Virgo Collaboration, B. P. Abbott, R. Abbott, T. D. Abbott, F. Acernese, K. Ackley, C. aAdams, T. Adams, P. Addesso, and et al. Multi-messenger observations of a binary neutron star merger. *Astrophys. J. Lett.*, 848(2):L12, 2017.

[265] The LIGO Scientific Collaboration, the Virgo Collaboration, B. P. Abbott, R. Abbott, T. D. Abbott, F. Acernese, K. Ackley, C. Adams, T. Adams, P. Addesso, and et al. Estimating the Contribution of Dynamical Ejecta in the Kilonova Associated with GW170817. *ArXiv e-prints*, October 2017.

[266] The LIGO Scientific Collaboration, the Virgo Collaboration, B. P. Abbott, R. Abbott, T. D. Abbott, F. Acernese, K. Ackley, C. Adams, T. Adams, P. Addesso, and et al. GW170104: Observation of a 50-Solar-Mass Binary Black Hole Coalescence at Redshift 0.2. *ArXiv e-prints*, June 2017.

[267] F. X. Timmes and Dave Arnett. The accuracy, consistency, and speed of five equations of state for stellar hydrodynamics. *Astrophysical Journal, Supplement Series*, 125(1):277–294, 11 1999.

[268] F. X. Timmes and F. D. Swesty. The Accuracy, Consistency, and Speed of an Electron-Positron Equation of State Based on Table Interpolation of the Helmholtz Free Energy. *Astrophysical Journal, Supplement*, 126:501–516, February 2000.

[269] S. Typel, G. Röpke, T. Klähn, D. Blaschke, and H. H. Wolter. Composition and thermodynamics of nuclear matter with light clusters. *Phys. Rev. C*, 81(1):015803, January 2010.

[270] Stefan van der Walt, S. Chris Colbert, and Gaël Varoquaux. The numpy array: A structure for efficient numerical computation. *Computing in Science & Engineering*, 13(2):22–30, 2011.

[271] Robert M. Wald. *General relativity*. The University of Chicago Press, Chicago, 1984.

[272] S. Wanajo, Y. Sekiguchi, N. Nishimura, K. Kiuchi, K. Kyutoku, and M. Shibata. Production of All the r-process Nuclides in the Dynamical Ejecta of Neutron Star Mergers. *Astrophys. J.*, 789:L39, July 2014.

[273] Shinya Wanajo. The r-process in proto-neutron-star wind revisited. *Astrophys. J. Lett.*, 770(2):L22, 2013.

[274] C. Winteler, R. Käppeli, A. Perego, A. Arcones, N. Vasset, N. Nishimura, M. Liebendörfer, and F.-K. Thielemann. Magnetorotationally Driven Supernovae as the Origin of Early Galaxy r-process Elements? *Astrophys. J. Lett.*, 750:L22, May 2012.

[275] R. T. Wollaeger, O. Korobkin, C. J. Fontes, S. K. Rosswog, W. P. Even, C. L. Fryer, J. Sollerman, A. L. Hungerford, D. R. van Rossum, and A. B. Wollaber. Impact of ejecta morphology and composition on the electromagnetic signatures of neutron star mergers. *ArXiv e-prints*, May 2017.

[276] K. Yagi and N. Yunes. I-Love-Q relations in neutron stars and their applications to astrophysics, gravitational waves, and fundamental physics. *Phys. Rev. D*, 88(2):023009, July 2013.

[277] B. Yang, Z.-P. Jin, X. Li, S. Covino, X.-Z. Zheng, K. Hotokezaka, Y.-Z. Fan, T. Piran, and D.-M. Wei. A possible macronova in the late afterglow of the long-short burst GRB 060614. *Nature Communications*, 6:7323, June 2015.

[278] B. Zhang and P. Mészáros. Gamma-Ray Burst Afterglow with Continuous Energy Injection: Signature of a Highly Magnetized Millisecond Pulsar. *Astrophys. J.*, 552:L35–L38, May 2001.